ISBN 978-84-92774-06-7

Prensas Universitarias de Zaragoza

Structural, magnetic and electronic properties of Re-based double perovskites

Colección de Estudios de Física

Vol. 77

Esta colección recoge las tesis presentadas en el Departamento de Física de la Materia Condensada de la Universidad de Zaragoza desde su constitución en 1987.

Colección de Estudios de Física Vol. 77

Structural, magnetic and electronic properties of Re-based double perovskites

Jan Marek Michalik

Prensas Universitarias de Zaragoza

Aquí va la hoja de créditos...

MOJEJ ŻONIE I CÓRCE

MICHALIK, Jan Marek

Structural, magnetic and electronic properties of Re-based double perovskites / Jan Marek Michalik. — Zaragoza : Prensas Universitarias de Zaragoza, 2009
XVI, 225 p. ; 24 cm. — (Colección de Estudios de Física ; 77)
Bibliografía: p. 199-210. — ISBN 978-84-92774-06-7

Perovskita–Tesis doctorales

549.641(043.2)

1.ª edición, 2009

Prensas Universitarias de Zaragoza. Edificio de Ciencias Geológicas, c/ Pedro Cerbuna, 12, 50009 Zaragoza, España. Tel.: 976 761 330. Fax: 976 761 063
puz@unizar.es http://puz.unizar.es

Impreso en España
Imprime: Servicio de Publicaciones. Universidad de Zaragoza
D.L.: Z-2298/2009

Index

Preface

Oxide half metals, i.e. materials with only one spin direction present in the Fermi level either parallel or antiparallel to the magnetization direction are being actively studied due to their potential applications in Spin Electronics. Among them, ferromagnetic double perovskites have attracted a lot of interest due to their high Curie temperature (T_C) and predicted half-metallicity. Re-based compounds are the most promising ones among the double perovskite family, exhibiting high Curie temperature up to 620 K.

In this Thesis the results of a study of the Re-based double perovskites will be presented. In the first chapter theoretical descriptions of the effects present in the double perovskite systems will be presented. Then, a short overview of the available data on the double perovskites will be given in order to explain the interesting properties exhibited by those compounds on the one hand, and allow better understanding of our results on the other.

During our study we have used a wide range of experimental methods available either in our laboratory or in large experimental facilities. The overview of the techniques involved in the study is presented in the second chapter of this thesis. A short description of the data collection and treatment is also given in this chapter, as well, with the aim of clarification of any doubts that may arise during reading.

Chapters three and four deal with the experimental results of the CrRe and FeRe based compounds respectively. We have decided to divide the experimental material in those two parts for easier handling of the large amount of data obtained. Both sections include the structural characterization of the samples studied by means of diffraction methods. The magnetic properties are characterized by means of both low and high (pulsed and static) fields magnetometry. In both cases a local probe method,

X-ray Magnetic Circular Dichroism was applied, in order to reveal the local magnetic moments arrangement, being of crucial importance for understanding the bulk magnetometry results.

In the fifth chapter the study of the electron doping of the Sr_2CrReO_6 double perovskite is addressed. The aim of such procedure and the difficulties found in the case of the chosen materials are highlighted. Models proposed in the text are verified on the basis of the diffraction, electron microscopy, fluorescence, magnetometry, XANES and EXAFS analysis.

Finally, a summary of the work and conclusions are comprised in a separate chapter. References are all collected in one last section for an easier handling of Bibliography. A list of abbreviations is also included at the end of the manuscript.

The preparation of this Thesis would not have been possible without the support of the directors: Prof. Czesław Kapusta (AGH – University of Science and Technology, Cracow, Poland) and Dr. José María De Teresa (ICMA, CSIC - University of Zaragoza, Spain). I am very grateful for the discussions, suggestions and their help with organizing the experimental work, analysing the data and writing this manuscript.

My stay at CSIC - University of Zaragoza in the Magnetism group would not have been possible without the support of Professor Ricardo M. Ibarra and Professor Pedro Algarabel as well as Dr. Clara Marquina who coordinated the SCOOTMO project (HPRN-CT-2002-00293) and who invited me to join the research team at Zaragoza. At this point, I should also mention the assistance of Mª Jesús García Lobera with organizing my collaboration with the University from the administration point of view.

I have to show gratitude for the sample preparation carried out by Dr. Javier Blasco and Rosa Córdoba. Without their knowledge and experience on the double perovskites synthesis the work would have been much more complicated.

I would like to express thanks to Dr. Clemens Ritter from Institut Laue-Langevin, Grenoble, France for his effort in the Neutron Powder Diffraction experiments together with the data analysis and indications. The collaboration on X-ray Absorption study of Prof. Joaquín García, Dr. Javier Blasco and Dr. Gloria Subías is appreciated as well. Fruitful discussions with Dr. Marcin Sikora, European Synchrotron Radiation Facility, Grenoble, France, his help with the preparation and performing of the XMCD experiments and the data analysis are also acknowledged.

Dr. Javier Blasco is also acknowledged for the collaboration on the diffraction patterns refinements and a lot of hints for making as much use of the data as possible.

I am grateful to Dr. David Serrate for introducing me to the subject of double perovskites, the research he was carrying out at the time I was starting the investigation at the CSIC - University of Zaragoza, fruitful discussions and his help whenever it was necessary.

I appreciate the experimental time at the Scanning Electron Microscopy Laboratory of the Jagiellonian University, Cracow, Poland given by Dr. Marek Michalik.

The collaboration on the anisotropy effects studies by means of Singular Point Detection methods with the group of IMEM del CNR Institute, Parma, Italy is kindly acknowledged.

Although not all the work we did together is included in this Thesis I have to recall Carlos Martín Sacristán (for his help at the laboratory and out-of-research talks we have had) and Amalio Fernández-Pacheco Chicón (my comrade-in-arms at the CCR laboratory battlefield). How wouldn't I mention my officemate Sergio Gutiérrez who had to suffer my poor Spanish and afternoon calls from my family abroad.

Also not included in this manuscript, but giving me an important experience on the wet chemistry synthesis routes, I acknowledge the collaboration with Prof. Mieczysław Rękas, AGH – University of Science and Technology, Cracow, Poland.

I would like to show appreciation for the contribution of the technical staff of the laboratories (all the people I haven't mention by name) we have been visiting during the gathering of the experimental material necessary in order to accomplish this Thesis: at University of Zaragoza, Spain; European Synchrotron Radiation Facility (beamlines BM29 and ID24), Grenoble, France; Solid State Physics and Materials Research (IFW), Dresden, Germany; High Field Magnet Laboratory (HFML), University of Nijmegen, Netherlands.

I should also acknowledge financial support obtained for scientific research from various institutions: SCOOTMO (HPRN-CT-2002-00293), EuroMagNET under the EU contract RII3-CT-2004-506239, and DGA (CAMRADS and PIP018/2005), Polish Ministry of Science and Higher Education, Spanish Ministry of Science (through projects MAT2005-05565-C02-02 and MAT2005-01221 including FEDER funding), European Synchrotron Radiation Facility (through the peer reviewed project MI739).

Last but not the least I have to show my sincere gratitude to Monika, my wife, for staying by me at difficult times of my research fellowship at Zaragoza, supporting me and believing my work would finally end with this manuscript. I cannot forget about my daughter, Marysia, who gave me a lot of happiness and the motivation for further work. I have to mention as well the support of my parents and parents-in-law who kept encouraging me for going on with the doctorate work.

Chapter 1

Theoretical introduction

In the following chapter the physics underlying the properties of the Re-based double perovskites will be introduced. The interest in those compounds emerged rapidly owing to their expected application in spin electronics. This requires polarized electric currents to be generated, transferred and detected. When dealing with spin polarised currents one should consider, apart from the properties like intensity or frequency of the current, the spin of the carrier. This new degree of freedom causes the existence of an additional scattering source of magnetic origin. Apart from the scattering on defects and phonons (thermally activated lattice vibrations) the interaction with magnetic moments takes place. This can be modified by an external magnetic field, the concept of the magnetoresistance emerging. The problem of the spin polarization of electric carriers is discussed in the subsection 1.1 - Spin polarization. Different types of magnetoresistance effects are addressed in the subsection 1.2 - Magnetoresistance (see page 6).

During our study, the importance of the orbital magnetic moment contribution to the overall saturation magnetization will be highlighted. The problem of the spin and orbital moments as well as the coupling of the two is raised in the subsection 1.3 - Spin - Orbit coupling (see page 16).

The importance of the Magnetocrystalline Anisotropy resulting from a strong lattice – magnetic moment coupling is discussed in the subsection 1.4. - Magneto-crystalline anisotropy.

The origin of the large saturation magnetization as well as its thermal variation have been investigated. Apart from the magneto-structural interplay and the thermally activated disorder of the magnetic moments other processes contribute to the lowering

of the saturation magnetization value. For the explanation of the observed behaviour we have introduced the Bloch model of the spin-wave excitations (see subsection 1.5 - Thermally assisted demagnetisation: spin waves).

In the last subsection of this chapter (1.6 - Modern materials for spin electronics) the materials with double perovskite crystallographic structure will be introduced.

1.1. Spin polarization

The energy spectrum of a free atom is changed drastically when it is assembled in the solid. In the free atom, electrons occupy available states compatible with quantum-mechanics rules that correspond to discrete energy levels. In the solid, those energy levels join together forming an energy band, being described through the density of sates (DOS). According to Pauli's principle only one electron can be described by a set of same quantum numbers (called a quantum state). The maximum number of electrons occupying a given shell is equal to $2n^2$, n being the principal quantum number. The spin quantum number m_s describes the electron spin s component along a particular direction (that can be chosen as a net magnetization direction). Hereafter we will refer to the electrons with spin pointing parallel to the net magnetization as spin-up electrons, and the opposite as spin-down electrons. The spin of the electron is an intrinsic property (angular momentum) related to its rotation (or spinning) about an internal axis. The allowed values of m_s are $\pm\frac{1}{2}$ corresponding to $\pm\frac{\hbar}{2}$ component of the spin angular momentum. Different spin states can possess the same energy, becoming degenerated states. The energy of the highest occupied level at $T = 0$ K is called the Fermi energy.

We can now calculate $N(E)$, the density of electronic states having energy between E and $E + dE$. Performing this operation separately for the spin-up (↑) and spin-down (↓) electrons we obtain the definition of the spin polarization at certain energy:

$$P(E) = \frac{N_{\uparrow}(E) - N_{\downarrow}(E)}{N_{\uparrow}(E) + N_{\downarrow}(E)} \tag{1.1}$$

In many Spin-Electronics devices the spin polarization at the Fermi energy (E_F) determines the magnetoelectronic properties. This is the case, for example, of magnetic tunnel junctions. This is the reason for the great importance of the spin polarization at the Fermi level [1, 2].

$$P(E_F) = \frac{N_{\uparrow}(E_F) - N_{\downarrow}(E_F)}{N_{\uparrow}(E_F) + N_{\downarrow}(E_F)} \tag{1.2}$$

As can be seen from equations (1.1) and (1.2) P can take any value between –1 and +1. The limit values (± 1) are characteristic for the class of material called half metals. De Groot pioneered the concept of half-metallicity in Mn-based Heusler alloys [3]. The technological importance of this class of compounds arises mainly from their potential applications in spin-electronics. There are several types of materials belonging to this class, the classification being made taking into account the type of the electric carrier at the Fermi level (localised or delocalised electrons) and its direction with respect to the quantisation axis determined by the magnetization direction. Half-metals of different types can have different conductivity type: metallic, semiconducting or even nonmetallic [2].

1.1.1. Spin (polarized) currents in electronic devices

The electronics based on semiconducting materials is approaching physical limits for further miniaturization of its components and several alternative technologies are being explored [4]. In this context, spin electronic devices are being actively investigated for applications such as data storage, fast data processing, non-volatile memories etc. [5]. On top of that, the most-extended application of magnetoresistive devices is in read heads [6].

Current effort in the field of spin-electronics takes two main different approaches. First the technology of giant and tunnel magnetoresistance (see subsection 1.2.2) is

being improved in the search for better performance materials and devices (magnetic RAM memories, hard disk read heads and storage materials). The other direction of study deals with the generation, transport and detection of spin-polarised currents i.e. the spin dynamics control to be implemented in new generation of logic devices (transistors, diodes etc…) or even multi-functionality devices combining memory and data processing on the same chip. As a result a spin-FET is a Field-Effect Transistor in which the source as well as the drain are ferromagnetic materials designed for the injection and detection of spin polarised currents. The conduction of such device depends on the spin orientation and can be controlled by the gate voltage. Moreover, the spin-MOSFET [7] based logic circuits can be assembled in so called reconfigurable logic gates. According to Tanaka et al. [8] such approach allows reducing the number of transistors in the logic gate for all symmetric Boolean functions from 48 to 10 in conventional MOSFET and spin-MOSFET technologies. The Light-Emitting Diode converts into spin-LED when the spin-polarised electrons are injected into the semiconductor. The emitted light is then circularly polarised.

First of all we have to point out the difference between the electric current, spin-polarised current and spin current (see Figure 1.1). In conventional electronics one deals with a current of electrons with randomly oriented spins. The spin-polarised current can be described as a movement of electrons forced by an applied bias possessing an imbalance of spin directions. In such a case one would deal with spin-up or spin-down polarised current. We can however imagine the situation when the possibility of forcing the spin-up and spin-down electrons to move in opposite directions allows generating in the same conductor two spin-polarised currents flowing in opposite directions (as proposed by Sharma [9]). Moreover assuming the identical intensities of the two currents we find the net charge and mass transport to be zero. This theoretical result will have some interesting consequences. First the ohmic resistivity would be diminished (as there is no transport of the electrons). In addition, the spin being a vector quantity (angular momentum) allows the quantum information to be transported through semiconducting devices.

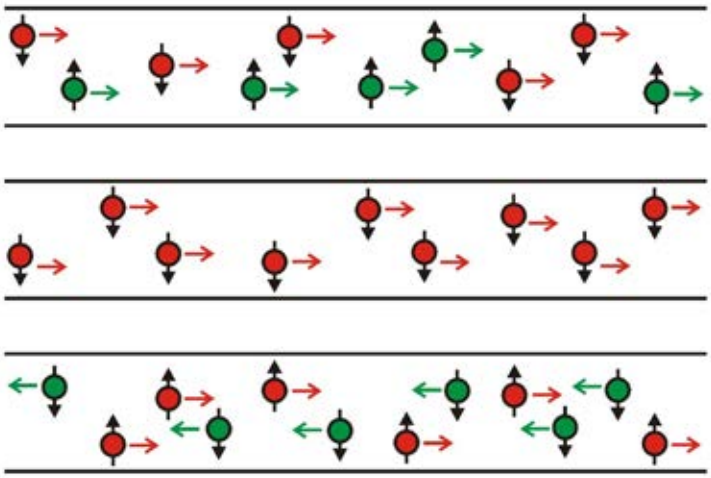

Figure 1.1. Top to bottom: random oriented spins of electrons, spin-polarised current with only spin-down electrons, spin current in two component model.

The first challenge, while the spin-based logic is to be implemented, is the generation of spin-polarised currents. Here the materials such as ferromagnetic semiconductors or half-metals are of great advantage and the latter will be discussed in section 1.6. The semiconductor transistors offer the amplification of the input signal, the feature being unavailable with metal-based devices although switches and valves are available in this technology. Moreover the semiconductor spintronics devices would be possibly more easily integrated with current equipment. However the question remains on the combination of metal/semiconductor connections that would not impede the spin transport across the interface. In particular there is a huge difference in DOS at the Fermi level between a magnetic metal and semiconductor resulting in very different conductivities. Thus, even having a polarised electrons source with high degree of spin polarization, the problem occurs when the current is to be injected into the logic device itself. Many approaches to solve the issue are made such as the injection through a tunnel barrier, however this remains out of the scope of this thesis. This together with the spin relaxation problem is extensively treated e.g. by Žutić et al. [10].

The most difficult challenge remains the spin-based quantum computer in solid-state structure design. In quantum computing the logic is not limited to conventional

binary (0 and 1) operations and the bit is replaced by a qubit (unit based on the spin-up and spin-down state), which does not have to be in one of the two states but is allowed to get their combination i.e. an unlimited number of states between 0 and 1.

1.2. Magnetoresistance

One of the most important effects in magnetoelectronics is the magnetoresistance (MR). Generally speaking MR can be defined as the response of electrical resistance to the applied magnetic field:

$$MR = \frac{R(H) - R(0)}{R(0)} = \frac{\Delta R}{R} \tag{1.3}$$

with *R(H)* and *R(0)* being the resistance with and without external magnetic field respectively. The value of MR is often presented as a percentage of *ΔR/R* (see equation (1.3)) where values much exceeding 100% can occur. From the application point of view the value of the magnetic field required to obtain the MR effect is an important parameter. If the magnetoresistance is large the material can be of technological relevance for the fabrication of the magnetic sensors or magnetic memories.

Hereafter we will give a short overview of various kinds of the magnetoresistive behaviour of matter distinguishing between the intrinsic and extrinsic MR.

1.2.1. Intrinsic magnetoresistance

1.2.1.1. Lorentz magnetoresistance

In the general case the magnetoresistance of nonmagnetic metals is positive, the resistance of the material increasing as a function of external magnetic field. Its origin is due to the Lorentz force that forces the electrons on spiral trajectories (longer than linear ones) and consequently reduces the longitudinal path of the electron between the collisions, increasing the resistance. The field (*H*) dependence of the effect is sometimes given by:

$$MR = aH^2 \tag{1.4}$$

a being a different constant for each metal. The magnitude of the effect is, however very low, being less than 1% at the applied field of 1 T except for Bi [11].

1.2.1.2. Anisotropic magnetoresistance

In case of ferromagnetic metals one can observe an effect (called Anisotropic Magnetoresistance – AMR) of change in the resistance while changing the relative orientation of the magnetic field and the electric current discovered by Lord Kelvin [12] in 19th century. The sign of this effect can be either positive or negative [13]. The electron scattering cross section depends on the shape of the electronic clouds. When the magnetization rotates these suffer deformations and rotations that arise from the spin-orbit coupling. The magnitude of AMR effect is small, a few percent, and depends on the Fermi surface of the material. Compounds exhibiting this effect had been commonly used in computer hard disk drives, read heads and other sensors until more efficient multilayer GMR sensors were introduced.

1.2.1.3. Spin-disorder magnetoresistance

The magnetoresistance effects can be also observed in ferromagnetic metals. The phenomenon is known under the name of the Spin-Disorder Magnetoresistance (SDMR). The effect exhibits a maximum at temperatures around the magnetic ordering temperature – T_C.

Observing the resistance versus temperature curves one observes different slope of the curve for the temperatures above and below the temperature of the magnetic ordering (i.e. in the paramagnetic and ferromagnetic regions respectively). The reason of the observed behaviour is the contribution to the resistivity from the randomly oriented spins scattering on local magnetic moments in the paramagnetic state. In the ferromagnetic state the scattering on the magnetic centres has a lower magnitude. The theory of the local and conduction electrons interactions is given by the De Gennes – Friedel [14] and Fisher – Langer [15] models for spin-disorder scattering.

The application of a large magnetic field is able to suppress the spin-dependent scattering contribution leading to a relative change of the resistance with respect to the zero field resistance. However, very large external fields are required in order to achieve reasonable change in resistance, thus making the application of the SDMR effect rather complicated.

1.2.1.4. Colossal magnetoresistance

Other source of intrinsic magnetoresistance is the so-called Colossal Magnetoresistance (CMR). The term CMR was originally applied to the mixed-valance manganites exhibiting a huge change in electrical resistance at the Curie temperature in the applied field of several Tesla in bulk and thin film samples [16, 17]. The origin of the effect is different, however, from the one of the SDMR. In the present case, the magnetic field drives a phase transition from an insulating paramagnet or charge ordered state to a ferromagnetically ordered metal. The expression CMR is also employed to describe the change of the resistance associated with a magnetic-field-driven transition from a higher resistance to a lower resistance state in the vicinity of the temperature at which the magnetic order changes e.g. the MR effect taking place in Ca_2FeReO_6 double perovskite at a structural transition [18]. Although the effect can reach extremely high percentage change of the resistance (up to 3000% in $La_{2/3}Ca_{1/3}MnO_3$ perovskite, according to De Teresa et al. [19]), the technological application of materials exhibiting CMR is limited due to the need of strong field to be applied in order to get reasonable effect and narrow temperature window in which the effect takes place (around the transition temperature), which reduces applicability.

1.2.2. Giant magnetoresistance

Electronic devices based on the Anisotropic Magnetoresistance effect are not too efficient and Colossal Magnetoresistance effect application involves certain technological limitations as explained before. The search for better performance materials was not leading to substantial improvements until the discovery of so-called

Giant Magnetoresistance (GMR) was announced in 1988. Systems exhibiting GMR are magnetic multilayers, where layers of ferromagnetic (e.g. Fe, Co or Ni) and non-magnetic (e.g. Cr or Cu) metals are stacked one on top of each other as presented in Figure 1.2.a. The widths of the individual layers are of nanometre size – i.e. only a few atomic layers thick. The GMR effect was reported by two groups independently, one led by Peter Grünberg and the other one by Albert Fert. Both investigators have been awarded with the Nobel Prize in Physics in the year 2007 [20]. The original experiments showing GMR were performed using a trilayer Fe/Cr/Fe system [21] and multilayers of the form $(Fe/Cr)_n$ where n could be as high as 60 [22]. Multilayer systems of Fe and Cr layers were studied before the GMR effect was disclosed due to the interesting magnetic properties. It was found that the coupling interaction strength between the magnetic layers depends on the thickness of the nonmagnetic layer [23]. For certain thickness of the non-magnetic layer, in the absence of external magnetic field magnetic layers are coupled antiferromagnetically. The application of a field stronger than the coupling interaction strength allows reversing the magnetization of one of the layers, reaching a state where the magnetization points in the same direction in all of the magnetic layers. Thus, a small change of magnetic field results in significant differences in electrical resistance of a system. Such properties made the GMR systems promising in the applications in magnetic data storage devices such as read-out heads.

In 1997 IBM launched the first read-out head based on the GMR effect and it became promptly the standard technology. Even thought the most recent read-out techniques are further developments of GMR, the data storage density of modern hard drives made the GMR read-heads insufficient, and they were substituted by TMR read heads starting in 2005 [24].

Now we shall focus on the origin of the magnetoresistance effect in the multilayer system. We will consider two measurement geometries: current in the plane (CIP) and current perpendicular to the plane (CPP). The direction of the current flow in both geometries is indicated in Figure 1.2.b. In general the GMR effect has larger value in

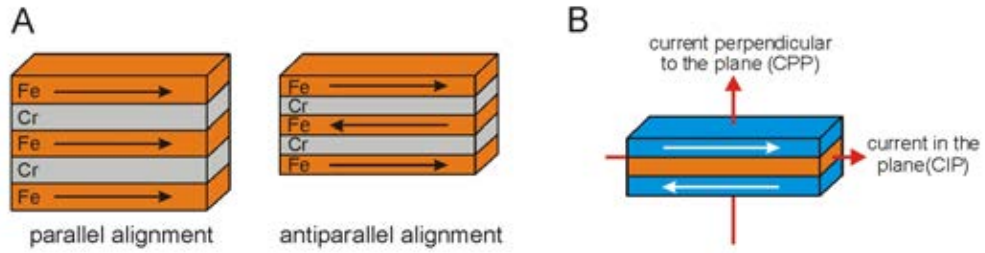

Figure 1.2. (a) Multilayer system of alternating Fe and Cr layers with Fe layers coupled parallel (left) and antiparallel (right). (b) Configurations of the GMR measurements. Non-magnetic layer is presented in orange, the magnetic layers are in blue with white arrows representing the magnetization direction. Red arrows indicate the direction of the current in the CIP and CPP measurement configurations.

the CPP configuration than in the CIP arrangement, however it was originally discovered in the latter one because the experiment is easier [21].

In the CIP measurement arrangement the electron averages the properties of the layers on the length scale of electron mean free path (typically a few nanometers). Consequently, if the spacing between the magnetic layers is larger than this value the GMR effect vanishes.

In the CPP measurement the electrons are injected into the device in such a way that the current has to cross both ferromagnetic layers and the nonmagnetic layer as well, passing through the device. The GMR effect in CPP configuration can be explained using the Mott's model. Within it we assume that the electric current can be treated as if it was composed of two independent components. Then, we will deal with one current of electrons with spin-down, and the other with spin-up. The resistance for each of the two components will be calculated separately, as it depends on the orientation of the spin of the electron with respect to the magnetization direction of the ferromagnetic layer. The simplified illustration of the two components model is presented in Figure 1.3.a and b for the parallel and antiparallel relative orientation of the magnetic layers. Leaving the first magnetic layer the electron enters the non-magnetic metal and the resistivity due to the scattering processes will be of the same value for spin-up and spin-down current component. Then in the second ferromagnetic

layer the scattering will be again spin-dependent thus resistivity will be different in case of spin-up and spin-down current. When the resistance of the nonmagnetic layer and the interface resistance are low compared to those of the magnetic layers the model becomes simple.

Let the magnitude of the GMR effect to be defined by:

$$GMR = \frac{\rho_{\uparrow\downarrow} - \rho_{\uparrow\uparrow}}{\rho_{\uparrow\uparrow}} \tag{1.5}$$

$\rho_{\uparrow\downarrow}$ and $\rho_{\uparrow\uparrow}$ being the resistivity for a antiparallel and parallel alignment of the magnetisation in the neighbouring layers. The scattering cross section is different for the parallel ρ^+ and the antiparallel ρ^- orientation of the spins with respect to the layer magnetization (as presented in Figure 1.3). Neglecting the resistivity of the nonmagnetic layer and the interface resistance we get for the parallel arrangement of two magnetic layers:

$$\frac{1}{\rho_{\uparrow\uparrow}} = \frac{1}{2\rho^+} + \frac{1}{2\rho^-} \Rightarrow \rho_{\uparrow\uparrow} = \frac{2\rho^+\rho^-}{\rho^+ + \rho^-}, \tag{1.6}$$

and for the antiparallel configuration:

$$\frac{1}{\rho_{\uparrow\downarrow}} = \frac{1}{\rho^+ + \rho^-} + \frac{1}{\rho^- + \rho^+} \Rightarrow \rho_{\uparrow\downarrow} = \frac{\rho^+ + \rho^-}{2}. \tag{1.7}$$

Putting (1.6) and (1.7) into (1.5) we get the GMR value as:

$$GMR = \frac{\left(\rho^+ - \rho^-\right)^2}{4\rho^+\rho^-}, \tag{1.8}$$

being large if the scattering cross sections differ significantly for the parallel and antiparallel alignment of the spin with respect to the magnetisation of the magnetic layer.

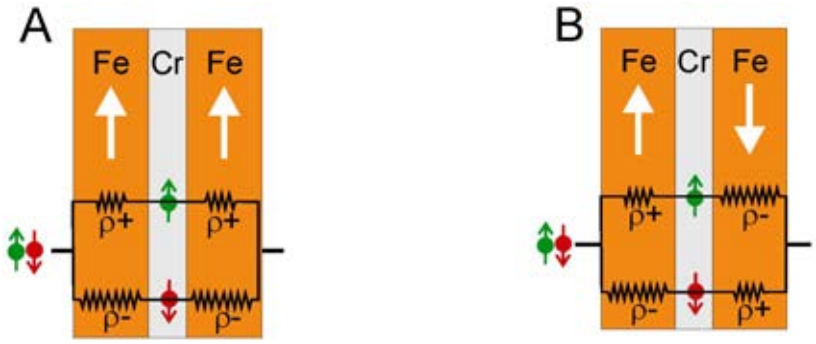

Figure 1.3. The two spin channels model for the current perpendicular to the plane measurement configuration for the multilayer system of alternating Fe and Cr layers with Fe layers coupled parallel (a) and antiparallel (b). ρ^+ and ρ^- denote parallel and antiparallel orientation of the spins with respect to the layer magnetization.

Of course, this is a simplified model. Rigorous treatments indicate that other relevant effects in CPP geometry are spin-dependent scattering events at the interfaces as well as spin accumulation effects at the interfaces which can be modelled as interface resistances. Interference effects between incoming electron waves and reflected waves at interfaces can be also relevant [25].

The properties of the multilayer devices have opened the possibility of applications in the electronic industry. The basic configuration of the GMR device is just a three-layered system which acts as a spin-valve. In such device a thin nonmagnetic layer separates two ferromagnetic layers. One of the magnetic layers is made of magnetically hard material (e.g. having large magnetic anisotropy enhanced by means of shape anisotropy or epitaxial stress, and in more advanced configuration using the additional antiferromagnetic layer) so its magnetisation does not suffer changes at low magnetic fields. In the magnetic read-head of a hard disk drive this layer acts as a reference for the magnetization direction. The other magnetic layer consists of a soft magnetic material and its magnetisation is easily reversed even by small magnetic fields. Consequently this layer is used for sensing the magnetization direction. The former layer is called a pinned layer and the latter a free layer. When a weak magnetic field, such as that from a bit on a hard disk, passes beneath such a structure, the magnetic orientation of the unpinned magnetic layer rotates relative to

that of the pinned layer, generating a significant change in electrical resistance due to the GMR effect. The low resistance means a current will be detected, and the computer computes a 1 bit. On the other hand a high resistance results in much weaker current and a 0 bit.

1.2.3. Tunnel magnetoresistance

In the above description of the GMR effect we dealt with the system made of magnetic layers interspaced with the nonmagnetic metallic layer. In the case of Tunnelling Magnetoresistance (TMR) the nonmagnetic spacer is replaced with the insulating layer. The effect is based on the tunnelling of the electrons through the insulating layer between two magnetic electrodes when the electric field is being applied.

Tunnelling of the electrons through the insulating layer can be explained on the basis of the quantum mechanics. Considering a squared potential barrier of height V_B, being larger than the propagating electron energy E, we get the electronic wave inside the barrier in the form:

$$\varphi(x) = Ae^{\kappa x} + Be^{-\kappa x} \tag{1.9}$$

where

$$\kappa = \sqrt{\frac{2m(V_B - E)}{\hbar^2}} \tag{1.10}$$

can be treated as an exponential decay of the wave amplitude while the electron is travelling inside the barrier. The transmission through the potential is only possible considering the quantum characteristics of the particles and in the field of classical mechanics the probability of finding an electron on the other side of the barrier would be zero.

The electrons inside the barrier are spin polarised with the spin polarization given

by the DOS in one of the electrodes. The spin is conserved along the way inside the insulating layer provided that there are no sources of depolarisation such as magnetic impurities or magnon excitations. In the Julliére model [26] the TMR effect of such junction is related to the spin polarizations of the two electrodes P_1 and P_2 (defined by the equation (1.1) at $E = E_F$) according to the relation:

$$TMR = \frac{2P_1P_2}{1 - P_1P_2}. \tag{1.11}$$

Putting $P_1 = P_2 = 1$ in the above formula and provided the ideal tunnel junction one would get $TMR = \infty$. This would be only possible having the electrode material to be an ideal half metal, avoiding any defects in the barrier (causing spin flips as already mentioned) and optimising the barrier/electrode interfaces (e.g. oxygen deficiency, phase separation, etc.). For reviews on magnetic tunnel junctions, see Moodera and Mathon [27] and Tiusan et al. [28].

Tunneling effect also has found its application in the generation of spin-polarised currents. The idea relies on the use of a ferro- or ferrimagnetic insulating tunnel barrier. In such device the barrier height is different for spin-up and spin-down electrons due to the exchange splitting of the electronic bands. This method of creating spin-polarised currents is known under the name of spin filtering. For a review on spin filtering, see Moodera et al. [29].

1.2.4. Intergrain tunnel magnetoresistance

The Intergrain Tunnelling Magnetoresistance (hereafter abbreviated as ITMR) can be observed in granular materials that exhibit two indispensable properties: spin polarization in the grain bulk and insulating grain boundary thin enough for the tunnelling to take place. This scenario is fulfilled e.g. in polycrystalline granular material and the effect is strongly depending on the extrinsic properties of the grains (size, surface defects, impurities), grain boundary nature [30] and material microstructure. Let us consider a system of conducting grains separated by thin insulating grain boundaries and a magnetic field being applied to the specimen. In the

simplest model the magnetisation direction points in random direction in each of the grains building the material if the applied field is equal to the coercive field (H_C) of the material. For larger applied field the magnetization tends to align in one direction, eventually reaching a perfect ordering (magnetization of each pair of neighbouring grains points in the same direction) at the saturation field (H_S). One can treat the grains and the insulating boundary as ferromagnetic electrodes separated by insulating layer (an assemble of electrodes in the insulating matrix) explaining the conduction of such system in terms of tunnelling conductivity. In the previous section we assumed the direction of the magnetization in the ferromagnetic layers of MTJ to be either parallel or antiparallel, in both cases the relative angle between magnetisation directions being either $\theta = 0°$ or $\theta = 180°$. In the case of granular material we have to describe the conductance G of the material as a function of θ. As θ is randomly distributed it is necessary to take the average of this quantity. Therefore we obtain [31]:

$$G = G_{ef} \int_0^{2\pi} g(\theta) d\theta \int_0^{\infty} d(\kappa l) f(\kappa l) \left(1 + P^2 \cos\theta\right) e^{-2\kappa l}, \tag{1.12}$$

where $g(\theta)$ and $f(\rho l)$ are the distribution functions of the magnetic configuration at a given field and barrier parameters through the electron path, P is defined as in equation (1.1) at Fermi energy E_F and $\langle \cos\theta \rangle^2 = m^2$, m being the reduced magnetization of the system. It varies from 0 to 1 while applied magnetic field changes from H_C to H_{SAT}. Assuming the barrier properties to be independent of the external magnetic field the integration in κl results in constant prefactor (λs). Thus we obtain from (1.12) the magnetoconductivity (in analogy with MR equation (1.3)) equation:

$$MC = \frac{G(H) - G(H=0)}{G(H=0)} = P^2 m^2, \tag{1.13}$$

and defining $R = \frac{1}{G}$:

$$MR_0 = \frac{R(H) - R(H=0)}{R(H=0)} = -\frac{P^2 m^2}{1 + P^2 m^2}, \tag{1.14}$$

$$MR_h = \frac{R(H) - R(H=0)}{R(H)} = -P^2 m^2 \tag{1.15}$$

we get the magnetoresistance in ITMR.

1.3. Spin - Orbit coupling

A classical description of the spin-orbit interaction takes into account the atom nucleus viewed from the reference frame of the electron. The nucleus is then treated as a moving charge producing a magnetic field *B*, proportional to the angular momentum operator $\hat{L}$. The magnetic field is interacting with the spin magnetic moment $m_s = \frac{-e}{m_e}\hat{S}$ (e being the electron charge, m_e the electron mass and $\hat{S}$ the spin momentum operator). Therefore the interaction between *B* and m_s is proportional to $\hat{L} \cdot \hat{S}$. This approach however gives the proportionality constant to be incorrect. The proper value can only be obtained treating the electron as a relativistic particle.

The spin-orbit interaction Hamiltonian found with the relativistic approach is given by:

$$\hat{H}_{SO} = \frac{1}{2m_e c^2}\frac{1}{r}\left(\frac{\partial V}{\partial r}\right)\hat{L} \cdot \hat{S} = \xi\left(\hat{L} \cdot \hat{S}\right) \tag{1.16}$$

V being the unperturbated Coulomb potential. The $\hat{L} \cdot \hat{S}$ product can be written as

$$L \cdot S = \frac{1}{2}\left(J^2 - L^2 - S^2\right) \tag{1.17}$$

Consequently the energy of spin-orbit interaction is dependent on the angular momentum quantum number *J* and can be approximated by:

$$E_{SO} \approx \frac{1}{2}\hbar\langle\xi\rangle\left[J(J+1) - L(L+1) - S(S+1)\right] \tag{1.18}$$

so the total energy of state is also dependent on J and moreover $(2J+1)$ times degenerated. This degeneration can be removed by application of an external magnetic field.

Spin-orbit coupling affects the half-metallic properties of the material due to the mixing of the spin up and spin down components of the Bloch states. Considering the weak spin-orbit coupling strength (ξ) compared to exchange splitting (Δ_{ex}) i.e. $\xi << \Delta_{ex}$, the spin-orbit coupling contribution can be treated as a perturbation in the Schrödinger Hamiltonian. This results in the lowering of the polarization of the electrons at the Fermi level depending on the spin-orbit coupling strength. Considering the strong spin orbit coupling i.e. $\xi \cong \Delta_{ex}$ (the theoretical framework to approach the SO coupling problem is the Dirac equation) the half-metallicity is destroyed $P(E_F)$ being the lower the higher ξ. However in certain cases even the strong spin-orbit coupling and large orbital moments do not destroy the half-metallic state.

1.4. Magneto-crystalline anisotropy

Spin-orbit interaction Hamiltonian introduced in the previous subsection is no longer valid for atoms embedded in the solid. Due to the interaction with the neighbouring atoms (explained e.g. by the Ligand Field theory) L and m_L are no longer good quantum numbers, and the Hamiltonian needs to be diagonalized with other set of eigenfunctions. Such new Hamiltonian results in the anisotropy of the bonding, and consequently in magnetocrystalline anisotropy - MCA.

The link between the SO interaction and MCA is a straightforward consequence of the coupling of the spin and orbital moments on the one hand and the anisotropic electron charge distribution interaction with the crystal electric field on the other [32]. Magnetocrystalline anisotropy is consequently determined by the orbital state of the magnetic ion and the surrounding anisotropic crystalline field (the anisotropy of the *d*

orbitals arising from the ligand field) hence the orbital moments are strongly coupled to the anisotropic lattice. This interaction is transferred to the spin-moment system via the spin-orbit coupling, resulting in *d*-electron spins being coupled to the lattice as well. The orbital magnetic moment is preferably pointing to a particular crystallographic direction, however the spin-dependent part is more easily turned by an external magnetic field.

In general, the MCA can be treated as the energy needed to rotate the magnetization from the easy to hard magnetization axis (in the absence of magnetostatic effects in the bulk and the shape anisotropy). It corresponds to the difference of the spin-orbit energy between those two cases. One can calculate an effective torque acting on the magnetization deviated by an angle γ from the easy axis relating it to the anisotropy energy (defined above).

The magnetocrystalline anisotropy is the dominant kind of magnetic anisotropy provided shape anisotropy can be neglected. In fact for large particles (or grains in the bulk) of spherical-like shape one observes no shape anisotropy.

Large MCA of the material results in a magnetization process that involves a three-step mechanism. First the growth of the magnetic domains with the magnetization direction favourable with respect to the magnetic field occurs, at the expense of the size of the domains with direction of the magnetization opposing the field. At higher fields the domain rotation mechanism becomes significant. At fields high enough to overcome the anisotropy energy the magnetization of the domains oriented randomly with respect to the field is switched to the magnetization axis closest to the applied field direction. The field of such strength is called the anisotropy field H_A. The application of fields higher than H_A results in a coherent rotation being a process at which all the magnetic moments are rotated into the field direction not being any longer aligned along particular crystallographic axis.

One of the possible methods of investigation of the anisotropy field strength is so called Singular Point Detection method that will be introduced in the subsection 2.2.1.5.

1.5. Thermally assisted demagnetisation: spin waves

Bloch proposed in 1930 the first model of collective excitation of the spins, rather than a single spin reversal as the lowest energy excitation [33]. Possible realization of such excitation is presented in the Figure 1.4. Low-energy excitations are quantized with the quantization unity called a magnon. The early considerations made by Bloch assume a low number of spin waves in the material so that the interactions between the spin waves can be neglected.

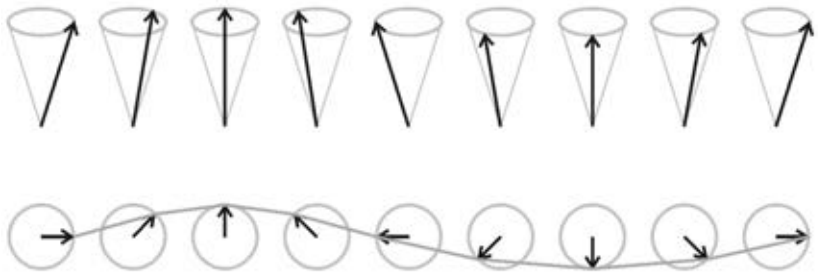

Figure 1.4. Spin wave along the spin line. Upper row: perspective view, lower row: top view of the spins along one wave length.

Within the Bloch model the spontaneous magnetization M of a ferromagnetic material varies with temperature T following the relation (1.19), M_0 being a spontaneous magnetization at 0 K. The magnetization calculated with this equation fits the experimental data nicely at low temperatures. At higher temperatures however, it becomes insufficient.

$$M = M_0\left(1 - aT^{3/2}\right). \tag{1.19}$$

A lot of effort has been made in order to establish a complex model of spin-wave excitations in ferromagnetic materials (see for example references [34] and [35]). The case of antiferromagnetism [36] or ferrimagnetism [37] becomes even more

complicated due to the existence of two non-equivalent sublattices.

In a ferromagnetic material the lowest energy state is obtained with all spins being aligned parallel. The Heisenberg model gives the interaction strength between the nearest spins (in positions p and $p+1$):

$$U = -2J \sum_{p=1}^{n} \vec{S}_p \cdot \vec{S}_{p+1} \tag{1.20}$$

where J is the exchange constant, $\hbar\vec{S}_p$ is the momentum of the spin.

Equation (1.20) can be rewritten as:

$$U = -\frac{1}{2}\sum_p \vec{\mu}_p \cdot \vec{H}_p \tag{1.21}$$

where the magnetic moment at the p-site is given by the Lande factor g and proportionality factors:

$$\vec{\mu}_p \equiv -g\mu_B \vec{S}_p, \tag{1.22}$$

the effective magnetic field acting on that moment is:

$$H_p \equiv -\frac{2J}{g\mu_B}\left(\vec{S}_{p-1} + \vec{S}_{p+1}\right) \tag{1.23}$$

and the ½ factor arises from the fact that the spin should not be counted twice: once as the source of the field and second time as a magnetic moment in the field. The rate of a spin momentum change depends on the magnetic moment associated with a spin and the effective field as can be derived on the basics of the classical mechanics:

$$\hbar\frac{d}{dt}S_p = \vec{\mu}_p \times \vec{H}_p. \tag{1.24}$$

This leads to the set of nonlinear equations containing the products of the spin-components in the orthogonal coordinates. However one can find a solution being the

mathematical description of a propagating wave (see e.g. [38] for detailed mathematical considerations). As a result, a dispersion relation for a one-dimensional spin wave is given by:

$$\hbar\omega = 4JS(1-\cos ka)\,. \tag{1.25}$$

The same relation can be obtained on the basis of quantum mechanics. Expanding the cosine term in equation (1.25) and assuming $ka<<1$ we get quadratic dependence of the frequency with the wave-vector k, that for all the crystal structures of regular space group gets a form:

$$\hbar\omega = \left(2JSa^2\right)k^2\,. \tag{1.26}$$

The original $T^{3/2}$ Bloch's equation can be obtained treating spin waves as noninteracting Bose particles with constant effective mass and the energy of spin wave being proportional to its wave-vector k^2 (thus increasing proportionally to inverse squared wave-length λ^{-2}). The deviations from the theoretical formula derived with above limitations arise from the divergence of the energy spectrum from the k^2 law, dynamical interaction between spin waves and kinematical interaction between them [35]. The corrections should be then applied to the Bloch's formula. The terms to be added due to the energy spectra are proportional to $T^{5/2}$ and $T^{7/2}$ and the dynamical interaction leads to the T^4 like term. The kinematical interaction contribution requires advanced theoretical treatment and eventually it vanishes as reported by Dyson in the abovementioned reference. Including the corrections to the equation (1.19) we get:

$$M(T) = M(0)\left(1 - a_0T^{3/2} - a_1T^{5/2} - a_2T^{7/2} - a_3T^4 + \ldots\right), \tag{1.27}$$

leaving the equation opened for the additional terms arising from additional experimental conditions. It is to be mentioned that in the experimental range of $0 < T < \frac{1}{2}T_C$, the term a_3T^4 in equation (1.27) is less than 2 – 4% of the $a_0T^{3/2}$ term. In low temperatures, consequently, the effect of the interaction of the spin waves

would not be observed in a real ferromagnet.

A comment should be added on the Bloch's law application in case of half metallic compounds. It was presented by Solontsov [39] that the $T^{5/2}$ not only arises from the magnon-magnon interactions but also represents the low temperature variation of magnetization in the saturated isotropic ferromagnets with one of the electron sub-bands partially filled at the same time as the other remains unoccupied (half-metallic behaviour). The latter statement found its experimental proof by the NMR results in the FeMo and FeRe based double perovskites as presented by Zając et al. [40].

In this thesis we will apply the Bloch's law to high field magnetization results obtained for the Sr_2FeReO_6 double perovskite.

1.6. Modern materials for spin electronics

The new market of the spin electronics demands new magnetic materials: magnetic semiconductors and half metallic ferromagnets to be developed. Although the term was primarily used for Mn-based Heusler alloys, the predictions of half-metallicity have been extended to other double-exchange oxides such as Fe_3O_4 [41], CrO_2 [42], perovskite manganites [43] and apart from them the double perovskites. For a review article on Oxide Spintronics, see Bibes and Barthélémy [44]. Fe_3O_4 crystallising in the spinel structure with A sites occupied by Fe^{3+} ions and B sites by a mixture of Fe^{2+} and Fe^{3+} ions is a ferrimagnet with Curie temperature $T_C = 858\ K$. The negative spin polarisation arises from the overlap of the spin-down Fe t_{2g} states with O *2p* states and is experimentally found to range from 40% to 80% [45]. Among spintronics devices based on Fe_3O_4 the magnetic tunnel transistor with magnetite emitter [46] and CIP GMR structures [47] can be listed. However, the integration with semiconductors is still under investigation. Chromium oxide belongs to the binary oxides group. The ferromagnetic ordering of the Cr magnetic moments exists in temperatures below 395 K. The Fermi level lies in the half-full $d_{yz}\pm d_{zx}$ band. Andreev reflection experiments with CrO_2/superconductor contacts have indicated a spin

polarization of 97% at low temperature [48]. The TMR value obtained in magnetic tunnel junctions having CrO_2 and Co electrodes with Cr_2O_3 and a CrO_x-AlO_x composite tunnel barrier are 8% [49] and 24% [50] respectively. Manganites crystallising in a simple perovskite structure with a parent compound $LaMnO_3$ (LMO) have been extensively studied. One of the focal points of the study was the potential application in MTJ, after Park et al. [51] demonstrated spin-polarisation larger than 90% by the spin-resolved photoemission experiments. LMO itself is an antiferromagnetic charge transfer insulator, however substitution of the La^{3+} ions by divalent ions (e.g. Sr^{2+}) results in a transition to a metallic and ferromagnetic states for certain substitution levels. The TMR values obtained in magnetic tunnel junctions exceeds 1000% [52].

1.6.1. Double perovskites: structural and magnetic properties of most common compounds

The investigation of the double perovskite oxides dates back to 1961 when a ferromagnetic behaviour of Re-based double perovskites was reported by Longo and Ward [53]. Afterwards a slow progress was present until 1998 when the publication of Kobayashi et al. [54] on the half-metallic properties of Sr_2FeMoO_6 renewed interest in this class of compounds. Later, the half-metallicity was also demonstrated by first principles calculations of the DOS in Sr_2FeReO_6 [55] (see Figure 1.6). Possible spin-electronics applications arising from the electronic structure caused a rapid advancement in the study of the double perovskites. Physics of the system involves a wide range of effects making them a challenging subject of investigation. This involves the interplay of the crystallographic structure and both electronic and magnetic properties.

Double perovskites (DP's) belong to a large family of oxides with general formula $A_2BB'O_6$ (*A* being a large divalent or trivalent alkaline earth ion, *B* and *B'* transition metal ions). The *A* ions are 12-fold coordinated to oxygen. *B* and *B'* atoms are located in the centre of the oxygen octahedra. In case of a significant size or valence difference between *B* and *B'* ions they occupy an alternating crystallographic

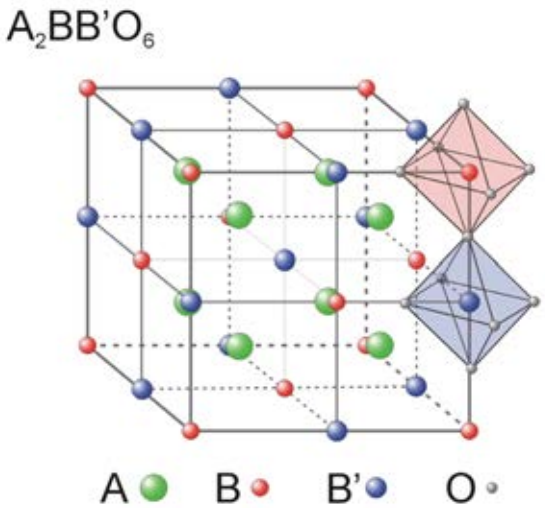

Figure 1.5. Ideal cubic perovskite structure having a chemical formula $A_2BB'O_6$. Oxygen atoms form octahedra around alternating *B* and *B'* ions.

sites i.e. *B* type atom has only *B'* neighbours and vice versa so BO_6 and $B'O_6$ octahedra are arranged in two interleaving *fcc* sublattices. Such configuration is known under the name of an ordered double perovskite. If the size or valence difference is diminished the ordering becomes more difficult to obtain and the amount of structural defects increases. This subject will be treated in more detail in the following subsection. The basic crystallographic structure being a cubic one can be described in terms of the $Fm\bar{3}m$ space group (see Figure 1.5). Due to the mismatch of the *A* ions and *B* (*B'*) ions sizes the octahedra can undergo cooperative tilting in order to obtain a configuration that is more favourable from the energetic point of view.

While the *A* cation size is getting smaller, an empty space arises around it and needs to be filled up. Space groups exhibiting lower symmetry replace then the cubic structure. Using Glazer's terminology [56] the $a^0a^0c^-$ octahedral tilt is responsible for the occurrence of the tetragonal structure (*I4/m* space group), while the monoclinic structure ($P2_1/n$ space group) arises from the $a^+b^-b^-$ tilt. Such tilts shift the oxygen atoms from their ideal positions giving rise to additional diffraction peaks. For small distortions a unit cell with cubic symmetry is allowed for the structural refinements of the diffraction data. The tetragonal distortion requires a new unit cell to be defined. Its main axes are defined along the cubic [110] and [-110] directions. The lattice

parameters of the tetragonal cell are defined as:

$$\begin{aligned} c &= c_{cubic} = c_{tetra} \\ a_{tetra} &= \frac{a_{cubic}}{\sqrt{2}} \end{aligned} \quad . \tag{1.28}$$

Having $a_{cubic} = c$ prior to the distortion the tetragonal distortion parameter t can be introduced in order to quantify the distortion strength:

$$t = 1 - \frac{a_{tetra}\sqrt{2}}{c} . \tag{1.29}$$

As in the case of simple perovskites a tolerance factor can be defined. This would allow the anticipation of the crystallographic structure on the basis of the tabulated ionic radii due to the mismatch between the A site cation and the space available inside the oxygen octahedra. The main difference with respect to the perovkites is that the double perovskite structure requires two distances ($B - O$ and $B' - O$) to be taken into account. Consequently the double perovskite tolerance factor f can be defined as:

$$f \equiv \frac{r_A + r_O}{\sqrt{2}\left(\langle r_B \rangle + r_O\right)} . \tag{1.30}$$

where r_i is an effective ionic radius of the *i-th* atom ($i = A, B, B',$ O) whose values are tabulated by Shannon [57] and $\langle r_B \rangle$ arises from the average of the $B(B') - \mathrm{O}$ radii. Equation (1.30) is not, however, useful for experimental use, but can be approximated replacing ionic radii with the interatomic distances $d_{j\text{-}O}$ ($j = A, B, B'$) in the $A\mathrm{O}_{12}$, and $B(B')\mathrm{O}_6$ polyhedra. The latter parameter can be obtained via the diffraction spectra analysis as explained in section 2.3.3. With such approach, we obtain the observed tolerance factor parameter f_{obs}:

$$f_{obs} = \frac{d_{A-O}}{\sqrt{2}\langle d_{B-O} \rangle} . \tag{1.31}$$

Accuracy of the estimation of the oxygen atoms positions is of primary

importance while calculating the experimental value of the tolerance factor. Consequently Neutron Powder Diffraction is privileged to X-Ray Diffraction in estimating bond lengths. This is due to the fact that x-rays are weakly scattered from the oxygen atoms compared to neutrons. The differences that arise between calculated and experimental values of the tolerance factors are mostly due to the fact that theoretical one is based on the tabulated ionic radii for given valence obtained in different compounds (different chemical environments). Other source of uncertainty is related to the estimate of the valence of the *B* and *B'* ions in the double perovskite based on NMR, XAS, Mössbauer spectroscopy or optical conductivity experiments. Apparently it can be given as a general rule valid for all the members of the double perovskite family that $f > 1.05$ requires a hexagonal structure, for $1.05 > f > 1.00$ the cubic structure with $Fm\bar{3}m$ space group is the most likely one, for $1.00 > f > 0.97$ the compound has a tetragonal structure with *I4/m* space group, and finally for $0.97 > f$ the compound becomes monoclinic having $P2_1/n$ space group or orthorhombic. The calculated and observed *f* factors are displayed in the Table 1.1. for the compounds studied in this thesis.

In the ideal double perovskite the oxygen atoms are located between the *B* and *B'* ions on a straight line. However this statement is valid only for highly symmetric systems (and for small tetragonal distortions). Further lowering of the symmetry causes the deviation of the *B* – O – *B'* angle from 180 degrees due to tilting of the BO_6 and $B'O_6$ octahedra. This consequently affects the electronic interactions along *B* – O – *B'* – O – *B* paths.

The interest in the double perovskites as potentially interesting for applications at room temperature arises from their high magnetic ordering temperature (T_C) and high spin polarisation. The T_C of the particular samples studies within the scope of this thesis will be discussed in the experimental section. The changes in the magnetic ordering temperature as well as other magnetic properties for double perovskite compounds with different composition will be discussed. In Table 1.1 Curie temperatures of the investigated double perovskites are listed.

Table 1.1. Tolerance factors (experimental at room temperature and calculated according to the ionic radii expected for the given valence and coordination), space group (at low and room temperature) and Curie temperature of the Re-based compounds studied and Sr_2FeMoO_6 double perovskite for the sake of its historical importance. In the last column references related with the compound are given. Reduced table reproduced after D. Serrate et al. [58].

	Tolerance factor		Space group		T_C [K]
	Calculated	Experimental	4 K	RT	
Sr_2FeMoO_6	0.9766	0.9989	*I4/m*		400
Sr_2CrReO_6	0.9947	0.9996	*I4/m*	$Fm\bar{3}m$	620
Sr_2FeReO_6	0.9850	0.9984	*I4/m*	*I4/m*	400
Ca_2FeReO_6	0.9627	0.9522	$P2_1/n$	$P2_1/n$	522

Not less important is the predicted half metallicity of the double perovskites. As can be seen in the Figure 1.6.a the Fermi level of the Sr_2FeMoO_6 lies in the band formed exclusively by Fe ($t_{2g}\downarrow$) – O (*2p*) – Mo ($t_{2g}\downarrow$) sub-bands. Meanwhile there is a gap in the spin-up bands between Fe ($e_g\uparrow$) and Mo ($t_{2g}\uparrow$). This model holds true for Sr_2FeReO_6 (see Figure 1.6.b.) in which the Fermi level is located in the gap of the spin-up levels and non-zero DOS is due to the band formed by Fe ($t_{2g}\downarrow$) – O (*2p*) – Re ($t_{2g}\downarrow$). In both cases the gap has width of approximately 0.8 eV. Consequently bands lying at the Fermi level are 100% spin-polarised. It is important to mention that the case of FeRe-based compound cannot be treated in the same manner as the compound having Mo ions at *B'* site. This is due to the spin-orbit (SO) coupling in the Re being *5d* atom. The importance of SO coupling was already mentioned in section 1.3, and will be demonstrated later on for the Sr_2CrReO_6 and FeRe based compounds.

For a long time the simplest model, so called *ionic spin-only model*, of the occupation of the electronic bands was used for all members of double perovskites family. First we will discuss the splitting of the Fe *3d* and Mo *4d* bands and the consequences of their occupation. In the double perovskite the Fe^{3+} possessing five *3d* electrons and Mo^{5+} possessing one *4d* electron are located inside octahedra formed by

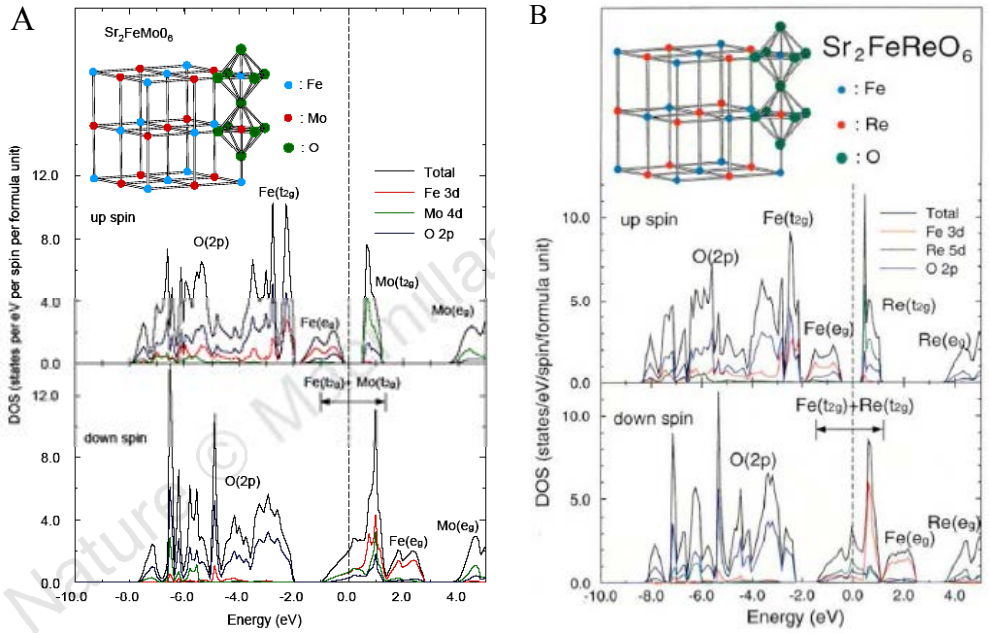

Figure 1.6. The density of states (DOS) of Sr_2FeMoO_6 (a) and Sr_2FeReO_6 (b) as calculated by Kobayashi [54, 55] The Fermi level lies in the band formed by Fe ($t_{2g}\downarrow$) – O (*2p*) – Mo/Re ($t_{2g}\downarrow$) sub-bands.

oxygen O^{2-} ions. This produces a potential removing the state degeneracy and separating new sub-bands by an energy Δ_{CEF} related to the crystal electric field. The total spin moment of the Fe atom ($S = \frac{5}{2}$) produces strong exchange splitting Δ_{ex} of the order of 2 – 3 eV. In case of Fe atom $\Delta_{ex} >> \Delta_{CEF}$. On the contrary in Mo atom exchange splitting is of an order of magnitude smaller than in *3d* metal so crystal electric field splitting is dominant. Both crystal field and exchange splitting act mutually with different strengths so in Fe ion the exchange splitting first removes the degeneration of the *3d* state with respect to the spin producing spin-up and spin-down sub-levels separated by Δ_{ex} which are further split giving rise to t_{2g} and e_g levels eparated by Δ_{CEF}. This is in sharp contrast to the situation in Mo ion where the crystal field splits the *4d* level into t_{2g} and e_g and the exchange interaction removes their spin degeneracy. Final energy levels diagram is presented in the Figure 1.7.a. The

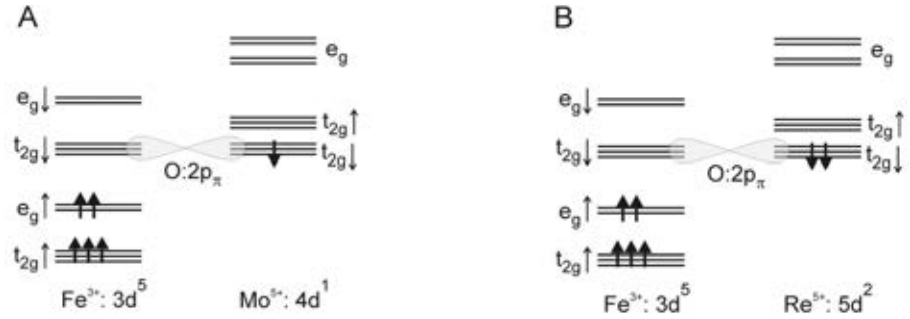

Figure 1.7. Energy levels diagram of Sr_2FeMoO_6 (a) and Sr_2FeReO_6 (b) as calculated by Kobayashi [54, 55]. The Fermi level lies in the band formed by Fe ($t_{2g}\downarrow$) – O ($2p$) – Mo/Re ($t_{2g}\downarrow$) sub-bands.

bold arrows in the figure have the meaning of the electrons with spin pointing parallel to the arrow direction. The magnetic interaction between neighbouring ions is established via the oxygen $2p_\pi$ orbitals. Similar considerations are valid for the FeRe-based compound if one does not introduce the spin-orbit coupling in the Re ion (compare Figure 1.7.b).

Now let us consider the system consisting of Cr^{3+} and Re^{5+} ions, having respectively $3d^3$ and $5d^2$ configurations. Forgetting for a while about the spin-orbit interaction we find the DOS at the Fermi level being non-zero only for spin-down Re t_{2g} and Cr t_{2g} orbitals. As in the previous case the gap of approximately 0.7 eV arises in the spin up band. Again the magnetic interaction is established by the oxygen π orbitals (see Figure 1.8). In the absence of SO interaction the t_{2g} and e_g states (arising from the splitting of the Cr and Re *d* states by the crystal field related to the oxygen octahedra) are the eigenstates of the Hamiltonian and thus do not hybridise with each other. In the real material the spin-orbit coupling is however not to be excluded. In Re metal the spin-orbit parameter $-\xi$ in equation (1.16) – of the t_{2g} states in the spin-orbit Hamiltonian is approximately 0.4 eV [59]. This number is decreased to 0.3 eV [60] in the double perovskite due to covalency. At first sight it is clear that the spin-orbit coupling, having similar magnitude to the gap in the majority channel, is capable of destroying the half metallic state. Considering the Hamiltonian the t_{2g} and e_g states are no longer the eigenstates and they are allowed to mix. This will result in the finite,

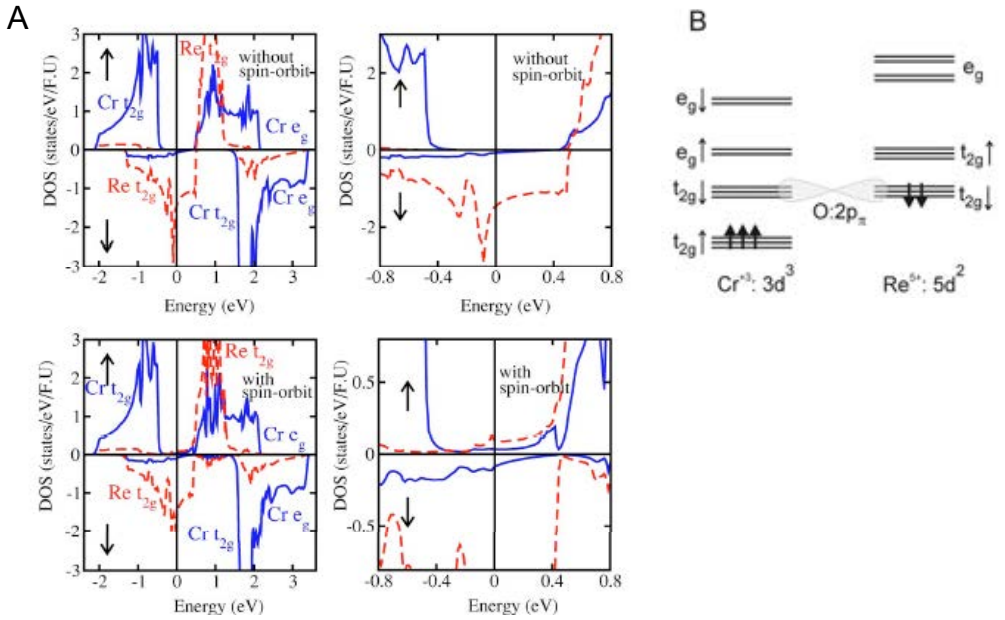

Figure 1.8. (a) The density of states for Sr_2CrReO_6 without spin-orbit coupling (upper row) and with spin-orbit coupling (bottom row) as calculated by Vaitheeswaran [61]. In the right panel the close-up of the Fermi energy region is displayed. Fermi level lies in the band formed by Cr ($t_{2g}\downarrow$) – O ($2p_\pi$) – Re ($t_{2g}\downarrow$) sub-bands in the case of absence of spin-orbit coupling, which does not remain true when the spin-orbit interaction is included (see text for details). (b) Energy levels diagram based on the same reference.

non-zero DOS in the majority spin channel. The pseudogap arising at the Fermi level mixes Re t_{2g}, Cr e_g and Cr t_{2g} states.

Last, we will discuss the expected magnetic moment of the double perovskite samples considering only the spin contribution. Let us begin with the Sr_2FeMoO_6. Theoretical saturation magnetisation (M_{ST}) can be calculated assuming the ferrimagnetic coupling between the *B* and *B'* sublattices. This results in the total spin of $5/2$ and $-1/2$ for Fe and Mo ions respectively. This would lead to the saturation magnetization per formula unit of 4 μ_B according to:

$$M_{ST} = |g_J|\mu_B\left(\frac{5}{2} - \frac{1}{2}\right) = 4\mu_B \qquad (1.32)$$

where $g_J \mu_B = -2$ is the Landé factor in case of unique spin contribution to the angular momentum. In the same way we can calculate M_{ST} for FeRe and CrRe based materials. These are listed in Table 1.2.

Table 1.2. Expected saturation magnetization per formula unit in the units of μ_B assuming spin only contribution for different *B* and *B'* combinations along with the total spin of each ion separately.

B / *B'*	Spin contribution		M_{ST} [μ_B/f.u.]
	B	*B'*	
Fe / Mo	$5/2$	$1/2$	4
Fe / Re	$5/2$	$2/2$	3
Cr / Re	$3/2$	$2/2$	1

The values listed in the table above have been taken for granted by various authors. However the model including spin-only contributions is not valid for both Re-containing configurations. The experimental data however could have been nicely fitted using this model. Two reasons are responsible for such situation. The first one is the presence of defects (see following subsections) that reduce the saturation magnetization. The second one is related to the lack of saturation of the magnetization in the Re-based samples in the low and moderate magnetic fields. As will be presented in the experimental section both affect the measurement of the magnetization in a way that cannot be neglected. We will also demonstrate that the orbital moment contribution has a value of one third of the spin moment for CrRe based double perovskite, as well as the need of the application of high field of several tens of Tesla in order to fully saturate the material.

1.6.1.1. Magneto-structural coupling in Re based Double Perovskites

Due to the strong spin-orbit coupling, the magnetostructural effects in the Re-based double perovskites are significant. We will focus on one aspect of the very rich experimental data available on the structural effects that occur under an applied magnetic field in these double perovskites. We refer to the magnetostructural

transition that occurs at about 140 K in Ca_2FeReO_6 (Westerburg et al. [62]). The structural transition occurs between two monoclinic phases with slightly different lattice parameters and different direction of the spontaneous magnetization axis [63]. It is very likely that the structural transition contributes to the increase of the magnetic anisotropy due to the strong magnetostructural coupling in Re based double perovskites. Moreover a colossal magnetoresistance effect around the magnetostructural transition has been disclosed for Ca_2FeReO_6 due to the coexistence between the high-temperature and low-temperature phases [18]. The consequences of such a transition and its impact on the magnetic properties of the material (saturation magnetization, coercive field and remanence) will be discussed in the experimental sections on the basis of the high-field magnetization data.

1.6.1.2. Enhancing the Curie temperature: electron doping

The search for the highest possible Curie temperature in the double perovskites has led to the idea of performing an electron doping in order to enhance the strength of magnetic interactions, and consequently the T_C. Recent results have shown that the electron doping of A_2FeMoO_6 double perovskites achieved by partial substitution of divalent A^{+2} with trivalent La^{+3} [64] (see Figure 1.9) and Nd^{+3} [65, 66] (see Figure 1.10) ions is a way of increasing the Curie temperature. Thus, T_C increases of 70 K for 50% La doping and of 90 K for 40% Nd doping have been reported. However, in most of the studied series other effects can contribute to the T_C increase apart from electron band-filling effects such as steric effects. The task of separation of the two was undertaken by Serrate et al. [67, 68] in *fixed bandwidth* samples (see Figure 1.11). The elimination of the steric effects contributing to the reinforcement of the ferromagnetic interaction between the Fe ions allows concluding on the following scenario: additional electrons promoted by La doping enhance the double perovskite double exchange magnetic interaction. The spin of the conduction electrons are aligned antiparallel to the localised Fe^{3+} electrons (possessing the spin of $5/2$ as discussed in the previous subsection). They transmit the information on the magnetic state to the neighbouring Fe ions.

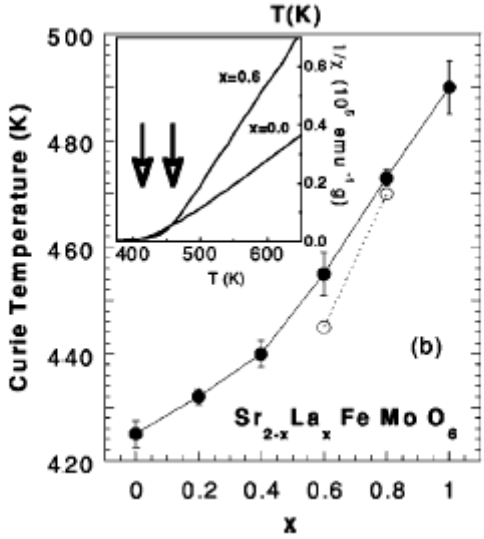

Figure 1.9. Curie temperature as a function of La doping level (x) in $Sr_{2-x}La_xFeMoO_6$ (closed and open circles belong to the samples from different batches). Figure redrawn after Navarro et al. [64].

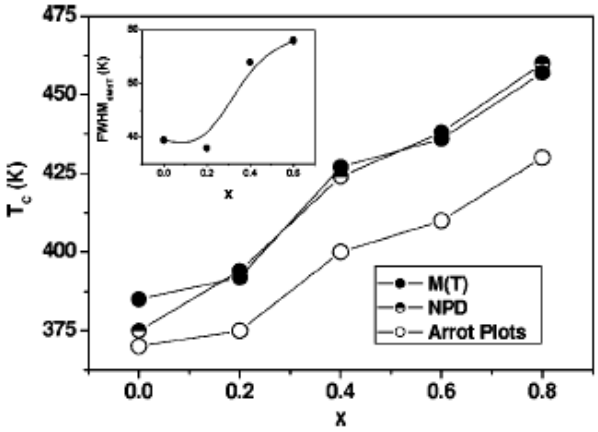

Figure 1.10. Curie temperature as a function of Nd doping (x) in the $Nd_xCa_{2-x}FeMoO_6$ series estimated on the basis of the magnetization versus temperature measurements (closed circles), neutron powder diffraction data (semi-closed circles) and Arrot plots (open circles). Figure redrawn after Rubi et al. [66].

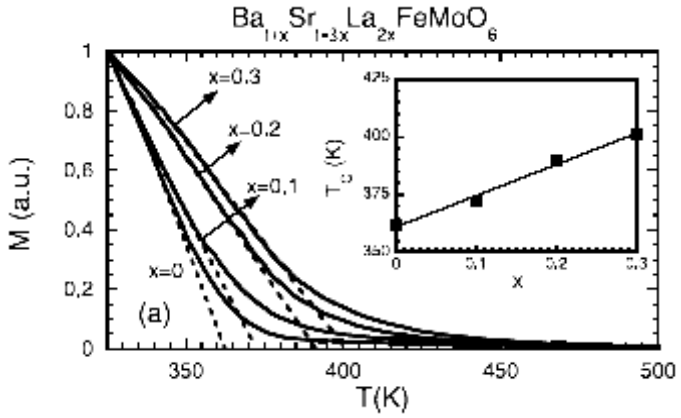

Figure 1.11.Main panel: Normalised at 325 K magnetization as a function of temperature for different doping levels (x) for the $Ba_{1+x}Sr_{1-3x}La_{2x}FeMoO_6$ series along with the extrapolation of the magnetization curves from the maximum slope to the ordinate axis in order to estimate the T_C. In the inset: The T_C as a function of the doping (x). Figure redrawn after Serrate et al. [68].

1.6.1.3. Importance of the crystallographic structure quality: defects

Also, extrinsic effects such as a large increase in the number of structural defects cannot be excluded in those samples. The most common type of defect is the so-called antisite (*AS*) defects i.e. misplaced *B* ions occupying the ideal positions of *B'* ones and vice versa. The amount of such defects depends strongly on the ionic radius and valence of the *B* and *B'* ions and is much higher in the case of CrRe based materials compared to the FeMo and FeRe based ones. In the perovskites studied in this thesis the *AS* amount is higher in CrRe based samples than in the FeRe series due to the similar ionic size for Cr^{3+} and Re^{5+} ions being different for Fe^{3+} (0.615 Å, 0.58 Å and 0.645 Å respectively [57]).

The experimental evidence for structural defects can be obtained by diffraction methods. However, only direct probe methods such as NMR [40] or Mössbauer spectroscopy have enough resolution to distinguish different environments that experience misplaced ions [69] including the oxygen vacancies [70]. In the Figure 1.12 different coordination of the misplaced ions is marked. In case of perfect ordering each *B*(*B'*) ion has only the *B'*(*B*) neighbours. The misplaced *B* ion has a total of six *B*

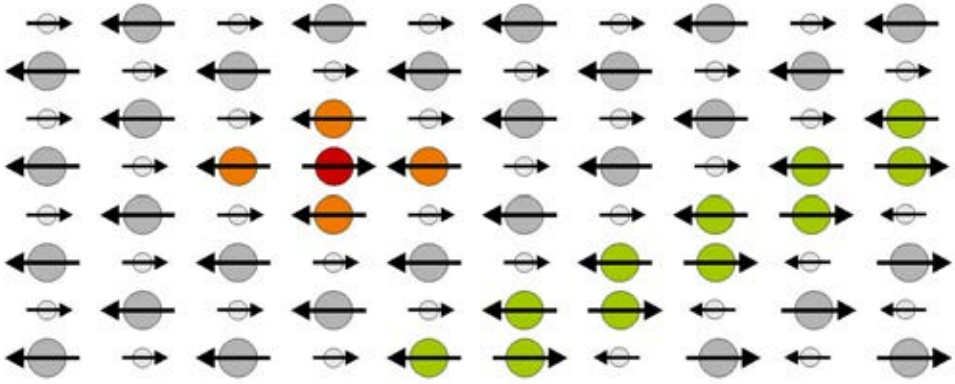

Figure 1.12. Schematic (reduced to two dimensions) view of the arrangement of the *B* and *B'* ions in the double perovskite structure. Ions drawn in grey occupy ideal crystallographic positions and have only neighbours of different type (*B'* for *B* and vice versa). The red ion is the *AS* one and has only the same type of ions surrounding it (thus, they have 6 nearest neighbours of same kind). The nearest neighbours of the *AS* atom are marked in orange and has one of the same type and five different-type adjacent atoms. The antiphase boundary is formed by the ions marked in green. On the both sides of the boundary the double perovskite structure is kept however the magnetic ordering is changed in the way that makes the *B*(*B'*) ions to be antiferromagnetically arranged on one side with respect to the equivalent ions on the other side of the boundary.

ions in its neighbourhood (four in the two dimensional representation in the Figure 1.12). The ions surrounding an antisite experience five different type ions and only a single of its own type. This situation is valid for low level of *AS* disorder. For high concentration of defects the antiphase boundaries can be formed. However as proved experimentally by Navarro et al. [71] by means of High Resolution Electron Microscopy and by Greneche et al. [72] by means of Mössbauer spectroscopy, the density of antiphase boundaries is rather low even in highly defective samples.

All kinds of defects are not only structural imperfections, but also the local magnetic structure is affected. This fact is a straight consequence of magnetic moments being associated with the ions in the structure. One can imagine two possible situations: the misplaced ion conserves its magnetic moment direction assigned to a perfect site or it acquires the magnetic moment characteristic for the new location i.e.

it inverts its moment direction with respect to the perfect position. It was presented on the basis of theoretical calculations that in the case of Fe based materials (Sr_2FeMoO_6 and Sr_2FeReO_6) defective Fe ions are conserving the orientation of the magnetic moment of the original ion leading to the antiferromagnetic coupling of the Fe-Fe pairs [73]. The model proposed assumes the superexchange interactions between the *AS* Fe and in-place Fe ions that can stabilize the ferrimagnetic configuration even for low concentration of *AS* defects. For higher *AS* concentrations the antiferromagnetic superexchange mechanism becomes even more efficient. The observed reduction of the saturation magnetization value was also predicted by the *ab-initio* linear muffin-tin orbital (LMTO) with atomic sphere approximation (ASA) calculations (see for example [74]). Different defects configurations result then in different magnetic moments at different crystallographic sites. Those summed up give different overall magnetization of the material that depends on the amount of the defects and their spatial distribution.

As a consequence of the *AS* disorder the saturation magnetization is lowered. The experimental formula (as was proposed by Balcells et al. for the Sr_2FeMoO_6 double perovskite, see reference [75]) giving the dependence of the saturation magnetization at low temperatures for different levels of *AS* and doping assuming spin-only contribution.

$$M_S = (1-2x)m_{Fe} - (1-2x)m_{Mo}\,. \tag{1.33}$$

where m_{Fe} and m_{Mo} are the magnetic moments of Fe and Mo ions respectively and $x = AS$ (hereafter we will use the italic letter to denote the amount of antisites abbreviated with *AS*).

The $x = AS$ parameter is defined by the percentage of *AS* defects in the way that 0% indicates defect-free structure fully ordered and 50% means fully disordered sample, i.e. the single perovskite phase instead of the double perovskite one. This can be calculated on the basis of the diffraction data refinements giving the occupations of the perfect *B*(*B'*) sites by the *B*(*B'*) atoms and the occupations of the same sites by the

B'(*B*) atoms. Defining *B[B]* and *B'[B]* as the number of *B* and *B'* atoms occupying *B* sites we can write:

$$AS(\%) = \frac{B'[B]}{B[B] + B'[B]} \cdot 100\% \,. \tag{1.34}$$

Not going into the details of the calculation of m_{Fe} and m_{Mo} we can introduce the parameter M_{ST} being the saturation magnetization in the case of perfect crystallographic ordering. This can be calculated as presented at the beginning of this section assuming the spin-only contributions (in an ionic model). In that way we can rewrite the relation (1.33) as:

$$M_S = M_{ST}(1 - 2x) \,. \tag{1.35}$$

This formula was successfully applied to the high pulsed magnetic fields Sr_2CrReO_6 magnetization measurements results, giving a perfect agreement of the corrected for the *AS* level saturation magnetization with theoretical predictions [76].

The way of estimating the *AS* amount from the diffraction data and its reliability will be described in the experimental section for FeRe and CrRe based compounds separately as their diffraction patterns differ.

Chapter 2

Experimental techniques and data analysis

The aim of this chapter is to introduce the reader to the techniques employed in the study of the Re based double perovskites. Also some large international experimental facilities (European Synchrotron Radiation Facility, Institute Laue-Langevin) and purpose-built laboratories (High Field Magnet Laboratory, Solid State Physics and Materials Research - IFW) that were involved in the study will be introduced. Complex characterization of the investigated materials requested a wide range of experimental techniques to be used.

2.1. Sample preparation

There are several techniques available that allow obtaining single-phase double perovskite samples. One can mention wet chemistry methods (sol-gel) or solid-state reaction. Physical properties of the samples synthesized with different methods can differ. This applies mostly to the microstructure and electrical transport properties.

2.1.1. Solid state synthesis of ceramic samples

The polycrystalline Sr_2CrReO_6 sample has been synthesized with the solid-state reaction technique. Stoichiometric amounts of $SrCO_3$, ReO_3 and Re, and Cr_2O_3 were mixed and pressed into pellets. ReO_3/Re ratio was set to 5/1 according to the expected Re valence in the resulting compound. The pellets were heated at 1375 ºC during 2 h in an atmosphere of Ar/(Ar/H_2) in proportions 90/(9.8/0.2) with heating and cooling rates of 7 ºC/min.

The A_2FeReO_6 samples have been synthesized using the same technique as the

CrRe based material. Stoichiometric amounts of A_2CO_3 (A = Ba, Sr and Ca), Fe_2O_3, ReO_3, and Re (with the same ReO_3/Re ratio as in previous case), were carefully mixed and pressed into pellets. The pellets were heated at 1000 ºC during 3 h in an atmosphere of Ar (nominal purity 99.9995%) with heating and cooling rates of 7 ºC/min. Contact between pellets and crucible is minimized in order to avoid Re loss.

In both cases the heating of the pellets followed by grinding and mixing was repeated several (3 – 4) times. The progress of the synthesis was checked by x-ray diffraction so that the end of chemical reaction could be observed. Resulting material shows pure double perovskite structure with no (or with low amount) impurities.

2.1.2. Lanthanide doped samples: questions about stability of electron doped material

The polycrystalline samples of $Sr_{2-x}Ln_xCrReO_6$ with the nominal doping level x = 0.1, 0.2, 0.3 and 0.5 and Ln = La, Nd or Sm have been synthesized with the solid-state reaction technique as well. Stoichiometric amounts of $SrCO_3$, Ln_2O_3 (Ln = La, Nd or Sm), Cr_2O_3, Re and ReO_3 (the Re/ReO_3 ratio was fixed according to the expected Re valence of the final compound) were mixed, ground and pressed into pellets. The pellets were calcined in an Ar stream at 1350 ºC for 2 h. This process was repeated several times up to XRD showed the end of chemical reaction (3 - 4 steps). The problem that occurred during the synthesis was the impossibility of obtaining single-phase samples. This was more evident with the higher doping levels. In order to avoid additional phases to come up an excess of chromium oxide was needed. A doping level higher than x = 0.5 was not possible to achieve, so we focused our study on the samples with doping up to x = 0.5. However, even in the case of this low doping level, the single double perovskite phase is hard to obtain because the desired phase occurs only within a narrow range of synthesis conditions and additional phases appear frequently.

The modification of the basic synthesis route and the out-of-stoichiometry amount of materials introduced in the reaction as well as the presence of impurities and

additional phases made it necessary to raise doubts about the resulting compound. The questions to be answered are: is the excess of chromium evaporated, built into the sample main phase or forms an impurity? why the Cr content is to be increased while the doping increases?, and last but not less important: is the main part of the sample really a double perovskite?

Sample synthesis has been carried out by Dr. Javier Blasco and Rosa Córdoba in the framework of collaborative work.

2.2. Bulk characterization methods

A large number of macroscopic properties of the material can be investigated easily by means of experimental methods that can be generally called as bulk methods. In the case of materials being under investigation in this thesis these are the magnetometry and the four point resistivity measurements.

2.2.1. Magnetometry

A large part of the work during the examination of the properties of the double perovskite investigated was dedicated to the magnetic properties of the material. The experiments have been performed both in high and low temperature range but not only under magnetic fields that can be easily obtained with the commercial use devices in the laboratories. Some large experimental facilities allowing the user to achieve very large magnetic fields have also been used.

2.2.1.1. SQUID magnetometry

SQUID – Superconducting Quantum Interference Device is a commonly used and commercially available experimental device that allows measuring a wide range of magnetic properties of the material. For our studies the possibility of measuring magnetization induced by a constant magnetic field was the most important one.

The idea of the interferometer is based on the Josephson tunnelling effects

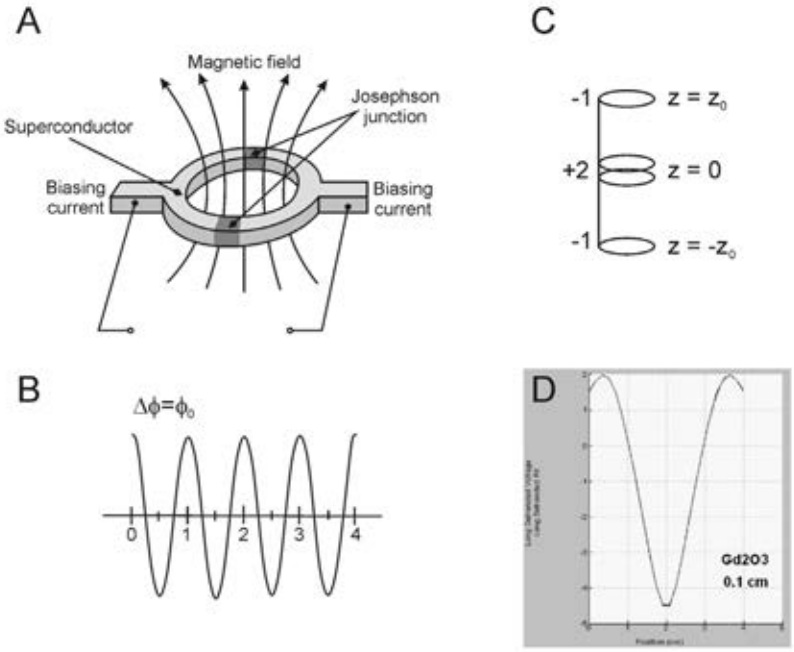

Figure 2.1. The SQUID coil consisting of two Josephson Junctions connected in parallel (a). A magnetic field flux passing through a closed loop results in oscillating output signal (b), with a period equivalent to a change of a flux of one fluxoid (φ_0). The set-up of the pick-up coils of the MPMS-5S and MPMS-XL SQUIDs (c). Numbers indicate the amount of spirals of each coil and the sign the direction of the winding. The signal generated in the pick-up system while moving the Gd_2O_3 sample on the way of 4 cm along the symmetry axis of the pick-up system (d) showing two maximums and a minimum at 2 cm (being the centring point) along with the dipole approximation curve showing perfect fitting.

through so called Josephson junction (JJ). Such junction consists of two layers of a superconductor separated by a very thin (~10 Å) insulating layer. Magnetic flux through a loop made of two JJ's connected in parallel (see figure Figure 2.1.a) is quantized, and the unit of quantization, called fluxoid, is $2 \cdot 10^{-15}$ Wb, which corresponds to $2 \cdot 10^{-7}$ emu.

Low field magnetic measurements have been performed using the SQUID by Quantum Design located at the Magnetic Measurements Service of the ICMA. The pickup system consists of three superconducting coils: two peripheral of them with

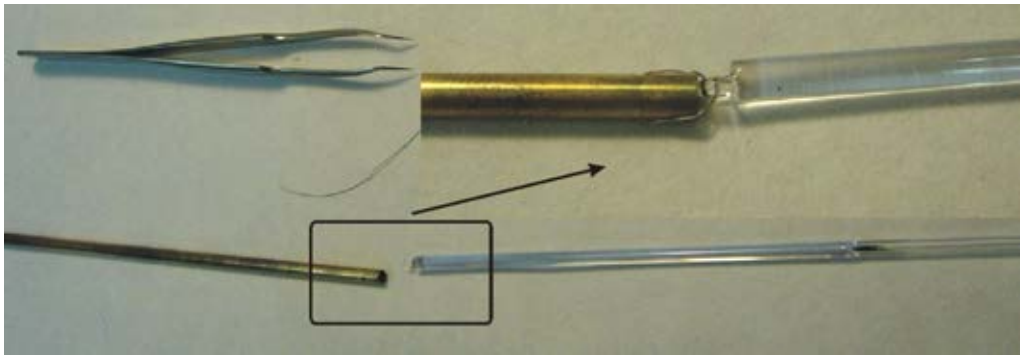

Figure 2.2. A quartz tube for high temperature measurements (bottom right) with the ground sample inserted (dark part in the middle of the tube). Magnified the bottom end of the oven-ready sample holder with the quartz tube attached by a very thin wire.

one spiral only and the third in the middle having an opposite direction of a winding, with two spirals (see Figure 2.1.c). Such kind of pick-up system setup assures higher accuracy comparing to the others having more spirals in the coil. As the sample is passed through the pick-up coils the output voltage is generated thus allowing estimation of the magnetic flux through the pick-up coils. Collected data is then fitted with the theoretical dipole-like signal (see Figure 2.1.d). In that way the magnetization M is determined with the accuracy of 10^{-5} emu.

Low temperature measurements (5 K – 300 K) can be performed with solid or ground samples, however it is preferable to use solid pieces in order to avoid movement of unfixed grains. More complicated are the measurements at high (300 K – 800 K) temperatures. This requires usage of quartz tubes of less than 4 mm of outer diameter (due to the oven diameter), and about 1 mm of inner diameter (see Figure 2.2). Sample is to be put inside the tube, protected by the glass fibre and fixed by a quartz stick welded to the tube. The quartz tubes were prepared by the Glass Service of the ICMA in Zaragoza. Welding of the protective stick was done in-house using an acetylene-oxygen welder.

Systematic errors can occur when the length of the sample in the direction of the movement through the pickup coils is bigger than 1 mm. A larger sample produces a voltage signal that cannot be fitted with the ideal magnetic dipole approximation

resulting in a systematic error (e.g. for a 5 mm sample the accuracy of a measurement is about 5 % lower comparing to the point-like sample). Other source of error is the weight uncertainty. A precision balance allows accuracy levels of 0.1 mg so the relative error is diminished for heavier samples. It is clear that the error in SQUID magnetization measurements occurs not only due to the equipment accuracy but other factors.

2.2.1.2. Vibrating Sample Magnetometer

Vibrating Sample Magnetometer (VSM) equipment provides the possibility of measuring the magnetization of solid samples even at high temperatures (up to 850 K). The heating and cooling rates are much higher than in case of the SQUID installation with the oven. On the other hand the accuracy of the measurement is lower compared to the one of a SQUID. The principle of the instrument is the electromotive force, v_m, produced by the magnetized sample oscillating in the middle of compensated pick-up coils.

$$v_m = M \cdot K\omega A \sin(\omega t) \tag{2.1}$$

where K is the geometrical constant, A is the amplitude of the vibration, ω is the vibration frequency and M is the magnetization of the sample to be determined.

2.2.1.3. High pulsed fields

The pulsed field experiments have been performed at the high magnetic field laboratory in the Institute for Solid State Physics and Materials Research (IFW) in Dresden, Germany. The equipment there allows obtaining magnetic fields as large as 50 T in a 24 mm bore (see Figure 2.3). The short-pulse magnet is developed by National High Magnetic Field Laboratory (NHMFL), Tallahassee, USA. The capacitor bank of 1 MJ forms the coil alimentation [77].

The magnetic field increases sinusoidally to a maximum field in 10 ms then decreases almost sinusoidally to zero field in 10 ms. A small reverse field that allows

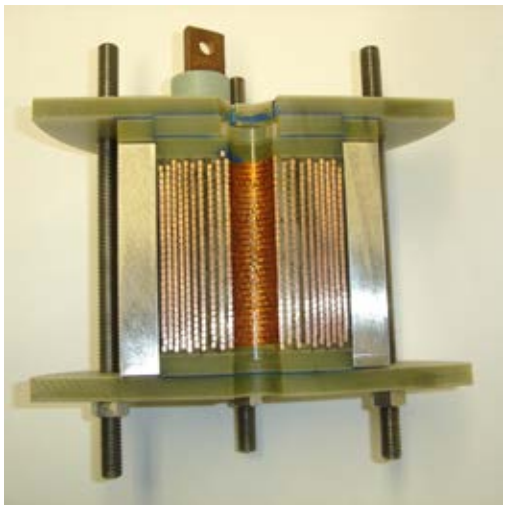

Figure 2.3. On the left: photograph of the experimental station in the IFW laboratory. The pulsed field coil is located in the cylindrical structure protected by the wood/steel box visible in the bottom. On the right the crosscut through the 50 T coil developed by NHMFL for IFW laboratory.

the measurement of the sample coercivity can follow the maximum field pulse (see Figure 2.4). Operating temperature range is 1.5 K to 300 K.

The sample magnetization is measured through the signal induced in a pick-up coil calibrated with a ferrite sample. Pick-up coils are combined with two compensation coils with the aim to remove the spurious signals generated in the wiring by an alternating magnetic field [78]. However not all the false readout can be removed by the coils forming a compensation system. This remaining signal has to be estimated by performing two-step experiments. One high-field shot is to be made without the sample placed in the pickup coils and the "zero" signal is to be collected. This is followed by the high-field shot with the sample and the "zero" signal collected earlier is to be subtracted. As one can imagine a very high accuracy of the temperature stabilization is of critical importance, because of the thermal effects that influence both the compensation system and the electronics response to the field. This procedure gives good effects when the magnetization measured is the saturation magnetization

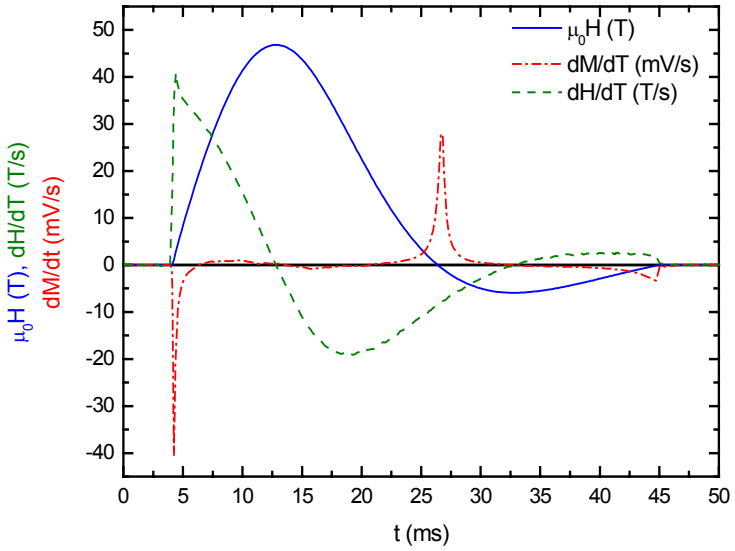

Figure 2.4. Time evolution of the magnetic field pulse (solid line). The sharp rise to the maximum value of 47 T lasts for 10 ms, and the field is stable within 1 T for 2.5 ms. The maximum of inversed field occurs at 30 ms and its value is –6 T. Dashed line is the derivative of the field versus time and the dash-dot one is the derivative of the magnetization versus time.

and no paramagnetic contribution is present. In case of a magnetically non-saturated material the manipulation of the data gives reasonable effects, but additional care is needed.

2.2.1.4. High static fields

Other possibility of investigation of the high field magnetic properties is available by means of high static field magnets. The study presented in this Thesis was accomplished in the High Field Magnet Laboratory (HFML) of the University of Nijmegen, Netherlands. The Bitter type magnet developed in National High Magnetic Field Laboratory (NHMFL), Tallahassee, USA [79] allows, coupled with the 20 MW (40 kA at 500 V) power supply and a specially designed cooling system [80], obtaining static fields as high as 33 T in the 32 mm bore. Maximum power can be used for 3 h without breaks. See Figure 2.5 for the view of one of the three static field experimental stations available in the Laboratory.

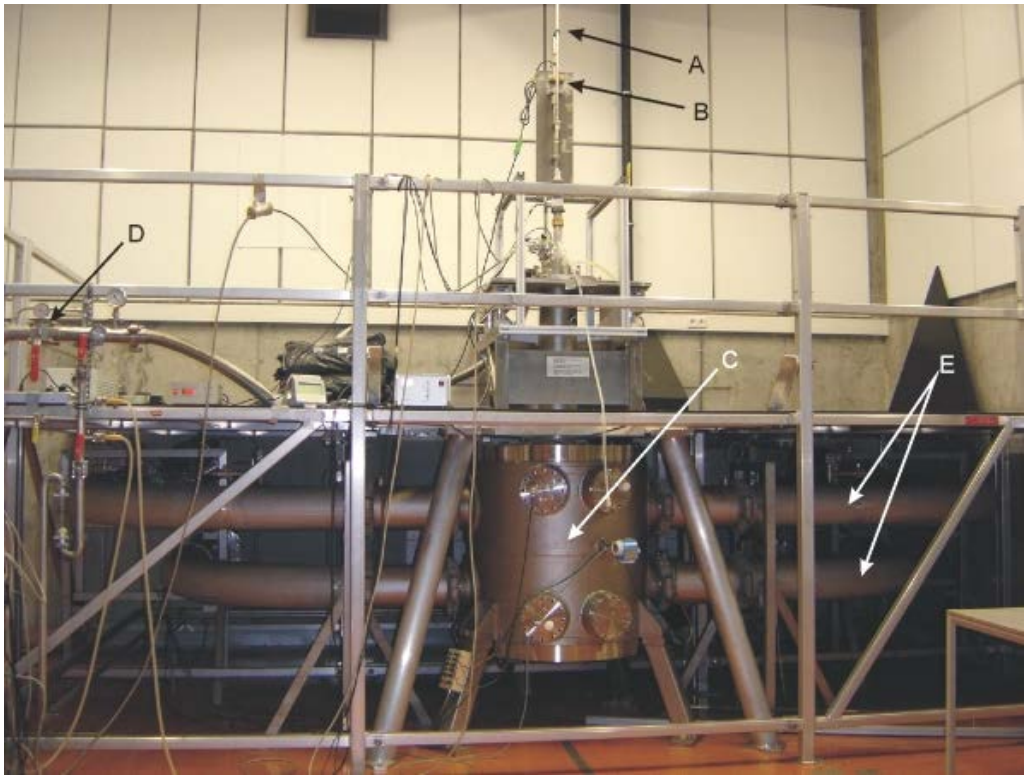

Figure 2.5. The experimental station at HFML. A – sample holder, B – motor moving the sample inside the coil in the homogenous field region between the pick-up coils, C – chamber for the sample cryostat, pick-up coils, Bitter magnet and its cooling installation, D – gaseous helium installation for the flow cryostat, E – cooling water pipes.

In the experiment, the static magnetic field is first stabilized and the magnetization is measured with the extraction method via two pick-up coils connected in series-opposition (serial connected with opposite winding direction). A bulk Ni sample with similar volume to our samples has been used for calibration of the absolute value of the magnetization. The measurements were performed in the temperature range 4 K to 300 K. The use of static magnetic fields is preferred in this kind of investigation to the use of pulsed magnetic fields in order to avoid spurious signals arising from fast field variations (see previous section).

2.2.1.5. Singular Point Detection

Although at first sight, the measurements of the magnetization in the polycrystalline materials does not allow obtaining detailed information on the anisotropy field (H_A) due to the averaging over all crystallographic directions, Singular Point Detection method overcomes this problem. In the single crystal measurement, depending on the relative orientation of the hard magnetization axis and the applied magnetic field, one observes a singularity at the saturation point (due to the connection of the two functions describing the magnetization: one constant vs. applied field at $H > H_A$ and second one, below H_A, where the magnetization is field dependent). On the contrary in the polycrystalline material the *M(H)* curve is smooth thus not allowing the estimate of the anisotropy field. However it has been shown by Asti and Rinaldi [81] that the "smooth" magnetization curve possesses a "memory" of the anisotropy field. Soon after, a theory for the effect was developed by the same authors [82] for different crystallographic systems. Early approach proposed in abovementioned reference was limited however to the case of material exhibiting small enough grains to be treated as single magnetic domains. Further improvements of the theory [83] dealing with multidomain approach allow nowadays the investigation of the anisotropy fields of a wide range of polycrystalline materials. Care however is needed as the conductivity of the sample itself is affecting the results of the measurements in the way that H_A value obtained on the rising part of the magnetic field pulse may differ from the one obtained on the falling part, difference being bigger for samples exhibiting better conductivity [84].

The idea of extracting the value of anisotropy field from the polycrystalline material magnetization data requires analysis of the consecutive derivatives of the magnetization with respect to the applied magnetic field i.e. $\partial^n M / \partial H^n$ for n depending on the crystallographic structure and the orientation of the magnetic hard axis with respect to the crystallographic unit cell vectors. Instead of being calculated numerically the derivatives are being measured directly with the experimental set-up. Then the singularities in the almost smooth magnetization curve are visible in the

appropriate order derivative curve.

Measurements of H_A on the polycrystalline double perovskite samples together with the data analysis have been performed in the framework of collaborative work by the group of F. Bolzoni from MASPEC del CNR Institute, Parma, Italy.

Experimental equipment at the Institute consists of a 60 Tesla purpose built magnet supplied by the 1.09 MJ (0.243 F) capacitor bank. The detailed information on the installation can be found in reference [85].

2.2.2. Resistivity

In the investigation of the electrical properties a method for measuring the resistivity of the material is of great importance. The simplest way to measure the resistance of the material is to make two contacts and measure the drop of the voltage while letting the current pass through the contacts. However, when the resistance of the contacts becomes comparable to the resistance of the sample the contacts conducting the current need to be separated from the contacts between which the voltage is measured. In such way the contact resistance is not measured together with the sample resistance. For the semiconducting bulk samples and for measuring low resistivities of good conductors the most suitable is the four contacts arrangement of the electrodes then. In the Figure 2.6 the sketch of one of possible geometries of the measurement is presented. The resistivity of the material is then given by:

$$\rho = G\frac{V_{2-3}}{I_{1-4}} \tag{2.2}$$

G being the correction factor depending of sample shape and dimensions as well as the arrangement of electrical contacts, $I_{1\text{-}4}$ the current passing through the contacts *1* and *4*, and $V_{2\text{-}3}$ the voltage between the contacts *2* and *3*.

Equation (2.2) is only valid assuming the homogeneity of the sample (at least

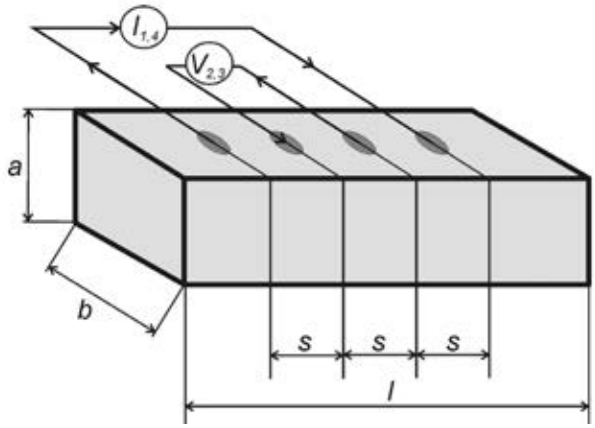

Figure 2.6. Scheme of the four point resistivity measurement of a bulk sample (see text for details).

from the point of view of its electrical properties). The geometrical factor is simplified when the all contacts are equally spaced (with the spacing *s*) and aligned in a straight line. The *G* factor takes its most simple form when the above statement about the arrangement of the contacts is true and one deals with a sample of infinite volume. However the case is usually more complicated. In our work we used samples of finite length and rectangular or quadratic ($a = b$ in the Figure 2.6) cross section. The details of the derivation of the geometric factor for such case can be found in references [86]. The correction for the geometric factor *G* becomes more important for the sample of the cross section height (*a*) comparable to contact spacing and reaches the limit of the semi-infinite volume for a quasi-infinite sample (i.e. very large *l*) with the contact spacing $s << a$.

Corrections are not necessary if we deal with the measurement of the relative change of the resistance of the material e.g. while an external magnetic field is being applied. In such case we do normalize our data to the value of the resistance without the magnetic field being applied. This allows the comparison between the samples of different geometric factors to be done without an uncertainty arising from the correction terms being added.

The contacts (dark ovals in the Figure 2.6) for the magnetoresistance measurements have been done using “silver paste”. The “silver paste” is a solution of

silver particles in a two-component epoxy. Its great advantage is a good adherence to a porous material. The wiring is done with 0.25 mm copper wires. The connection sample-contact-wire becomes stable and of low resistance after heating the sample with wet contacts and wires attached for 45 minutes at 180 ºC in the oven.

The measurement is done with the current direction being changed i.e. an alternated sign of excitation bias and averaging two measurements for each experimental data point. This assures that the effects related to the thermoelectric voltages (due to a gradient of temperatures in the sample space and non-equal Joule heating of the all contacts) and an electronic offset very likely to appear in a source and measuring unit are not affecting the measurement.

Magnetoresistance measurements have been performed using the PPMS equipment located at the Magnetic Measurements Service of the University of Zaragoza. The field is stabilized during the measurement and is not changing when the experimental point is being taken. This allows discarding the third component of the measurement error, which is a current induced in the wiring by the changing magnetic field (see chapter 2.2.1.3).

2.3. Crystallographic structure, microstructure and chemical composition

2.3.1. Diffraction methods

Diffraction methods have become a fundamental tool for the structural characterisation and they have also been applied to the samples studied in this thesis. The X-Ray Diffraction (XRD) and Neutron Powder Diffraction (NPD) allow studying the long range ordering and thus a determination of the crystallographic structure on the one hand, and the deviations from a perfect ordering on the other hand. The usefulness of both the short wave x-rays and neutrons arises from the possibility to tune their wavelength so that it closely matches the interatomic distances in the solid (i.e. becomes of the order of ~1 Å). The most important in the diffraction theory is the Bragg equation:

$$n\lambda = 2d_{hkl}\sin(\theta);\ \mathrm{n} = 1, 2, \ldots \tag{2.3}$$

It links the incident particles (x-ray photons, electrons or neutrons) wavelength λ, the angle between the propagation vector of the incident/outgoing wave and the scattering planes (θ). The distance in real space between the parallel crystallographic planes (d_{hkl}) is defined as:

$$\frac{1}{d_{hkl}^2} = \frac{h^2}{a^2} + \frac{k^2}{b^2} + \frac{l^2}{c^2} \tag{2.4}$$

where *h, k, l* are the Miller indexes and *a, b, c* the crystallographic lattice constants in real space. One can limit the considerations on the origin of the diffraction pattern to the unit cell owing to the periodic structure of the crystal. Spatial distribution of the atoms in the unit cell for the given direction of the incident wave propagation vector and given observation direction causes the waves scattered on the distinct atoms to have different phase shifts. Those phase shifts cause the interference of the propagating waves to be either destructive or constructive.

2.3.1.1. X-ray Diffraction

Photons of the incident x-ray beam interact with the cloud of electrons, which surrounds the nucleus. The cross section of such interaction is proportional to the atomic number *Z*. Therefore it is not possible to probe the structures composed of light atoms with good accuracy. Also certain positions of such atoms cannot be resolved.

The amplitude of the scattered wave is given by:

$$F_{hkl} = \sum_j f_j \exp\left\{2\pi\left(u_j h + v_j k + w_j k\right)\right\} \tag{2.5}$$

j being the index of the atom in the unit cell, u_j, v_j, w_j are the atom coordinates and f_j is the amplitude of the scattering of the atom (scattering factor). If the experiment is performed using a powder sample, one observes diffraction peaks with intensity $\left|F_{hkl}\right|^2$ at angles (2θ) fulfilling the Brag condition (2.3). The form factor *f* depends on

the atomic number of the scattering atom, and is strongly reduced at high 2θ angles. This is due to the size of the cloud of scattering electrons, being of the order of ~1 Å, whitch results in phase shifts of the waves scattered from different parts of the electron cloud.

X-ray diffraction was used to determine the synthesis process progress, the crystallographic structure and the purity of the compound. The measurements have been performed at the X-ray Diffraction and Fluorescence Analysis Service at the ICMA using the Rigaku RTP 500 RC diffractometer with rotating anode and equipped with a graphite monochromator. The used wavelength is that of Cu $K\alpha_{1,2}$ being 1.5405 and 1.5444 Å. Diffraction experiments have been accomplished by Dr. Javier Blasco and Rosa Córdoba, and the diffraction patterns have been analysed in collaboration with Dr. Javier Blasco.

2.3.1.2. Neutron Powder Diffraction

Neutron diffraction is a complementary technique to x-ray diffraction in structural studies. Neutrons interact with the atom nucleus and with the electron spin. Thus, magnetic ions give substantial scattering due to the interaction of the magnetic moment of the neutron with the unbalanced electron spins. The nuclear scattering amplitude becomes described with:

$$F(q) = \sum_j b_j \exp\left[\frac{iqr_j}{\hbar}\right] \qquad (2.6)$$

Similarly to equation (2.5) the scattering occurs at the atom located at a position given by a vector r_j. The form factor *f* used in XRD is replaced with the scattering length *b* having units of length. The factor *b* is dependent on the nuclear properties of the atom and has no simple correlation with the atomic number. It becomes even negative for hydrogen, giving a large contrast when compared to other atoms. Moreover, due to the small size of the nucleus with respect to the thermal neutron wavelength (point-like scattering), there will be no dependence of *b* with the scattering

angle θ. Detailed considerations can be found for example in reference [87].

In the case of ferromagnetic and antiferromagnetic materials, below certain ordering temperature, all the magnetic moments will become oriented with respect to some axis, within a magnetic domain. To each magnetic atom magnetic scattering amplitude D may be ascribed. It can be treated in similar manner as the nuclear scattering amplitude is. Consequently apart from the Bragg diffraction peaks, arising from the three-dimensional ordering in crystal structure and nuclear scattering, additional peaks will appear being dependent on the ordering in the magnetic unit cell. If the magnetic unit cell is equivalent to the chemical unit cell, the magnetic and the nuclear Bragg peaks will be located at the same position in 2θ units. On the other hand, if the magnetic cell does not coincide the chemical cell, magnetic Bragg peaks will occur in new positions corresponding to a super-structure long-range order. Above the ordering temperature, no magnetic order is present, and thus no long-range magnetic scattering contribution to the diffraction pattren will be present.

The NPD measurements presented in his thesis have been performed at the Institute Laue-Langevin (ILL) at Grenoble, France. This part of the work has been done in close collaboration with Dr. Clemens Ritter. Experiments have been performed at two high-resolution two-axis diffractometers: D1A and D2B. The layout of these apparatus is presented in the Figure 2.7.

D1A is an instrument designed for standard crystallographic problems. It gives excellent results with the Rietveld fitting method owing to its near perfect Gaussian peak-shape in the 2θ-range 30° to 150°. The high resolution over a wide range of scattering angles permits the refinement of up to 150 structural parameters by the Rietveld method. The monochromator consists of 30 Ge crystals, and the counter of 25 ^{3}He detectors. The counter can be swept through 0° to 2θ = 160° for the highest angle counter, usually in steps of 0.05°. Sample temperature can be controlled over a wide range: 1.5 K – 600 K with cryofurnace (300 K in the cryostat) and even < 1000 ºC in the furnace.

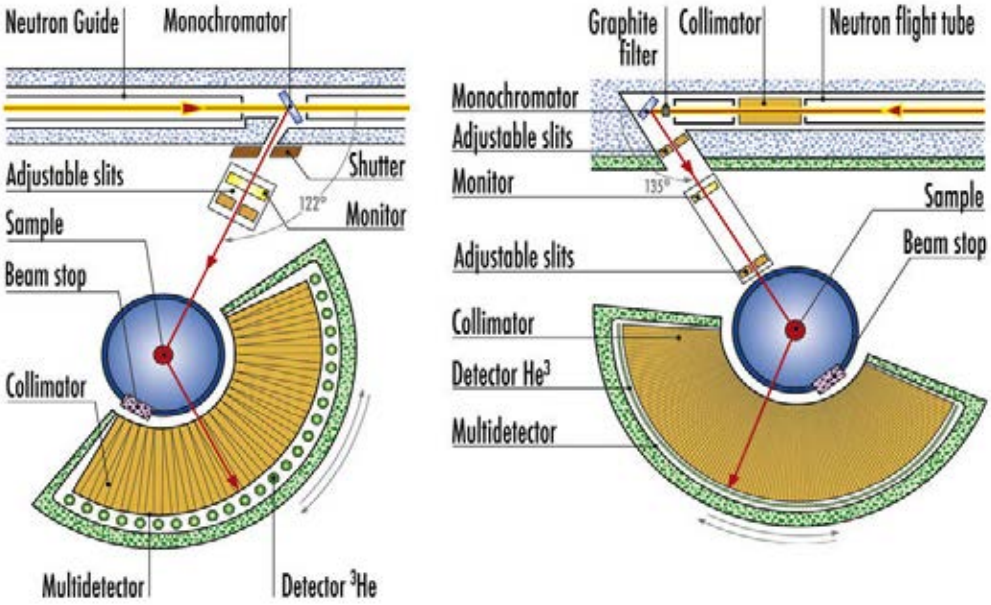

Figure 2.7. Layout of the two diffractometers that have been in use for the experiments presented in this thesis: D1A (on the left) and D2B (on the right). See text for detailed description.

D2B diffractometer allows obtaining a full pattern after 100 steps of 0.025° in 2θ the scan being repeated for improved statistics. The 2θ-range is 5° to 165°. The monochromator is composed by 28 Ge [115] crystals and the detector is made of 64 ^{3}He counting tubes. Sample temperature can be controlled in the 1.5 K – 1000 K range.

2.3.1.3. Rietveld refinement of the diffraction data

The Rietveld method [88] of the diffraction spectra analysis, a so called "whole pattern" method, is nowadays implemented in various software designated to examine the experimental data. In the Rietveld refinement of the data the quantity:

$$S = \sum_i w_i \left(Y_{i(obs)} - Y_{i(calc)} \right)^2 \qquad (2.7)$$

being the weighted difference between the observed $Y_{i(obs)}$ and calculated $Y_{i(calc)}$

patterns is minimised by a least-squares algorithm. The calculated pattern is modelled using the formula:

$$Y_{i(calc)}(x) = I_0\left[\sum_k k_h F_h^2 m_h L_h P_h(x) + I_b\right] \tag{2.8}$$

where: I_0 is the incident intensity, k_h is the scale factor for the particular phase (denoted as h; for single phase sample $h = 1$), F_h^2 – the structure factor for particular reflection, m_h – reflection multiplicity, L_h – correction factors on intensity, $P(\Delta_h)$ – peak-shape function and I_b is the background contribution.

The background contribution can be modelled by an empirical or semi-empirical function – usually a polynomial with some refinable parameters. The peak-shape function is used for modelling the Bragg peak shape in the calculated pattern. It can have several forms, however a pseudo-Voigt (an approximation of the Voigt function) is most widely used for x-ray diffraction and constant wavelength neutron diffraction. It consists of a mixing of Lorentzian (L) and Gaussian (G; originating from instrumental contribution) contributions:

$$G(x) = \frac{2}{\Gamma}\sqrt{\frac{\ln 2}{\pi}}\exp\left[-\frac{4\ln 2}{\Gamma^2}x^2\right] \tag{2.9}$$

$$L(x) = \frac{2}{\pi\Gamma}\frac{1}{1+\left(4/\Gamma^2\right)x} \tag{2.10}$$

$$P(\Delta_h) = \eta L + (1-\eta)G \tag{2.11}$$

η being the pseudo-Voigt mixing parameter and Γ - full-width at half-maximum (FWHM). Additionally the peak-shape function is to be modified by an asymmetry-function putting an extra intensity on the “low angle” side of the peaks at low 2θ (and opposite on very high 2θ). This is due to a peak asymmetry arising from the divergence of the diffracted beam at low angles [89] and sample thickness effect. The variation of Γ with 2θ is modelled separately for the Gaussian and Lorentzian

component separately:

$$\Gamma_G^2 = U\tan^2\theta + V\tan\theta + W \tag{2.12}$$

$$\Gamma_L = X\tan\theta + Y/\cos\theta \tag{2.13}$$

U, *V*, *W*, *X* and *Y* being refinable parameters.

The quality of the fit can be judged using several parameters: weighted-profile *R* value

$$R_{wp} = \left\{ \sum_i w_i \left[y_{i(obs)} - y_{i(calc)} \right]^2 \Big/ \sum_i w_i \left[y_{i(obs)} \right]^2 \right\}, \tag{2.14}$$

goodness-of-fit (χ^2)

$$\chi^2 = R_{wp} / R_{ex} \tag{2.15}$$

and the Bragg-intensity *R* value

$$R_{Bragg} = \left\{ \sum_{hkl} \left| I_{hkl(obs)} - I_{hkl(calc)} \right| \Big/ \sum_i w \left| I_{hkl(obs)} \right| \right\}, \tag{2.16}$$

where $I_{hkl} = m \cdot F_{hkl}^2$, m is the multiplicity of the peak and *F* is defined as in equations (2.5) and (2.6).

The quality of the fit is estimated giving the information on how close the R_{wp} value is approaching the expected R_{ex} value, the latter being calculated taking into account the number of observations and the number of parameters (reflecting the quality of the data i.e. counting statistics). χ^2 should approach 1 in case of a good quality fit. Variations of R_{Bragg} give direct information of the improvement of the structural model during the fitting. Detailed information on the Rietveld method can be found in reference [90].

Diffraction data presented in this thesis have been analysed by means of FULLPROF software [91]. For the successful Rietveld refinement with FULLPROF program some data have to be known prior to the beginning of the procedure. We refer to structural data such as the space group and unit cell constants (inter atomic distances and angles similar to the expected ones). That allows the generation of the theoretical pattern and estimation of the background and profile parameters making it possible to refine more parameters in the following steps. The refinement of the x-ray diffraction data allows a full structural model including inter atomic distances, bond angles, site occupancies and structural defects for desired number of phases to be made. Moreover for NPD data the magnetic model can be included, the calculations of the pattern being made for nuclear and magnetic scattering separately. The quality parameters can be extracted separately for both contributions. From the magnetic part of the model the magnetic moments of the particular ions can be estimated. The limitation of the powder diffraction is the lack of possibility of estimate the components of the magnetic moment along every crystallographic direction for all crystallographic structure. For cubic structure and randomly oriented grains the information of the direction of the magnetic moment with respect to the crystallographic axes is lost and only the absolute value of the magnetic moment can be extracted. For the structures with lower symmetries more information can be obtained. In the case of the tetragonal crystallographic system (and more generally in uniaxial crystals) it is possible to separate the *z*-axis component and the one lying in the *xy*-plane. In the monoclinic one, all of the components (along *x*, *y* and *z*-axis) are available. Mathematical considerations on the problem can be found in reference [92]. As a consequence in the diffraction spectra one would observe a change of the intensity of the diffraction pattrens due to the magnetic scattering for a unique peak (a sum of the diffraction intensities on (100), (010) and (001) planes) in the case of the cubic structure, of the two resolved peaks and depending on the magnetic moment direction (a sum of the diffraction intensities on the (100) and (010) planes on the one hand and (001) plane on the other) for the crystals with uniaxial symmetry, and finally of three separate diffraction peaks (diffraction on the (100), (010) and (001) planes) in the case of even lower symmetries. Only in the last case a full set of the angles

describing the magnetic moment orientation with respect to the main crystallographic directions can be found during the refinement of the diffraction data.

2.3.2. Scanning Electron Microscopy

Scanning Electron Microscopy (SEM) allows obtaining the information on the microstructure of the samples. This is of primary interest, as the grain size and the way the grains are "packed" together help to understand properly the transport properties of the compound. Moreover, microscopes equipped with an x-ray detector allow investigating the chemical composition of the specimen. In SEM microscope the sample is irradiated with an electron beam of high energy (typically 5 – 30 keV). The sample surface should be ideally coated (using carbon or gold) to avoid charging effects and the sample needs to be fastened to the sample-holder with conducting glue in order to assure that the current flows out of the sample. The focal spot of the beam and consequently the spatial resolution of the microscope depend on: the accelerating voltage, probe current (10^{-12} A – 10^{-6} A) and working distance (the distance from the objective lens to the sample surface). On the one hand, the higher the voltage the better resolution can be obtained. On the other hand, high voltage increases the risk of charging the sample. The beam is moved over the sample surface by a set of magnetic and electrostatic lenses (scanning mode). The incident beam penetrates the sample up to a few micrometers depending on the accelerating voltage and chemical composition of the sample. Electrons interacting with the material cause several effects, as can be seen in the Figure 2.8. Depending on the detector used different signals can be measured, however it is important to keep in mind that the material volume from which the information is obtained is different for each kind of emitted signal.

Secondary electrons (SE) are excited by the incident beam by the inelastic interactions between the incoming electrons and weakly bonded electrons i.e. conduction or valence electrons. The generation region is close to the surface, up to approximately 10 nm. The contrast of SE-signal depends mostly on the tilt of the sample and the topography of the specimen surface.

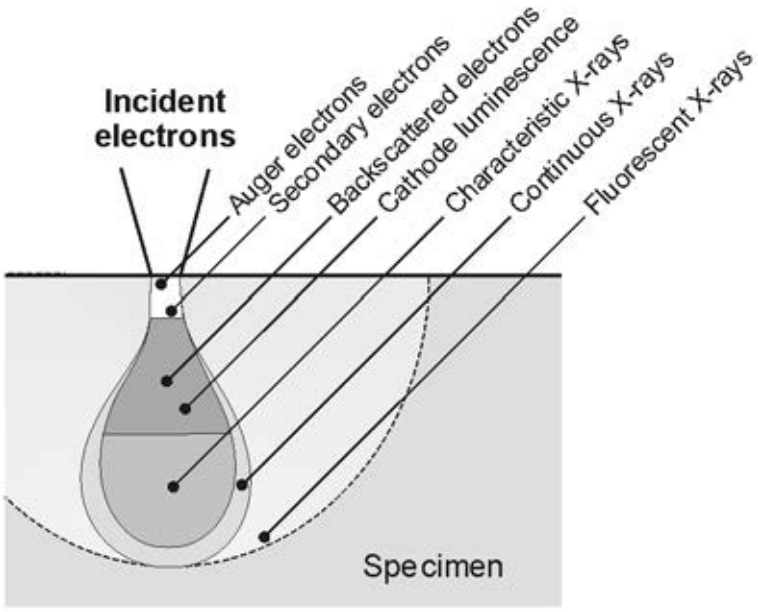

Figure 2.8. Interaction between incident electrons and specimen.

Backscattered electrons (BSE) are the electrons of the incident beam that have been elastically backscattered on the sample electrons or nuclei. The amount and direction of the backscattered electrons varies with the composition, surface topography, crystallinity and magnetism of the specimen. Very useful is the fact that the contrast of the BSE-signal depends on the atomic number (the larger Z, the brighter the spot). It allows the building of two-dimensional images with the contrast varying with the composition of the specimen. BSE are generated in a larger interaction volume compared to SE, resulting in worse spatial resolution.

X-rays (more precisely characteristic x-rays) are emitted when the atom is excited by hole creation in a deep electron shell and returns to its ground state by means of x-ray emission. The energy of x-ray photons is characteristic for the electronic configuration of the atom. The spatial resolution is even lower than BSE since x-rays are collected from much larger sample volume. Using this technique (called Energy Dispersive X-ray Spectroscopy – EDS) allows obtaining the information about the chemical composition of the investigated material or spatial distribution of specific element (mapping).

SEM experiments were carried out in the Electron Microscopy Service in the University of Zaragoza using a JEOL-JM6400 microscope equipped with eXL-10 x-ray detector from Link Analytical, and in the Scanning Electron Microscopy Laboratory of Biological and Geological Sciences of the Biology and Earth Sciences Faculty in the Jagiellonian University (Cracow) using HITACHI S-4700 field emission microscope with NORAN Vantage EDS system. In those experiments, the electrons were accelerated at 20 kV.

2.3.3. Fluorescence

In the x-ray fluorescence experiment the primary x-ray beam irradiates the sample. For a beam of wide energy range, the photoelectric effect occurs for different atoms in the solid. Then, during the deexcitation process, the characteristic x-ray radiation is being emitted. The fluorescent radiation can be analysed either by sorting the energies of the photons (energy-dispersive analysis) or by separating the wavelengths of the radiation (wavelength-dispersive analysis).

The technique is complementary to the EDX measurement as the fluorescence measurements allow quantitative chemical composition determination (provided some reference material is measured prior to the investigated compound). However the equipment is dedicated only to such experiments and consequently allows better accuracy and already mentioned quantitative analysis. Measurements have been performed in the X-ray Diffraction and Fluorescence Analysis Service in the University of Zaragoza.

2.4. Synchrotron methods

The X-ray Absorption Spectroscopy (XAS) became a very powerful analytical and research tool mostly owing to two reasons. Even though the basic quantum description of the x-ray absorption was known from 1930's it was not until 1971 when Sayers, Stern and Lytle [93] gave a description of essential physics underlying the process and a simple method of data analysis. This together with the availability of high-flux and tuneable, high energy resolution synchrotron radiation beamlines caused

the number of XAS experiments to grow rapidly. The potential of the XAS being a short-range order technique can be fully used while accompanied with some complementary method allowing a long-range order examination (such as diffraction methods). XAS is widely used in various scientific fields such as material science, metallurgy, electronics or biology.

2.4.1. X-rays interaction with matter

Several effects occur when x-rays irradiate a material. The cross section of each process depends on the material itself and on the energy of the incident beam. For the highest energies (above 1 MeV) the positron-electron pair creation occurs. In low and moderate energy region several effect occur giving rise to an overall interaction cross section. These are: the photoelectric absorption, Compton scattering and Thomson scattering. In all abovementioned processes an excitation of the material (or more precisely of the atoms building the matter) takes place. The decay of the matter can be realized either by fluorescence, luminescence or Auger electrons. The transmitted beam propagates with the same direction as the incident beam, however it has lower intensity.

The number of processes that take place in the matter being placed in the x-ray beam gave the possibility of inventing several experimental techniques. The first criterion to be taken into account is the signal-to-noise (S/N) ratio. Best overall S/N is achieved in transmission geometry, which will be addressed in the following paragraphs. If the surface sensitivity were of particular interest (e.g. adsorbates on the surface) then the most beneficial would be the detection of the current produced in the sample – Total Electron Yield (TEY). In the case of diluted samples the fluorescence detection is the most reasonable set-up in which the background is reduced. Finally the X-ray Excited Optical Luminescence (XEOL) allows the visible light or the UV light detection in case of luminescent samples.

2.4.2. XANES and EXAFS experiments

In the X-ray Absorption experiments the interactions of the photons with matter

are studied by measuring the absorption of x-ray beam as a function of the energy of the beam given by

$$E = \hbar\omega \tag{2.17}$$

The x-ray absorption coefficient is determined from the decay of the intensity of the photon beam with the distance *dx* (see Figure 2.9.a) given by:

$$\mu(E) = -\frac{d}{dx}\ln\frac{I}{I_0} \tag{2.18}$$

being the straight consequence of the exponential absorption law:

$$I = I_0 \exp[-\mu(E)x] \tag{2.19}$$

For the low energy photons (below 100 keV) the dominant process is the photoelectric effect. In this process, the photon is completely absorbed transferring its energy to the ejected electron called a photoelectron.

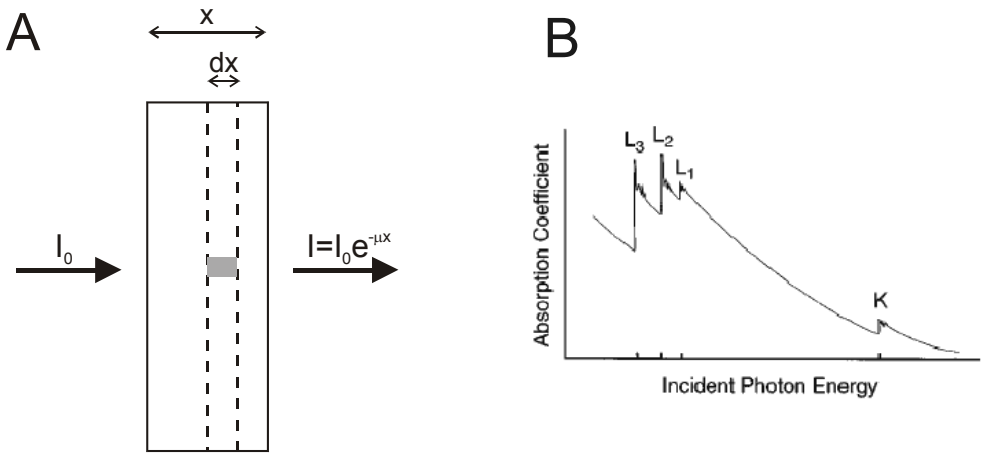

Figure 2.9 (a) Schematic view of the absorption of the x-ray beam with the incident intensity I_0 in a sample of a thickness x. The intensity of the beam leaving the sample is then given by equation (2.19). (b) The example of the absorption coefficient as a function of energy plot showing four absorption edges (K, L_1, L_2 and L_3). The oscillatory features above the edge are also visible.

When the incident photon energy increases several features of the absorption coefficient spectra can be seen as presented briefly in Figure 2.9.b. These are:

a. The decrease of the absorption of the beam with increasing energy.

b. Sharp rise of the absorption at certain energies called “the absorption edge”. Those steps occur when the photon energy reaches the ionisation energy of one of the deep inner-shell of the atom as can be seen in the Figure 2.10. The transition always occurs to unoccupied states lying above the Fermi energy in the energy scale. As the absorption edge is a unique feature of the absorbing atom, it allows the selection of a particular atom in the compound. As one can imagine, the possibility of choosing the absorber is of a great importance while examining the properties of the material depending on chemical or structural environment of particular ions. L-edges are suitable for the experiments on atoms of higher atomic number for which K-edge energy can be difficult to reach. In addition L_2 and L_3 edges are of special interest in transition metal studies as they probe the symmetry of the d-orbitals.

c. Oscillations above the absorption edge that can provide a wide range of the structural information of the investigated material. As already mentioned, this information can be obtained by selecting different atoms in the compound, which produces a wide range of information of a local structure of the material.

The latter two features are described in the following paragraphs separately, due to the different origin and the different physical interpretation. The absorption edge region (up to about 30 eV above the edge) is described by XANES (X-ray Absorption Near Edge Structure), while the small oscillations in higher energies are interpreted by means of EXAFS (Extended X-ray Absorption Fine Structure).

The X-ray absorption measurements have been performed at the BM29 beamline of the European Synchrotron Radiation Facility (ESRF) in Grenoble, France. The general purpose of this beamline is the conventional x-ray absorption spectroscopy.

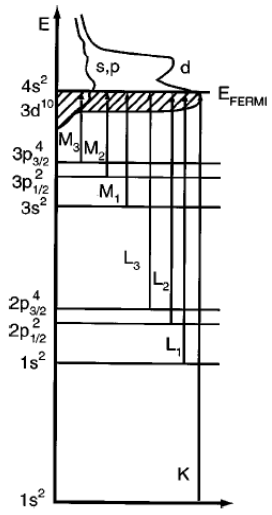

Figure 2.10. Excitations of the core electrons to the Fermi energy and corresponding absorption edges labels.

The BM29 beamline is also suitable for the measurements requiring high beam stability (e.g. pressure cell experiments). Apart from the standard XANES and EXAFS experiments, the Energy Scanning X-ray Diffraction (ESXD) and Single Energy X-ray Absorption Temperature Scan (being the temperature dependent measurement at fixed energy) are also possible. The energy range of the beamline is 4 keV to 74 keV and the energy resolution is much higher (3 to 5 times) than the spectral broadening of the K and L absorption edges. Such wide range allows studying the K-edge of the elements in the range $22 < Z < 76$. For $Z > 76$ probing at the L-edges is required.

The BM29 line is coupled with a bending magnet source, and equipped with a high quality double crystal monochromator from Kohzu-Seiki Corporation, Japan. The monochromator is equipped with a helium gas cooling system to minimise thermal perturbations to the energy of the monochromatic beam. With the assistance of a resistive heating element, the operating temperature of monochromator can now be kept within the temperature range of the minimum in the thermal expansion of silicon ($T \sim 125$ K). An operating geometry of the monochromator is in the vertical plane with the first crystal directing the Bragg reflected beam upwards. The second crystal in the monochromator Bragg diffracts the beam through a fixed exit point – parallel

with the horizontal plane of the incident white beam, though vertically offset by 25 mm. The stability of the fixed exit of this monochromator is characterised as 2 μm vertical offset at 2 m distance, between any specified energies defined by the crystal angles. The monochromator design allows for simple changes of the crystal pairs in use. Our experiment requirements made us use the Si(111) crystal pairs having corresponding operational energy ranges of 4.5 keV to 24 keV. The intrinsic energy resolutions is approximately $1 * 10^{-4}$ for such monochromator. This is well inside the core hole lifetime broadening of the absorption edges within their operational energy ranges. The intensity of the beam leaving the monochromator is then measured – before reaching the experimental station – by the I_0 ionisation chamber.

Using the ionisation chambers, detection efficiency is controlled by the gas species, gas pressure and applied voltage of the chamber. Typically for an EXAFS experiment, the efficiency of this first chamber is selected to be operational with 20 to 30 % absorption of the fundamental energy and 50 to 80 % in the rear chamber and operate with 1000 V potential across the 3 cm ionisation gap. The absorption is adapted via the partial pressure of the ionisation gas, whilst the chamber is backfilled with a helium gas buffer to 2 atm.

The experimental end-station of the beamline we used is a closed cycled helium cryostat that operates in the 20 K to 450 K range. This cryostat is designed so that the sample is mounted from a vertically suspended sample stick; vibration decoupled from the closed cycle refrigerator cold head. Sample holder allowing the measurement of up to three samples has been used.

After the cryostat the second beam intensity monitor – ionisation chamber I_1 is located. The reference sample holder and a third intensity detector I_2 follows this detector, in order to allow reference spectra to be recorded.

2.4.2.1. X-ray Absorption Near Edge Structure spectra features

In XANES analysis, the pre-edge region, the position, the shape of the absorption edge and the spectra above the edge are examined. The absorption edge defines the

ionisation threshold to continuum states. Edge position in the energy scale is used to determine the valence state of the absorber. The energy at which the absorption edge is located can be estimated in two ways. First method is to find the maximum of the derivative $\frac{d}{dE}\mu(E)$, which corresponds to the inflection point of the spectra. The alternative definition of the absorption edge states that the energy corresponding to the absorption edge is located where the half of absorption step is achieved. The edge is shifted towards higher energies with increasing oxidation state. Shift usually varies linearly with the valence state of the absorbing atom. Plotting values of the edge energies for the investigated material along with references one can determine the valence state of the ion in the investigated material with quite good accuracy. Proper choice of the reference samples with known oxidation state of the absorber and its local coordination is then of great importance.

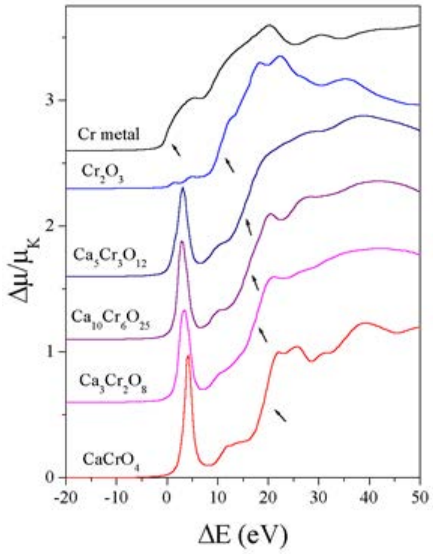

Figure 2.11. Normalised XANES spectra (displaced vertically) measured at the Cr at K-edge for different compounds, showing the dependence of the pre-edge structure on the symmetry at the Cr crystallographic site (octahedral position of Cr in Cr_2O_3 building a corundum structure, tetrahedral lattice site of Cr ion coordinated by four oxygen atoms in $CaCrO_4$). Arrows denote the inflection point of the spectra being the position of the edge. Energy scale is relative to the absorption edge of metallic Cr (5989.0 eV).

Features of the spectra before the sharp rise of the absorption and on the rising part are caused by the electronic transitions to empty bound states and contain the information on the details of local symmetry (see Figure 2.11.), bond length, charge state and orbital occupancy. The probability of the transition is controlled by dipolar selection rules. It can be given as a general rule that:

- For metallic material XANES spectrum reflects the conduction bands in the metal;

- If the absorbing ions are located in a crystallographic position with octahedral coordination the spectra shows two small resonance features at the pre-edge region. These are associated to the transitions of 1*s* electron into antibonding orbitals with octahedral symmetry.

- The tetrahedral configuration of the closest neighbourhood of the absorber with lack of inversion centre gives rise to a single, intense and well resolved pre-peak. It can be ascribed to a dipole allowed transition of 1*s* electron to an unoccupied antibonding t_{2*} tetrahedral orbital.

The features above the absorption edge are dominated by multiple scattering of the photoelectrons having low kinetic energy. The peak in the absorption spectra visible just above the absorption edge energy is historically called a white line. This name dates back to times when the detection was made on x-ray sensitive film and a white line was visible due to a strong absorption. The shape of the absorption peak, or, more precisely the area below the peak gives also some useful information. Subtracting the absorption background (using for example an arctangent function) and fitting the edge with Lorentz peaks for a set of data, the occupation of the orbitals can be determined. A literature example of the white line corresponding peak for the 5*d* metals measured on its L_3 edge is presented in the Figure 2.12. As will be shown in the 5^{th} chapter the possibility of direct investigation of the unoccupied states was used for our sample series to determine the influence of electron doping on the material.

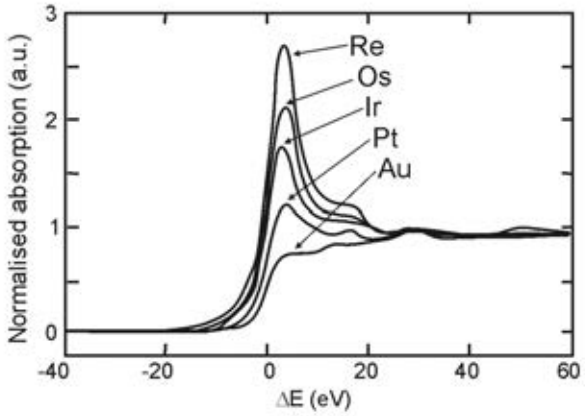

Figure 2.12. L_3 edges XANES spectra for 5d metals (energy scale relative to the absorption edge). Absorption peak is due to transitions from $2p_{3/2}$ to $5d$ states. The intensity of the peak falls being the highest for the Re atom through Os, Ir, and Pt. For Au one observes no peak, which indicates the $5d$ states to be completely occupied. Figure redrawn form reference [94].

Extended X-ray Absorption Fine Structure data analysis

The oscillations in the absorption spectra occur whenever other atoms surround the absorbing atom closely. This happens in solids, liquids and in molecular gases. The EXAFS component does not show up when the absorption takes place in noble gases or in mono-atomic vapours.

The explanation of this phenomenon comes out from the wave nature of the electrons i.e. electron in the atom before the excitation and the ejected photoelectron as well. The absorption of the x-ray photon causes the ejection of the photoelectron with the kinetic energy equal to the difference between the incident photon energy (E) and the inner shell binding energy (E_0). Using the quantum equation describing the wave associated with such electron one gets the photoelectron wave vector k ($k = \frac{2\pi}{\lambda}$, λ being the de Broglie wavelength) equal to

$$k = \sqrt{\frac{2m}{\hbar^2}\left(E - E_0\right)}. \qquad (2.20)$$

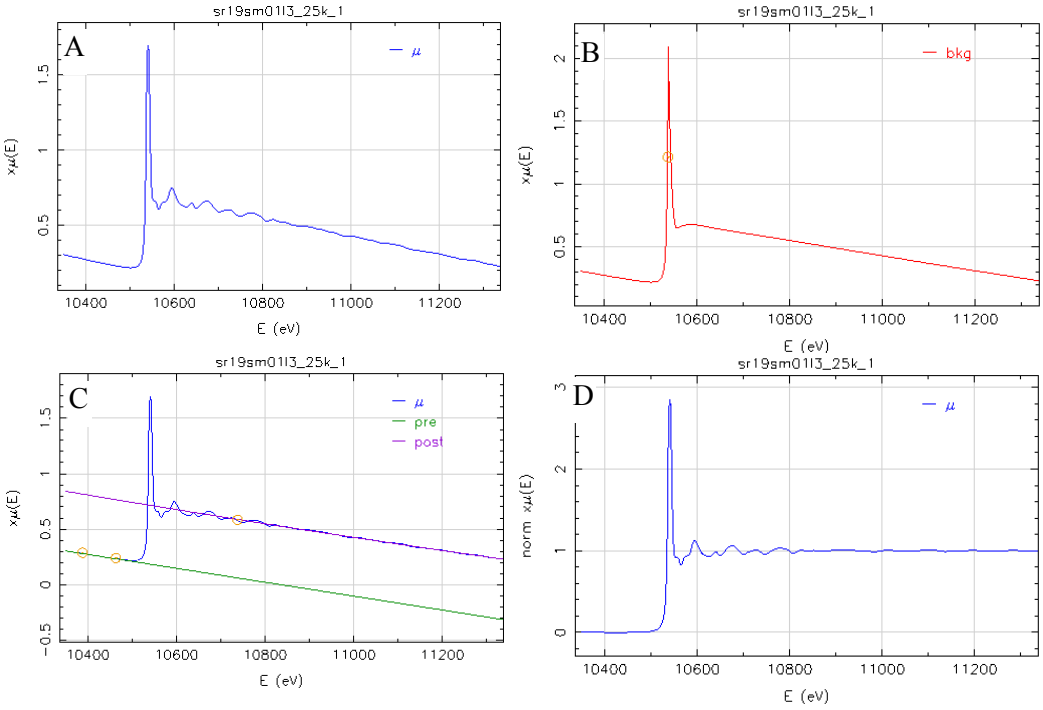

Figure 2.13. Data measured at the BM29 beamline in ESRF, Grenoble at the Re-L_3 edge in the $Sr_{1.9}Sm_{0.1}CrReO_6$ sample: (a) The absorption spectra as measured - $\mu(E)$; (b) fitted atomic background - $\mu_0(E)$; (c) straight lines are the linear fits of the pre-edge (lower line) and post-edge (higher line) regions; (d). the normalised absorption spectra - $\chi(E)$.

When the propagating wave meets neighbouring atoms and becomes scattered, each of the scattering centres turns out to be the source of a new spherical wave. The interference of the initial wave emitted from the absorbing atom, and the scattered waves affects the probability of the photoelectric effect to take place. As the energy of x-ray changes, the *k*-vector also is changed. This leads to the interference, which can be either constructive or destructive.

Measured absorption spectra $\mu(E)$ after subtraction of the smooth atomic background $\mu_0(E)$ and normalization is called the XAFS spectrum: $\chi(E)$. The steps to be followed are presented in the Figure 2.13.

The background to be subtracted is defined as the modification of the free atom-like absorption combined with the correction due to binding the absorber in the solid.

This leads to a polynomial shape of the background curve (usually a cubic spline). It has to be noticed that the background should not be the polynomial of too high order in order to avoid too strong modification of the data. The normalization factor $\Delta\mu_0$ is the value of the total change of the atomic background far from the absorption edge. It can be defined as the difference between the pre-edge and post-edge signal intensity. Using such definition one gets the XAFS (EXAFS) spectrum as:

$$\chi(E) = \frac{[\mu(E) - \mu_0(E)]}{\mu_0(E)}. \tag{2.21}$$

Considering only the contribution from single scattering from the surrounding atoms the EXAFS spectra can be described as a sum of sine terms in the *k*-vector space [95]

$$\chi(k) = \sum_i A_i(k)\sin(2kR_i + \delta_i + \varphi). \tag{2.22}$$

Each term (denoted by *i*) in equation (2.22) represents the contribution of a spherical shell of equivalent atoms lying at the distance R_i from the scattering centre (R_1 describes the nearest neighbours, R_2 – next nearest neighbours and so on). The phase shift parameter φ takes it origin in quantum mechanical wave nature of the backscattering. The δ_i parameter is the central atom wave phase shift of the final state and has larger contribution to the overall phase shift comparing to φ due to the fact that a propagating photoelectron is affected by the potential of the absorbing atom twice. The amplitude factor $A_i(k)$ depends on the atomic number of atoms in the coordination shell N_i, the photoelectron backscattering amplitude $F_i(k)$, Debye-Weller factor $e^{-2k^2\sigma_i^2}$ (thermal and structural disorder in the coordination shell) and the free path of the photoelectron λ_i. The amplitude is reduced by the factor S_0^2 describing the multi-electron excitations that accompany the photoelectric effect and is treated as constant in function of energy. Introducing all the above parameters, one gets the amplitude from the equation (2.22) as:

$$A_i(k) = \frac{N_i}{kR_i^2} S_0^2 F_i(k) e^{-2k^2\sigma_i^2} e^{-R_i\lambda_i} . \qquad (2.23)$$

Useful information can be obtained only by doing the Fourier transform (FT) of the $\chi(k)$ spectra according to equation (2.24).

$$\chi_\alpha(R) = \int k^N \chi(k) e^{-ikr} W_\alpha(k) dk . \qquad (2.24)$$

The integration is performed over whole range of *k*-vector, however the data range is limited by the $W_\alpha(k)$ being the window function. Usually the range of the window falls between 3 and 12 Å^{-1} and the data below and over those limits is multiplied by zero in the FT. The index α indicates that the result of FT is dependent on the window function parameters. The EXAFS signal is weighted with *N*-th power of *k* that allows the compensation of the decay of the signal for higher *k*-vector values. The modulus of the quantity obtained in equation (2.24) exhibits peaks that correspond to coordination shells. The information on the position of the particular atoms in the *i*-th shell will not be resolved. However the peaks in FT appear in the positions R_i corresponding to the distance from the absorbing atom to the *i*-th coordination shell. The amplitude of each peak depends on the amplitude of the EXAFS signal $\chi(k)$ and consequently is related to the number of atoms in the shell, the disorder parameter, the atomic weight of the atoms in shell and the *k*-vector space chosen. While using the FT to convert the *k*-space to *R*-space attention must be paid to the fact that useful information in the experimental data is limited to the finite range of *k*-vector and *R* range as well. The limitation in the *k*-space bears it origin in the Debye-Waller factor. Its effects become more pronounced for shorter wavelengths of the photoelectron. Consequently the EXAFS spectra should be cut off at a *k*-vector value about or slightly higher than 10 Å^{-1} corresponding to $k \approx \frac{1}{\sigma}$. The *R*-space limitation is mainly due to the finite lifetime τ of a core-hole ($\tau = \frac{\hbar}{\Delta E} < 10^{-15}$ sec for a core hole level of more than 1 eV width ΔE) and the photoelectron mean free path length.

2.4.3. XMCD under high pulsed magnetic fields

The principles of the dichroism have been known already in the 19th century. However only the visible light range was available for the experiments. The Faraday [96] and magneto-optic Kerr [97] effect have been observed. It was not until 1987 when the first results of the absorption of circularly polarised synchrotron light were presented by Schütz and co-workers [98], and a rapid development of the technique began. Since then the X-ray Magnetic Circular Dichroism (XMCD) method has become a very powerful experimental tool in exploring magnetic properties of the matter. Having in mind certain limitations it allows the quantitative determination of orbital and spin moments and their anisotropies.

The XMCD experiment requires a circularly polarised photon beam – produced out of plane of the synchrotron ring in the insertion devices: bending magnets, undulators or wigglers, or in plane by the helicoidally arranged undulators [99], the latter having better polarization factor and higher intensity. An external magnetic field in the sample space is also needed. The direction of the field is defined by the incoming x-ray beam polarization direction: it has to be either parallel or antiparallel to the helicity of the radiation. During one XMCD measurement two separate absorption experiments are to be performed i.e. with two opposite rotations of the x-ray helicity to be used, or with the magnetic field being applied in two antiparallel directions being subsequently applied. Such way of performing the experiment is necessary having in mind the XMCD signal defined as:

$$\mu_{XMCD} = \Delta\mu = \frac{\mu_+ - \mu_-}{2} \tag{2.25}$$

μ_+ and μ_- coefficients are related with the XANES absorption spectra as:

$$\mu_{XANES} = \frac{\mu_+ + \mu_-}{2} \tag{2.26}$$

and the “+” and ““ signs having the meaning of the signal collected with opposite

sense of the beam polarization with the external magnetic field remaining unchanged or two measurements with the opposite magnetic field direction having the polarization of the beam fixed. During the interaction of the polarised x-ray photons the angular momentum $\hbar$ or $-\hbar$ (in the case of right or left circular polarisation respectively) is transferred to the excited photoelectron. In the case of the spin-orbit split levels the momentum can be transferred in part to the spin. As $p_{1/2}$ and $p_{3/2}$ levels (corresponding to L_2 and L_3 edges respectively) have opposite spin-orbit coupling ($l - s$ and $l + s$) the spin polarization of the excited photoelectron will be opposite at the two edges. Owing to the selection rules the maximum of the dichroism signal will occur when the quantization axis of the valence *d*-shell will be parallel to the photoelectron spin direction. It would happen also in case of the *d*-shell possessing an orbital moment. The spin polarization is given by the equation (2.27) as a normalised difference of the number of the spins with different direction (parallel - $n_{\uparrow\uparrow}$ or antiparallel - $n_{\uparrow\downarrow}$) with respect to the photon wave-vector [98]. The orbital polarization is proportional to the number of photoelectrons (n_{m_l}) excited to the state with orbital quantum number (m_l) normalised to the total number of excited photoelectrons as states equation (2.28).

$$P_S = \frac{n_{\uparrow\uparrow} - n_{\uparrow\downarrow}}{n_{\uparrow\uparrow} + n_{\uparrow\downarrow}} \tag{2.27}$$

$$P_l = \frac{\sum_{m_l} m_l n_{m_l}}{\sum_{m_l} l \cdot n_{m_l}} \tag{2.28}$$

Using above formulas spin and orbital polarization of the photoelectrons at the L_2 and L_3 edges can be derived: $P_S = -0.5$ and $+0.25$ for L_2 and L_3 edge respectively, and $P_l = 0.75$ for both L_2 and L_3 absorption edges. As presented schematically in the Figure 2.14 assuming only the spin polarization of the valence shell one would get the opposite sign of the spectra for the L_2 and L_3 edge reflecting the opposite sign of the spin-orbit coupling. The spin as well as orbital moment can be derived from the

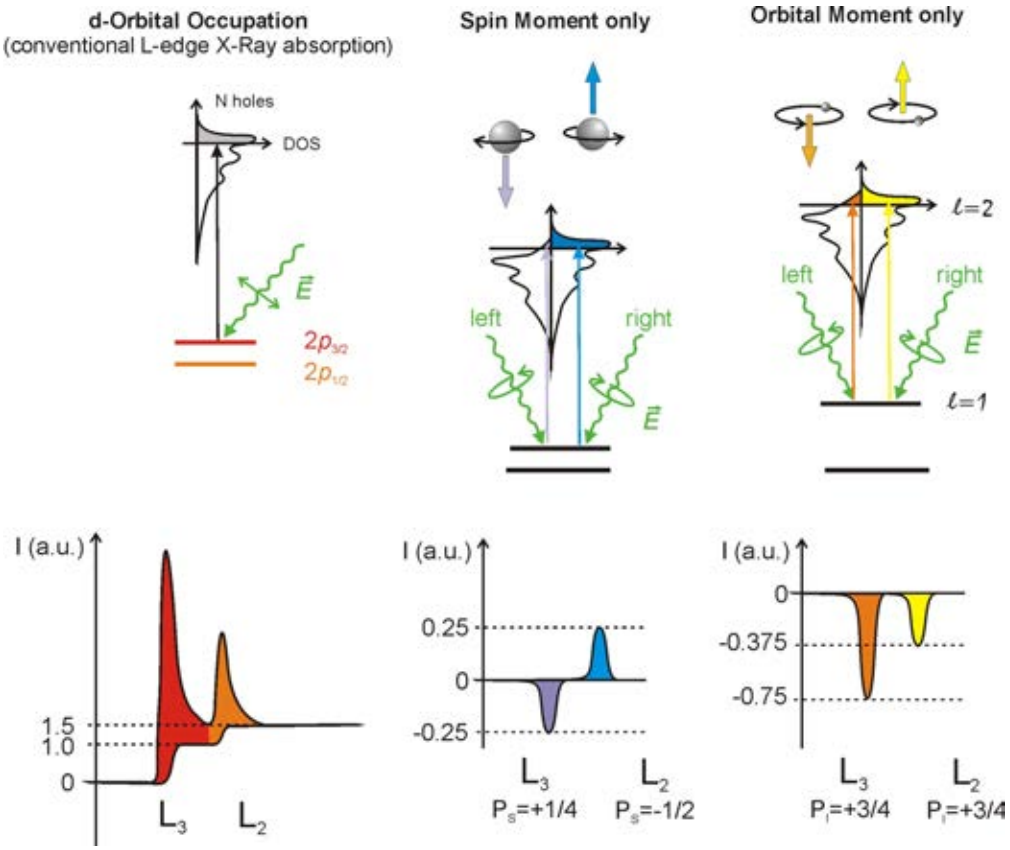

Figure 2.14. Electronic transitions in L-edge XAS and XMCD in the one-electron model. Transitions occur from *2p* core shell to the levels above the Fermi level. In XAS, intensity is proportional to the *d*-holes number while in XMCD orbital and spin moments can be derived from the spectra by Sum Rules equations. XMCD spectra in the bottom row correspond to spin-only and orbital-only polarization. Upper row of the figure redrawn after figure 1 in reference [107]. Bottom row corresponds to the calculation described in the text.

corresponding absorption intensities.

The way to extract the spin and orbital contribution to the magnetic moment from the experimental XMCD spectra is the application of the sum-rules [100] that can be written as (2.29) [101]. Under certain conditions the spin (m_s) and the orbital (m_l) magnetic moment can be estimated independently or the ratio of the two (m_l/m_s) can be derived.

$$m_l = -\frac{4}{3} N_d \frac{\int_{L_2+L_3} (\mu_+ - \mu_-)}{\int_{L_2+L_3} (\mu_+ + \mu_-)}$$

$$m_s = -(N_d)\left(1 + \frac{7\langle T_Z \rangle}{2\langle S_Z \rangle}\right) \frac{6\int_{L_3} (\mu_+ - \mu_-) - 4\int_{L_2+L_3} (\mu_+ - \mu_-)}{\int_{L_2+L_3} (\mu_+ + \mu_-)} \tag{2.29}$$

where*:* N_d is the number of the holed in the final *d*-state, $\langle T_Z \rangle$ is the magnetic dipole operator for transitions to *d*-states, $\langle S_Z \rangle$ the spin operator, $\mu_+ - \mu_-$ is the XMCD signal as in equation (2.25) and $\mu_+ + \mu_-$ have the meaning of XANES absorption as given by equation (2.26).

The XMCD experiments are usually performed under static, relatively low magnetic fields (see for example [102 – 105] for the reference on the magnetic dichroism study in various compounds belonging to the double perovskites family). The possibility of measuring the XMCD signal under high fields is a great step forward in studies of magnetic materials, which is nowadays possible thanks to the use of pulsed magnetic fields. Our measurements (pioneer in XMCD under high pulsed magnetic field to the best of our knowledge) have been performed at the ID24 energy dispersive beamline (see Figure 2.15 for the overview of the experimental hutch of the beamline) of the European Synchrotron Radiation Facility (Grenoble, France) [106].

The set-up developed by the ESRF sample environment group (see Figure 2.16) allows the application of various experimental techniques, x-ray absorption and XMCD among others. The coil producing the magnetic field has the outer diameter of 30 mm, bore diameter of 11 mm and 20 mm length. The coil bore is kept in vacuum. Maximum diameter of the sample is 3 mm. The detailed description of the system can be found in reference [108]. The coil is powered by the capacitor bank of 4 kJ, 3 kV (2.5 kV allows obtaining a magnetic field of 26 T) and 1 mF. The pulse is half-sine-shaped with the decreasing part deformed due to the resistive coil heating and has a duration of 650 μs (with the maximum lasting for 150 μs). Double pick-up coil system

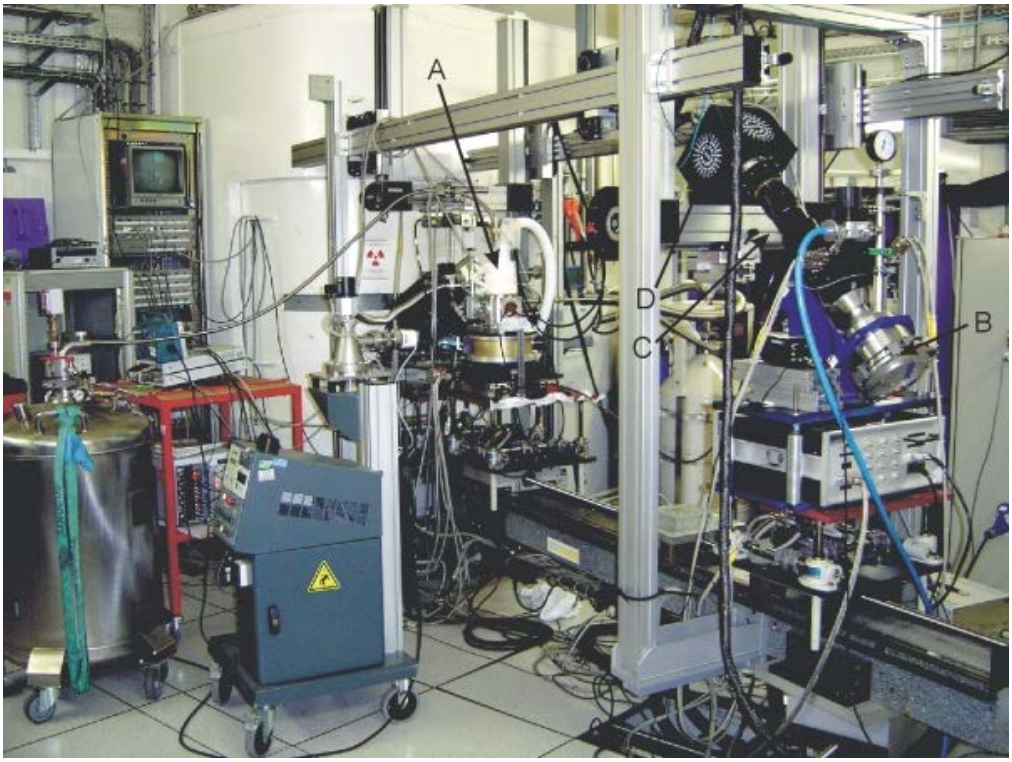

Figure 2.15. Overview of the ID24 beamline experimental hutch. A – the sample cryostat with the pulsed field coil (see Figure 2.16 for detailed view), B – fluorescent P47 phosphor screen with 100 ns for 10% afterglow and 3 μs for 1% afterglow, C – 25 mm diameter multichannel-plate image intensifier with 100 ns minimum gating, D – FReLoN (Fast Read Low Noise) CCD camera. Parts B, C and D of the optic/electronic system are connected by high-aperture tandem lens system.

is used for the field characterization, as the pick-up voltage is proportional to dB/dt.

The original (used during the first experimental session) coil with a liquid nitrogen cooling system allowed the repetition rate of one 26 T shot per 90 s. A new design (used in the most recent experiments) consisting of two coaxial coils separated by the cooling slit has improved the repetition rate by a factor of 10.

The pulsed field system accompanied by a high performance of the optics (spatial and spectral beam stability and small focal spot) and electronics (fast acquisition owing to the detector and gating system) of the ID24 beamline allows investigating

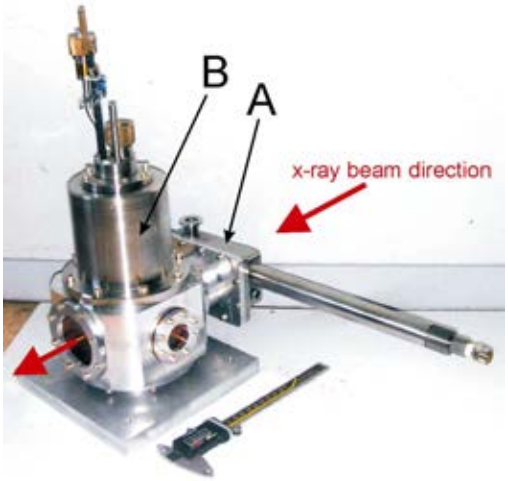

Figure 2.16. View of the ESRF developed set-up for high magnetic fields and low temperatures. The sample cryostat (a) with sample holder valve at the backside allowing sample insertion in the direction parallel to the beam direction. (b) - the magnetic field vessel.

the magnetic properties of the material under extreme conditions. More details concerning the synchronization of the optics with the field and readout can be found in [109].

During the experiment four symmetry cases are recorded in order to minimise the systematic errors. The XMCD signal is then obtained by flipping the helicity of the incoming beam – right circular polarization (RCP) and left circular polarization (LCP), and the magnetic field direction – H(+) and H(-). The collected spectra are averaged over a large number of repetitions [110]. A single measurement sequence is, consequently, as follows: RCP & H(+), RCP & H(-), LCP & H(-), LCP & H(+). The XMCD signals are calculated for RCP and LCP independently. This method, though complicated and time consuming, considerably reduces systematic errors and assures the magnetic origin of the signal obtained.

Chapter 3

Sr_2CrReO_6 – parent compound for the Lanthanide doped series

In this chapter we will present the results of the study of the Sr_2CrReO_6 double perovskite. This will include a complex structural characterization involving X-ray diffraction and neutron powder diffraction (NPD), magnetic ordering and its temperature evolution by means of NPD and detailed bulk magnetic characterization using commercially available SQUID magnetometer as well as high magnetic fields generated by both static and pulsed technique. We will also discuss the orbital moment carried by the Re ion including recent results of X-ray Magnetic Circular Dichroism (XMCD).

The double perovskite Sr_2CrReO_6 has become an interesting investigation object due to at least two reasons. First, apart from its predicted high level of spin polarization at the Fermi level (as described in the first chapter), it exhibits a high Curie temperature (T_C) being reported as large as 620 K [111]. Moreover high quality thin films of this material can be grown by sputtering techniques [112], opening the possibility of technological applications.

The data presented correspond to the Sr_2CrReO_6 samples belonging to two different batches. The main difference between the two is the amount of the *AS* defects. Other factors like purity (presence of undesired secondary phases) are similar and the amount of impurities is low. One of the samples (DP73) was used for the neutron diffraction experiments as well as for high pulsed magnetic fields measurements (bulk magnetic properties and XMCD). The other sample (DP78) was investigated under high static fields. We will also refer to the former in the last chapter

treating it as a reference for our electron-doped series and X-ray Absorption Spectroscopy experiments.

3.1. Crystallographic and magnetic structure investigated by diffraction methods

X-ray diffraction patterns have been collected after each synthesis step as described in Chapter 2. This allowed the control of the process. After finishing the sample preparation, spectra in a large 2θ range were collected in order to get reliable crystallographic data before using the sample for further experiments. In the Figure 3.1 the experimental data for the DP73 sample along with the fit is presented. The fit indicates that the main phase is indeed a double perovskite corresponding to the Sr_2CrReO_6. Apart from the main phase two impurity phases are also visible. These are the metallic Rhenium and $Sr_{11}Re_4O_6$. The Bragg peaks corresponding to those phases are hardly visible in the data. Quantification of the patterns give 99.3(3) %, 0.05(1) % and 0.65(8) % for the double perovskite, metallic Re and $Sr_{11}Re_4O_6$ respectively. Such high purity causes that the impurity phases are not required in the fitting model in order to achieve reasonable results.

Table 3.1 Data (space group – at room temperature, lattice parameter and antisite number) obtained from the Rietveld Refinement of the θ-2θ X-ray diffraction patterns taken at room temperature for Sr_2CrReO_6 samples belonging to two different batches.

	DP78	DP73
Space group	$Fm\bar{3}m$	$Fm\bar{3}m$
Lattice parameter	7.8152(1)	7.8152(1)
AS (%)	13.5	15

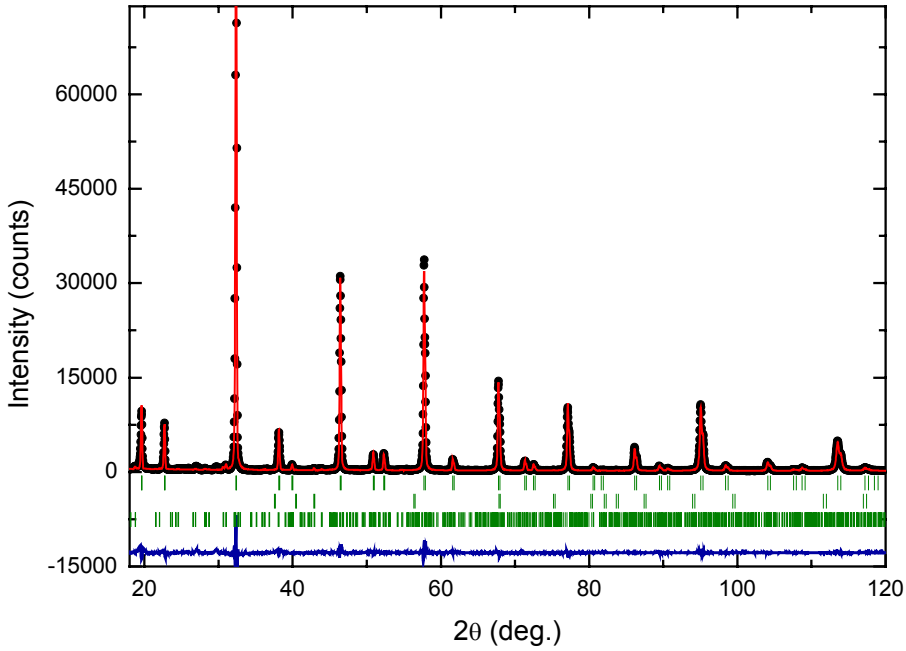

Figure 3.1. Rietveld refinement of the x-ray diffraction data at room temperature for the DP73 sample. Closed circles stand for the experimental points, the line for the calculated fit. The difference between the observed data and fit is plotted with the line in the bottom. In between the allowed Bragg positions are marked for the main Sr_2CrReO_6 double perovskite phase in the first row, the second and third are for the impurity phases: metallic Re and $Sr_{11}Re_4O_6$.

3.1.1. Estimate of defects amount

According to the formula introduced in chapter 1 the saturation magnetization of the double perovskites is strongly influenced by the structural defects. A correct estimate of the amount of the antisite defects is of primary interest in our case, as we aim to demonstrate the importance of the orbital contribution to the saturation magnetisation. The ordering of the Cr and Re ions is reflected in the diffraction patterns. Apart from the Bragg reflections arising from the crystallographic structure some superstructure peaks are visible (e.g. (111), (113) and (331)). The intensity of these reflections is particularly sensitive to the defects. In the Figure 3.2.a. the close-up of the (111) Bragg peak area (the centre of the peak is at 19.65º) is presented. Simulated patterns are also plotted in order to clearly show a strong dependence of the peak height on the *AS* percentage. According to equation (1.34), 0% of *AS* means a

perfectly ordered double perovskite and 50% stands for a completely disordered structure being no longer a double perovskite but a single perovskite. Consequently, the strongest reflection is visible for the former case, while the peak disappears completely when the *AS* amount reaches a 50% limit. At least two approaches can be proposed for the analysis of the *AS* amount estimate based on the behaviour of the Bragg peaks whose intensity depends on the superstructure. First, the area below the particular peak can be analysed. One can integrate the area below the experimental data (including the background signal intensity) and compare it with the integrated simulated pattern in the same 2θ range. The result of this procedure would lead to the series of numbers related to the difference of the experimental and simulated intensities. This can be plotted against the *AS* percentage (or other quantity related to the occupancies of the *B* and *B'* sites). If the absolute value is plotted (as in the Figure 3.2.b. – red curve, open circles) a minimum corresponding to the best fit will occur. This approach however is not only time consuming, but is also limited to only one peak at a time. The interplay between the defects and other structural parameters as well as possible impurities quantification (giving rise to the diffraction pattern in the vicinity of the peak analysed) may also influence such analysis.

As mentioned in the second chapter of this thesis Rietveld refinement is a whole pattern approach. Owing to the possibility of analysis the influence of every fit parameter (such as – interesting in the case being discussed – cation occupancies) on the overall fit quality, one can estimate the *AS* amount with a high accuracy. One can profit from the R_{Bragg} fit quality parameter, being directly dependent on the intensities: observed and theoretical. The dependence of the R_{Bragg} on the *AS* amount is presented in the Figure 3.2.b – blue curve, closed circles. Similarly to the analysis discussed above it shows a minimum when the occupancies of the cation *B*(*B'*) sites are fitted with the best accuracy. This approach assures that not only the change in *AS* amount is taken into account but also all other fit parameters are changed simultaneously.

The situation becomes much more complicated in case of multi-phase samples. In the case of the Sr_2CrReO_6 (DP73) sample we have to refine also two impurity phases

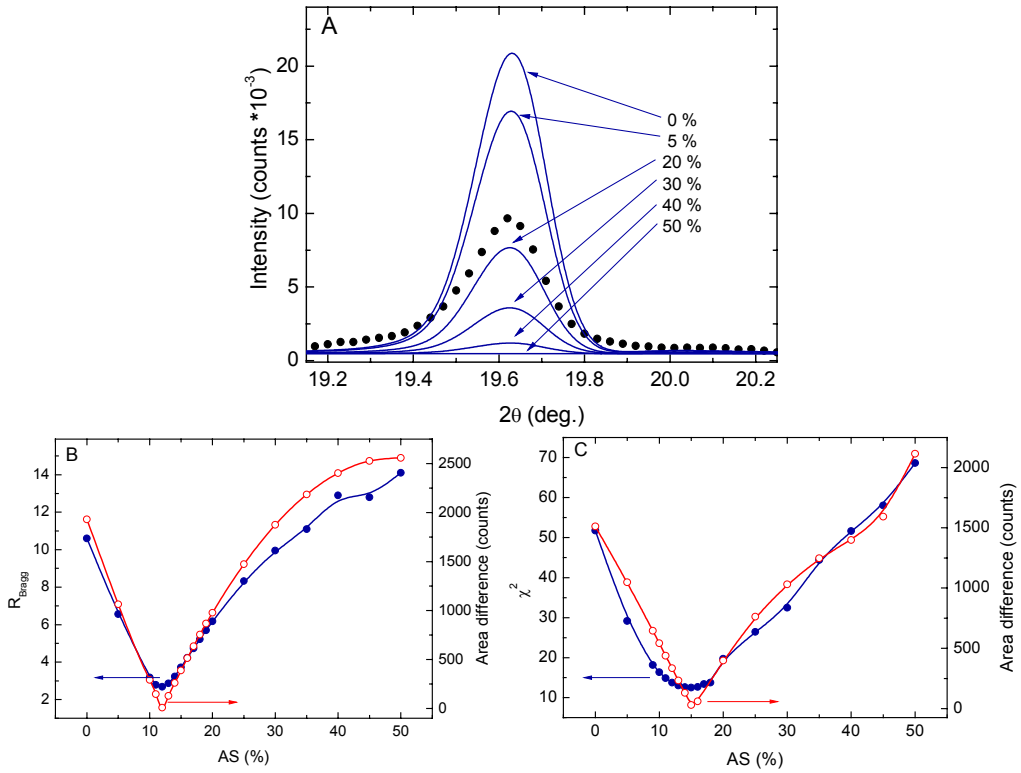

Figure 3.2. (a) Rietveld refinement of the θ-2θ X-ray diffraction data in the range between 19° and 20.4° corresponding to the (111) Bragg peak. The experimental result is plotted with closed circles. The simulated data corresponding to different amount of antisite defects is plotted with lines. For a complete disorder (50% of *AS*) one can observe a zero intensity of the diffraction peak. (b) Quality of the fit factor (R_{Bragg}) – closed circles, left axis and the difference between the area below the (111) Bragg peak in the experimental data and simulated patterns – open circles, right axis plotted against the *AS* defects percentage. Both quantities show a minimum at the estimated *AS* level (≈12%). The calculations of the simulated patterns have been simplified excluding variations of all other fit parameters apart from cation occupancies resulting in the underestimation of the cation disorder. (c) Quality of the fit factor (χ^2) – closed circles, left axis and the difference between the area below the (111) Bragg peak in the experimental data and simulated patterns – open circles, right axis plotted against the *AS* defects percentage. Calculations include the secondary phases. All data correspond to the DP73 sample.

($Sr_{11}Re_4O_{24}$ and metallic Re). For refinements including the impurities the number of parameters is much larger compared to the previous situation (with no secondary

phases) and varies from 33 to 50 depending on the approach. The analysis of the fit quality also complicates. On the one hand the peak area analysis gives good results. On the other hand, the R_{Bragg} parameter can be extracted for all the phases separately (the weighted average is also available). However, it seems that the χ^2 is a better one. This is due to the fact that weighting the R_{Bragg} for each phase giving the average is influenced by a very large error coming from the secondary phases. In the Figure 3.2.c the χ^2 and the absolute value of the difference of the experimental and refined (111) peak show a minimum around 15% of *AS* (in agreement with the Rietveld refined defects amount).

This procedure can be, of course, applied to the x-ray diffraction as well as to the neutron powder diffraction data. The presented case of a cubic compound is the easiest one. In the case of lowered symmetry the Bragg peaks are often split into two close peaks. However this does not prevent the analysis of the defects of the crystallographic structure. As will be shown in next chapter in a tetragonal and a monoclinic structures the estimate of *AS* percentage is also possible and gives reasonable results.

3.1.2. Lattice constants and magnetic configuration as a function of temperature

As already mentioned, neutron powder diffraction allows studying both the crystallographic structure and the magnetic ordering at the same time. The equipment used in ILL, Grenoble, allows the examination of the variation of a wide range of crystallographic parameters and the evolution of the ordering of magnetic moments in a temperature range from 5 to nearly 1000 K. Apart from the lattice constants we have refined, during the diffraction patterns analysis, the distances between the ions, the angles of the bonds and the occupancies of the crystallographic sites. Some of the obtained parameters are listed in the Table 3.2. All neutron powder diffraction data is obtained for the DP73 sample.

Table 3.2. Data (space group, lattice parameter, cation – oxygen distance and angle, magnetic moment associated with a cation, *AS* defects percentage and fit reliability factors) obtained from Rietveld refinement of the θ - 2θ neutron diffraction patterns taken at 5 and 710 K for the DP73 sample. Corresponding spectra are shown in Figure 3.3.

	T = 5 K	T = 710 K
Space group	*I 4/m*	$Fm\bar{3}m$
a (Å)	5.51650(6)	7.85309(14)
c (Å)	7.81178(8)	-
Cr – O_1 (Å)	1.941(3)	1.976(3)
Re – O_1(Å)	1.966(3)	1.951(3)
Cr – O_3 (Å)	1.993(5)	-
Re – O_3 (Å)	1.913(5)	-
Cr – O_1 – Re (°)	173.5(1)	180.00(15)
Cr – O_3 – Re (°)	180.00(30)	-
Cr moment (μ_B)	2.73(10)	-
Re moment (μ_B)	-0.40(11)	-
AS (%)	16	15.6
Bragg *R*-factor	2.7	6.2
Magnetic *R*-factor	7.6	-
χ^2	8.1	3.1

The route for refining the experimental neutron diffraction data usually begins in the high temperature range. This is for two reasons. First, the Sr_2CrReO_6 compound is found to be cubic in temperatures above 250 K (while tetragonal in lower temperatures). Second, the temperature of magnetic ordering is estimated to be around 600 K. If we deal with the diffraction spectra taken above both temperatures, the amount of the Bragg reflections is lowered due to a higher symmetry and there are no magnetic Bragg peaks present. Both cause the amount of the refined parameters to decrease. In such a case the improvement of the refined model can be observed more easily. Moreover, the actual stoichiometry can be refined more accurately. In the Figure 3.3 the diffraction patterns measured in the low and high temperature are presented. The refinements have been performed taking into account only the main, double perovskite phase with a nominal stoichiometry Sr_2CrReO_6.

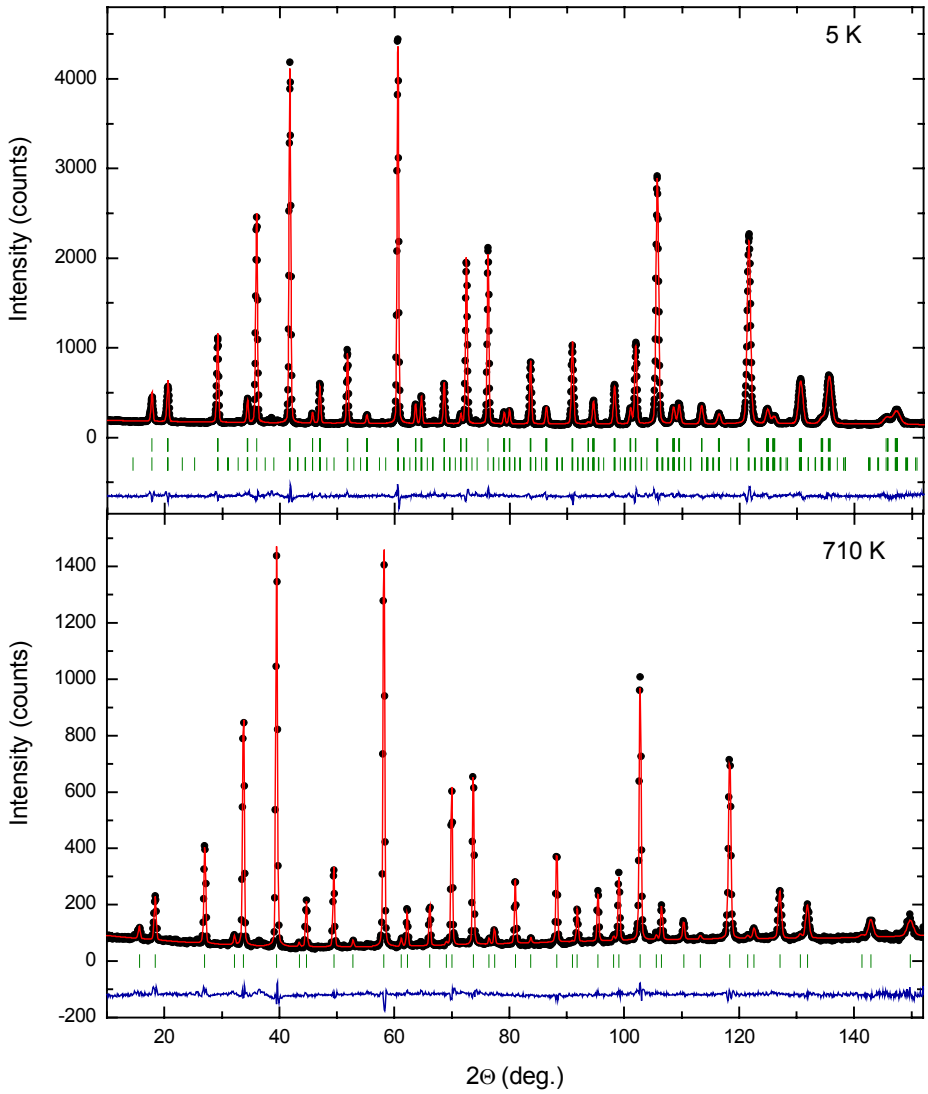

Figure 3.3. Rietveld refinements of the neutron diffraction data at 5 K (upper panel) and 710 K (lower panel). Closed circles stand for the experimental points, the line for the calculated fit. The difference between the observed data and fit is plotted with the line in the bottom. In between the allowed Bragg positions are marked for the main Sr_2CrReO_6 double perovskite phase in the first row, the second row in the low temperature data is for the peaks arising from the magnetic super-cell.

As expected, the crystallographic structure is found to be cubic (with the $Fm\bar{3}m$ space group) in high temperature (710 K). At the same temperature the refined amount of antisite defects is 15.6%. The lattice constant ($a = b = c$ in the cubic structure) is

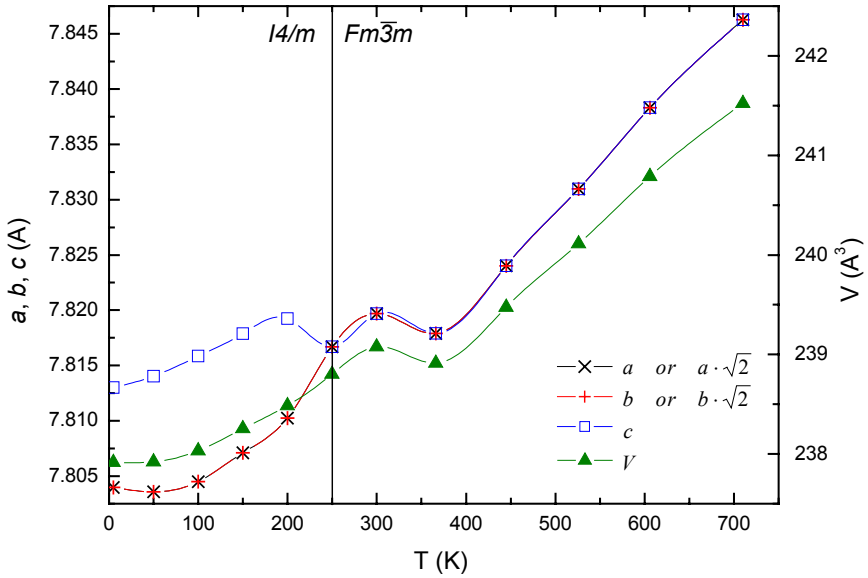

Figure 3.4. Lattice constants and the volume of the unit cell obtained from the Rietveld refinements of the θ-2θ neutron diffraction data. The $a(b)$ lattice parameter is multiplied by $\sqrt{2}$ in the case of tetragonal structure. A small variation visible around 350 K is rather related to the change of the sample environment (cryo-furnace/furnace) than to any physical effects.

found to be 7.85309(14) Å. As expected, and observed in other double perovskite type compounds, when lowering the temperature the unit cell shrinks. The unit cell volume is lowered by 4 $Å^3$ and the change of the volume is associated with a simultaneous shortening in the three crystallographic directions as can be seen in the Figure 3.4. The unexpected variation of the lattice parameters around 350 K cannot be associated to a structural transition of any kind, and has rather its origin in the change of the sample environment from the cryo-furnace to the furnace at this temperature. This affects the collection of the data, as the geometry (beam – sample – detector) has to be realigned then.

The structural transition temperature, T_S, was estimated to be about 250 K from the diffraction data refinements. Below this temperature a small tilting of the octahedra cannot be longer described in terms of the cubic structure. The actual structure is tetragonal with the *I4/m* space group. Below T_S the oxygen atoms are not equivalent.

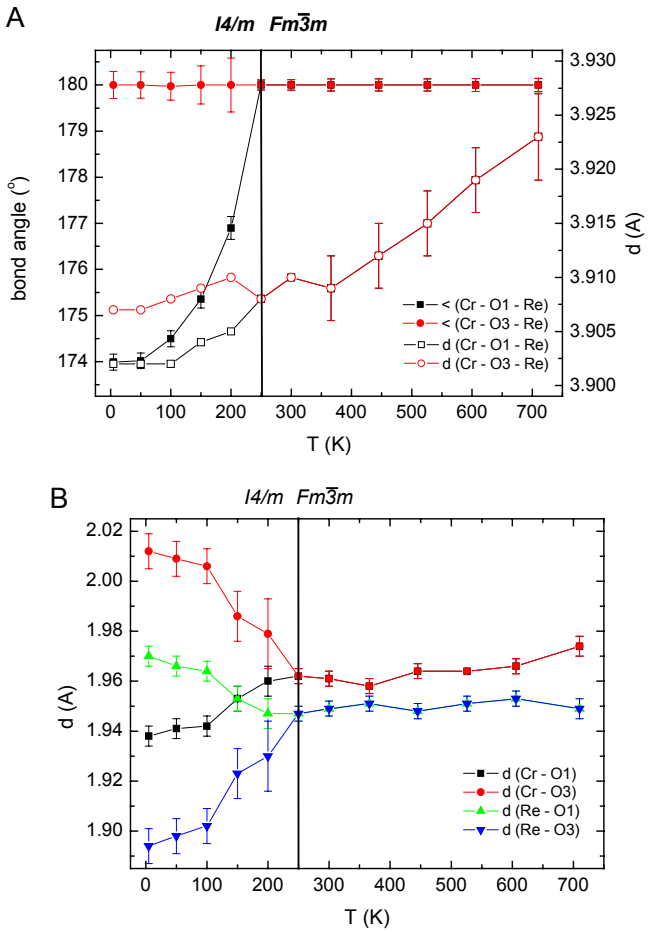

Figure 3.5. (a) Cr – O_i – Re bond angle (left axis) and the Cr – O_i – Re bond length (right axis). (b) the distance between a cation (Cr/Re) and the oxygen atoms. In both O_1 denotes four equivalent the atoms lying in the basal plane while O_3 are the oxygen atoms laying between Cr and Re cations in the [001] direction i.e. the apical ones. The structural transition temperature between the tetragonal and the cubic phases is also marked.

Two apical oxygen atoms do not change their position, while the four lying in the (001) plane collectively shift their positions. Hereafter we will refer to the apical atoms as O_3 and the atoms lying in plane as O_1. As can be seen in the Figure 3.5, the Cr – O_1 – Re angles deviate from 180º while the Cr – O_3 – Re angles remain equal 180º. At low temperature (5 K), in the tetragonal structure, the deviation of the former is as high as 6º compared to the cubic cell. The tetragonal distortion parameter *t* defined by relation (1.33) is found to be 0.0012 at 5 K. The size of the octahedra

formed by the oxygen atoms around Cr is bigger both in the cubic and the tetragonal structure than the one surrounding the Re cation. This fact can be anticipated taking into account the ionic radius of the Cr^{3+} and Re^{5+} ions being equal to 0.615 Å and 0.58 Å respectively [57]. Below the structural transition temperature the Re octahedron is shrank in the [001] direction and the Cr octahedron is expanded. In the basal plane oxygen atoms are also displaced.

All structural effects described above should have their repercussion in the magnetic and electronic properties of the material. The deviation from the ideal 180º bond angles disturbs the pdd-π coupling via the Cr(t_{2g}) – O($2p_\pi$) – Re(t_{2g}) states. On the other hand, the distortion is not as strong as in monoclinic compounds so the pdd-σ coupling in the Cr(e_g) – O($2p_\sigma$) – Re(e_g) states is not reinforced. Moreover the path along the Cr – O – Re – O – Cr atoms is no longer linear. Consequently the movement of the electric carriers at the Fermi level, formed by Cr ($t_{2g}\downarrow$) – O ($2p_\pi$) – Re ($t_{2g}\downarrow$), is more difficult resulting in the enhancement of the resistivity.

From the refinements of the diffraction spectra below the magnetic ordering temperature one can obtain the evolution of the magnetic moments associated with the magnetic ions in the compound. In case of Sr_2CrReO_6 these are the Cr^{3+} and Re^{5+} cations. As discussed in section 1.6.1 Cr ions posses three electrons at the Fermi level with spins pointing in one direction and Re ions two electrons with opposite spin direction. This leads to the overall magnetic moment of 1 μ_B per formula unit. In case of the sample under investigation the magnetic moment of the Cr cation is found to be 2.73(10) μ_B corresponding to the $Cr^{2.7+}$ ion. This value is in a good agreement with the model concerning one electron of the Re (nominally Re^{5+}) being shared among Cr and Re ion. In such case the actual oxidation of the Cr should be treated as $Cr^{2.5+}$. The magnetic moment associated with Re ion is found to be –0.40(11) μ_B. The analysis of the Re magnetic moment is more complicated as the orbital contribution to the magnetic moment is important. Moreover there are some uncertainties concerning the magnetic from factor of the Re^{5+} ion thus in the Rietveld refinements we are using the Mo^{5+} form factor.

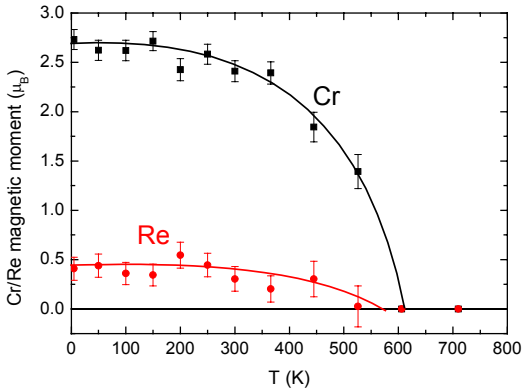

Figure 3.6. Cr and Re magnetic moment as a function of temperature for Sr_2CrReO_6. Re moments are multiplied by –1. Solid lines are guidelines for eyes.

The evolution of the magnetic moments of the Cr/Re ions with the temperature (see Figure 3.6) shows the expected behaviour lowering their value as the temperature rises. Plotting the estimated magnetic moments values against the temperature we get the temperature for which the magnetic contribution to the diffraction pattern is not present to be 600 K. As will be demonstrated later this value coincides with the one obtained from the magnetisation measurements. As a remark it has to be said that the value of the Re magnetic moment is obtained with less accuracy compared to the Cr related value. In the former the sigma squared accuracy parameter is of the same order of magnitude as the obtained number, while in the latter is one (or two) order of magnitude smaller

3.2. Magnetic properties

Magnetic measurements under low fields, performed using SQUID magnetometer, allow obtaining a quite wide range of parameters related to the magnetic properties of the material. As in the case of the structural study, the purity of the material is of primary interest. Any magnetic impurities can give rise to some undesired signal contributing to the measured data. For example, in Fe-based double perovskites, the presence of ferromagnetic impurities (presumably Fe) has been identified and quantified by analysing the magnetization behaviour above T_C [113]. In

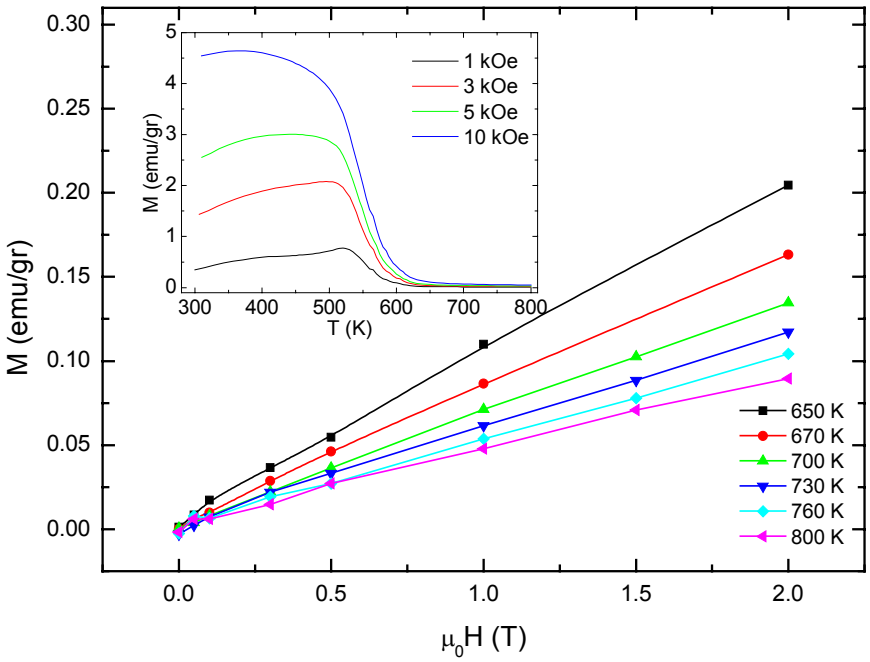

Figure 3.7. Magnetization versus field curves measured with the SQUID magnetometer for the Sr_2CrReO_6 in different temperatures (listed in the figure) above the Curie temperature. In the inset: magnetization versus temperature curves under applied fields of 1, 3, 5 and 10 kOe.

our case, such type of impurities is less probable because our compounds do not contain the Fe element, but traces of ferromagnetic materials cannot be completely discarded as they can come as impurities in the starting materials. On the other hand, from the diffraction experiments, we get that the samples are of a good quality and show only traces of impurities that are below 1% of the total sample volume. Even taking into account the $Sr_{11}Re_4O_{24}$ as a magnetic impurity it has to be kept in mind that its Curie temperature is believed to be about 15 K [114], thus in higher temperatures it will not give rise to the ferromagnetic signal from the sample. In the Figure 3.7 the isotherms of the Sr_2CrReO_6 sample in the paramagnetic range are presented (in the inset the thermal dependence of the magnetisation under different applied magnetic fields is presented assuring the isotherms to be taken in non-magnetic range). The curves are linear (as expected for a paramagnetic state) except for a tiny ferromagnetic signal giving rise to a non-linear contribution at low fields. This can be ascribed to small magnetic impurities. The magnetisation coming from such impurities can be

estimated performing a linear fitting of a high field (0.5 to 2 T) data. Extrapolating the obtained linear approximations to zero field at all temperatures we obtain an average magnetisation of about 0.005 emu/gr, value being 2000 times smaller than the saturation magnetisation expected for Sr_2CrReO_6. This allows discarding any important influence of ferromagnetic impurities to calculate the saturation magnetization of the compound.

3.2.1. Low field range

The double perovskites have attracted much attention not only due to their half-metallic character (or nearly half-metallic as discussed in section 1.5.1) but also owing to their high Curie temperature. Let us begin with the estimate of the magnetic ordering temperature from the bulk magnetisation measurements. In the main panel of the Figure 3.8 the magnetisation curve is presented as a function of temperature measured under an applied field of 1 T. The T_C can be estimated in at least two ways. One can search for the minimum of the first derivative of the magnetisation curve (i.e. $\partial M(H,T)/\partial T$, T being the temperature and H the external field applied to the sample during the measurements). The other method is to linearly extrapolate the part of the magnetization curve where the maximum slope is present, and look for the intersection with the ordinate axis (the temperature axis). The Arrot's plot method could have been also used if description under mean-field approximation were correct. We preferred the use of the other two methods. However high accuracy of the T_C estimate is not the main topic in this thesis. The temperature of the magnetic ordering, estimated using the maximum slope extrapolation technique is about 600 K. Magnetisation measurements under the applied fields up to 5 T show a lack of magnetic saturation, as can be seen in the inset (left) in the Figure 3.8. The maximum magnetisation values are 0.91 and 0.89 μ_B/f.u. at 5 and 300 K respectively. The lack of change of the maximum magnetisation between the two temperatures is in agreement with the high field data (30 and 50 T) that show a constant value of the saturation magnetisation in the range of temperatures up to 300 K. On the contrary the coercive field is significantly lower at 300 K compared to the low temperature measurement. It drops

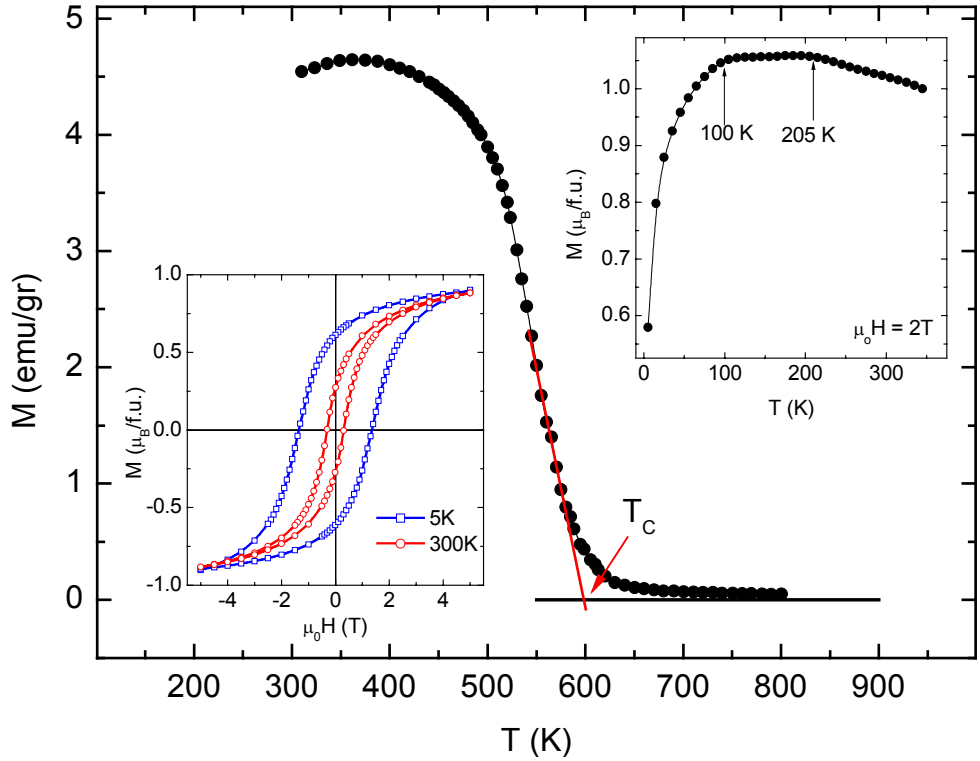

Figure 3.8. Magnetisation versus temperature curve showing a clear ferromagnetic transition around 600 K (obtained from the extrapolation of the magnetisation curve from the maximum slope range to the ordinate axis). Left inset: magnetisation loops measured in SQUID magnetometer at 5 and 300 K. It is clearly visible that the curves remain opened under the applied field of 5 T showing a lack of magnetic saturation under low magnetic fields. Right inset: magnetisation versus temperature curve taken under the applied field of 2 T showing a sharp change of the slope on heating around 100 and 205 K. All data correspond to the DP73 sample.

from 1.35 T at 5 K to less than 0.5 T at 300 K.

As the low-field measurements have not been presented yet we will not discuss the coercivity of the material in detail at this point. However the subject is not trivial and will be discussed later on the basis of the high (pulsed and static) field data. The coercivity however, can be investigated not only by the direct magnetisation loops measurements. We have performed an experiment measuring the magnetisation of the Sr_2CrReO_6 under an applied field of 2 T on heating, after applying the –5 T field in the

lowest temperature (5 K). In that manner we obtain the magnetisation versus temperature curve in the temperature range from 5 to 350 K (see right inset in the Figure 3.8). At first sight it is visible that a sharp increase of the magnetisation value is present up to 100 K approximately. This behaviour is in clear opposition to the expected lowering of the magnetisation on temperature rise for a saturated ferromagnet. Above 100 K the magnetisation remains constant and starts to drop above 205 K. On the one hand we cannot apply the theoretical behaviour of a ferromagnet in the saturated state to the material investigated as we have already seen that in low field range Sr_2CrReO_6 remains not saturated. On the other hand as presented by Serrate at al. [58] in the case of Sr_2FeReO_6 one observes the drop of magnetization between 5 and 350 K of 40% (in the same kind of experiment, under the same conditions as discussed here). The behaviour of magnetisation could be associated to two effects. One would be the change in the magnetic arrangement in the vicinity of $T = 100$ K, other, the enhancement of coercivity around this temperature. The first one can be discarded on the basis of the Rietveld refinements of the NPD data in the temperature range where the magnetic ordering is present. First the fits are done using same model of magnetic ordering in the whole temperature range, and no significant variations of the quality-of-the-fit parameters are observed. Moreover within the model used we obtain the evolution of the magnetic moments associated with Cr/Re ions, finding that they do not exhibit unusual variations (as can be seen in the Figure 3.6). In order to find out whether the transition to a state with a higher magnetic anisotropy is accompanied with the structural transition we have to investigate more closely the temperature evolution of structural parameters (obtained form neutron powder diffraction experiments and presented in the Figure 3.5). The resolution of the data in the temperature scale and the experimental error combined with the refinement accuracy prevent us from concluding that any structural transition apart from the cubic structure to the tetragonal one at 250 K is taking place.

3.2.2. High pulsed and static field experiment

In order to achieve the saturation magnetization in Re-based double perovskites, very high magnetic fields are required. This is evident from all previously reported

magnetization hysteresis loops in Re-based double perovskites, typically measured only up to 5 T (see e.g. refs. [111, 115, 117, 118]). After performing the experiments under high pulsed and static magnetic fields we can conclude that the Sr_2CrReO_6 double perovskite is only magnetically saturated under applied field beyond 20 T (as presented in the Figure 3.9). The reason for this magnetically-hard behaviour (with large coercive and saturation fields) in Re-based double perovskites is thought to be the strong spin-orbit coupling on Re ions [58, 118]. Our magnetization measurements results in Sr_2CrReO_6 obtained under pulsed magnetic fields up to 47 T allowed, for the first time, a realistic evaluation of the saturation magnetization in a Re-based double perovskite [76]. After high pulsed magnetic fields experiments we have performed the measurements under static fields up to 30 T [119] confirming that Sr_2CrReO_6 requires around 20 T in order to saturate the magnetization. In the pulsed-fields experiments we have used a Sr_2CrReO_6 sample with about 15% of antisite disorder and for the static field experiments the one with slightly lower antisite level, 13.5%. As a consequence we measure a saturation magnetization M_S of 0.96 μ_B/f.u. and 1.00 μ_B/f.u. in the two reported experiments respectively. In Figure 3.9 the magnetization measurements under pulsed and static magnetic fields at 4.2 K are shown and compared with the data taken in a SQUID magnetometer at 5 K. The first piece of information extracted from this figure is that the standard measurements of the magnetization up to a few Tesla are not sufficient to give precise values of the saturation magnetization in this compound. Whereas the magnetizations are $\approx$ 0.85 μ_B/f.u. and $\approx$ 0.9 μ_B/f.u. at 5 T, the saturation magnetization is $\approx$ 0.95 μ_B/f.u. and $\approx$ 1.00 μ_B/f.u in case of the DP73 and DP78 samples respectively, the value being reached under applied magnetic fields beyond 20 T. The second piece of information drawn from this figure is the high value of the saturation magnetization, which is much higher than that expected in the ionic model if we take into account the amount of antisite disorder in our sample (15% and 13.5%). As explained before, the expected saturation magnetization in the ionic model or in models that do not include spin-orbit coupling is 1 μ_B/f.u. in Sr_2CrReO_6 if we do not consider the influence of antisite disorder [61]. Nevertheless, the influence of antisite disorder is crucial in the

saturation magnetization of double perovskites. The simplest model to describe such an influence is the assumption of a linear decrease of the saturation magnetization with the number of antisites and eventually the disappearance of spontaneous magnetization for the maximum level of antisites (50% according to definition as in equation (1.34)). This leads to the expression given by the equation (1.35). This assumption works fine in the case of Sr_2FeMoO_6 as explained in the introduction. For our samples, with $AS = 0.15$ and 0.135, we expect M_S to be 0.7 and 0.73 μ_B/f.u respectively which are much smaller than the experimental values (0.95 and 1.00 μ_B/f.u.) The difference is significant (37%), which gives confidence to conclude that the saturation magnetization predicted by the ionic model is much lower than the real one (see Table 3.3). If we use the prediction of the DFT calculation that takes into account the spin-orbit coupling in Re ions, the saturation magnetization for a Sr_2CrReO_6 sample without antisites should be 1.3 μ_B/f.u. [61] and the following dependence with the antisite content is expected if the abovementioned model is assumed: $M_S = 1.3 \cdot (1 - 2 \cdot AS)\,\mu_B$/f.u. For a sample with $AS = 0.15$ the prediction would be $M_S = 0.91$ μ_B/f.u. and for $AS = 0.135$ $M_S = 0.94$ μ_B/f.u, in good agreement with the experimental values.

In Figure 3.9 we present the theoretical upper limits, calculated within the frame of the two approaches described above i.e. in the spin-only (ionic) picture and including the spin-orbit coupling. Our measurements strongly suggest the necessity of incorporating the spin-orbit coupling in the description of the physics of Sr_2CrReO_6, including the magnetization. DFT calculations of the evolution of the saturation magnetization in Sr_2CrReO_6 with the level of antisites when including and not including the spin-orbit interaction are currently being performed by Vaitheeswaran et al. and will allow better understanding of the influence of antisites. The Re orbital moment has been predicted and found to be parallel to the Fe or Cr spin moment and antiparallel to the Re spin moment [102, 104], which explains why the actual saturation magnetization is larger than previously considered.

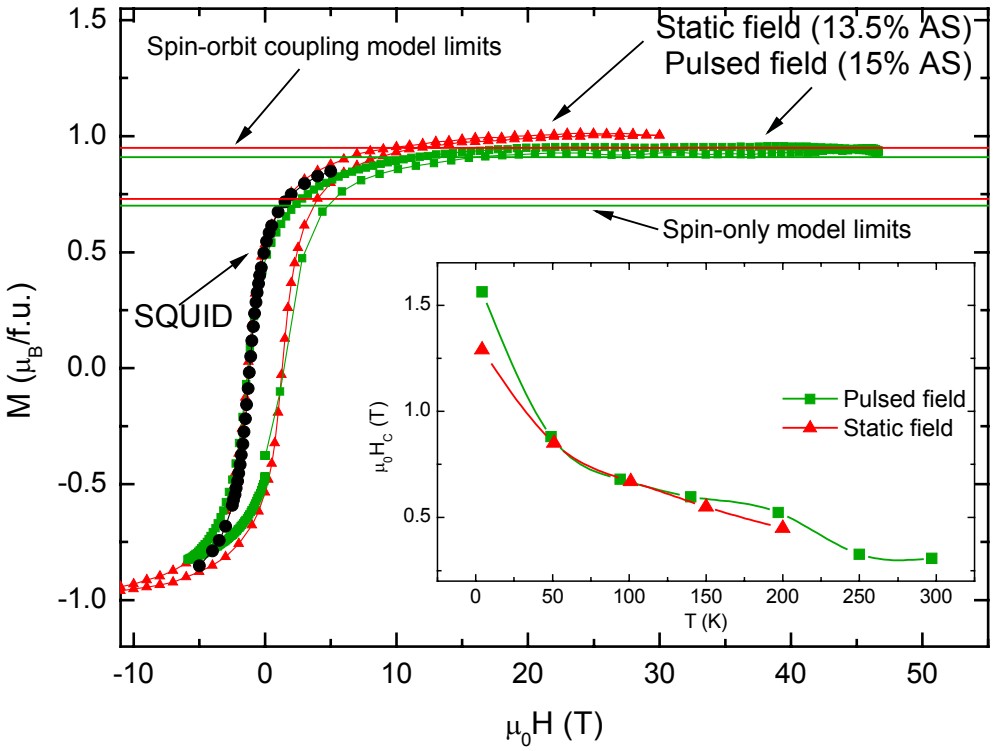

Figure 3.9. Magnetisation curves measured in the high field range under pulsed (green line) and static (red curve) fields up to 50 and 30 T respectively, compared with the measurement in the SQUID magnetometer in the field up to 5 T. In the figure, actual antisite defect amount is indicated. Solid lines stand for the magnetisation limit in the spin-only ionic model and the model including spin-orbit coupling (with given *AS* percentage.) In the inset: values of coercive field of the Sr_2CrReO_6 obtained from the pulsed (green line) and static (red line) measurements. The experiments under pulsed fields have been performed using DP73 sample and under static fields for the DP78 one.

The temperature evolution of the saturation magnetization of the two samples with different defects amount is very similar. Apart from small differences in the value (caused by the *AS* disorder) and some variation in the pulsed-field results (rather due to the data manipulation described in section 2.2.1.3 than to actual physical effects) M_S varies smoothly over the temperature range from 4.2 to 200 or 300 K in case of static as well as pulsed field measurements. We will not go deeper into the details of the temperature dependence of the magnetization in the case of Sr_2CrReO_6 until when focusing later on the discussion on the $BaSrFeReO_6$ double perovskite.

Table 3.3. Summary of the magnetization measurements of the Sr_2CrReO_6 double perovskite samples possessing different amounts of antisite defects (*AS* given in %) investigated by pulsed and static magnetic field magnetometry. The values of the measured and theoretical saturation magnetization (in μ_B/f.u.) are listed (see text for details concerning the two models applied). Also the value of the coercive field ($\mu_0 H_C$ in Tesla) of the material is given.

	Pulsed field (50 T), DP73	Static field (30 T), DP78
AS (%)	15	13.5
Saturation magnetisation (at 4.2 K) (μ_B/f.u.)	0.96	1.00
Expected saturation magnetisation (spin-only model with given *AS* amount) (μ_B/f.u.)	0.7	0.73
Expected saturation magnetisation (S-O coupling included and given *AS* amount) (μ_B/f.u.)	0.91	0.94
Underestimate with the spin-only model (%)	37	37
Coercive field (5 K) (T)	1.56	1.29

From our measurements we can evaluate the coercive field (H_C) in the temperature range 4.2 K-300 K as well. The temperature dependence of the H_C is plotted in the inset of the Figure 3.9. One can observe the lowering of H_C with the increase in temperature. The coercive field increases from 0.31 T at room temperature up to 1.56 T at 4.2 K and from 0.45 at 200 K to 1.29 T at 4.2 K for each of the two samples respectively. Apart from the usual increase of the coercive field in ferromagnetic materials when decreasing the temperature due to the weakening of thermal assistance in magnetization reversal, it seems that an additional mechanism is contributing to this sizeable change. This mechanism can be the lowering of the crystal symmetry from cubic to tetragonal below room temperature in Sr_2CrReO_6 as previously observed by neutron diffraction. A strong Re orbital moment causes the magnetocrystalline anisotropy to be important. Due to the strong magnetostructural coupling in Re-based double perovskites, it is very likely that this structural change contributes to the increase of the magnetic anisotropy and, as a consequence, of the

coercivity

As we have already shown, the orbital moment carried by a Re^{5+} is of primary importance for the physical properties of the Sr_2CrReO_6 (and presumably for other Re based double perovskites). In order to get a reliable value of the orbital moment m_L (or at least the fraction of m_L with respect to spin moment i.e. the m_L to m_S ratio) one can use the X-ray Magnetic Circular Dichroism (XMCD) method. We have already presented that the material saturates magnetically only under applied fields larger than 20 T. Here we will beneficiate from the possibility of performing the XMCD experiment in the high field range, the field being generated with the pulsed technique. The details of the experimental setup are given in the section 2.4.3.

The presented values of the magnetic moment contributions have been derived using the sum rule equations (as explained in the section 2.4.3). First, the integration of the XMCD and XAS signals over the energy ranges corresponding to the L_2 and L_3 edges is needed. In order to calculate the m_L to m_S ratio such operation is sufficient due to the fact that the *d*-holes number (see equations (2.29)) is cancelled out on dividing m_L by m_S. For the calculations of the absolute values of the spin and orbital contributions to the Re magnetic moment the *d*-holes number $n_d = 5.3$ was used as proposed by Majewski et al. [102] The magnetic dipole operator for transitions to *d*-states, $\langle T_Z \rangle$, is averaged to zero because the measurements are performed for a polycrystalline (powder) sample with random crystallographic axes orientations. For the calculations, a degree of circular polarization of 75 % for both polarization orientations was considered.

The experimental results are presented in the Figure 3.10 along with the calculated m_L/m_S ratio obtained under different applied magnetic field. A resulting magnetic moment per one Re ion (m_{Re}) is found to be –0.45 μ_B at $H = 260$ kOe and $T = 8$ K. The field dependence of the (m_{Re}) qualitatively follows the magnetization loop obtained from the pulsed field experiments discussed earlier (see Figure 3.11).

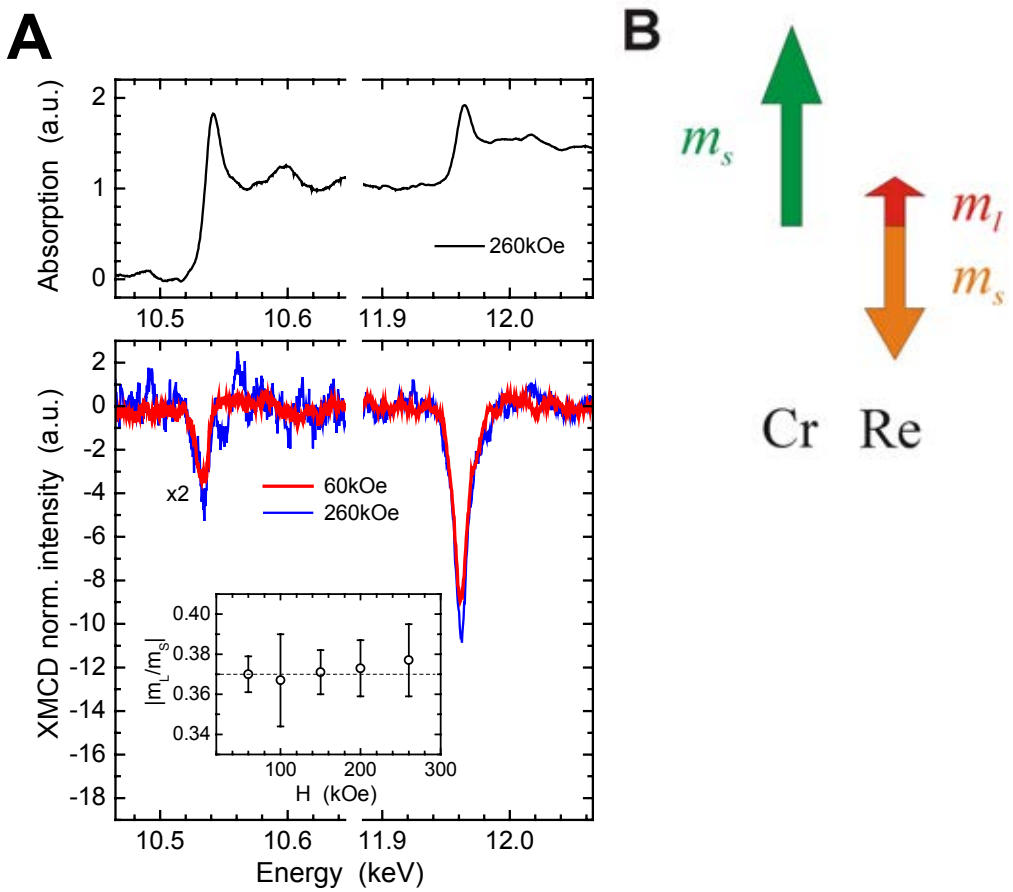

Figure 3.10. (a) X-ray absorption spectra of the L_3 and L_2 edges of Re in Sr_2CrReO_6 and the XMCD signal obtained under applied field of 6 (red line) and 26 T (blue line). The L_3 edge absorption spectra intensity is multiplied by a factor 2 for better view. In the inset: absolute value of the calculated m_L to m_S ratio as a function of magnetic field. (b) The spin and orbital contributions for the Cr^{3+} and Re^{5+} ions. The spin parts of the magnetic moment are coupled antiferromagnetically while the orbital moment of the Re ion points in the direction of spin component of Cr ion resulting in enhanced saturation magnetization.

Regarding the temperature dependence of the XMCD signal, it coincides with the magnetization as a function of temperature curve within the experimental error bar as presented in Figure 3.12. The most important however is the absolute value of m_L/m_S, which is found to be 0.37. Such high orbital contribution to the magnetic moment of

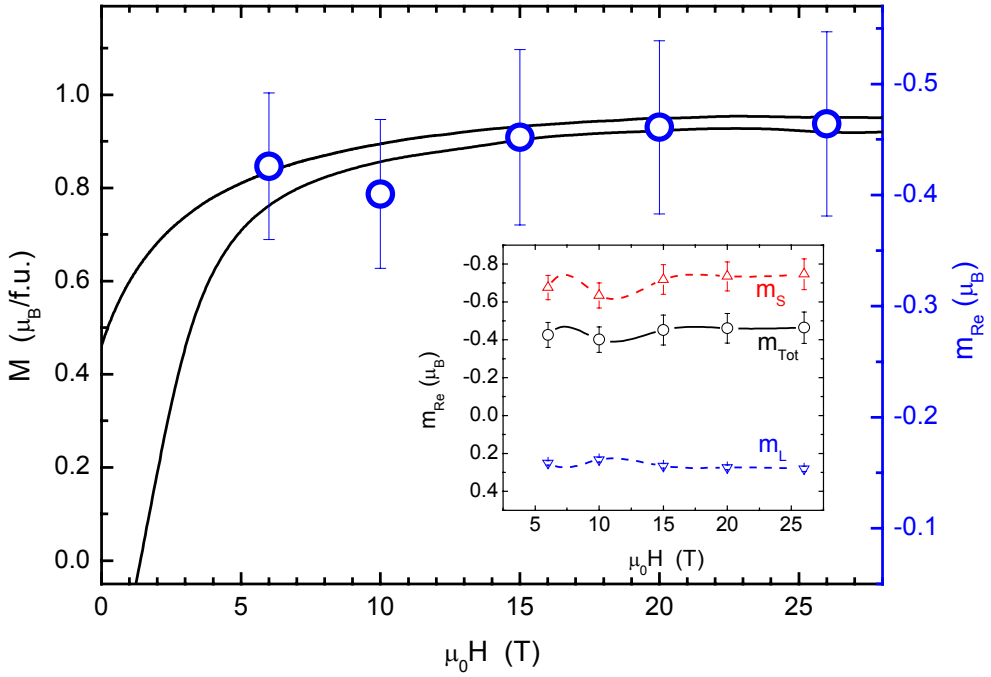

Figure 3.11. Magnetization at pulsed-field at 5 K (left axis) and total magnetic moment at the Re site (right axis) derived from XMCD signal measured at 8 K (see text for details). In the inset: spin and orbital contributions to the Re magnetic moment along with the total magnetic moment per Re ion.

Re ion surely will influence the magnetic properties of Sr_2CrReO_6. As the m_l and m_s components have opposite direction (the former parallel to the Cr spin moment and the latter antiparallel) the overall saturation magnetization is no longer 1 μ_B/f.u. as predicted in analogy to the FeMo based compounds (and taken for granted by many authors for the double perovskites containing Rhenium). Its value should be recalculated taking into account the orbital moment associated with the Re site. Also other properties like the high coercivity arising from magnetostructural coupling have been proved to arise from the Rhenium nonzero orbital moment.

Let us get back to the bulk magnetisation measurements. By using the previously introduced mathematical expression $M_S = M_{ST} \cdot (1 - 2 \cdot AS)$ μ_B/f.u., one can get the

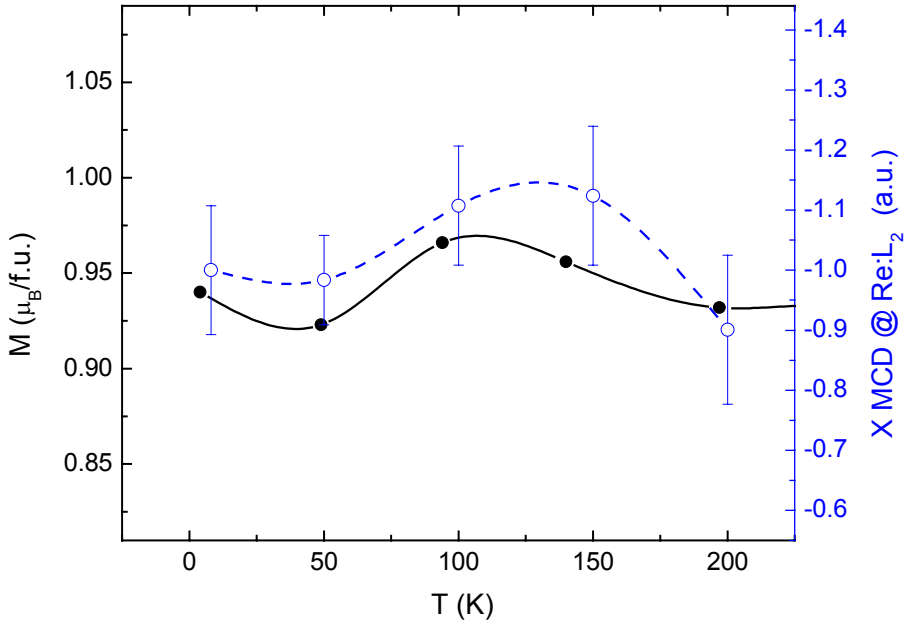

Figure 3.12. Temperature evolution of the XMCD signal measured under 26 T at the Re:L_2 edge (integrated area of the XMCD peak) - dashed line and the bulk magnetization under pulsed magnetic field of 50 T- solid lines.

M_{ST} value provided M_S and AS are known. Consequently we obtain $M_{ST} \approx 1.37$ μ_B/f.u. for both samples investigated by high field magnetometry. This value is close to the theoretical predictions in Sr_2CrReO_6 by Vaitheeswaran et al. [61]. Moreover a noninteger value of the theoretical saturation magnetization indicates that half metallicity is lost in this compound, even though the spin polarization has been calculated to be around 90% [61].

.

Chapter 4

FeRe-based double perovskites

The second part of our study was dedicated to the A_2FeReO_6 series (A_2 being Ca_2, Sr_2 and BaSr). Although the work is related to the magnetic properties of the material, similarly to the case of Sr_2CrReO_6, we have decided to summarize this part in a separate chapter. The series itself stands for a subject of a study due to the fact that it allows the investigation of the magneto – structural interplay. As will be shown later, the crystallographic structure has a great impact on the magnetism of the double perovskites being under investigation.

For the static field magnetization experiments, we have chosen high-quality polycrystalline samples belonging to the A_2FeReO_6 series. The samples have been synthesized by the solid-state reaction technique as described in section 2.1. The Rietveld refinements of the x-ray powder diffraction spectra performed with FULLPROF software (see chapters 2.3. and 3.1.) indicate that all samples are mainly double perovskite phase with some small impurity traces. At room temperature the crystal structure is cubic ($Fm\bar{3}m$ space group) for $BaSrFeReO_6$, tetragonal (*I4/m*) for Sr_2FeReO_6, and monoclinic ($P2_1/n$), for Ca_2FeReO_6. The Ca_2FeReO_6 sample shows a structural transition (between two monoclinic phases) at temperature below 140 K [63, 117, 120] which has a significant impact on various properties [63, 117, 120, 121]. The level of antisite disorder (*AS*) defects, estimated by the x-ray patterns analysis is found to be very low for the Fe-based samples. In the previous case of Sr_2CrReO_6, the *AS* amount was higher (*AS* = 13.5%) than in the A_2FeReO_6 series due to the similar ionic size (the effective ionic radius with the 6 nearest neighbours coordination) of Cr^{3+} (0.615 Å) and Re^{5+} (0.58 Å) ions compared to Fe^{3+} (0.645 Å) [57]. Hereafter we define the percentage of *AS* defects as can be found from equation (1.34) so that 0% indicates defect-free structure fully ordered and 50% means fully disordered sample, i.e. the single perovskite phase instead of the double perovskite one. The saturation

magnetization of the FeRe based material should change with a variation of the *AS* level as given by equation (1.33). In our samples the amount of *AS* is only 0% for Ca_2FeReO_6, 0.5% for $BaSrFeReO_6$ and 2% for Sr_2FeReO_6 (see also Table 4.1). This allows the investigation of the magnetization in good quality samples, without the need of significant corrections due to structural defects, leading to clear interpretation of the results. The room temperature x-ray diffraction patterns for $BaSrFeReO_6$, Sr_2FeReO_6 and Ca_2FeReO_6 are presented in the Figure 4.1 a, b and c respectively. The simulated patterns for different levels of *AS* disorder (0% and 5%) are presented in its inset.

Table 4.1. Data on the structural parameters (space group, lattice constants and angles – if applicable as well as the percentage of antisite defects) of different double perovskite samples belonging to the A_2FeReO_6 series.

Compound	Space group	Lattice parameters	Antisites (%)
$BaSrFeReO_6$	$Fm\bar{3}m$	a = 7.9642(2) Å	0.5
Sr_2FeReO_6	$I4/m$	a = 5.5613(1) Å c = 7.9015(2) Å	2
Ca_2FeReO_6	$P2_1n$	a = 5.4029(1) Å b = 5.5278(1) Å c = 7.6865(1) Å β = 90.055(3)	0

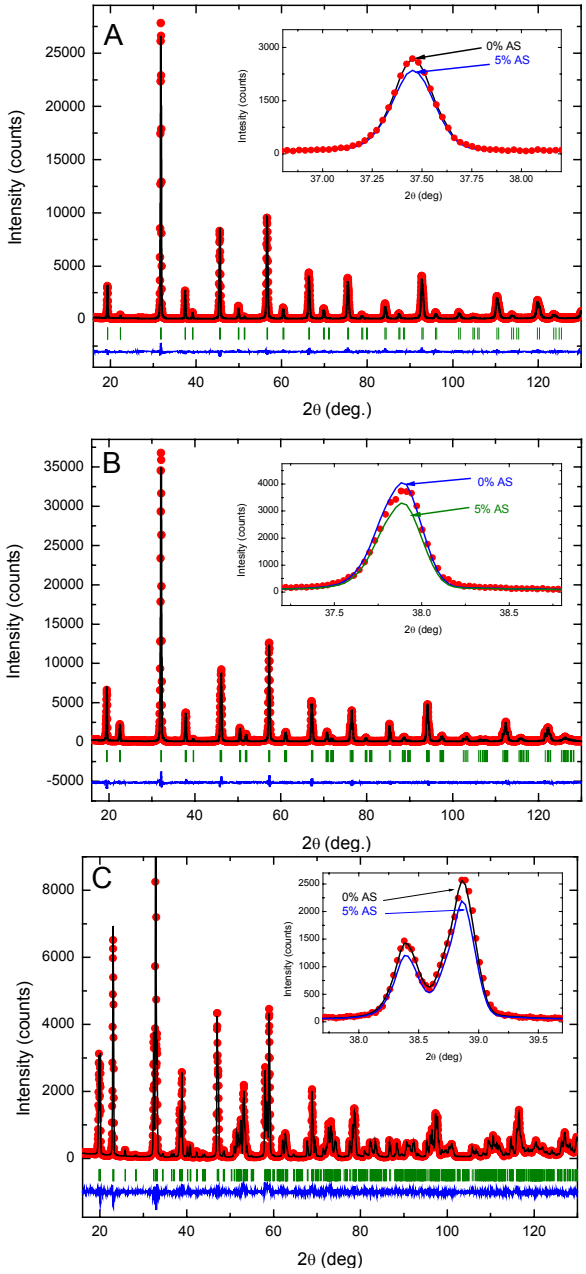

Figure 4.1. Rietveld refinement of the x-ray diffraction data at room temperature. Closed circles stand for the experimental points, the line for the calculated fit. The difference between the observed data and fit is plotted with the line in the bottom. In between, the allowed Bragg positions are marked. The data corresponds to $BaSrFeReO_6$ (a), Sr_2FeReO_6 (b) and Ca_2FeReO_6 (c) double perovskites. In the insets the close-ups of the diffraction peaks particularly sensitive to the antisite disorder are presented along with simulated patterns for different defects amount.

4.1. A_2FeReO_6 low field magnetic properties

The basic magnetic characterization of the A_2FeReO_6 series was performed in the low field regime in order to check the purity of the material from the point of view of magnetic impurities and estimate the temperature of the magnetic ordering. The low temperature magnetization loops measured under an applied field up to 5 T clearly show the lack of magnetic saturation as can be seen in the Figure 4.2.

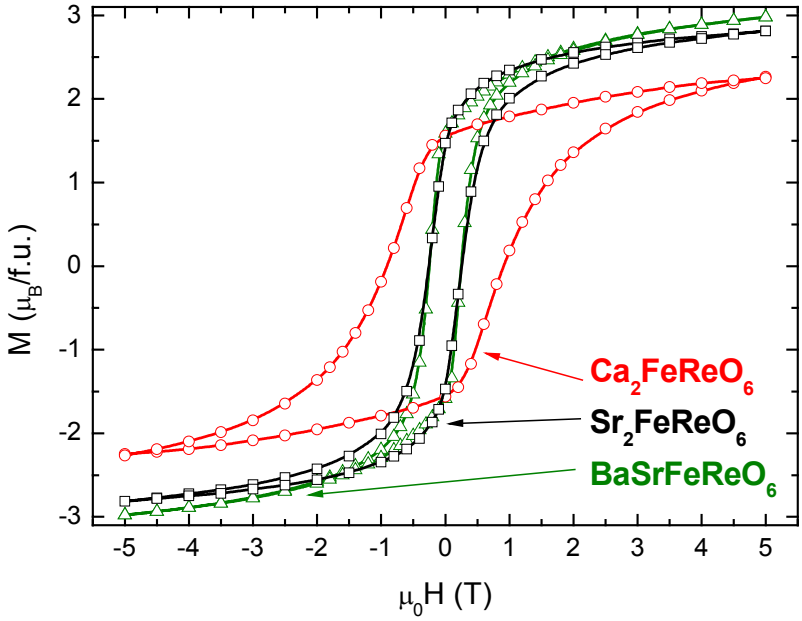

Figure 4.2. Low temperature (5 K) magnetisation loops obtained with the SQUID magnetometer for different double perovskite samples. Open circles, squares and triangles correspond to Ca_2FeReO_6, Sr_2FeReO_6 and $BaSrFeReO_6$ samples, respectively. Ca_2FeReO_6 shows much larger coercive field compared to the two remaining samples - $BaSrFeReO_6$ and Sr_2FeReO_6 having nearly the same coercivity. It is clearly seen that the material is not saturated under applied fields of 5 T.

The magnetization values at 4 K under 5 T for $BaSrFeReO_6$, Sr_2FeReO_6 and Ca_2FeReO_6, are respectively found to be 2.98 μ_B/f.u., 2.81 μ_B/f.u., and 2.25 μ_B/f.u.. These values are lower than the presumed M_S value in spin only ionic model: 3 μ_B/f.u. (see chapter 1.6.1 for the details on the model). As will be shown hereafter, the field of 5 T is much below the saturation field of these materials, which does not permit

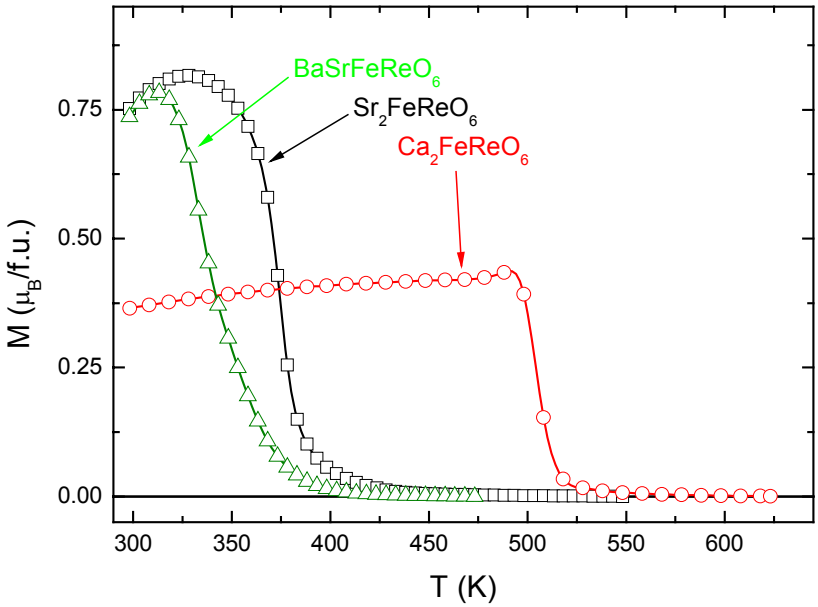

Figure 4.3. Magnetisation versus temperature curves obtained under the applied field of 1 kOe. Open circles, squares and triangles correspond to Ca_2FeReO_6, Sr_2FeReO_6 and $BaSrFeReO_6$ samples, respectively. The Curie temperature is estimated on the basis of the presented data as an intersection of the linear extrapolation of the maximum slope part of the curve onto the ordinate axis. Results are given in Table 4.2. The contribution from the magnetic impurities estimated from the high temperature magnetization versus applied field curves is subtracted from the data.

reliable investigation of their M_S and consequently does not allow the testing of different models proposed for the description of the magnetic and electronic properties of these compounds. We shall comment here that the coercive field of the Ca_2FeReO_6 is found to be 0.99(5) T, much larger compared to both $BaSrFeReO_6$ and Sr_2FeReO_6 showing H_C close to 0.25(5) T. This fact is the first indication of the impact of the crystallographic structure on the magnetic interaction strength. This subject will be addressed in more details in the following subsections, as it should be discussed together with the saturation magnetization and remanence. This is possible only on the basis of the high magnetic field measurements.

The temperature of the magnetic ordering has been estimated from the high temperature magnetization data (from 300 K up to 475 K, 550 K and 650 K for

$BaSrFeReO_6$, Sr_2FeReO_6 and Ca_2FeReO_6 respectively) measured using the vibrating sample magnetometer. The Curie temperature is also defined here as the point of the intersection of the ordinate axis with the linear extrapolation of the maximum slope region of the magnetization curve. The T_C is then found to be ≈360 K, ≈410 K and ≈520 K for $BaSrFeReO_6$, Sr_2FeReO_6 and Ca_2FeReO_6 respectively (see Figure 4.3). We have subtracted a signal that is clearly coming from the tiny magnetic impurities. A strong ferrimagnetic ordering leading to such high Curie temperatures established by the electron hopping between Fe t_{2g} and Re t_{2g} orbitals via Oxygen $2p_\pi$ orbitals should be strongly dependent on the lattice parameters. The lowering of the distances between the interacting ions reinforces the ferromagnetic state while the deviation of the Fe – O – Re bond angle from 180º causes the hopping to be less efficient and consequently weakens the magnetically ordered state. The interplay of the two processes should lead to the increase of the T_C while changing the A ion from Ba_2 to Sr_2, and finally to the decrease of the T_C for $A_2 = Ca_2$. One can see that the trend to increase the Curie temperature is different from that predicted by this simple model, and some other process should be introduced to describe the T_C vs. A ion size dependence. As discussed by Serrate et al. [58] the hybridisation of the oxygen orbitals opens the possibility of establishing a new interaction channel via the O $2p_\sigma$ orbitals for the e_g Fe and Re electrons.

We have recently examined the already published data [122] on the XANES study of the A_2FeReO_6 series (see Figure 4.4). Owing the courtesy of Dr. Javier Blasco we were able to explore the data with the approach that is addressed in more details in the fifth chapter. The data covers a wide range of the A_2 site occupancies so it allows the investigation of the impact of the mean ionic radius of the A site anion on the physical properties. The $\langle r_A \rangle$ varies from 1.61 Å for Ba_2, through 1.52 Å for BaSr, 1.44 Å for Sr_2, 1.39 Å for CaSr, 1.36 Å for $Ca_{3/2}Sr_{1/2}$ to 1.34 Å for Ca_2.

We have extracted the pre-edge region of the XANES signal at the K absorption edge of Iron by fitting the experimental data with a tanh function (keeping the edge

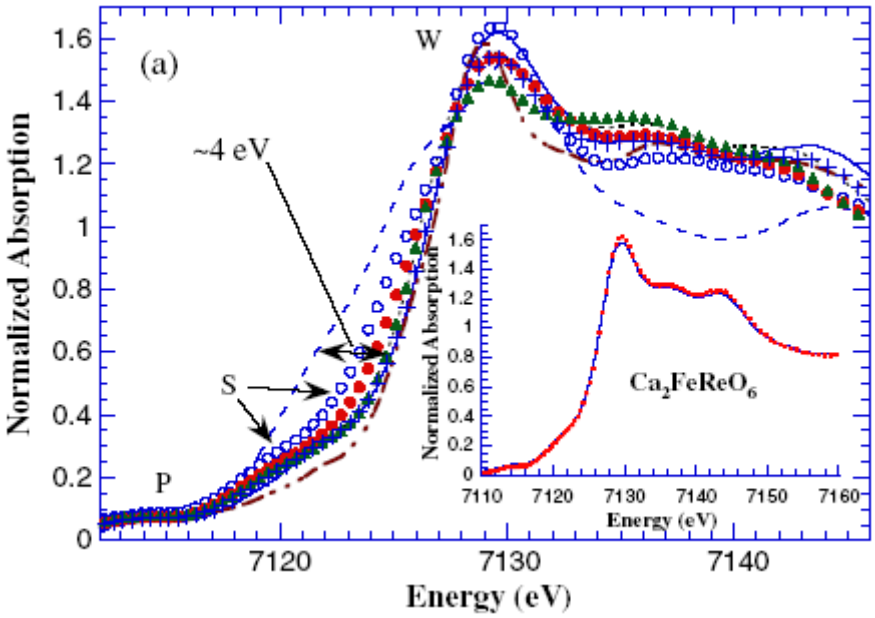

Figure 4.4. Original plot from the reference [122]: XANES spectra of the A_2FeReO_6 and reference samples at the Fe K edge at 40 K, A_2 being Ba_2 (open circles), BaSr (filled circles), Sr_2 (triangles), CaSr (dotted line), $Ca_{3/2}Sr_{1/2}$(+), Ca_2 (solid line), $LaFeO_3$ (chain curve) and FeO (dashed line). Inset: comparison of the XANES spectra at 40 K (points) and room temperature (line) for Ca_2FeReO_6. The letters W, S and P denote white line, shoulders and pre-edge features, respectively.

jump fixed to 1, and the inflection point to the absorption edge energy estimated by Herrero et al. [122]) and the Lorentz shaped peak in the white line region. From the point of view of our interest the most interesting is the region denoted in the Figure 4.4 as P as the intensity of this feature is related to the dipole forbidden transition *1s* – *3d* that is quadrupole allowed. Relatively important contribution to the absorption signal at this energy range cannot be only ascribed to the quadrupole transitions. It was reported that the transition becomes dipole allowed if there is a mixing of O *2p* and Fe *3d* states due to a spreading of the *4p* band [123] or due to the hybridisation of Fe *3d* – O *2p* orbitals (as was demonstrated for binary oxides [124]).

In the Figure 4.5 we have plotted the area of the P feature as a function of the

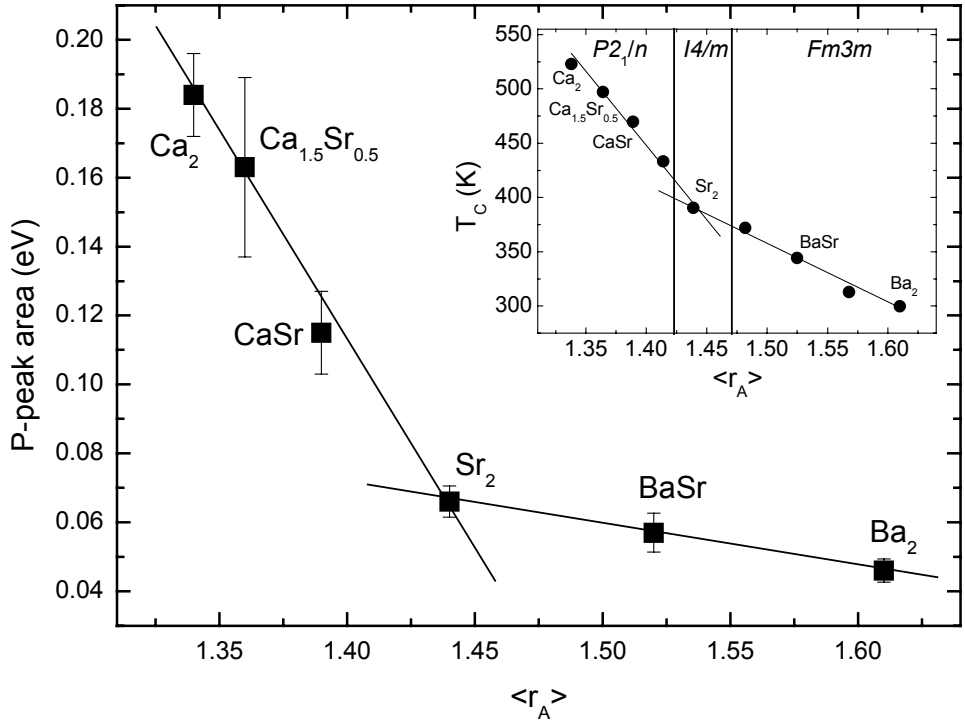

Figure 4.5. The area below the pre-edge peak denoted as P in the Figure 4.4 plotted versus the mean ionic radius at the A site for the A_2FeReO_6 series. In the inset: Curie temperature of different members of the FeRe based double perovskites as a function of the mean ionic radius at the A site (T_C and structural data after De Teresa et al. [118]).

mean ionic radius at the A site. The analysis was limited to this energy range as the complicated shape of the absorption edge makes it impossible to treat the white line separately of the edge itself (which means the S labelled features of the XANES signal cannot be extracted not taking the white line into account). Moreover the absorption edge width is affected by the A ion type as it depends not only on the local distortion around the absorbing atom, but also on the scattering power of the A ion.

Surprisingly, the trend of the changes of the P-peak area versus $\langle r_A \rangle$ follows a linear trend, the slope of the linear fit being different for the monoclinic and cubic compound (the tetragonal structure seems to be the intermediate one). We can ascribe such behaviour to the increase of the hybridisation efficiency, resulting in increased DOS in the energy levels diagram of Fe ions, coming from the Oxygen *p* orbitals. As

can be seen in the inset of the Figure 4.5. similar behaviour is visible in the Curie temperature versus mean ionic radius plot as was demonstrated by De Teresa et al. [118]. Those facts together give a strong support to the already introduced explanation of the anomalous rise of T_C in the A_2FeReO_6 series by the Oxygen $2p_\sigma$ channel of magnetic interaction.

The amount of magnetic impurities was estimated by the extrapolation of the linear (paramagnetic) part of the magnetization curve onto the ordinate axis (see Figure 4.6). The extrinsic magnetization caused by the impurities is estimated to be ≈ 0.065 emu/gr, ≈ 0.25 emu/gr and ≈ 0.05 emu/gr for $BaSrFeReO_6$, Sr_2FeReO_6 and Ca_2FeReO_6 respectively. Those values correspond to 0.2%, 0.7% and 0.1% of the saturation magnetization value measured for the $BaSrFeReO_6$, Sr_2FeReO_6 and Ca_2FeReO_6 respectively. The small amount of impurities in the material does not allow their detection and identification with the x-ray powder diffraction, thus being impossible to conclude what kind of impurity gives rise to the magnetization of the samples above the magnetic ordering temperature.

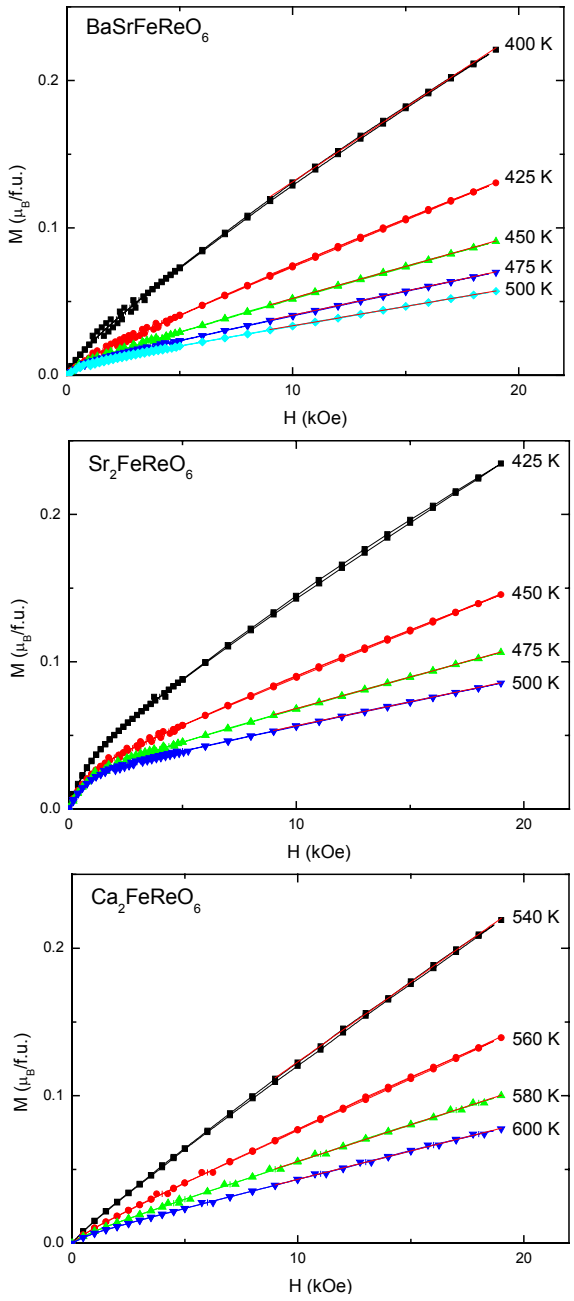

Figure 4.6. Magnetisation curves at different temperatures above the temperature of the magnetic ordering for $BaSrFeReO_6$, Sr_2FeReO_6 and Ca_2FeReO_6 (as indicated in the figures). Extrapolation of the high-field range data (1 – 2 T) onto the magnetization axis allows the estimate of the magnetic impurities amount.

4.2. A_2FeReO_6 low temperature magnetism under high magnetic fields

Measurements under low temperature conditions (liquid helium temperature $T = 4.2$ K) allow the investigation of the saturation magnetisation dependence on the A_2 cation in the A_2FeReO_6 series. Apart from this property, the coercivity of the material tends to change together with the varying mean ionic radius at the *A* site - $\langle r_A \rangle$. Surely, more interesting results are obtained taking into account the temperature variations, however as we have demonstrated in case of Sr_2CrReO_6, the nonzero orbital moment carried by the Re ion is of a great importance in the Re-based double perovskites. Moreover, the important issue of the lack of magnetic saturation in magnetization measurements under applied field of 30 T has led us to propose the magnetically disordered grain boundaries model. Thus, let us discuss the low temperature results first, before going to the temperature evolution of the magnetic properties. In Table 4.2 we present the summary of the results obtained with the magnetization measurements under applied field up to 30 T at 4 K. The first feature that is clearly visible is the variation of the coercive field (H_C) between different members of the A_2FeReO_6 series. The increase in H_C with decreasing average ionic radius has been ascribed to the increase in anisotropy and orbital contribution to the overall magnetic moment as presented by magnetic and magnetotransport measurements [118] as well as directly by x-ray magnetic circular dichroism [104]. The maximum measured values of magnetization are, as already mentioned, not equivalent to the saturation magnetization. Taking into account the formula given in chapter 1 (see equation (1.34)) and putting the number of *AS* defects obtained from x-ray powder diffraction patterns and maximum measured value of magnetisation as M_S on the left hand of the equation, we are able to calculate M_{ST}. This will have the meaning of the magnetization that would be measured in the maximum field assuming a perfect ordering of a double perovskite structure. Equation (1.34) will then get the form:

$$M_S(\max) = \frac{M_S(\exp)}{1 - 2 \cdot AS} \tag{4.1}$$

with $M_S(exp)$ being the value of the magnetization measured at 4 K under 30 T, AS the percentage of antisite defects defined as in equation (1.33) and $M_S(max)$ is the expected saturation (maximum) magnetization in case of absence of any structural defects. We will comment on the calculated values later on.

Table 4.2. Data on significant parameters (Curie temperature, coercive field, experimental magnetization value under 30 T at 4 K, estimated and theoretical saturation magnetization) of the investigated Re-based compounds. The estimated saturation magnetization has been calculated using the magnetization value found at 30 T and the level of antisites found with x-ray diffraction (see text for details). The error bar has been estimated taking into account possible errors in sample weight, in the determination of the antisite level, the contribution from the tiny ferromagnetic impurities, and in the case of Sr_2FeReO_6 the absence of complete saturation under 30 T. For Ca_2FeReO_6, under 30 T the compound is still far from saturation and only a lower limit can be given.

Compound	T_C (K)	$\mu_0 H_C$ (T)	M (μ_B/f.u.) at 30 T	M_S (μ_B/f.u.) estimated	M_S (μ_B/f.u.) theoretical
$BaSrFeReO_6$	360	0.24	3.27	3.30(5)	-
Sr_2FeReO_6	410	0.26	3.23	3.36(8)	3.4 ref. [127]
Ca_2FeReO_6	520	0.99	3.12	>3.12(1)	-

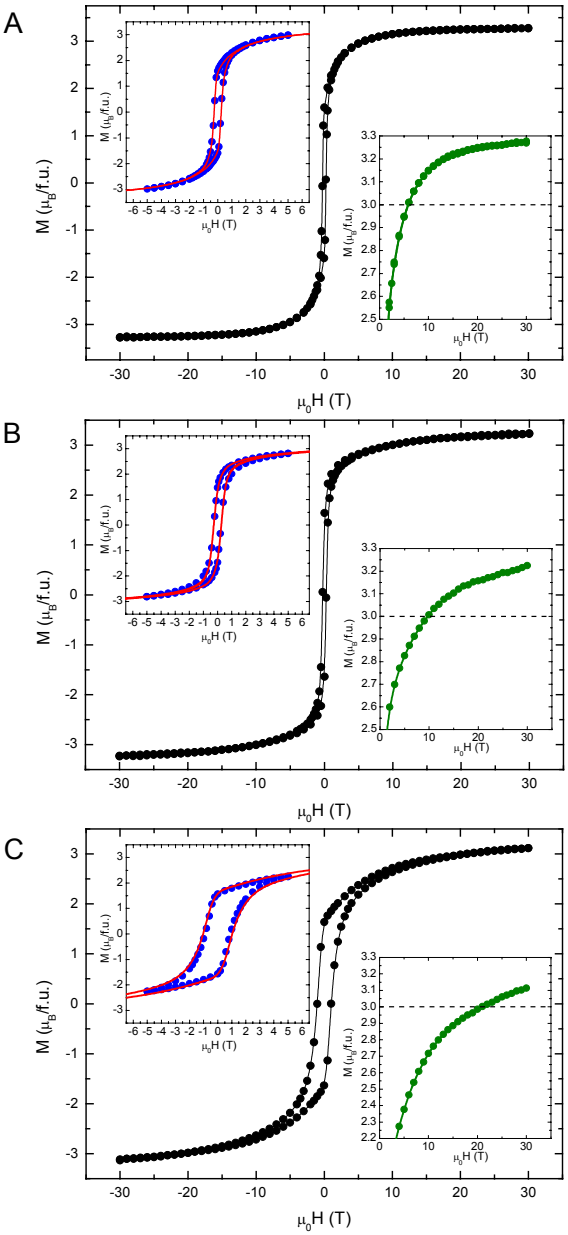

Figure 4.7. Magnetization versus applied field curves for $BaSrFeReO_6$, Sr_2FeReO_6 and Ca_2FeReO_6 in (a), (b) and (c) respectively. Upper insets in each panel: comparison of the SQUID magnetization measurements (blue circles) with the high static field magnetization data (solid red lines) showing a perfect agreement of the two. Bottom insets: high field parts of the magnetization loops (solid green lines) compared with the spin only ionic model 3 μ_B/f.u. limit of the saturation magnetization shown with dashed lines.

In the Figure 4.7.a we show the magnetization hysteresis loop at 4 K up to 30 T of the $BaSrFeReO_6$ sample. Under the maximum field of 30 T the magnetization is found to be 3.27 μ_B/f.u., much above the previously assumed (with the spin only ionic model) value of 3 μ_B/f.u. As can be noticed in the inset of this figure, this compound is almost saturated under 30 T. This fact, together with the small value of *AS* (0.5%), allows us to establish the value of 3.30(5) μ_B/f.u. for the M_S of this compound. It is important to notice that the results obtained with SQUID magnetometer up to 5 T superimpose to the results of the high field measurement in this field range, as shown in the inset of the Figure 4.7.a. The coercive field of this compound at low temperature is around 0.24 T. For the sake of completeness we report the remanent magnetization to be around 50% of the saturation value.

The measurements on Sr_2FeReO_6 are shown in Figure 4.7.b. In this case, under the maximum field of 30 T the magnetization is found to be 3.23 μ_B/f.u. at 4 K and 3.17 μ_B/f.u. at 100 K. The coercive field of this compound at 4 K is around 0.26 T, as previously reported [116, 118]. The remanent magnetization is also around 50% of the saturation value. However, in this compound the tendency to saturation is less clear than for $BaSrFeReO_6$ and it seems that a few more Tesla are required to achieve saturation. The slight increase of the magnetization between 100 K and 4 K (about 0.06 μ_B/f.u.) also allows us to discard any kind of spurious paramagnetic signal that could contribute to the measurement at 4 K. Taking into account the level of antisite defects in this sample, one can estimate the M_S of this compound to be 3.33(5) μ_B/f.u. by using the expression introduced before. This value is a rough approximation because the lack of complete magnetic saturation at 30 T is clearly visible. The maximum measured value is close, however, to the theoretical value of 3.4 μ_B/f.u. calculated in reference [127].

The lack of magnetic saturation under 30 T is also evident in the Ca_2FeReO_6 sample. The results for this sample are shown in Figure 4.7.c. Under the maximum field of 30 T the magnetization is found to be around 3.12 μ_B/f.u. at 4 K and at 100 K. The coercivity of the double perovskites seems to be sample dependent mainly due to

the presence of structural defects. Defects such as antiphase boundaries [125] can give rise to domain wall pinning centres, which can be very important in these compounds. The coercive field of this compound at 4 K is around 0.99 T. Due to the presence of a substantial orbital moment in Re-based compounds, an increase of the intrinsic magnetocrystalline anisotropy can explain the enormous coercivity enhancement in the monoclinic samples. The remanent magnetization is again found to be around 50% of the saturation value. We ascribe the lack of increase of the M_S in the temperature range between 100 K and 4 K to the fact that a structural transition between two monoclinic crystallographic structures takes place in this compound below 120 K [116, 120] (see the following subsection for the analysis of the temperature dependence of the magnetic properties). The low-temperature phase has larger coercivity and maybe slightly lower saturation magnetization than the high-temperature phase but this is not possible to establish from our measurements due to the lack of saturation. On the other hand, it has been recently shown that the competition between these monoclinic phases with different conductivity gives rise to a colossal magnetoresistance effect [18]. The lack of magnetic saturation at 30 T in this compound prevents us from establishing an accurate value for M_S even though we can state that it will be larger than the value obtained at 30 T, 3.12 μ_B/f.u.

4.2.1. Re orbital contribution to overall saturation magnetization

As can be clearly seen, the maximum value of the magnetization that can be measured in fields up to 30 T, even not being the saturation magnetization, overcomes the limit given by the spin-only ionic model of the magnetism of the double perovskites. From the experimental point of view this can be straightforwardly associated to the existence of the important contribution coming from the orbital component of the heavy Re ions. The first attempts to explain the physical properties of $A_2FeRe(Mo)O_6$ with modern theoretical approaches did not assign an important role to the Re orbital moment [55]. Such a model involves hopping interactions between the Fe and Re (Mo) ions and is able to explain the origin of the significant spin magnetic moment on the non-magnetic Re (Mo) ions in the ferromagnetic double

perovskites. Within the same model, the half-metallicity is explained via the splitting of the spin-up and spin-down subbands of the Re (Mo) ions, that is caused by the same hopping interactions which create the magnetic moment on the *B'* site ions [55, 126]. Even though such simple model works satisfactorily to explain the basic magnetic and electronic structure properties, one cannot extend the conclusions that are valid for the Mo-based double perovskites to the field of the Re-based ones. As was pointed out in the theoretical section of this thesis, the spin-orbit coupling constant of the Re ion has a value of 0.5 eV (lowered in the solid having the perovskite structure to 0.4 eV, which is still a large one). This is not the case in Mo, so it is now clear that an important ingredient in the description of Re-based double perovskites would be the significant spin-orbit coupling at Re ions producing a large Re orbital moment. This approach was introduced to the theoretical calculations by Jeng and Guo who calculated using a LSDA+U (Local Spin Density Approximation with Coulomb repulsion) approach that for Sr_2FeReO_6, the spin (m_S) and orbital (m_L) moments for Fe/Re are m_S = 3.91/-0.85 and m_L = 0.077/0.26 respectively. The cited values are given in μ_B/atom. Putting all those numbers together, a total magnetic moment of 3.4 μ_B/f.u. [127] can be found for Sr_2FeReO_6. This prediction is in good agreement with our experimental results just shown, 3.33(5) μ_B/f.u..

A nice agreement of our experimental result with the theoretical predictions supporting the latter is not the only conclusion to be drawn. In all the studied samples, the maximum magnetization has a non-integer value (and is far from the nearest integer values of 3 or 4 μ_B/f.u. so it is not the fault of the measurement uncertainty or defective material). If one considers the double perovskite material to be a half-metal , its ground state magnetization per formula unite should be an integer value. It is well-known that half-metals should have integer magnetic moments in order to accomplish the existence of a single occupied spin subband at the Fermi level as discussed by Coey and Sanvito [2]. This rule-of-thumb is a straight consequence of the integer number of total electrons (spin-up plus spin-down electrons) combined with the gap at the Fermi level in one of the spin subbands (either spin-up or spin-down) required to account for only one spin direction at the Fermi level. From our finding of non-integer

magnetization, we can infer that this condition is not satisfied in A_2FeReO_6 and, as a consequence, these compounds cannot be half metals. Vaitheeswaran et al., who have calculated that the inclusion of the spin-orbit coupling in Ba_2FeReO_6 will lead to the destruction of the half-metallic gap, have reliably given theoretical support to our finding [128] (see also the theoretical introduction in this thesis for some more details on the topic).

4.2.2. Approach to saturation magnetization

The electrical conductivity of the ceramic pellets of the double perovskite materials is controlled mainly by the influence of the highly resistive grain boundaries. This statement holds true as long as the samples are of good quality in terms of microstructure i.e. the grains composing the material are in good contact, giving a compact material. If this is not the case the mobility of the electric carriers will be strongly influenced (diminished) by a lack of conduction paths through the sample as the amount of the "air gaps" between the grains (porosity) is high. The importance of the grain boundaries is clear taking into account the values of the resistivity reported for the single crystals of Sr_2FeMoO_6 being of the order of several tens of mΩ cm (see e.g. reference [129]). In the case of ceramic pellets, the resistivity is dependent on the synthesis procedure and the electrical properties of the material vary from semiconducting to metallic, the absolute value of resistivity being several orders of magnitude higher compared to single crystals [130]. However, the experimental results are in disagreement with the standard intergrain tunnelling magnetoresistance model described in section 1.2.4. This has led us to the introduction of a modified model taking into account not only the insulating boundary between the grains but also a magnetically disordered grain boundary (see Figure 4.8). The outer layer of the boundary would act then as a potential barrier in the TMR model as explained in section 1.2.3. Provided that the barrier width is small enough, a tunnelling process will occur and the TMR effect magnitude will depend only on the spin polarisation of the carriers in the grain bulk (in this approach we treat the grain cores as the electrodes and the grain boundary as an insulating spacer). The situation becomes more complex, however, when the magnetically disordered state is introduced in the model.

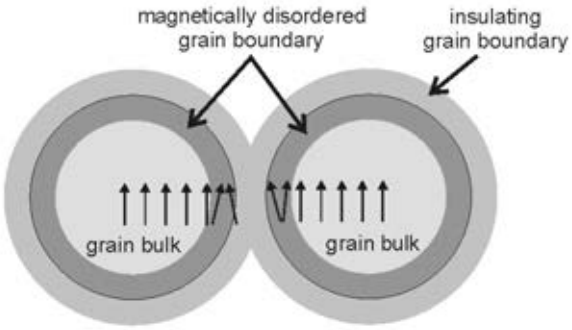

Figure 4.8. Schematic view of the cross section of the two ferromagnetic grains. The grain core is surrounded by two kinds of layers: a magnetically disordered grain boundary and an insulating cover (outermost layer). The arrows indicate the spin direction and are drawn for only one crystallographic site for clarity.

It was proposed that the grain boundary magnetic state in $(Ba_{0.8}Sr_{0.2})_2FeMoO_6$ is a spin-glass like state [58]. Such statement was supported by the successful fit of the high-field magnetoresistance results through a magnetic saturation law with a functional form widely used in spin glasses with weak random anisotropy field [131]. In the proposed model weak anisotropy means that the exchange field is stronger than the random anisotropy field. In such case a local ferromagnetic magnetization changes its direction significantly only over a distance of a range of a correlation length (R_a^3). Several theoretical approaches have been proposed for the systems with weak random anisotropy (Spin Glasses, Correlated Spin Glasses, Ferromagnets with Wandering Axis etc.) [132]. In our study we did not mean to develop a new complex model of the magnetically disordered grain boundary state. We would rather use the model that well described experimental magnetoresistance curves.

In sharp contrast to the transport properties in granular materials the overall magnetization is mainly influenced by the bulk magnetization i.e. the inner part of the grain. This is due to the difference of the volume of the material that can be treated as a boundary and the volume that is closed inside the grain. As long as the size of the grains is sufficiently large the boundary atoms represent the minor part. However the lack of saturation in applied fields as high as 30 T can be ascribed to the lack of ordering in the highly disordered grain boundary region. It was confirmed by the

XMCD study of the local Fe magnetic moments that the grain boundary (at least 5 nm deep) is magnetically harder than the grain core and this fact was ascribed to the elevated level of *AS* disorder at the grain boundary [105]. De Teresa et al. also proposed larger hardness of the grain boundary compared to the grain core on the basis of the magnetoresistance measurements [133]. The extremely large magnetic field needed for forcing the grain boundary to order magnetically is inconvenient from the technological application point of view. It has been already shown that Re-based double perovskites are not half metals due to the spin-orbit interaction strength. Both facts complicate the possibility of applying those materials in bulk form in real devices.

To study the approach to saturation magnetization we have applied the model with the functional form given by equation (4.2) to describe the magnetic behaviour of the grain boundaries.

$$M(H) = a \cdot \left(1 - \frac{b}{\sqrt{H}}\right) \tag{4.2}$$

Here ***a*** has the units of magnetization and ***b*** is a constant depending on random anisotropy (β_r^2), the exchange strength ($\alpha^{3/2}$) and the distance for which the local easy axes becomes uncorrelated (R_a). The formal dependence on the abovementioned parameters is as follows:

$$b = R_a^3 \frac{\beta_r^2}{15 \cdot \alpha^{3/2}}. \tag{4.3}$$

This model can be used in cases when the anisotropy is weaker than the exchange strength, and for the magnetic fields smaller than the exchange field (so called low field regime). The fitting of the model was performed in the range of several Tesla downward from the maximum of 30 T (exact range of the fitted data is given in the Table 4.3).

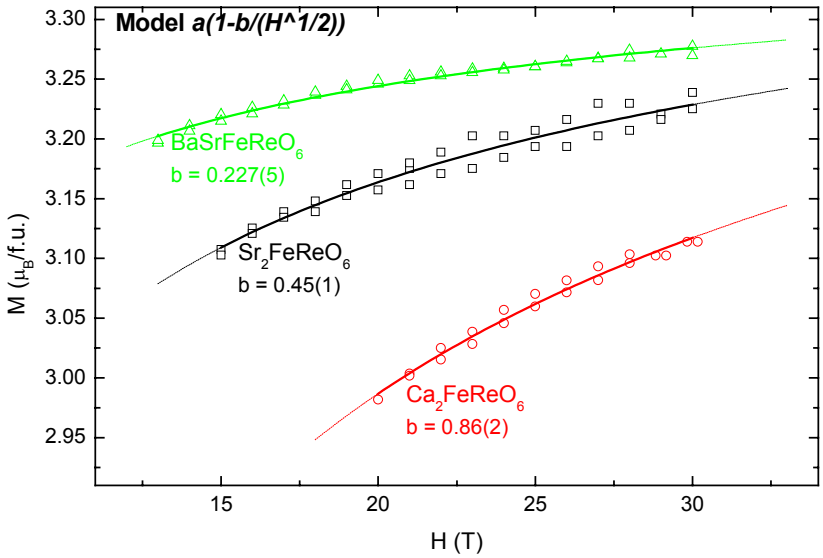

Figure 4.9. Fit of the magnetization data at 4.2 K with the model described in the text. Open circles, squares and triangles denote Ca_2FeReO_6, Sr_2FeReO_6 and $BaSrFeReO_6$ samples, respectively. Dashed lines are obtained from fitting the model to the experimental data, and solid lines show the fitting range.

In the Figure 4.9 we present the experimental data along with the fitted model. The *b* parameter of the fit changes from 0.86(2) through 0.45(1) to 0.227(5) for Ca_2FeReO_6, Sr_2FeReO_6 and $BaSrFeReO_6$ respectively (see Table 4.3). We can discard the influence of the *AS* disorder as the explanation of such a wide range of ***b*** parameter values, owing to the high quality of the samples and a very low *AS* defects content. One can see that the definition of the *b* coefficient involves two competing properties – random anisotropy energy and the exchange strength. As the magnetic and magnetostriction measurements show [58, 116, 118], the increase in anisotropy that takes place when lowering the mean ionic radius at the A site could explain the evolution of the ***b*** parameter. Moreover, the XMCD data also indicate stronger orbital contribution as the mean radius of the alkali earth ions decreases [104]. As a consequence, it seems that a strong random anisotropy at the grain boundaries could be at the basis of the lack of magnetic saturation in these compounds.

Table 4.3. Data on the results of the fitting of the experimental magnetisation data with the model described in the text. The *a* and *b* parameters from the equation (4.2) are listed. The fitting range is also indicated.

	Fitting parameters		Fitting range (T)
	a	***b***	
$BaSrFeReO_6$	3.41(8)	0.227(5)	13 – 30
Sr_2FeReO_6	3.51(7)	0.45(1)	15 – 30
Ca_2FeReO_6	3.69(7)	0.86(2)	20 – 30

We shall now comment on the scale factor ***a*** of the model discussed. As already mentioned it has the units corresponding to the magnetisation of the material. Indeed its meaning is the maximum saturation magnetisation that can be only achieved in the infinitely large external field limit. We assume that the lack of saturation is only due to a magnetic disorder in the grain boundary i.e. the grain core should be already in a magnetically saturated state. Thus a good approach would be to separate both contributions: M_{core} and M_{gb} being magnetisation of the grain core and the magnetisation of the grain boundary respectively:

$$M(H) = M_{core}(H) + M_{gb}(H) \tag{4.4}$$

As a consequence, above a certain field, which can be understood as a grain core saturation field, the only changing contribution would be the one having its origin in the rising level of magnetic order in the grain boundary. Thus we have tried to modify equation (4.2) accordingly. We have obtained the model described by the relation:

$$M(H) = M_{core} + M_{gb} \cdot \left(1 - \frac{b}{\sqrt{H}}\right) \tag{4.5}$$

with M_{core} being constant with respect to the field H (beginning from a certain value of the applied field) and the varying term dependent on the grain boundary contribution. It occurs, however, that M_{core} and M_{gb} become strongly correlated, and there is indeed no difference in the models given by equations (4.2) and (4.5). As the magnetisation value depends on the volume of the material giving rise to the signal in the

magnetization measurements, it is clear that some constrains should be introduced. This would be for example the grain size and assumed thickness of the grain boundary. The ceramic pellets are not good candidate for such study as the grain size varies as has been observed by Scanning Electron Microscopy experiments (see the following chapter for some examples). We have not consequently been able to extract more detailed information of the grain boundary contribution to the magnetisation. Further insight could be obtained by performing the magnetisation measurements on thin film samples with well-defined microstructure or using the bulk material obtained with the sol-gel synthesis method due to more uniform grain size in this kind of samples.

4.3. Temperature evolution of magnetic properties

The temperature dependence of the magnetization for Ca_2FeReO_6 and $BaSrFeReO_6$ samples is presented in the Figure 4.10.a and in the lower inset of Figure 4.11 respectively.

In the case of the Ca_2FeReO_6 sample some anomalous temperature dependence of the magnetization is visible in the low temperature range – below 175 K (Figure 4.10.a). The maximum value of the measured magnetization is 3.12(1) μ_B/f.u. and is stable in the range of 0.02 μ_B/f.u. up to 140 K. Eventually it drops at 180 K to 3.04 μ_B/f.u. The latter temperature is reported [133] to be close to the temperature of the structural transition between two monoclinic phases with slightly different lattice parameters and different direction of the spontaneous magnetization axis [63]. In the Figure 4.10.b we plot the coercive field (H_C) versus the temperature. It exhibits two linear slopes as a function of temperature. The change of the slope occurs about 130 K, around the structural transition temperature. The maximum value obtained for H_C is 1.03 T at 4 K. It decreases fast up to 110 K by more than 50% and changes much slower from 0.33 T at 140 K to 0.21 T at room temperature. In the latter temperature interval the coercivity follows the normal linear trend as in other double perovskite family materials not undergoing any magnetostructural transition. It is very likely that

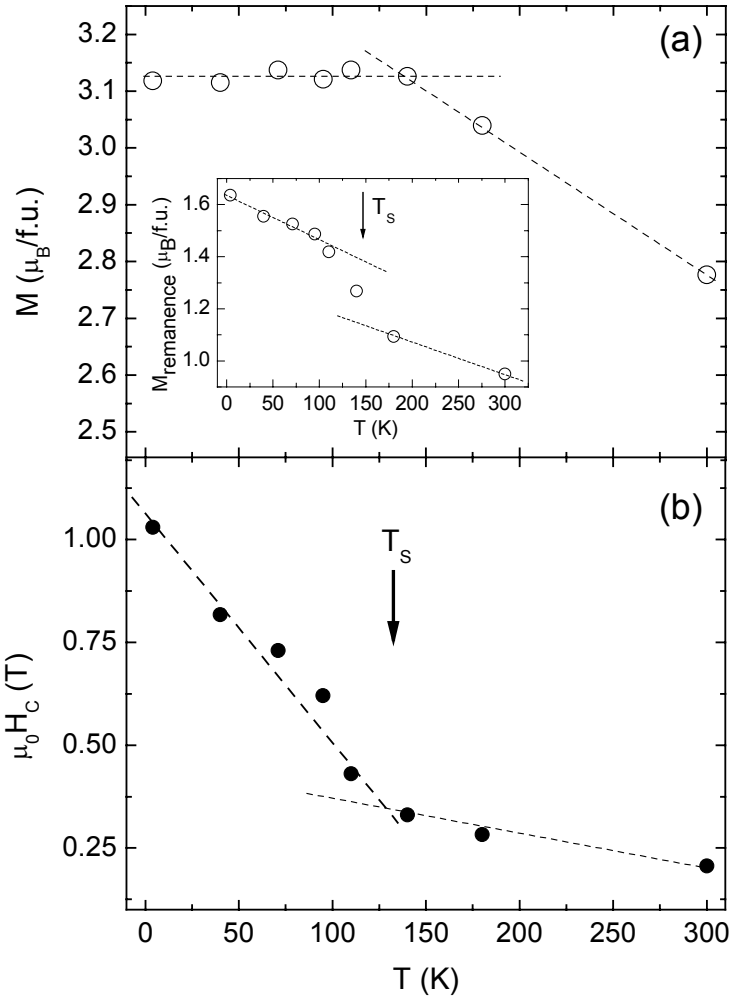

Figure 4.10. Magnetization under 30 T (a) and coercive field (b) of the Ca_2FeReO_6 sample as a function of temperature. Dashed lines are guidelines for the eye. Inset: remanence at a temperature range 4 – 300 K; dashed lines are guidelines for the eye.

the structural transition contributes to the increase of the magnetic anisotropy due to the strong magnetostructural coupling in Re based double perovskites. Concerning the remanence of Ca_2FeReO_6 a change of the linear slope is visible and the fastest change is occurring between 100 K and 175 K (see the inset in the Figure 4.10.a). A colossal magnetoresistance effect around the magnetostructural transition has been disclosed for Ca_2FeReO_6 due to the coexistence of the high-temperature and low-temperature phases [18].

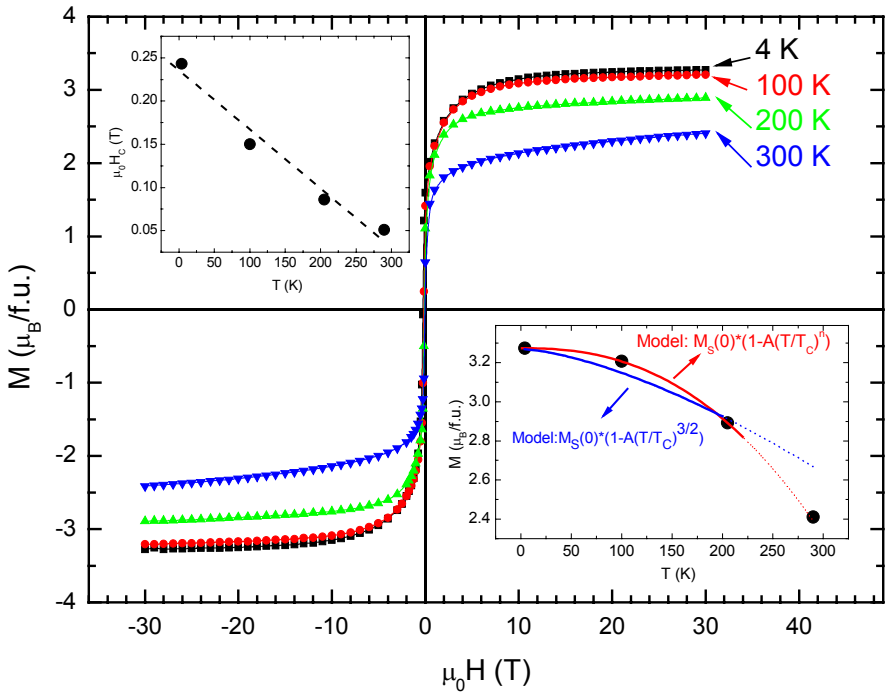

Figure 4.11. Magnetization curves at different temperatures (4, 100, 200 and 300 K) for $BaSrFeReO_6$. Upper inset: coercive field dependence on the temperature (dashed line is a visual guideline). Lower inset: the evolution of saturation magnetization with temperature (circles), the fitting with the model described in text, and the curve obtained with the $T^{3/2}$ Bloch law.

We have also measured the magnetisation loops under different temperatures for the $BaSrFeReO_6$ sample. We have investigated the temperature dependence of the magnetisation using the Bloch model. This approach was only possible for the cubic $BaSrFeReO_6$ sample due to several features exhibited by this particular compound. First of all, the magnetisation of this sample under 30 T is the closest one to the saturation magnetization while in the case of the remaining Fe-based samples (Ca_2FeReO_6 and Sr_2FeReO_6) the maximum value of magnetization obtained is still far from the saturation (see Figure 4.9 and Figure 4.11). The structural transition in the Ca_2FeReO_6 sample also influences the values of the magnetization measured making it impossible to use the Bloch model. The details on the analysis of the thermal dependence of the magnetisation of the $BaSrFeReO_6$ sample are given in the following subsection. Here, we will only comment on the other bulk magnetic properties of the

material i.e. the coercivity and the remanence. In sharp contrast to the Sr_2CrReO_6 and Ca_2FeReO_6 compounds the coercive field follows a linear dependence with the temperature (see upper inset in the Figure 4.11) and it changes from 0.05 T at 300 K to 0.24 T at 4 K. The remanence is about 50% of the saturation magnetization value and is lowering linearly with increasing temperature. Such temperature dependence could have been anticipated taking into account the absence of any structural transition in the investigated temperature range and thus a lack of important changes in the O – Fe – O – Re – O bond angles. Consequently there should be no other mechanism but the thermal assistance in magnetization reversal usual in ferromagnetic materials.

4.3.1. Spin wave model of saturation magnetization

The original $T^{3/2}$ Bloch law does not satisfactorily fit our results in contrast to the results given by Lofland et al. for the Sr_2FeMoO_6 double perovskite (see ref. [134]). On the other hand, the detailed analysis of the *Nuclear Magnetic Resonance* (NMR) data done by Zajac et al. (see ref. [40]) reveals a $T^{5/2}$ dependence of the Mo hyperfine field in this compound, as can be expected in half-metallic compounds [135]. Consequently, a model with the exponential parameter free and fixed saturation magnetization i.e. $M(T) = M(0) \cdot \left[1 - A_n \left(\frac{T}{T_C} \right)^n \right]$ was proposed [136]. Fitting leads to the value of n=2.4, which is very close to the 5/2 exponent proposed for half-metals. The fit along with the experimental data is displayed in the lower inset of figure and compared with the curve obtained from the original $T^{3/2}$ Bloch law. The Bloch exponent value (n) found is large in comparison with 1.5 for most ferromagnets. However, at low temperatures, when only the low order excitations are taken into account, the ferrimagnet spin-waves dispersion spectra is very similar to that of a perfect ferromagnet. At higher temperatures one should observe the acoustic and optical branches in the dispersion spectra for both magnetic subsites, the Fe and the Re one, separately. The unusual behaviour observed as a function of temperature could be associated with the existence of antiferromagnetic correlation due to the Fe-Re coupling.

4.4. Singular Point Detection studies

The SPD experiments have been performed using two samples belonging to the A_2FeReO_6 series ($A_2 = Ca_2$ and BaSr). Temperature range of the experiments was 80 K – 240 K and 120 K – 300 K for Ca_2FeReO_6 and $BaSrFeReO_6$ respectively. In the Figure 4.12 we present the value of the anisotropy field plotted against the reduced temperature (T/T_C). We observe a lowering of H_A on the increase of the temperature as expected. In the lowest measured temperature the value of the anisotropy field is ≈ 65 kOe and ≈ 75 kOe for $A_2 = Ca_2$ and BaSr respectively. Those values are much lower than the maximum magnetic fields we have been applying in our high static field magnetization measurements described earlier.

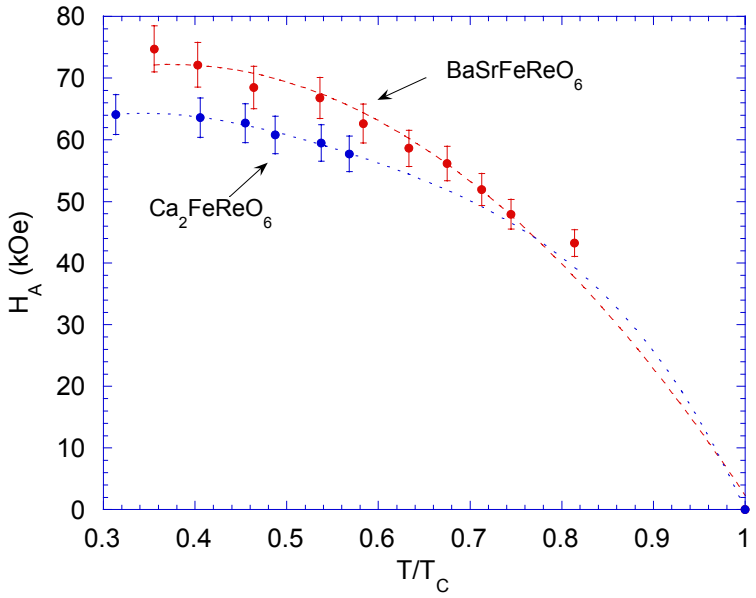

Figure 4.12. The anisotropy field dependence on the sample temperature for $BaSrFeReO_6$ and Ca_2FeReO_6 double perovkites. The temperature scale has been normalised with respect to the Curie temperature of the material.

Direct comparison between two samples presented in the Figure 4.12. would rather be impossible due to several reasons. First, the Ca_2FeReO_6 material exhibits a structural transition at temperature about 140 K, which affects not only structural parameters but also the magnetic properties as will be shown in the following

subsections. Moreover the quantitative analysis of the differences between the A_2 = BaSr and A_2 = Ca_2 samples would be possible only calculating the anisotropy energy, as they belong to different crystallographic systems (cubic and monoclinic respectively). A first consequence of the crystallographic lattice distortion, leading to the lowering of the crystal symmetry, is the appearance of the preferred magnetization orientation. On the other hand the orbital magnetic moment contribution to the magnetization changes its value on the lowering of the symmetry as shown by Sikora et al. [104]. Other important factor in the SPD measurement would be the resistivity of the material as already discussed [84]. In case of the two samples we have studied the difference in resistivity is of a factor 10^5 at low temperature, the conductance being higher for BaSr sample.

4.5. XMCD studies

We have already shown that the orbital contribution due to the strong spin-orbit coupling in the Re ion is of a great importance for the physics of the Re-based double perovskites. In the previous chapter we have discussed the magnetic dichroism studies of the Sr_2CrReO_6 under high pulsed magnetic fields. We have performed the X-ray Magnetic Circular Dichroism experiments for one member of the A_2FeReO_6 series, namely Ca_2FeReO_6 (see reference [137] for the details of the experiment and the data analysis). The data analysis was carried out focusing on two aspects. One aspect was the search for the spin and orbital contributions to the overall magnetic moment of the Re ion, and the second one was more focused on the possibility of tracking the structural transitions and their impact on the magnetism of the material studied.

The sum rule analysis of the XMCD spectra was much more complicated than in the case of Sr_2CrReO_6. Recent improvements of the ID24 beamline allowed collection of more data in order to make the statistical analysis more accurate [108]. On the one hand, this allows better estimate of the magnetic moment components. On the other hand, it requires more attention in the selection of the high quality data in order to minimize the errors. Applying the sum rules analysis for the XMCD spectra (see

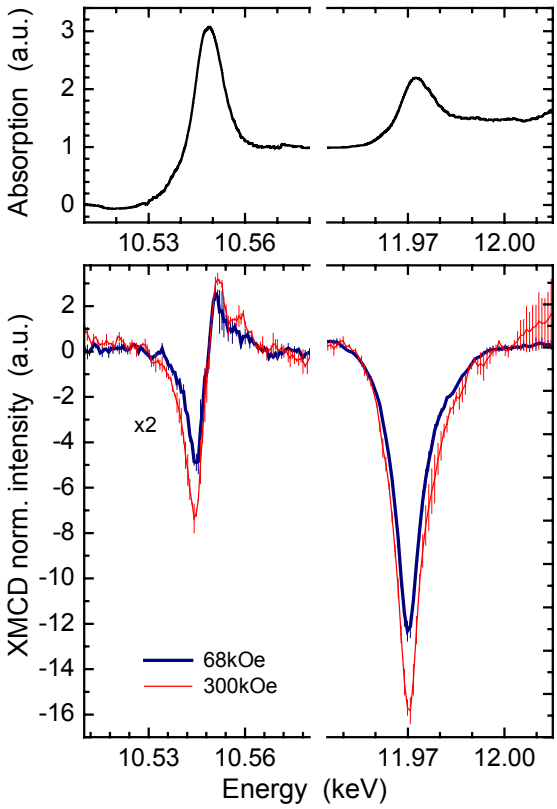

Figure 4.13. XANES and XMCD at 10 K spectra (top and bottom panel respectively) of the L_3 and L_2 Re edges in Ca_2FeReO_6. The shape of the L_3 edge spectra is strikingly different from the one obtained for the Sr_2CrReO_6.The intensity of the XMCD signal also changes with the increase of magnetic field from 7 to 30 T (blue and red curve respectively).

Figure 4.13), obtained as an average of all collected spectra (excluding one contaminated with spurious signals) the total magnetic moment carried by the Re ion, as well as the orbital to spin moment ratio were derived. For the calculations, a degree of circular polarization of 75 % for both polarization orientations was considered. For the total magnetic moment estimation the *d* holes number $n_d = 5.8$ was used, rather than 5.3 as previously reported by Majewski et al. [102]. At this point however, we will prevent ourselves from commenting on the spin and orbital contribution to the magnetic moment separately. As both quantities are proportional to the number of the *d*-holes detailed analysis would only be possible provided the reliable value of this parameter is known.

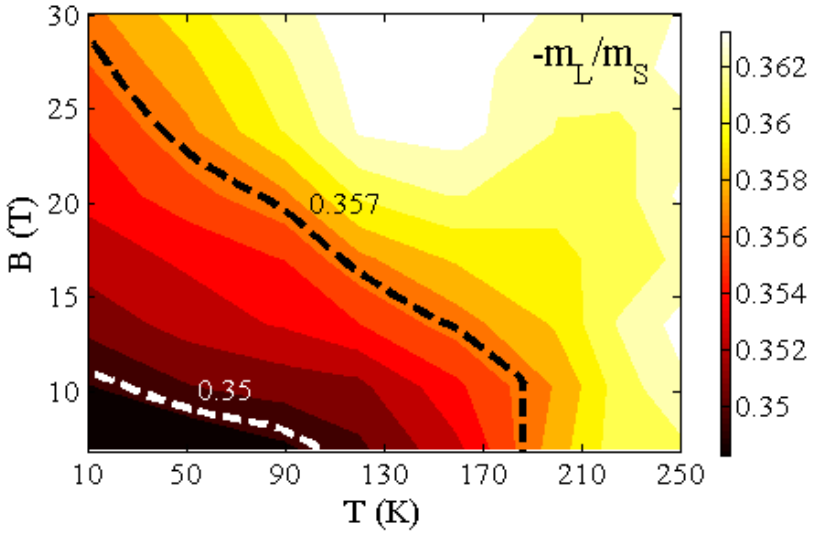

Figure 4.14. Evolution of the m_L/m_S ratio measured at 64 points of *B-T space*. The brighter colors denote higher absolute value of the orbital-to-spin moment ratio. Iso- m_L/m_S curves are presented at arbitrary values as guides for the eye. Absolute uncertainty of the single point data after a two dimensional smoothing is ~0.002. See text and ref. 137 for more details.

A sum rules analysis was performed and the temperature and field variation of the orbital-to-spin moment ratio (m_L/m_S) of rhenium moment was derived. As expected by Hund's rules, the ratio is negative. Orbital moment is not quenched, which is consistent with strong spin-orbit coupling of heavy, $Z = 75$, Rhenium ions. However the absolute value of $m_L/m_S \sim 0.36$ is significantly lower than 0.5 (1.0) expected for $Re^{5+\,(6+)}$ free atoms, which indicates that the octahedral coordination to oxygen and the crystalline field of oxygen 2*p* orbitals plays an important role as well. The results of the orbital-to-spin moment ratio determination over the entire *B-T* space studied in the experiment is presented in Figure 4.14. The smallest absolute value of $|m_L/m_S| = 0.348(10)$ is observed at $T = 10$ K and $B = 6.8$ T. This result is nearly equal to the one obtained under low static fields up to 5 T by Majewski et al. [102]. As a consequence, we assume that the results obtained under pulsed fields are correct and the drawn conclusions are beneficial for deeper understanding of the double perovskite physics. A significant field-induced evolution at low temperature is revealed, $|m_L/m_S|$ increasing to 0.357(9) at $T = 10$ K and $B = 30$ T. A rise with temperature is observed

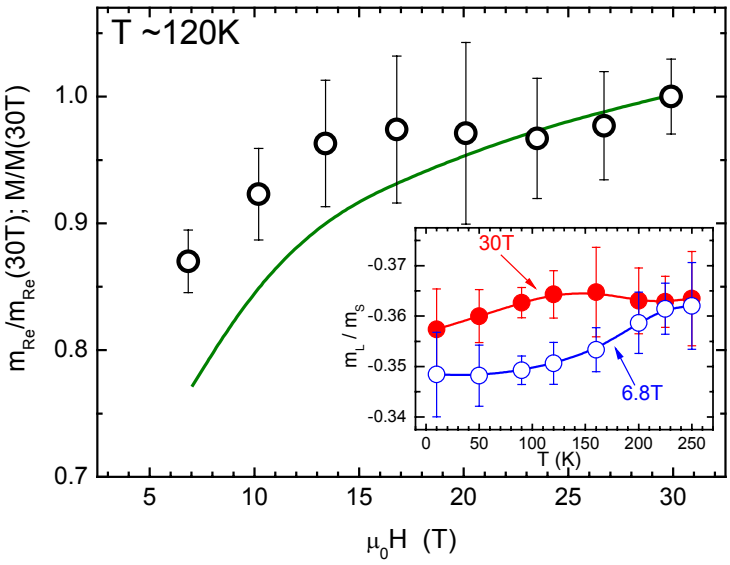

Figure 4.15. Magnetic moment of Rhenium plotted against the applied magnetic field (open circles) along with static field bulk magnetization measurement under 30 T (solid line) normalized at 30 T for Ca_2FeReO_6. In the inset the ratio of the orbital and spin magnetic moments of Re under applied fields of 6.8 and 30 T is plotted against the temperature.

in the entire field range, showing a 'saturation' at the value of $|m_L/m_S| \approx 0.362(6)$ at $T = 250$K. It is clear that in the temperature range well above the phase transition, i.e. $T > 200$K, the m_L/m_S value is almost independent in the probing field range. This indicates that the method used is sensitive enough to trace the structural transitions influence on the local magnetic moments arrangement.

The field dependence of the bulk magnetization (solid line in the main panel of the Figure 4.15) shows no saturation as previously reported. The Rhenium magnetisation, on the contrary, seems to saturate at about 15 – 20 T what is more evident close to the transition temperature T ~ 120 K. This result can be naturally explained assuming a larger magnetization of the Re sublattice in the insulating phase than in the metallic one, and taking into account that the bulk magnetization is determined by the difference between the Fe and Re sublattice magnetization. As the Fe magnetization has spin origin, it is not expected to change significantly across T_S. [17] Therefore, the bulk magnetization is expected to decrease below T_S due to the

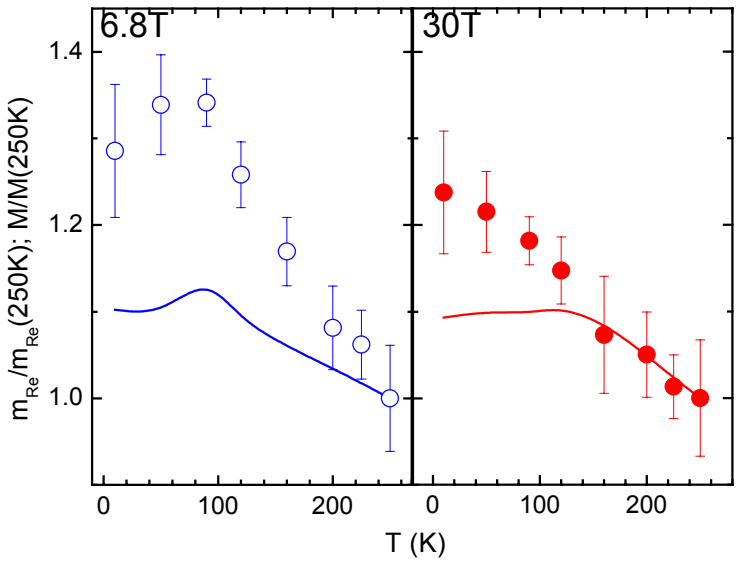

Figure 4.16. Magnetic moment of Rhenium (circles) under applied fields of 6.8 and 30 T together with the bulk magnetization at the same fields (solid line) plotted versus temperature and normalized at 250 K.

larger magnetization of the Re sublattice in the insulating phase, which is antiparallel to the Fe one. Upon application of magnetic field at or below T_S, first, the magnetic alignment is favored and an increase of bulk and Re magnetization are expected. However, simultaneously, the high-temperature metallic phase is favored, which has smaller (larger) Re (bulk) magnetization. The overall effect is the tendency of the Re sublattice magnetization to a constant value at high fields at 120 K where the effect of the magnetic field on the phase coexistence is the strongest as also shown in the magnetoresistance measurements [18] (as can be observed in the Figure 4.15).

In Figure 4.16 comparison of the bulk magnetization of the material and the evolution of the magnetic moment calculated from XMCD as a function temperature is shown for 6.8 and 30 T. These show a nice agreement at higher temperatures only. Below T_S a considerable excess of 10-15% in the normalized Re magnetization is observed with respect to the bulk one. Under low field the structural transition is reflected in both, Rhenium magnetic moment and bulk magnetization at about 100 K. On the contrary, under 30 T, the bulk magnetization is constant below 130 K (see

Figure 4.10 for details) meanwhile the Re magnetic moment follows a linear growth down to the lowest temperature (10 K). This further reinforces the hypothesis of higher Re sublattice magnetization in the insulating phase compared to the metallic one. Thus, we put forward that the decrease of the relative Re to bulk magnetization upon transition from insulating to metallic phase can be explained by the change in the Re t_{2g} electronic levels and consequently in the Re sublattice magnetization. At this moment, we cannot discard that the canting of the Fe magnetic moments in the insulating phase could also play a role, however further study on the local magnetism of Fe would be certainly needed in order to give strong conclusions. Both phenomena will affect the hopping integral of the double-exchange-like interaction and thus will have strong impact on the electronic properties of the compound studied.

Chapter 5

Lanthanide doping of Sr_2CrReO_6: in the search for high Curie temperature by electron doping

The electron doping achieved via a partial substitution of a divalent ion with a trivalent one is claimed to be the way to enhance the temperature of magnetic ordering in FeMo-based compounds, as already discussed in the first chapter. In order to study the influence of the electron doping on the Sr_2CrReO_6 double perovskite we have synthesized three series of samples where the divalent Sr ions are partially replaced by La^{3+}, Nd^{3+} and Sm^{3+}. The nominal stoichiometry of the samples is $Sr_{2-x}Ln_xCrReO_6$ (Ln = La, Nd and Sm). The degree of substitution was 10%, 20%, 30% and 50% (x = 0.1, 0.2, 0.3 and 0.5). We have also tried the 70% doping (x = 0.7) but the samples with such high doping certainly were not of good quality. However, even in the case of this low doping level, the single double perovskite phase is difficult to obtain because the desired phase occurs only within a narrow range of synthesis conditions and, often, additional phases come up. The use of three kinds of doping cations will allow us to separate the steric effects from the electric ones. Steric effects appear due to the smaller ionic radius of Nd^{3+} (1.27 Å), La^{3+} (1.363 Å) and Sm^{3+} (1.24 Å) with respect to Sr^{2+} (1.44 Å). On the other hand the trivalent nature of the doping cation will increase the electron population at the Fermi level, which could be important in CrRe compounds but never studied until now. From the point of view of magnetic properties both kinds of effect cannot be treated separately. As we have already seen in the previous chapters the strength of magnetic interactions depends on the distance between *B* and *B'* ions (Cr and Re in the current case) and the angle of the *B* – O – *B'* bonds. Such bond angles are equal to 180° in a perfect cubic structure only.

Let us recall the equation 1.34 that allows calculating the tolerance factor for the double perovskite compounds. The *t* value permits to predict the crystallographic structure provided the ionic radii of ions in the structure are known. In our case we shall need to calculate the mean ionic radius at the *A* site at first. It is related to the Ln ion and the doping level by the following equation:

$$\langle r_A \rangle = \frac{(2-x)\cdot r_{Sr^{2+}} + x \cdot r_{Ln^{3+}}}{2} \qquad (5.1)$$

where x is the doping level and *r* is the ionic radii at appropriate coordination and oxidation state. In fact this parameter alone can be used in order to systematize the study of the doping impact on physical properties. Having done such calculations, we may calculate the tolerance factor. Both quantities ($\langle r_A \rangle$ and *t*) are displayed in the Table 5.1. The latter is changing from 1.005 for the parent Sr_2CrReO_6 ($\langle r_A \rangle = 1.44$ Å) down to 0.987 ($\langle r_A \rangle = 1.39$ Å) for Sm doped sample with the nominal doping level x = 0.5. Both values are within the limits assuming the cubic structure to be most probable, the lower is however close to the tetragonal limit (0.97).

We have already raised some doubts about the real stoichiometry of the doped Sr_2CrReO_6. In this chapter, we will try to present enough information to either prove that electron doping is taking place in the system or demonstrate that it is not present. Various experimental techniques will be used ranging from scanning electron microscopy (SEM) together with energy dispersive spectroscopy (EDS) through neutron powder diffraction (NPD), x-ray absorption (XANES and EXAFS) to transport and magnetometry (SQUID and VSM) measurements. Until final conclusions will be drawn we will avoid using other sample labeling than nominal stoichiometry (e.g. sample with nominal stoichiometry $Sr_{1.5}La_{0.5}CrReO_6$ will be labeled as La x = 0.5).

Table 5.1. Mean ionic radius at the *A* crystallographic site $\langle r_A \rangle$ and theoretical tolerance factor *t* dependence on doping level and kind of dopant calculated as described in the text.

Doped elements (and doping level)	$\langle r_A \rangle$ (Å)	t
Sm (x = 0.5)	1.3900	0.987
Nd (x = 0.5)	1.3975	0.990
Sm (x = 0.3)	1.4100	0.995
Nd (x = 0.3)	1.4145	0.996
Sm (x = 0.2)	1.4200	0.998
La (x = 0.5)	1.4208	0.998
Nd (x = 0.2)	1.4230	0.999
La (x = 0.3)	1.4285	1.001
Sm (x = 0.1)	1.4300	1.002
Nd (x = 0.1)	1.4315	1.002
La (x = 0.2)	1.4323	1.003
La (x = 0.1)	1.4362	1.004
x = 0	1.4400	1.005

5.1. Microstructure and chemical composition

SEM imaging was performed in order to check the microstructure and chemical composition homogeneity of the samples. Prior to the insertion of the specimen into the measurement chamber it was covered by a Carbon layer (about 15 nm thick) in order to prevent undesired charging of the sample surface. As introduced in the second chapter of this thesis, we have performed our measurements in two laboratories. In both microscopes the accelerating voltage used was 20 keV.

In the Figure 5.1 we show a result of a simulation of the electrons trajectories while propagating through a Nd x = 0.1 sample. We have used the Casino program based on the Monte Carlo algorithm [138]. With the 20 keV accelerating voltage and a spot of an electron beam of 10 nm we see that the penetration depth is about 2.5 μm. The backscattered electrons are generated up to the depth of 10 μm. Considering a

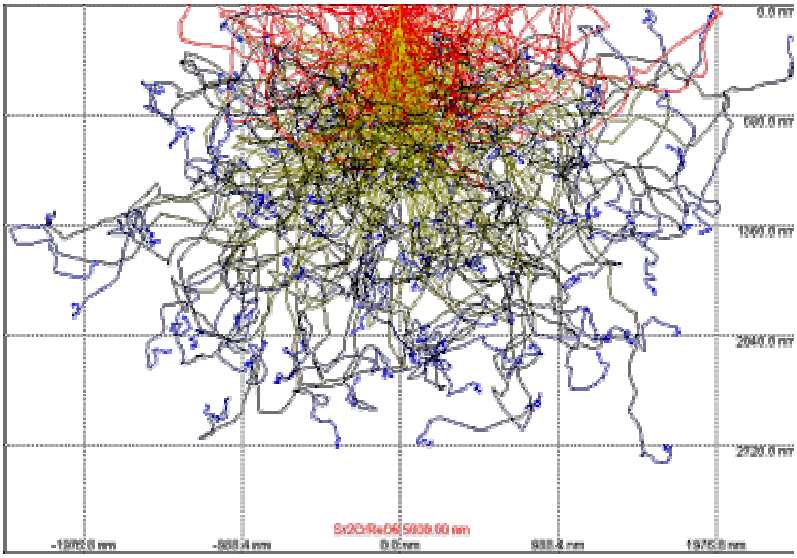

Figure 5.1. Monte Carlo simulation of the trajectories of the electrons from the electron gun propagating through Sr_2CrReO_6 sample with 10% (x = 0.1) Nd doping for 20 keV beam energy and 10 nm spot. Red lines show the paths of the backscattered electrons, yellow to blue are the electrons that are absorbed in the specimen and the colour means the lowering of the energy (yellow means higher while dark blue goes to zero energy).

spatial resolution of the backscattered electrons we see that these are leaving a sample with a distribution having width of 2 μm (for a simulated 10 nm beam spot). The x-rays generation is taking place in a sample volume reaching 2.5 μm. The depth from which the information on the chemical composition is collected is strongly dependent on the element and the characteristic x-rays energy (see Table 5.2) due to the mass absorption coefficients. A maximum of the x-ray signal for the less absorbed line is usually equivalent to the radiation generated between 0.3 and 1 μm depth.

The SEM images taken with secondary electrons (mainly probing the topography and microstructure) show that the samples are composed of close packed grains, with sizes ranging from a few microns to ~50 μm (see Figure 5.2 and Figure 5.3). The size of the well distinguishable grains is getting lower as the doping level increases. Together with the disappearance of big grains the material becomes more uniform in grain size, however the intergrain regions become more important in the overall volume.

Table 5.2. Energies of the characteristic x-rays for emission lines used in the EDX experiments to inspect the composition of the doped double perovskite samples.

Element	Line	Energy (eV)
O	$K\alpha_1$	524.9
Cr	$K\alpha_1$	5414.72
Re	$L\alpha_1$	8652.5
Sr	$K\alpha_1$	14165
Nd	$L\alpha_1$	5230.4

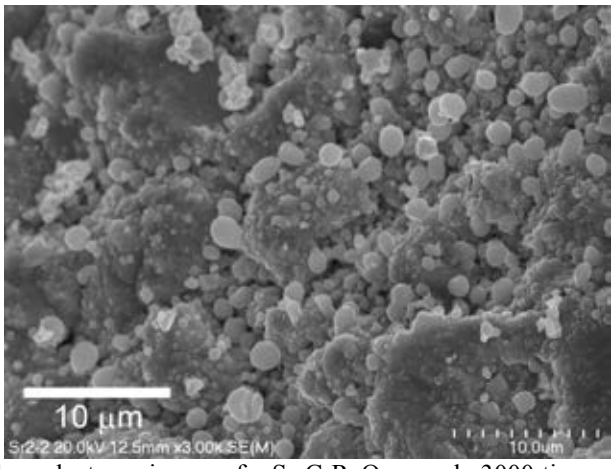

Figure 5.2. Secondary electrons image of a Sr_2CrReO_6 sample 3000 times enlarged. The scale bar corresponds to 10 µm.

The secondary electron imaging allowed us to discard the Sm doped samples from the first batch as we observed completely different microstructure from the one presented in these images. This clearly indicated the need of a modification of synthesis conditions for doped samples. SEM images gave also a first indication that the doping levels above 0.5 not only disturb the double perovskite structure, but also completely change the microstructure and the way the initial oxides form the new material during the synthesis.

The images taken with backscattered electrons, which tend to portray the chemical information, indicate that the chemical composition is quite homogeneous

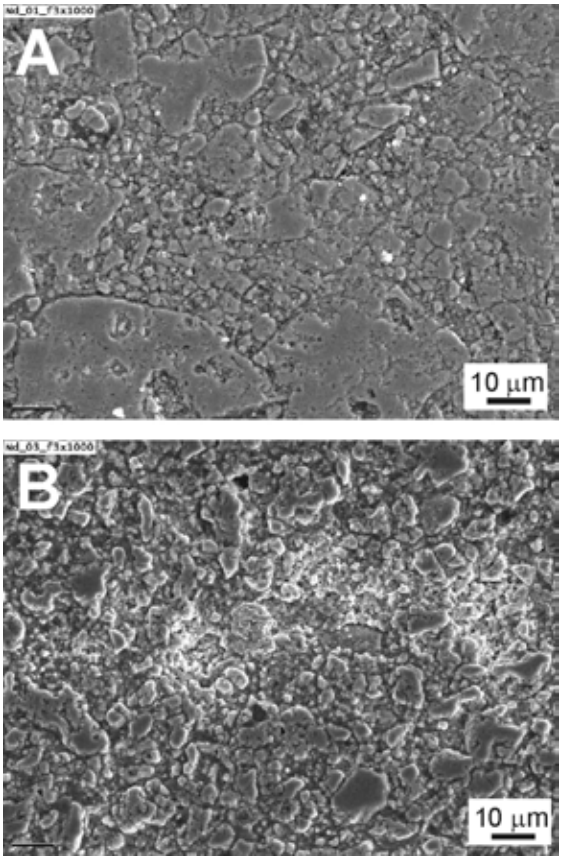

Figure 5.3 Secondary electrons images of a $Sr_{1.9}Nd_{0.1}CrReO_6$ (a) and $Sr_{1.7}Nd_{0.3}CrReO_6$ (b) samples 1000 times enlarged. The scale bar corresponds to 10 μm. A difference of the grains sizes in both samples is clearly visible.

across the entire sample (see Figure 5.4), although slight differences in content are visible in the intergrain regions. The latter ones are presented in the Figure 5.5. For a bulk polycrystalline material with microstructure showing large amount of grains the chemical analysis by means of EDX spectroscopy with SEM microscope has to be treated with care. First the light elements are poorly detectable with this method. Moreover the geometry of the measurement is affected by the sample surface imperfections among the intergrain regions, which can be treated as valleys between the grains. At such points the emission of both X-rays and backscattered electrons takes place uniformly in space and not all the signal is collected by the detector. In addition, considering a spatial resolution, the information on the material composition is averaged over the grains and the intergrain region itself.

Graphs presented in the Figure 5.5 show the characteristic X-rays signal intensity as a function of the electron beam position over a 5 μm line scan. The line scan was taken in the area containing the big grain, the area between the grains and the smaller grain (looking from the bottom left part of the line). The main feature, which is visible in all samples, is the decrease in Oxygen content in the area between the grains. The same behaviour, in some smaller scale, is also present in case of the other elements. The content of all elements present in the material seems to be constant throughout the grain, and also is of the same magnitude in the neighbouring grains. Only in the case of Oxygen one can see that its content rises as reaching the grain boundary (of the order of one half of the signal measured far from the boundary). In case of Strontium we observe very weak signal compared to other elements as the $K\alpha_1$ line is strongly absorbed.

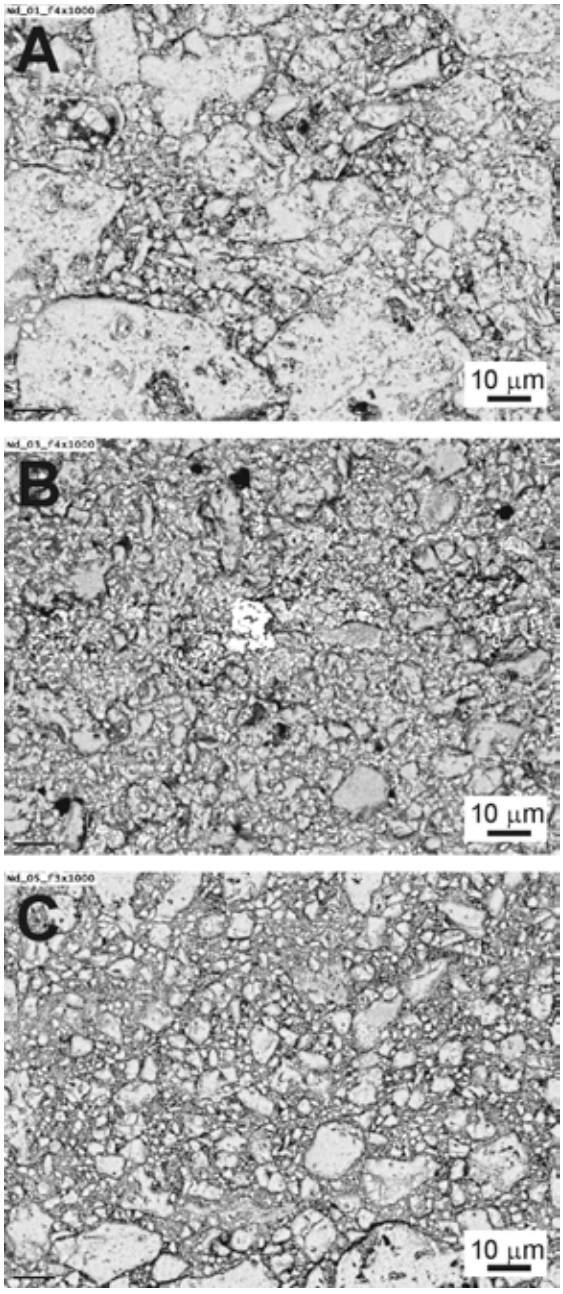

Figure 5.4. Backscattered electrons images of a $Sr_{1.9}Nd_{0.1}CrReO_6$ (A), $Sr_{1.7}Nd_{0.3}CrReO_6$ (B) and $Sr_{1.5}Nd_{0.5}CrReO_6$ (C) samples 1000 times enlarged. The scale bar corresponds to 10 μm. A difference of the grains sizes and the size variation within the sample is clearly visible. Apart of the metallic Re impurity in the $Sr_{1.7}Nd_{0.3}CrReO_6$ (white grain in the middle of the B image) all the samples exhibit good homogeneity.

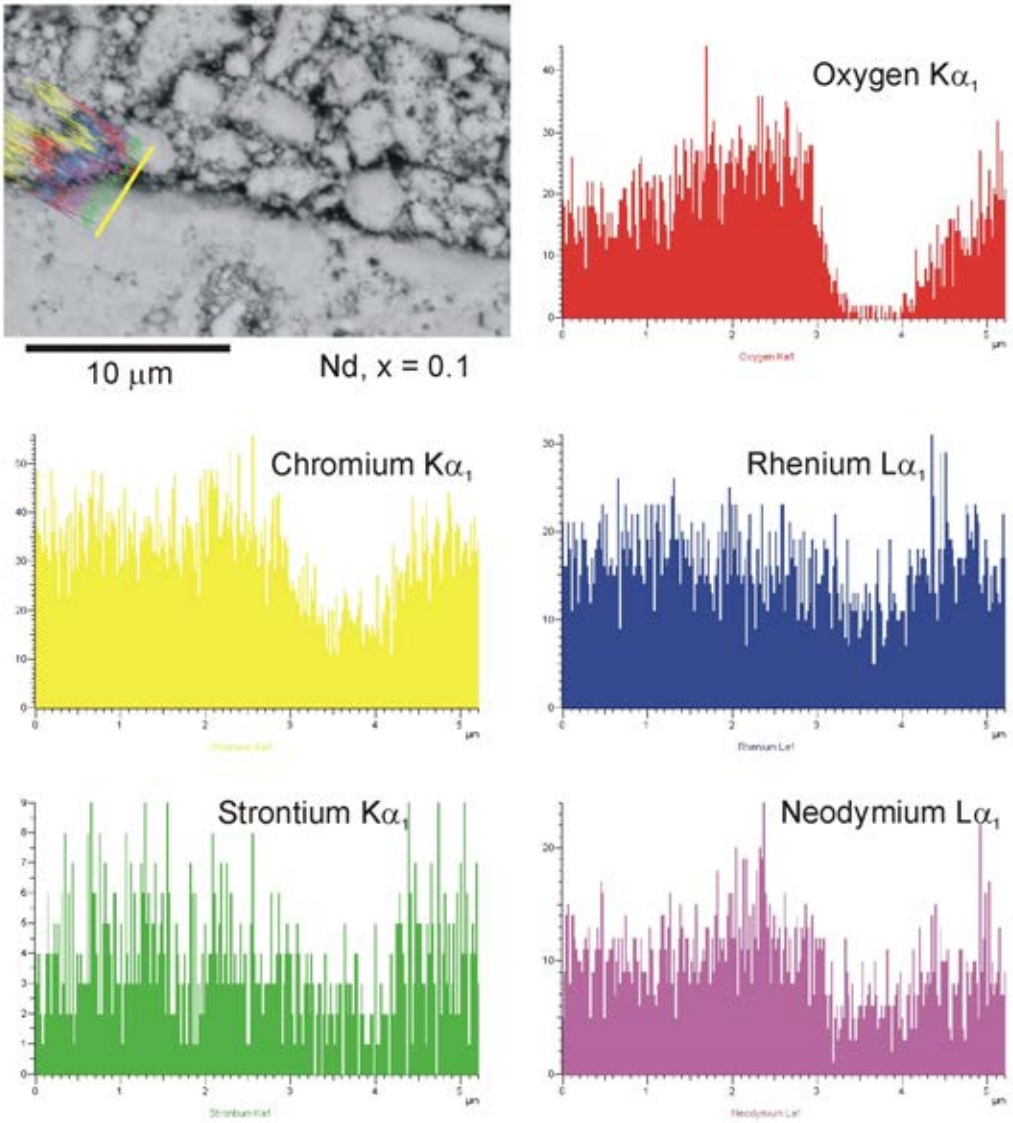

Figure 5.5 The backscattered electrons image at x5000 magnification. Line scan was taken at a region indicated by the yellow line. On the right the content of the elements (Oxygen, Chromium, Strontium, Lanthanum and Neodymium).

Similar analysis to the described above can be performed over a larger area of the sample. In such way averaged information of the content of the elements in the material is obtained. In the Figure 5.6 we present the EDX spectra for the parent Sr_2CrReO_6 compound. Two low-energy, not labeled peaks are due to Carbon coating

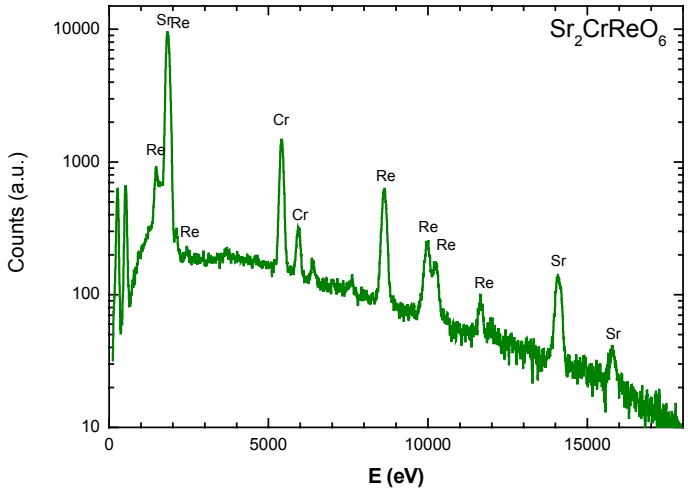

Figure 5.6. EDX spectra of the Sr_2CrReO_6 sample in logarithmic scale. The analysis of the peak intensities allows the estimate of the chemical composition.

and Oxygen. The rest of the lines represent characteristic x-ray radiation of the sample elements. The analysis of the relative intensities of the signal for different energies permits to conclude that the sample stoichiometry is in agreement with the expected one. More complex spectra are observed for doped samples. In the Figure 5.7 we present the data for the samples with theoretical formula $Sr_{1.8}Nd_{0.2}CrReO_6$ (left) and $Sr_{1.7}La_{0.3}CrReO_6$ (right). This time the quantification of the signal does not lead to an ordered double perovskite. The main difference is present in the Cr/Re ions ratio. Theoretically it should have a value of 1:1. As a result of the EDX analysis for all the samples from La and Nd doped series we can conclude that the out-of-stoichiometric Cr/Re ratio is getting bigger the larger the doping level is. It is clear that the nonstoichiometry of the doped samples requires further analysis.

Compared to EDX the fluorescence measurements are more precise. In the we present the results of the fluorescence measurements for the undoped sample together with the Sm x = 0.3 and Sm x = 0.5 samples. The results are in agreement with the EDX ones. We can see that the amount of doped Sm ions is close to the expected value. Moreover, the sum of Sr and Sm ions is nearly equal 2 as required. Then the Cr/Re ratio again deviates from 1 and a clear excess of Cr ions is detected.

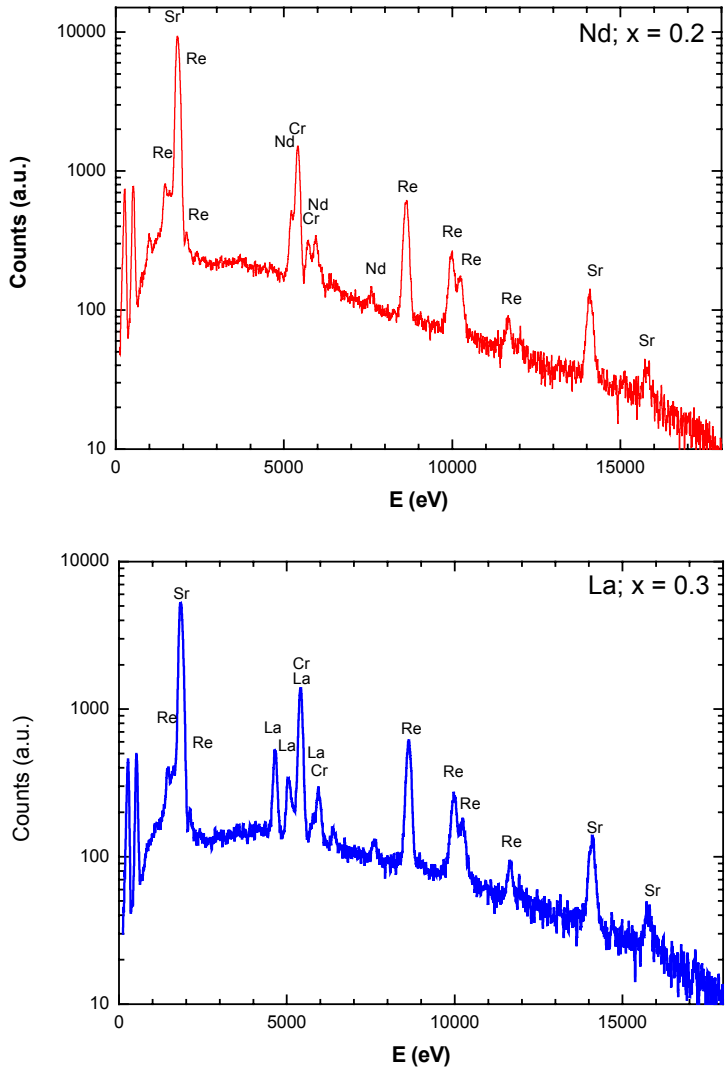

Figure 5.7. EDX spectra of the $Sr_{1.8}Nd_{0.2}CrReO_6$, and $Sr_{1.7}La_{0.3}CrReO_6$ (as indicated in the figure) sample in logarithmic scale. The analysis of the peak intensities allows the estimate of the chemical composition. In both spectra the difference of the position of the peaks coming from La and Nd in the energy scale are clearly visible.

Both fluorescence and EDX measurements seem to confirm that the doubts about the presence of electron doping are justified.

Table 5.3. Weight percentage of the ions forming the double perovskite samples for undoped and two Sm doped samples (x = 0.1 and 0.3). In last column the calculated chemical formula considering measured amounts of Sr, Sm, Cr and Re ions is presented. Oxygen stoichiometry is not refined.

	Sr Weight %	Sm Weight %	Cr Weight %	Re Weight %	Calculated formula
Undoped	38.09	-	11.88	39.09	$Sr_2Re_{0.96}Cr_{1.03}O_x$
Sm (x = 0.3)	32.00	10.35	12.65	35.01	$Sr_{1.7}Sm_{0.32}Re_{0.86}Cr_{1.11}O_x$
Sm (x = 0.5)	28.30	19.54	16.40	27.29	$Sr_{1.5}Sm_{0.6}Re_{0.68}Cr_{1.46}O_x$

5.1.1. Sources of nonstoichiometry

According to synthesis conditions (a slight excess of Chromium needed to stabilize the double perovskite phase as explained in chapter 2) a value slightly bigger than 1 for the Cr/Re ratio is possible. On the other hand Chromium is easily evaporated on heating the material during the synthesis process.

A lack of electron doping and forming of the structure that does not posses a perfect double perovskite ordering in this system can be explained on the basis of the strong stability of the electronic $Cr^{3+} – O – Re^{5+}$ state. In this case it will be necessary to prove that neither $Cr^{2+} – O – Re^{5+}$ nor $Cr^{3+} – O – Re^{4+}$ configuration is preferred while the Ln cations are introduced to the system. Such study is possible on the basis of the XANES analysis and will be presented in one of the following subsections. In the following we will focus on the crystallographic structure of the doped series studied by means of neutron powder diffraction results.

5.2. Modified double perovskite structure shown by neutron diffraction patterns analysis

The advantage of neutron diffraction with respect to x-ray diffraction in the case of the study of the double perovskites arises from the sensitivity of the former to the

light atoms. In our case oxygen atoms are much better "visible" with neutrons than with x-rays. The importance of the accurate estimation of oxygen atoms positions in the crystallographic cell becomes clear when we recall that the space group changes due to the change in size and geometry of the oxygen octahedra. We will divide our results in two parts. First we will focus on the high temperature neutron powder diffraction data, then we will describe the temperature evolution of the structural and magnetic properties. By "high temperature", we mean temperature high enough for the sample to be in cubic crystallographic structure and no magnetic contribution to the spectra. The latter is more easy to obtain because as will be shown later a structural transition takes place at very high temperatures in some cases, the samples thus approaching the temperatures at which they are synthesized.

5.2.1. Models proposed

Our first approach in the analysis of the diffraction patterns was to use a double perovskite structure with the antisite defects as an input of the Rietveld refinement procedure. Hereafter, we will call this an electron doping (e-doping) model. In this model we have at low temperatures the tetragonal crystal cell with *I 4/m* space group while at high temperatures the structure is cubic. In Table 5.4 we present the Wyckoff positions of the atoms in the tetragonal structure. In order to fulfill the requirements of the oxygen octahedra to tilt, the *x* and *y* coordinates of the oxygen atoms lying in plane are free to move. The apical oxygen atom can be moved along the *z*-axis freely so that the octahedra size can be changed. The occupations of the crystallographic sites are chosen in the way that, according to multiplicity of the site, the chemical formula is being preserved. As at the Cr and Re sites the antisite defects are present, the occupation is calculated for a sum of *B* at their ideal positions and [*B'*] antisites at *B* sites. In the case of electron doping model the Cr/Re ratio is kept to be equal 1. Concerning the magnetic moments at Re and Cr ions we use the magnetic form factor of Mo^{5+} and Cr^{3+} respectively. The reason for using the Molybdenum instead of Rhenium is that the form factor for the latter is not pre-defined in FullProf software. Moreover, it is impossible in neutron diffraction to distinguish the orbital part of the Re-moment without having a reliable magnetic form factor. In Table 5.6 we present a

set of crystallographic parameters for the refinements in cubic structure. The main difference is that only the displacements of the planar oxygen are allowed. This allows slight distortions of the octahedra, which are precursor of the tetragonal structure occurring at lower temperature. As it was in tetragonal structure case, the occupations of the *B* and *B'* are refined keeping fixed to one the Cr to Re ratio.

Table 5.4. Rietveld refinement input parameters (Wyckoff positions with multiplicity, site occupation for given stoichiometry and refinable parameters) for the tetragonal crystallographic system.

Atom	Site	Mult.	Free param.	Occupation	
				e-doping	no doping
O	e	4	z	0.25	0.25
O	h	8	x, y	0.5	0.5
Cr/[Re]	b	2	Occ.	$0.125, \frac{\sum \mathrm{Cr}}{\sum \mathrm{Re}} = 1$	$0.125, \frac{\sum \mathrm{Cr}}{\sum \mathrm{Re}} = \frac{1+\frac{x}{2}}{1-\frac{x}{2}}$
Re/[Cr]	a	2	Occ.		
Sr Ln	g	8	---	$\sum = 0.25$	$\sum = 0.25$

Table 5.5. Rietveld refinement input parameters (Wyckoff positions with multiplicity, site occupation for given stoichiometry and refinable parameters) for the cubic crystallographic system.

Atom	Site	Mult.	Free param.	Occupation	
				e-doping	no doping
O	e	24	x	0.125	0.125
Cr/[Re]	a	4	Occ.	$0.0208, \frac{\sum \mathrm{Cr}}{\sum \mathrm{Re}} = 1$	$0.0208, \frac{\sum \mathrm{Cr}}{\sum \mathrm{Re}} = \frac{1+\frac{x}{2}}{1-\frac{x}{2}}$
Re/[Cr]	b	4	Occ.		
Sr Ln	c	8	---	$\sum = 0.04\ 16$	$\sum = 0.04\ 16$

The model described above works fine for the refinement of neutron diffraction patterns of the doped double perovskites with low and moderate doping levels. When high doping level is reached i.e. x = 0.5 the fit is not reaching convergence anymore.

At this point, we have thought about improving the model. With the support of the EDX and fluorescence results, we put forward a modified model assuming the Cr to Re ratio to be dependent on doping. This model will be called hereafter a no-doping model. Concerning the Rietveld refinements, in the crystallographic part there is no difference with respect to the e-doping model both in tetragonal and cubic crystallographic systems. A total amount of Cr and Re ions in the structure is fixed to be $1+\frac{x}{2}$ and $1-\frac{x}{2}$ respectively where x is the doping level (e.g. for doping level x = 0.5 we would obtain the chemical composition $Sr_{1.5}Ln_{0.5}Cr_{1.25}Re_{0.75}O_6$). In this model the antisite defect cannot longer be defined as in the first chapter. We still include the misplaced ions in both models. A comment on the meaning of the antisite defects in the case of the no-doping model will be made later on, after the results of fitting the experimental data are presented.

For the sake of completeness we have to comment on the Debye-Waller (DW) factors refined in the fit. In the tetragonal structure both apical and in-plane oxygen atoms have the same value of this parameter changing simultaneously for both. In the cubic structure due to the symmetry operators there is only one Oxygen atom. The Cr and Re atoms (including *AS*) are also refined together so we have four ions having the same value of Debye-Waller factor. Finally, Sr and Ln ions are paired in terms of DW parameter as they occupy the same place.

5.2.2. High temperature regime: crystallographic structure obtained

In order to obtain reliable crystallographic structure of the doped samples (Ln = La and Nd) we have refined the diffraction data obtained at 710 K (Nd) and 913 K (La). Diffraction patterns are presented in the Figure 5.8 for the two series. Nd

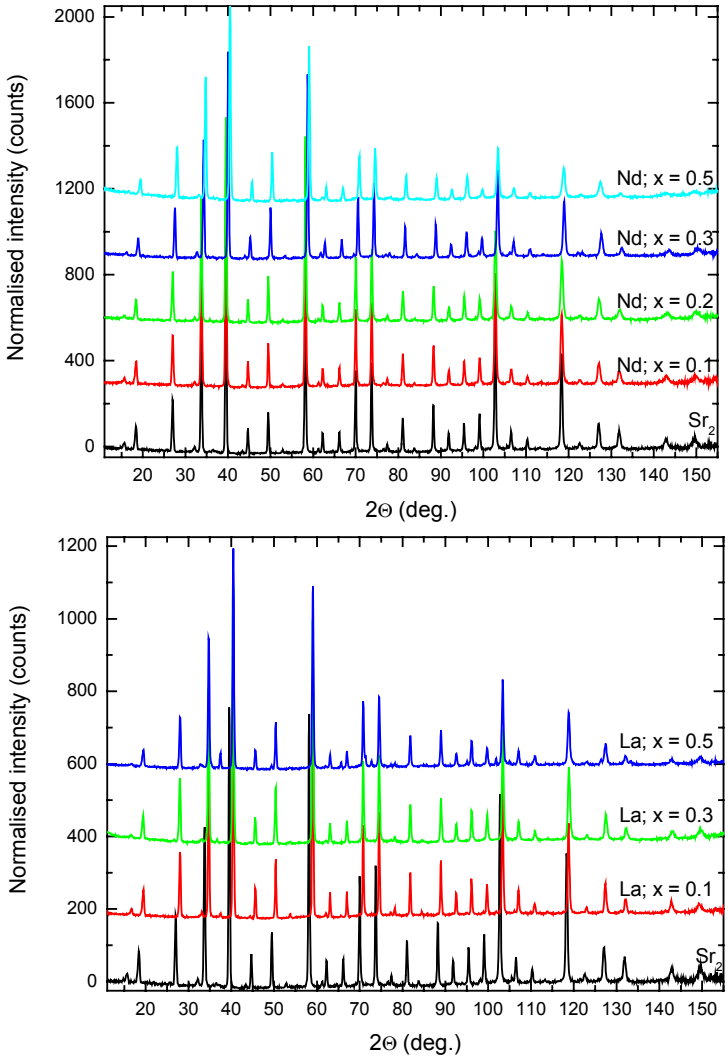

Figure 5.8. Neutron powder diffraction spectra for the Nd (measured under 710 K for x = 0.1, 0.2, 720 K for x = 0.3 and 1150 K for x = 0.5) and for the La (under 913 K for x = 0.1 and 0.5 and 973 K for x = 0.3) doped series. The undoped sample spectrum was obtained under 710 K. On higher doping levels peaks become broader, showing poorer crystallinity. The relative change of intensity of the diffraction peaks is due to the change of the Cr/Re ordering.

doped series consists of four samples with nominal doping of 0.1, 0.2, 0.3 and 0.5 while in the case of the La doping x is equal to 0.1, 0.3 and 0.5.

The electron doping model fits have been successful for all samples through all the doping levels. Only in the case of La x = 0.5 the introduction of the metallic Re

impurity was needed in order to improve the quality of the fit. Although the quality-of-the-fit parameters are reasonable in all cases we observe the R_{Bragg} to increase its value while the doping level raises. Using the electron doping model as an input we find the cubic structure for the doping level smaller than 0.5 for both Nd and La doping. At x = 0.5 the cubic structure is not reached even at the highest temperature measured. The detailed information on the crystallographic parameters obtained at high temperature is presented in Table 5.6 and Table 5.7 for La and Nd doping respectively.

Concerning the no-doping model, as can be seen in the abovementioned tables, the crystallographic parameters are only slightly changed with respect to the e-doping model. This refers not only to the structure and space group but also to unit cell dimensions, bond angles and lengths. The occupancy of the Cr and Re sites is, of course, different, which is the requirement of the model. Testing the quality of the fit we observe that the Bragg contribution to χ^2 is significantly lower for the doped samples assuming a lack of electron doping over whole series (except for Nd. x = 0.3 sample for which the opposite is true). Moreover the difference is more important at high doping levels indicating a correlation of some model parameters with x. The parameters that are directly connected to the doping level are the Cr and Re contents. This fact allows us to suggest the no-doping model to interpret better the results.

We have to comment now on the distribution of the Cr and Re ions in the case of the no-doping model, and the structural defects. For $\mathrm{Cr/Re} = 1$ and perfect ordering we have fully populated *B* and *B'* sublattices, each with only one kind of a cation. When the antisite defects appear the occupation of both sublattices remains 100%, but each misplaced Cr ion results in one Re cation at a wrong position. When the stoichiometry deviates from an ordered double perovskite one ($\mathrm{Cr/Re} \neq 1$) we have to place $1+\frac{x}{2}$ Cr and $1-\frac{x}{2}$ Re ions in the system. This can be accomplished in two ways. First we can have the Cr (*B*) lattice populated with $1+\frac{x}{2}$ ions resulting in

Table 5.6. Data on significant parameters (lattice constants, crystallographic site occupancies, bond angles and lengths as well as fit quality parameters) obtained from the Rietveld refinement of the neutron diffraction spectra for the Lanthanum doped samples with nominal stoichiometries: $Sr_{1.9}La_{0.1}CrReO_6$, $Sr_{1.7}La_{0.3}CrReO_6$ and $Sr_{1.5}La_{0.5}CrReO_6$. For each sample two columns of the data are displayed corresponding to the two models described in the text (electron doping and no doping). Although the lattice parameters remain almost unchanged the occupancies do change their value leading to better fit quality in case of "no-doping" model (see text for details).

	$Sr_{1.9}La_{0.1}CrReO_6$		$Sr_{1.7}La_{0.3}CrReO_6$		$Sr_{1.5}La_{0.5}CrReO_6$	
	e-doping	no-doping	e-doping	no-doping	e-doping	no-doping
a (Å)	7.8739(12)	7.8739(12)	7.8670(11)	7.8671(11)	5.5643(3)	5.5640(3)
c (Å)	-	-	-	-	7.8698(11)	7.8711(9)
Vol ($Å^3$)	488.16(14)	488.17(14)	486.88(16)	486.91(13)	243.67(4)	243.67(3)
B (Cr/Re)	81/19	83/17	74/26	82/18	71/29	81/19
B' (Re/Cr)	81/19	78/22	74/26	67/33	71/29	56/44
B-O_1(Å)	1.9791(26)	1.9790(26)	1.9691(36)	1.9697(50)	2.0032(2)	2.0036(3)
B-O_2(Å)	-	-	-	-	1.971(6)	1.9677(3)
B'-O_1(Å)	1.9578(26)	1.9579(26)	1.9644(36)	1.9639(50)	1.9315(3)	1.9319(3)
B'-O_2(Å)	-	-	-	-	1.964(6)	1.9673(82)
B-O_1-*B'*(º)	180.0(1)	180.0(1)	180.0(1)	180.0(2)	180.00(13)	180.00(3)
B-O_2-*B'*(º)	-	-	-	-	177.9(3)	177.89(33)
R_{wp}	4.79	4.80	9.72	5.15	4.88	4.23
R_{Bragg}	3.65	3.45	6.77	5.78	7.11	3.73

Table 5.7 Data on significant parameters (lattice constants, crystallographic site occupancies, bond angles and lengths as well as fit quality parameters) obtained from the Rietveld refinement of the neutron diffraction spectra for the Neodymium doped samples with nominal stoichiometries: $Sr_{1.9}Nd_{0.1}CrReO_6$, $Sr_{1.8}Nd_{0.2}CrReO_6$, $Sr_{1.7}Nd_{0.3}CrReO_6$ and $Sr_{1.5}Nd_{0.5}CrReO_6$. For each sample two columns of the data are displayed corresponding to the two models described in the text (electron doping and no doping). Although the lattice parameters remain almost unchanged, the occupancies do change their value leading to better fit quality in case of "no-doping" model especially for higher doping levels (see text for details).

	$Sr_{1.9}Nd_{0.1}CrReO_6$		$Sr_{1.8}Nd_{0.2}CrReO_6$		$Sr_{1.7}Nd_{0.3}CrReO_6$		$Sr_{1.5}Nd_{0.5}CrReO_6$	
	e-doping	no-doping	e-doping	no-doping	e-doping	no-doping	e-doping	no-doping
a (Å)	7.8560(15)	7.8560(15)	7.8551(14)	7.8552(14)	7.8753(18)	7.8759(2)	5.5618(9)	5.5627(4)
c (Å)	-	-	-	-	-	-	7.8729(28)	7.8734(12)
Vol ($Å^3$)	484.84(17)	484.85(16)	484.69(15)	484.70(15)	488.43(20)	488.54(1)	243.54(10)	243.63(5)
B (Cr/Re)	82/18	84/16	79/21	83/17	74/26	80/20	68/32	77/23
B' (Re/Cr)	82/18	79/21	79/21	73/27	74/26	65/35	68/32	52/48
B-O_1(Å)	1.9803(29)	1.9802(29)	1.9727(30)	1.9727(30)	1.9792(42)	1.9792(15)	2.0082(26)	2.0034(21)
B-O_2(Å)	-	-	-	-	-	-	1.9617(86)	1.9682(81)
B'-O_1(Å)	1.9477(29)	1.9478(29)	1.9548(30)	1.9549(30)	1.9584(42)	1.9587(45)	1.9283(26)	1.9333(21)
B'-O_2(Å)	-	-	-	-	-	-	1.9759(84)	1.9692(78)
B-O_1-*B*'(º)	180.0(1)	180.0(1)	180.0(1)	180.0(1)	180.0(1)	180.0(1)	180.0 (1)	180.0(1)
B-O_2-*B*'(º)	-	-	-	-	-	-	174.30(35)	174.85(32)
R_{wp}	5.57	5.60	4.22	4.25	4.33	4.47	3.96	3.15
R_{Bragg}	5.73	5.64	4.33	4.24	6.39	7.04	9.66	6.13

the under population of the *B'* sublattice (i.e. $2 \cdot \frac{x}{2} = x$ vacancies would occur). The analysis of the diffraction patterns does not support such scenario. The other possibility is to fill the *B'* lattice with all available Re ions, and the Cr ion would occupy the *B* lattice and the remaining empty places in the *B'* one. In the case of lack of antisite defects, this is a quite clear picture. However, we still have the *AS* defects, even in case of the no-doping model. The explanation can be better understood using the Nd x = 0.3 sample as an example. In this sample, we have 1.15 Cr ions and 0.85 of the Re. In the Table 5.1 we find the occupancy of the *B* site to be 80/20 (Cr/Re) and the *B'* site to be 65/35 (Re/Cr). Calculating the percentage of the Re ions in the *B'* and *B* sublattice we get that 23.5% of them is occupying the latter one, which is the main Cr lattice. This value can be defined as the *AS* amount in the no-doping model. In the e-doping model the occupations (for both lattices) are equal to 74/26, meaning 26% of *AS* defects.

Both models give very high *AS* value. In the e-doping model, according to the definition of *AS* percentage, the obtained value means that half of the volume of the material contains antisite defects (50% is the situation of a single perovskite phase). In the case of no-doping model we already introduce the defects by defining model requirements and the structure limitations, thus it is not so straightforward to conclude that the system is considerably disturbed.

The magnetism of the ordered double perovskites is mainly controlled by the interactions between the *B* and *B*' site cations via Oxygen *2p* orbitals. As a consequence, it is very sensitive to the ions that occupy the *B* and *B'* sites. In our case the introduction of the Ln atoms to the system possibly causes the Cr ions to further occupy the Re sublattice (due to on-purpose introduction of additional Cr and probable Re segregation and evaporation). Then we suppress some Cr – O – Re interaction paths and introduce Cr – O – Cr ones, which, up to now have been treated as undesired (appearing as a result of misplaced atoms – the antisites). We lack theoretical models calculating the magnetic and electronic interactions for the double

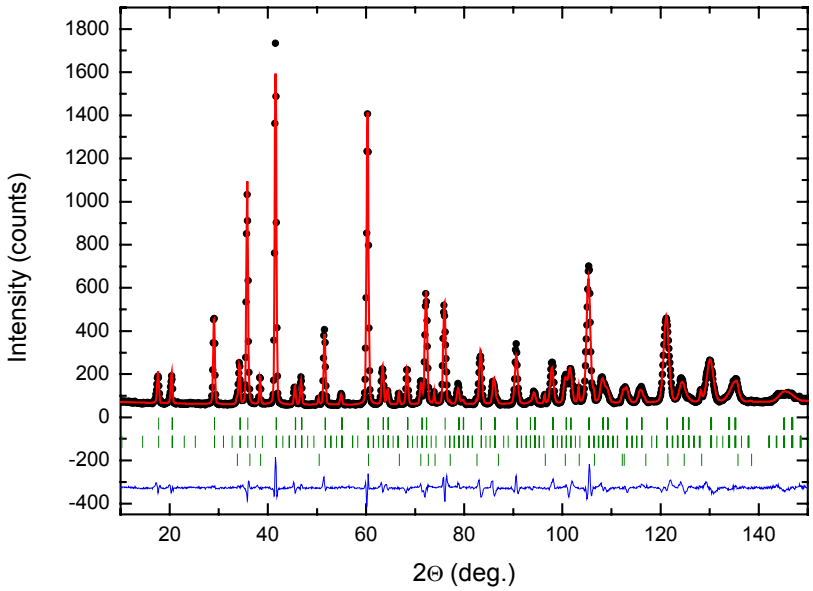

Figure 5.9. Neutron diffraction pattern taken at 2 K for the sample with Lanthanum doping (x = 0.5). Circles stand for the experimental data, solid line for the Rietveld refinement result. Line in the bottom is the difference between the experimental data and the fit. Ticks in between are the structural and magnetic Bragg reflections positions for the sample main phase and structural for metallic Re in the last row.

perovskite systems with high *AS* levels. We may assume however, that the neighboring ions of the same type will be antiferromagnetically coupled as observed for low or moderate amounts of defects. We will get back to the subject while analyzing the magnetic properties of the material later on.

5.2.3. Thermal evolution of crystallographic parameters and magnetic moments

The low temperature data become much more complex in term of analysis compared to the high temperature patterns due to the need of introduction of the magnetic parameters into the refinements input. Measurements have been performed between 2 and 10 K for different samples, however we do not expect any differences in lattice parameters in this range of temperatures. In the Figure 5.9 we present the low temperature (2 K) pattern of the La x = 0.5 sample along with the fitted spectra (consisting of structural and magnetic double perovskite parts and metallic Rhenium

impurity structural ingredient).

First, the analysis of the fit results as a function of temperature allows estimating the temperature of structural transition between tetragonal and cubic structures. At low temperatures all samples are tetragonal with different oxygen octahedra distortions. As can be seen in Table 5.8 the bond angle between Cr and Re via the in-plane oxygen atoms depends on the doping level. For the undoped sample this angle has a value of about 174° which is lowered for high doping levels down to approximately 167° for Nd x = 0.3 and La x = 0.5 samples. The angles along the c axis are not varying with doping within the fit accuracy. Also the unit cell dimensions do not show a systematic variation on doping.

Table 5.8. Data on low temperature crystallographic parameters (unit cell constants, bond angles and interatomic distances) obtained from Rietveld refinements of the neutron powder diffraction patterns for the two models described in the text. O_1 denotes the oxygen atom lying in the *xy* plane, while O_3 is the apical oxygen.

		a (Å)	*c* (Å)	Cr – O_1 – Re (°)	Cr – O_3 – Re (°)	Cr – O_1 (Å)	Re – O_1 (Å)
Electron doping							
	x = 0.0	5.5183(2)	7.8130(6)	173.99(17)	180.0(3)	1.938(4)	1.970(4)
	x = 0.1	5.5201(5)	7.8006(2)	170.7(5)	180.0(13)	1.972(11)	1.944(11)
Nd	x = 0.2	5.5199(4)	7.8123(1)	168.6(4)	180.0(10)	1.969(10)	1.953(9)
	x = 0.3	5.5211(4)	7.8115(3)	166.8(6)	180.0(13)	1.981(15)	1.950(13)
	x = 0.1	5.5184(2)	7.8042(2)	171.28(17)	180.0	1.963(4)	1.951(4)
La	x = 0.3	5.5179(6)	7.8035(9)	167.8(2)	180.0	1.989(5)	1.935(5)
	x = 0.5	5.5228(2)	7.8068(3)	167.7(3)	180.0(10)	2.008(7)	1.920(7)
No-doping							
	x = 0.0	5.5183(2)	7.8130(6)	173.99(17)	180.0(3)	1.938(4)	1.970(4)
	x = 0.1	5.5201(12)	7.8008(17)	170.55(54)	180.0(15)	1.965(13)	1.951(13)
Nd	x = 0.2	5.5200(4)	7.8122(11)	168.69(53)	180.0(13)	1.972(13)	1.951(13)
	x = 0.3	5.5212(3)	7.8115(8)	166.78(63)	180.0(15)	1.979(16	1.951(15)
	x = 0.1	5.5184(1)	7.8042(1)	171.43(16)	180.000(3)	1.962(4)	1.951(4)
La	x = 0.3	5.5165(5)	7.8031(14)	167.96(24)	180.00(43)	1.984(6)	1.938(6)
	x = 0.5	5.5200(6)	7.8010(14)	167.14(27)	180.0(44)	2.010(6)	1.918(7)

On increasing the temperature, all samples tend to minimize the octahedra distortions indicating the tendency to obtain the cubic structure at high temperatures. The

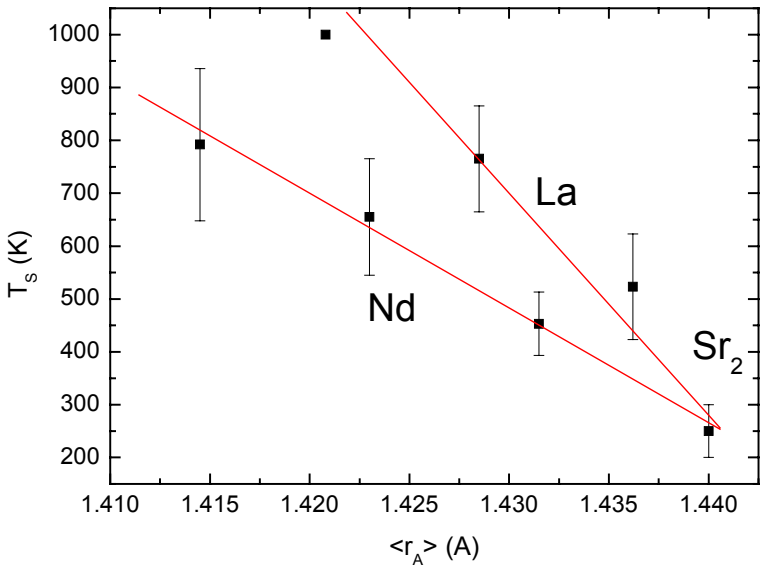

Figure 5.10. Structural transition temperature plotted against the mean ionic radius at the A site $(\langle r_A \rangle)$ obtained from the Rietveld refinements of the neutron powder diffraction patterns. The high temperature phase is cubic (with the $Fm\bar{3}m$ space group) whereas the low temperature phase is the tetragonal one (with the *I4/m* space group). The transition temperature is getting higher with the increase of doping level. Experimental points correspond to the mean value of the two temperatures for which better fits are obtained with different crystallographic structures. The error bars are corresponding to the highest temperature for which the tetragonal structure gives better fit quality and the lowest for which the cubic structure is obtained. They are strongly exaggerated compared to the experimental resolution of the neutron diffraction.

transition temperature is varying with doping and is dependent on the kind of Ln ions. As can be seen in the Figure 5.10 a dependence on doping is close to linear and two independent lines can be drawn. Experimental points in the figure correspond to the mean value of the two temperatures for which better fits are obtained with different crystallographic structures (i.e. highest temperature for tetragonal and lowest for cubic structure). The error bars correspond to the difference between those temperatures and thus are strongly exaggerated compared to the experimental resolution of the neutron diffraction.

Concerning the two models proposed for the doped Sr_2CrReO_6 we see that there is

no, within the experimental resolution, difference between the structural parameters of the samples. This refers not only to the unit cell constants, but also to the sizes and degree of tilting of the Cr and Re octahedra. Also, the tetragonal to cubic structure transition temperature is not altered while using any of the two models.

In contrast to the structural properties, the magnetic properties seem to be more dependent on the *B* and *B'* occupations, being the main difference between electron doping and no-doping models. This fact could have been expected considering that the magnetic interactions between Cr and Re ions are of different kind compared to Cr-Cr or Re-Re interactions.

The magnetic phase has been introduced to the fitting input file as a triclinic structure with a $P\bar{1}$ space group. The Cr ions are occupying *g* and *d* Wyckoff positions while the Re ions the *f* and *c* sites. All above sites have a multiplicity equal to 1. Lattice constants are chosen to be $a = b \neq c$ (in the same manner as in the nuclear scattering case giving the structural information). The angles are fixed along the fit, and $\alpha = \beta = \gamma = 90°$. Magnetic moments of Re and Cr are refined during the fitting using magnetic scattering form factors of Mo^{5+} and Cr^{3+} due to the reasons explained before. The free contributions of the magnetic moment are M_x and M_y (being the projections of the total moment along the [100] and [010] crystallographic axes). The M_z component (along the [001] axis) is constant and set to zero, as there is no significant change in the diffraction spectra for the diffraction on the (001) plane reflection. The introduction of the M_z contribution results instability and failure in reaching convergence. Such conditions result in the overall magnetic moment lying in the *xy* plane for both Cr and Re cations. The total magnetic moment carried by the Cr ions has opposite sign with respect to the Re ones.

In the Figure 5.11 we present the thermal evolution of the Cr and Re magnetic moments for electron doping (left column) and no-doping (right column) models for the Nd doped samples. From the first sight, it is clear that the results obtained with the former are characterized by much larger experimental error bars especially in the

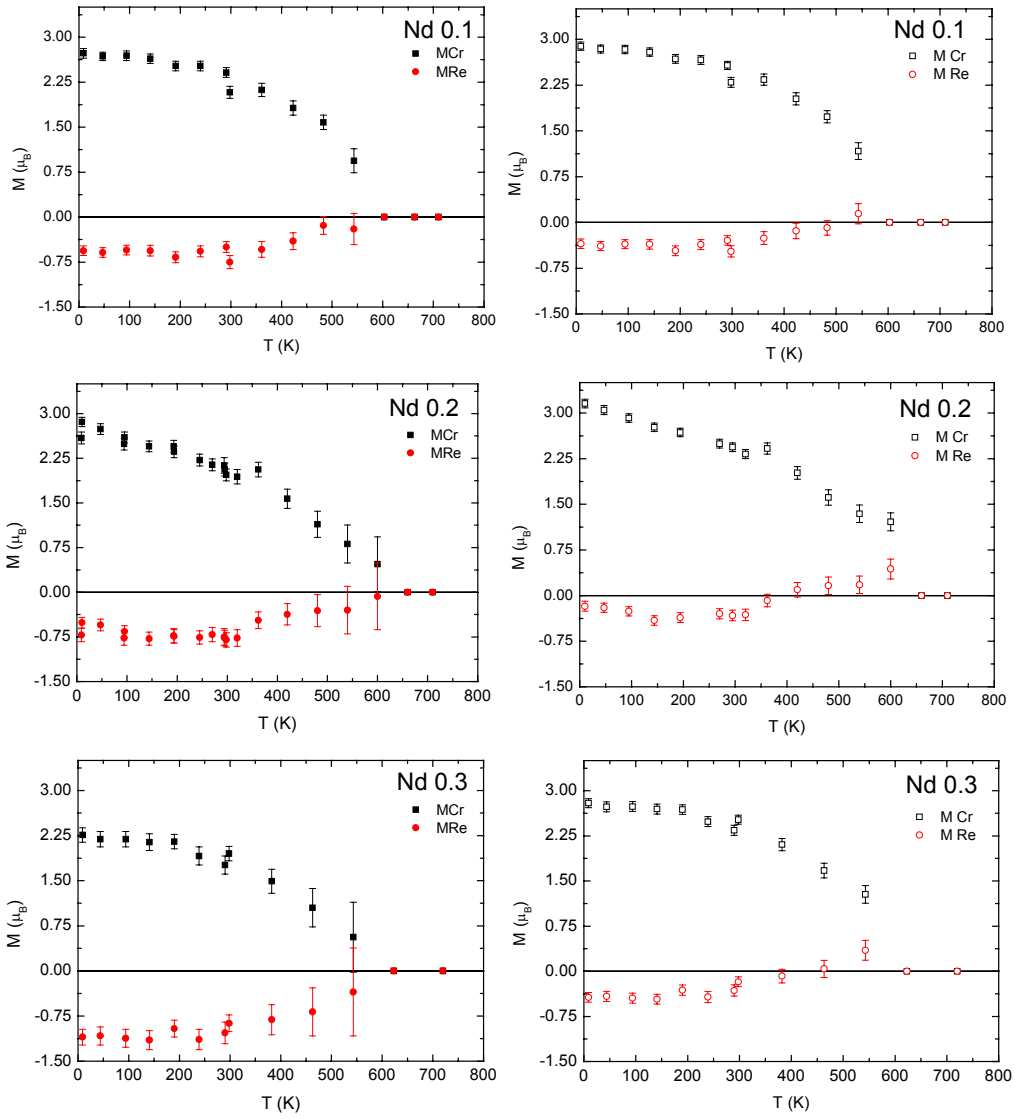

Figure 5.11. Thermal evolution of the magnetic moments of Cr and Re ions in the Nd doped series for the two models described in text (e-doping and no-doping models in the left and right column respectively) obtained on the basis of the Rietveld refinements of the neutron powder diffraction patterns. The desired stoichiometry of the samples is indicated in each graph. A striking feature is the change of the Re magnetic moment from antiparallel to parallel to the Cr magnetic moment for higher doping levels in the case of no-doping at high temperatures.

moderate and higher temperature range (close to the magnetic transition temperature). On the one hand, a rise in the measurement uncertainty around the transition

temperature is not surprising. On the other hand with the no-doping model errors are not growing while reaching the critical temperature. The absolute value of the magnetic moment of both Cr and Re seems to change depending on the structural model used. The Chromium moment is higher, while the Rhenium one is significantly lower for the no-doping model than in the e-doping model, the difference being bigger for higher x values. What is more striking, is the change of the sign of the Re magnetic moments that takes place well below the Curie temperature. Moreover this temperature is dependent on the doping level and changes from about 500 K down to 400 K for x = 0.1 and 0.3 respectively.

Similar behaviour is observed in case of La doped samples (see Figure 5.12). Again the magnetic moments are different for the two models. Error bars are bigger for the e-doping model than in the no-doping model, as it was the case in the Nd doped samples. In the case of the refinements done with the no-doping model we observe a change of the sign of the Re magnetic moments except for the La x = 0.1 sample. For x = 0.3 and 0.5 the temperature at which the inversion of the sign of the Re magnetic moment is about 400 K, similarly to Nd doped sample with x = 0.3.

Concerning the change of the absolute values of the Re and Cr magnetic moments we should stress that the total moment is the algebraic sum of the Rhenium and Chromium contributions and is higher for the no-doping model.

The reversal of the magnetic moment of the magnetic ions is rather unexpected in the ferromagnetic double perovskite system. The nature of the magnetic interaction between Cr and Re ions is causing the magnetic moments – M_{Cr} and M_{Re} – to be coupled antiparallel. The antiparallel ordering of the overall Re magnetic moment with respect to Cr moments is controlled by the exchange interactions via the oxygen orbitals and the spin-orbit coupling so it should not be dependent on the amount of Cr and Re in the system. On the other hand the overpopulation of the Cr ions and the lower than stoichiometric amount of Re ions together with the displaced Re ions causes the long range magnetic ordering to be strongly influenced. Moreover the

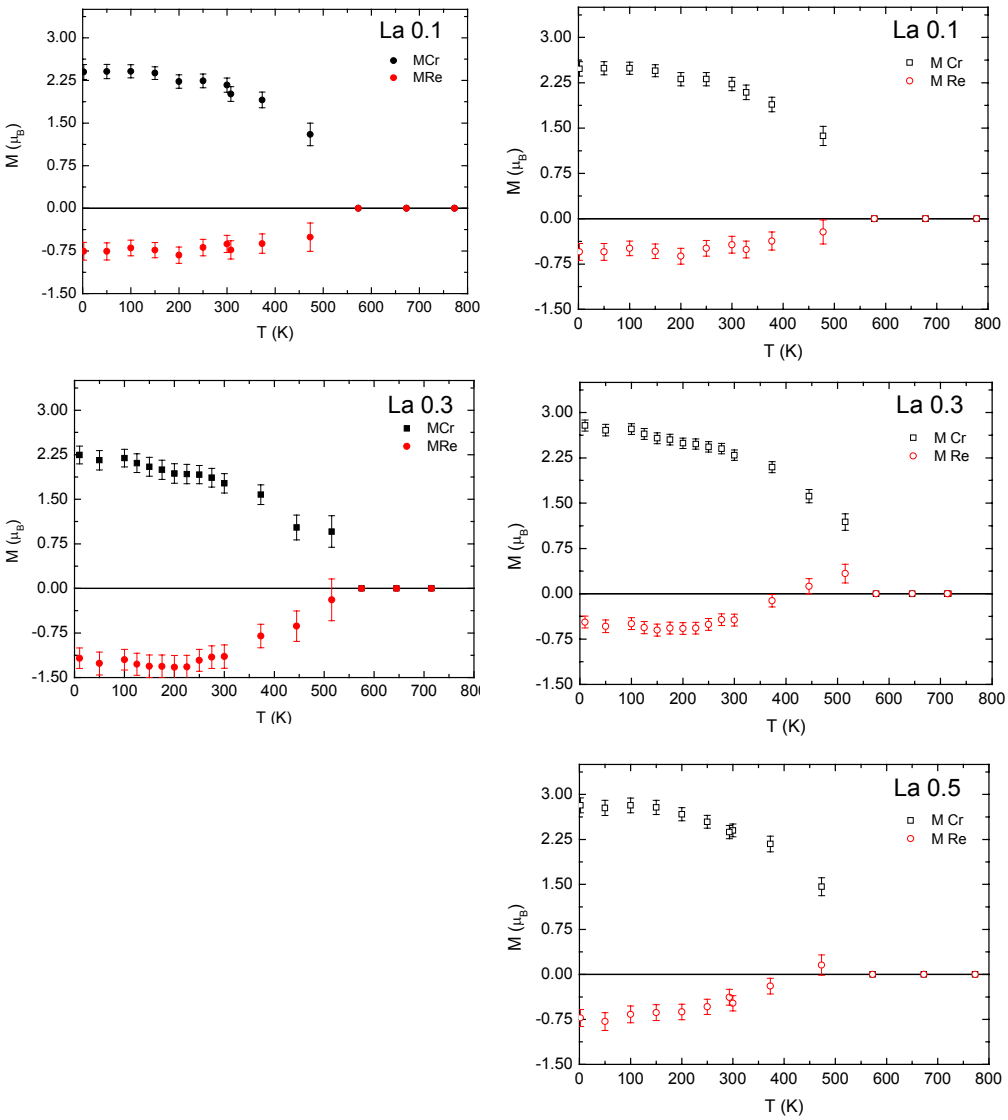

Figure 5.12. Thermal evolution of the magnetic moments of Cr and Re ions in the La doped series for the two models described in text (e-doping and no-doping models in the left and right column respectively) obtained on the basis of the Rietveld refinements of the neutron powder diffraction patterns. The La content in the samples is indicated in each graph. A striking feature is the change of the Re magnetic moment from antiparallel to parallel to the Cr magnetic moment for higher doping levels in the case of no-doping at high temperatures.

orbital and spin magnetic moments cannot be easily separated with neutron powder diffraction. Taking all above into account we refrain ourselves from developing a complex model of the reversal of the magnetic moments. XMCD measurements at

those high temperatures could be performed to study this point in detail.

Nevertheless we should point out that the magnetic ordering temperature is close to 600 K over all samples with different doping levels, and moreover this value remains true for electron doping and no-doping models.

In summary, concerning the models we are proposing for the Sr_2CrReO_6 with Ln substitution at a Sr site, from the neutron powder diffraction results we obtain some support to prefer the no-doping model. This conclusion comes especially from the goodness of the fits obtained with the Rietveld refinement, in good agreement with the fluorescence and EDX results shown before.

5.3. XANES and EXAFS studies

As we have already seen there are some doubts about the real stoichiometry of the Ln doped Sr_2CrReO_6 samples. Together with this problem, we are looking for the answer to the question about the possibility of the successful electron doping in the Sr_2CrReO_6 double perovskite. In order to determine whether the electron doping is indeed taking place, we need a local technique that would allow independent study of the electronic changes on Cr and Re atoms. Here we can take advantage of the x-ray absorption techniques. We have measured the X-ray Absorption Near Edge Structure (XANES) and Extended X-ray Absorption Fine Structure (EXAFS) spectra for Sr_2CrReO_6 doped with Neodymium and Samarium for doping level x = 0.1, 0.3 and 0.5. We were not able to measure the La-doped samples due to the proximity of the La L-edge and Cr K-edge. Due to the same reason we have studied only EXAFS of the Sm doped CrRe double perovskite. In this chapter, we will focus on the XANES range of the x-ray absorption spectra as it provides a lot of useful information on the electronic structure. On this basis, we should be able to demonstrate which of the models, electron doping or no-doping, is more probable in the Ln-doped double perovskite system.

XANES spectra were recorded at the Cr K- and Re $L_{1,2,3}$-edges whereas EXAFS

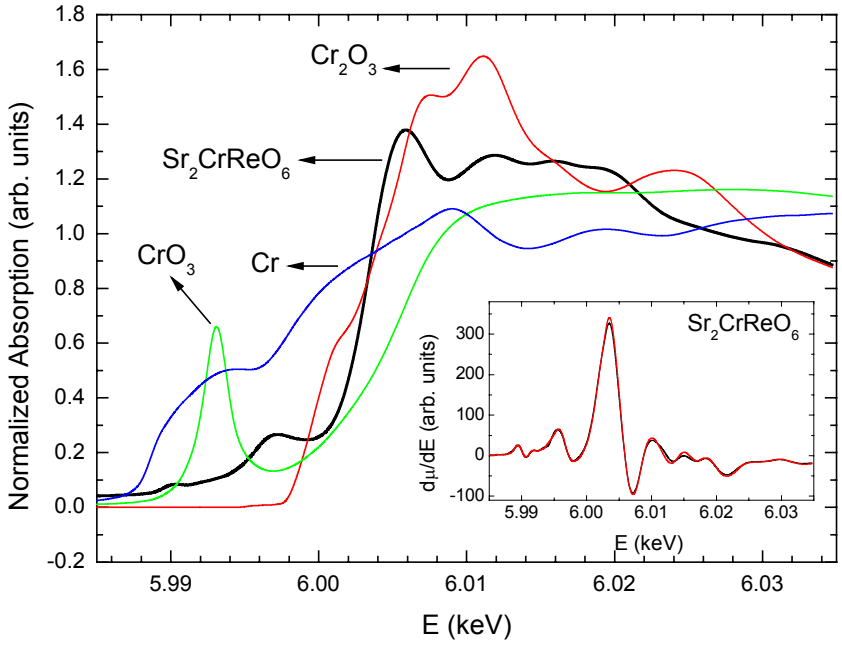

Figure 5.13. Normalised Cr K-edge XANES spectra for metallic Cr, Cr_2O_3, CrO_3 reference samples along with the spectra for Sr_2CrReO_6. In the inset the derivative of the XANES signal with respect to the incident photon energy showing a maximum at the edge position for the Sr_2CrReO_6 under 15 and 295 K.

spectra were taken at the Cr K and Re L_3-edges. The measurements were carried out at selected temperatures between 15 and 295 K. A Cr foil and a pellet of metallic Re were simultaneously measured for energy calibration at each respective absorption edge. The XANES spectra were normalized to the high energy part of each spectrum (~100 eV beyond the edge) after background subtraction. We have also recorded XANES spectra of Cr, Cr_2O_3, CrO_3 and $LaCrO_3$ as references for the Cr K-edge. Re, ReO_2, ReO_3 and $Sr_{11}Re_4O_{24}$ were also measured as standards for the Re L-edges.

In the Figure 5.13 we present the normalised XANES spectra of Sr_2CrReO_6 measured at Cr K-edge together with metallic Cr (Cr^0 standard), Cr_2O_3 (Cr^{3+} standard) and CrO_3 (Cr^{6+} standard). The K-edge is particularly sensitive to the local structure what is reflected for instance in the pre-edge region of the CrO_3. A sharp peak is visible at 5993 eV that can be ascribed to a dipole-forbidden transition 1s→*3d*. Such

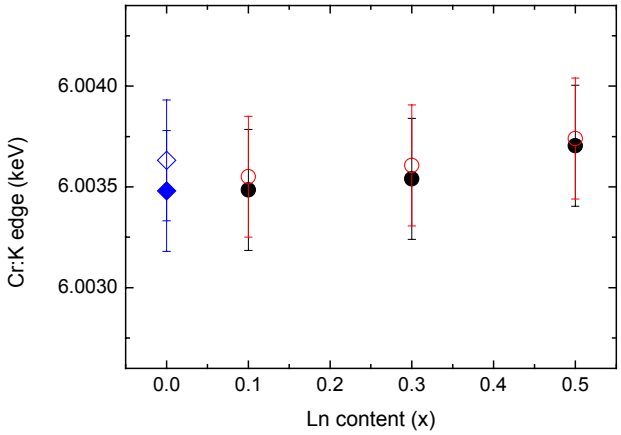

Figure 5.14. Edge position, defined as a maximum of first derivative of the normalised XANES, for Nd (open circles) and Sm (closed circles) doped material. Open and close symbol for the parent Sr_2CrReO_6 compound (x = 0.0) correspond to 300 and 5 K respectively.

features are observed in the tetrahedral coordination systems without an inversion center [139]. The Cr_2O_3 with the octahedral coordination shows less intense pre-edge features. The position of the edge was determined as a maximum of the first derivative (see e.g. the inset in the Figure 5.13 showing the $\partial\mu/\partial E$ function for Sr_2CrReO_6 at 15 and 290 K). As can be seen in the Figure 5.13 the absorption edge position is strongly dependent on the oxidation state of the material. On increasing the Cr valence, the edge shifts towards higher energies.

In case of the Ln-doped Sr_2CrReO_6 we do not observe a significant change of the absorption edge position while the doping level changes. Indeed the spectra for the doped samples are identical to that of the parent compound. In the Figure 5.14 we present the absorption edge positions as a function of Ln content – x for Nd and Sm doped samples along with the undoped Sr_2CrReO_6 at two temperatures. It is clearly seen that the edge energy remains constant within the experimental error. Consequently we may conclude that the Cr oxidation state is not changed upon doping which means that replacing the Sr cations by a rare earth ions does not change its 3+ state.

We have already seen that the pre-edge structure is significantly different for the

Sr_2CrReO_6 and the reference compounds. The K-edges of the transition metal ions are mainly attributed to the dipole *1s→4p* transitions. A low intensity of the features in the pre-edge region can be expected as the dipole transitions are several orders of magnitude stronger compared to quadrupole transitions [140]. The large intensity of these features can be, according to some authors, ascribed to the spreading of the *4p* band, which mixes then with *3d* orbitals [123]. Another mechanism that shall be considered is the Cr *3d*-O *2p* hybridization. It was demonstrated theoretically on binary oxides that transitions to the *3d*-like hybridized orbitals (made up of *3d* metal orbitals and *2p* Oxygen orbitals) could give rise to significant dipole transitions [124]. Both mechanisms would provide the dipole allowed *1s→np* component to the transition (and hence increase the intensity of the pre-edge features). In the double perovskite oxides, the transition metal ion (Cr in present case) is surrounded by 6 oxygen atoms and the hybridization of its d orbitals with the *2p* Oxygen takes place producing wide energy bands.

In order to extract the pre-edge region from the measured spectra we have fitted the normalised XANES with a function being a sum of a symmetric Lorentzian and hyperbolic tangent (tanh) functions. The fits have been done between 5.97 and 6.01 keV (we will comment on more details of such procedure later on for the Re L-edges). In the Figure 5.15 we present the experimental data of the parent compound (Sr_2CrReO_6) measured at 295 K, together with the fit with the empirical function. In the inset of the same figure the pre-edge region after removing the function obtained during the fitting from the experimental data is shown. In such way we clearly see that the pre-edge structure has a tri-feature aspect. Two well-defined peaks are labelled with A and C letters, and a shoulder between them with B. As a next step, the pre-edge structure was fitted with three Gaussian peaks. In this way we were able to calculate the area of each of the peaks. The C peak has the magnitude of the area one order of magnitude higher compared to the A peak. This procedure was repeated for the Sm and Nd doped samples in all doping range. The pre-edge structure of the Sr_2CrReO_6 and the Nd doped samples is presented in the Figure 5.16. It is clearly seen that the C

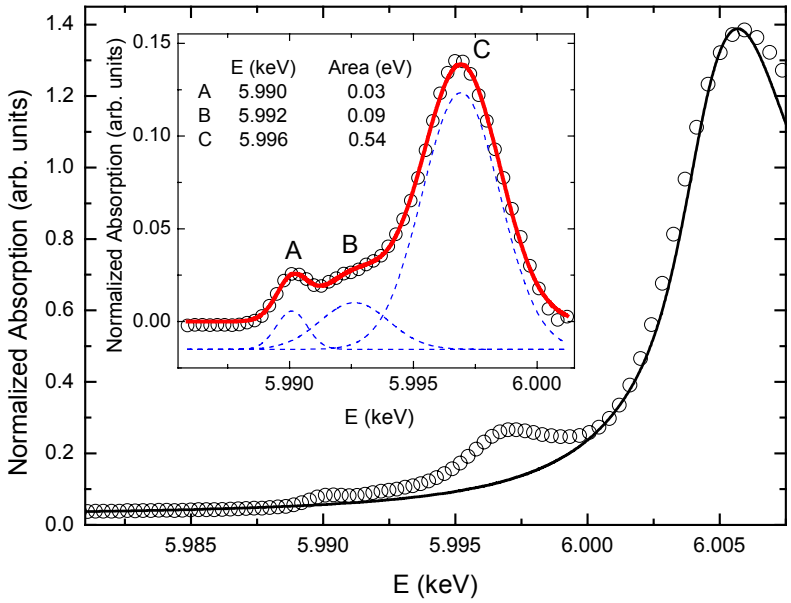

Figure 5.15. Normalised Cr K-edge XANES spectrum for Sr_2CrReO_6 at 290 K (open circles) together with the line obtained with the fitting procedure described in text. In the inset a close-up of the pre-edge features (circles) of the Cr K-edge. The continuous line is a fit result with three gaussian shaped peaks (dashed lines in the bottom) denoted as A, B and C. The position of the peaks and the areas below them are also indicated.

peak area decreases on doping, while the remaining two features do not change its magnitude. The same behavior is observed for the Sm doped samples (see the inset in the Figure 5.16). Moreover, none of the peaks changes its position in the energy scale, and remains at the same energy as for the parent compound. The detailed information can be found in the Table 5.9.

The A peak can be ascribed to pure quadrupole transitions [123, 141], and is extremely sensitive to the *3d* orbitals occupation as demonstrated for TiO_2. As a result it gives further support to the presence of Cr^{3+} in this double perovskite system [123]. On the contrary, the higher intensity of the C peak indicates that the dipole transitions are more likely to contribute to this part of the pre-edge region. Thus a dependence of the C peak area on the Ln-content can give some indication of the change of the overlapping of the Cr and O orbitals. Then it would be related to the degree of the Cr-O covalency.

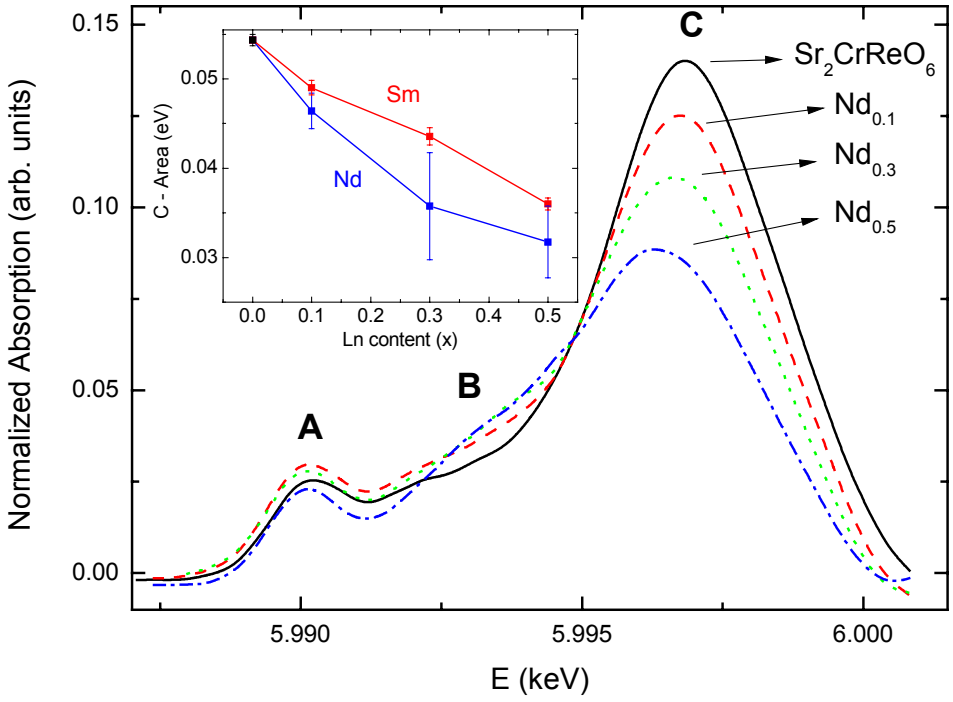

Figure 5.16. The details of the pre-edge Cr K-edge features after background subtraction for the Nd doped samples (as indicated in the figure) together with the parent compound. The three Gaussian components are denoted as A, B and C. In the inset the area below the C peak as a function of doping level for Sm and Nd doped material is presented.

Now we shall discuss the Re L-edges. For measurements on the Rhenium edges we have used the metallic Re (Re^0), ReO_2 (Re^{4+} standard), ReO_3 (Re^{6+} standard) and $Sr_{11}Re_4O_{24}$ ($Re^{6.5+}$ standard) as reference samples. ReO_3 has a crystal cell similar to double perovskites but possesses vacancies at the Sr positions. $Sr_{11}Re_4O_{24}$ is a Sr-deficient double perovskite in which the Re appears in two oxidation states: 6+ and 7+ in 1:1 proportion what leads to the average of 6.5+ [141]. In both compounds one observes the ReO_6 octahedra sharing corners. In ReO_2 the ReO_6 octahedra are also present, however in this case they share edges [142].

Table 5.9. Results of fitting of the pre-edge structure after background subtraction with three Gaussian shaped peaks. In the columns the energy of the center of the peak and the area below the peak are displayed, and the peaks are labeled A, B and C as in the Figure 5.15. Data correspond to the undoped compound (first data row), Nd and Sm doped samples (as indicated). The error in the estimate of the peak position is of 0.1 eV, while the area is calculated with 0.01 eV accuracy for A and B peaks and 0.05 eV for the C peak.

		A		B		C	
		position (keV)	area (eV)	position (keV)	area (eV)	position (keV)	area (eV)
	x = 0.0	5.9901	0.03	5.9926	0.09	5.9969	0.54
	x = 0.1	5.9900	0.04	5.9929	0.12	5.9968	0.46
Nd	x = 0.3	5.9900	0.03	5.9936	0.18	5.9969	0.36
	x = 0.5	5.9900	0.03	5.9935	0.13	5.9966	0.32
	x = 0.1	5.9901	0.04	5.9928	0.09	5.9969	0.49
Sm	x = 0.3	5.9902	0.04	5.9931	0.10	5.9969	0.43
	x = 0.5	5.9902	0.05	5.9930	0.10	5.9967	0.36

In the Figure 5.17 we present the XANES spectra measured at the L_1-edge for the Sr_2CrReO_6 and the reference materials. The L_1-edge is due to the *2s→6p* transitions. It provides information similar to that of K-edge. We have defined the position of the edge as a maximum of the first derivative of the absorption signal (see the inset in the Figure 5.17). The first derivative of the L_1-edge XANES shows a bimodal feature. The higher energy one reveals the chemical shift. The peak in the derivative has a center at an energy close to that of the half-height of the absorption edge. As can be seen the Sr_2CrReO_6 edge lies between the Re^{4+} and Re^{6+} standard. As it was the case for the Cr K-edge the rest of the double perovskite compounds (Ln-doped samples) show nearly identical spectra as the parent compound.

We can also relate the position of the edge to the nominal *5d* band occupation. In the Figure 5.18 we plot the energy of the centre of the high-energy first derivative

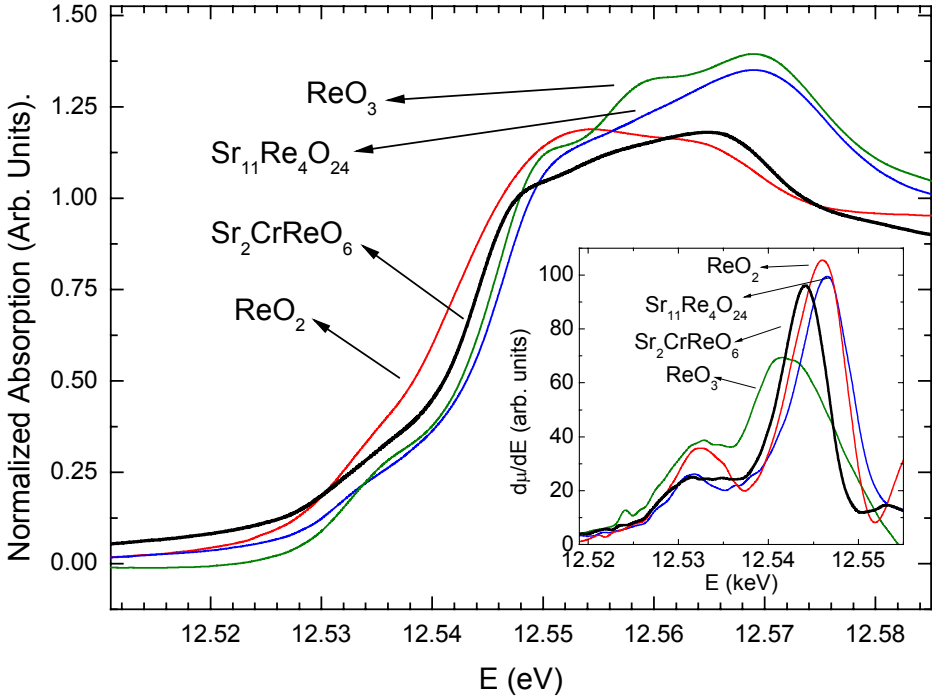

Figure 5.17. Normalised Re L_1-edge XANES spectra for reference compounds (ReO_3, $Sr_{11}Re_4O_{24}$ and ReO_2) together with Sr_2CrReO_6 sample. In the inset: first derivative of the XANES spectra around the absorption edge energy for the same compounds.

peak versus the number of the *5d* electrons. We can observe a linear relationship of the occupation of the d-band for the reference sample and the edge position. If we add to this plot the position of the energy for the undoped sample and the Ln-doped double perovskites we get the *5d* band electronic configuration to be $5d^2$. Such configuration is expected for the Re^{5+} ion. In the inset of the Figure 5.18 we present the edge position for the Sm and Nd doped samples. At first sight it is visible that there is no systematic relationship between the doping level and the absorption edge energy and within the experimental error the edge position remains constant. Consequently, for the doped samples we may assume the electronic configuration of $5d^2$ as for the parent compound. This means that doping of the Sr_2CrReO_6 double perovskite with Sm and Nd does not change the formal valence of Rhenium, which remains equal to Re^{5+}.

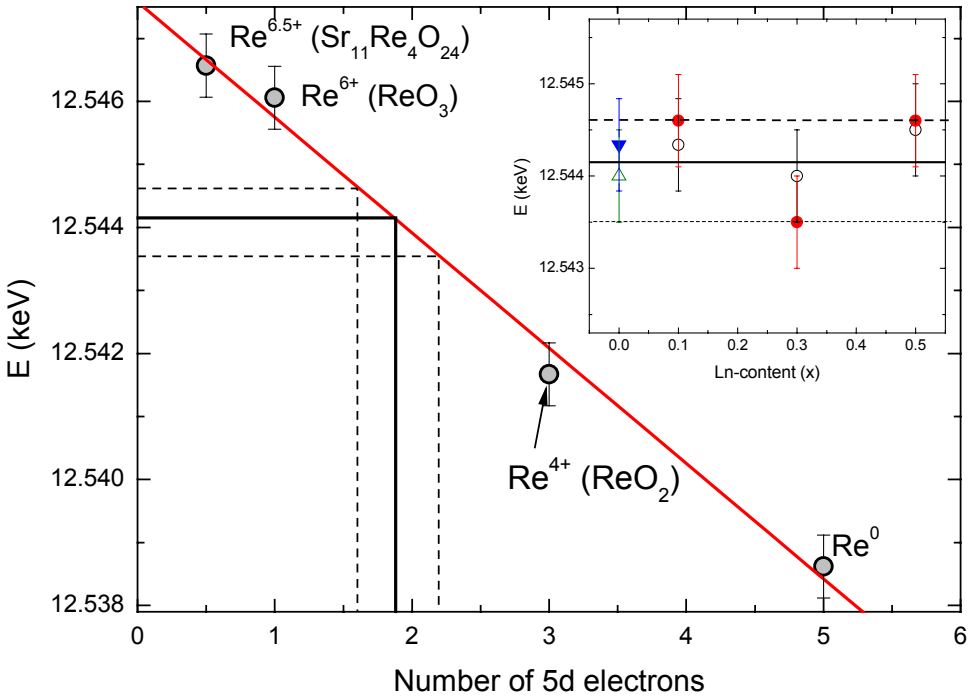

Figure 5.18. Re L_1-edge energy position plotted against the occupation of the 5d-band for the reference samples (circles) along with the linear fit. Solid line indicates the position of the edge for Sr_2CrReO_6 sample and relates it to the number of the 5d electrons. The dashed lines are the limit values of the lowest and highest energy at which the absorption edge is identified and thus the limit values of the 5d-band occupation. In the inset: edge positions for the Sm and Nd doped samples (closed and opened circles respectively) and the undoped material under 10 and 290 K (opened and closed triangles). Solid and dashed lines have the same meaning as in the main figure.

Now we will discuss the L_2 and L_3-edges. The absorption at those edges is caused by the excitation of the $2p_{1/2}$ or $2p_{3/2}$ core electrons respectively. The L_2-edge probes the $2p_{1/2} \rightarrow 5d_{3/2}$ while the L_3-edge the $2p_{3/2} \rightarrow 5d_{3/2}$, $5d_{5/2}$ transitions. Neither L_2 nor L_3-edge are very sensitive to the chemical shift. On both edges the double perovskite spectra are characterised by a strong white line that is expected in the systems with the empty *5d* states [143]. Concerning the reference compounds we observe one broad peak for both metallic Rhenium and ReO_2. The rest of the standards exhibit a double peak at $L_{2,3}$-edges. The same feature is observed in the double perovskite samples.

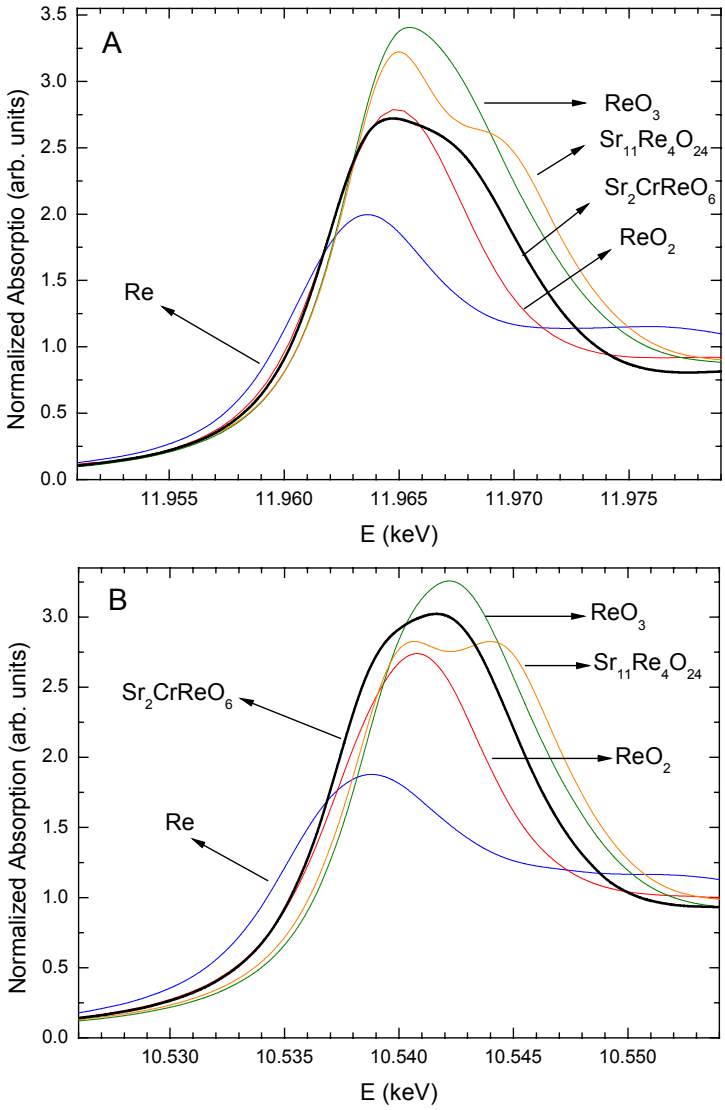

Figure 5.19. Re L_2-edge (a) and Re L_3-edge (b) XANES spectra for ReO_3, $Sr_{11}Re_4O_{24}$, ReO_2 and metallic Re standards as well as Sr_2CrReO_6 sample.

Such white line shape can be expected for the systems with octahedral coordination, and is generally explained as a result of the crystal field splitting of the d-orbitals into t_{2g} and e_g states [144]. The main difference between the L_2 and L_3-edge for the double perovskite compounds is that in the former case a stronger peak occurs at lower energies, while the opposite is observed for the latter edge. The same kind of $L_{2,3}$-edge spectra shape was observed for the Fe-based double perovskites [122]. The

normalised XANES spectra of the reference compounds and the undoped ones for L_2 and L_3 edge are presented in the Figure 5.19 a. and b. respectively.

We have fitted the L_2 and L_3 edges with a function being a sum of the hyperbolic tangent (tanh) and two symmetric Lorenzian components. This leads to an overall number of ten variables describing the positions of the absorption edge and the centres of each of the two Lorentz peaks as well as the width of the edge jump and the peaks. The number of the variables can be reduced by fixing the width of the edge jump so that it gets a value of about 5eV that can be expected for the L-edges core-hole. Then, the final functional form fitted is describing the XANES signal as a function of energy (E) as:

$$XANES = P_1 + P_2 \tanh\left(900 \cdot \left(x - P_3\right)\right) + \frac{P_4 \cdot P_5}{\left(P_5^2 + \left(E - P_6\right)^2\right)} + \frac{P_7 \cdot P_8}{\left(P_8^2 + \left(E - P_9\right)^2\right)} \qquad (5.2)$$

with nine variables. Putting as the initial parameters the inflection point of the spectra and the maxima of the two white line features as a position of the inflection of the tanh function and two Lorentzian peaks centres respectively, the fitting procedure works fine. An example of fits accomplished with function (5.2) are presented in the Figure 5.20a. and b. for L_2 and L_3-edge respectively. Fit for the L_2 edge was done between 11.94 and 11.98 keV and for L_3 between 10.51 and 10.56 keV. The intensity of the white line can be associated with the number of the d-holes thus allowing the estimate of the oxidation state. Several effects can interfere however making such study more difficult. Among them we shall mention the extent of the *5d* band to the conduction band which subsequently tends to delocalise the final state, the *5d* spin-orbit coupling and the multiplet effects between the *2p* core hole and the 5d holes [145]. It was also reported for the *4d* systems that the L_2-edges are less affected by the multiplet effects than L_3-edges [146].

After fitting the XANES spectra at both edges we have calculated the area of the white lines for all the reference compounds, the undoped Sr_2CrReO_6 and the Ln-doped

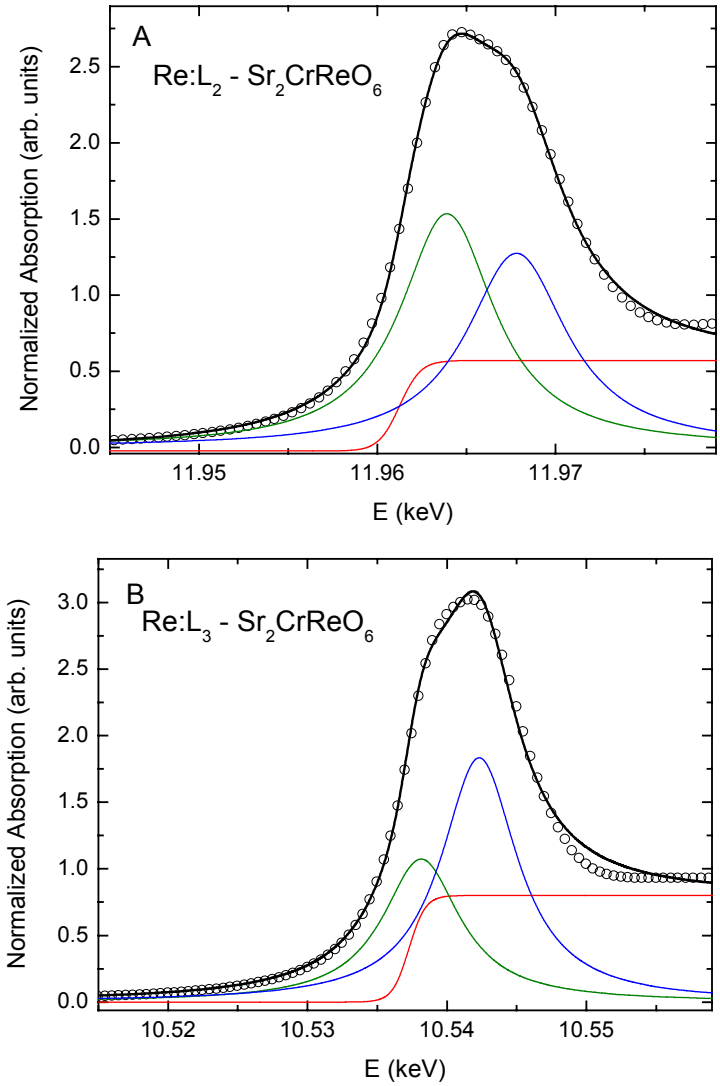

Figure 5.20. Re L_2-edge (a) and L_3-edge (b) XANES spectra for Sr_2CrReO_6 sample (circles) fitted with hyperbolic tangent and two Lorentzian components (solid lines below the spectrum). The result of the fit is plotted with the thick line.

samples. The calculation was done integrating the area below the Lorentz peaks obtained during the fitting separately for both and adding both quantities. In the Figure 5.21 we present the reference samples dependence of the white line area on the formal number of the d-electrons. As can be seen there is a linear dependence of the area below the white line and the number of the d-electrons. For the L_3-edge we do not present the data for the $Sr_{11}Re_4O_{24}$ as the fit result is rather doubtful.

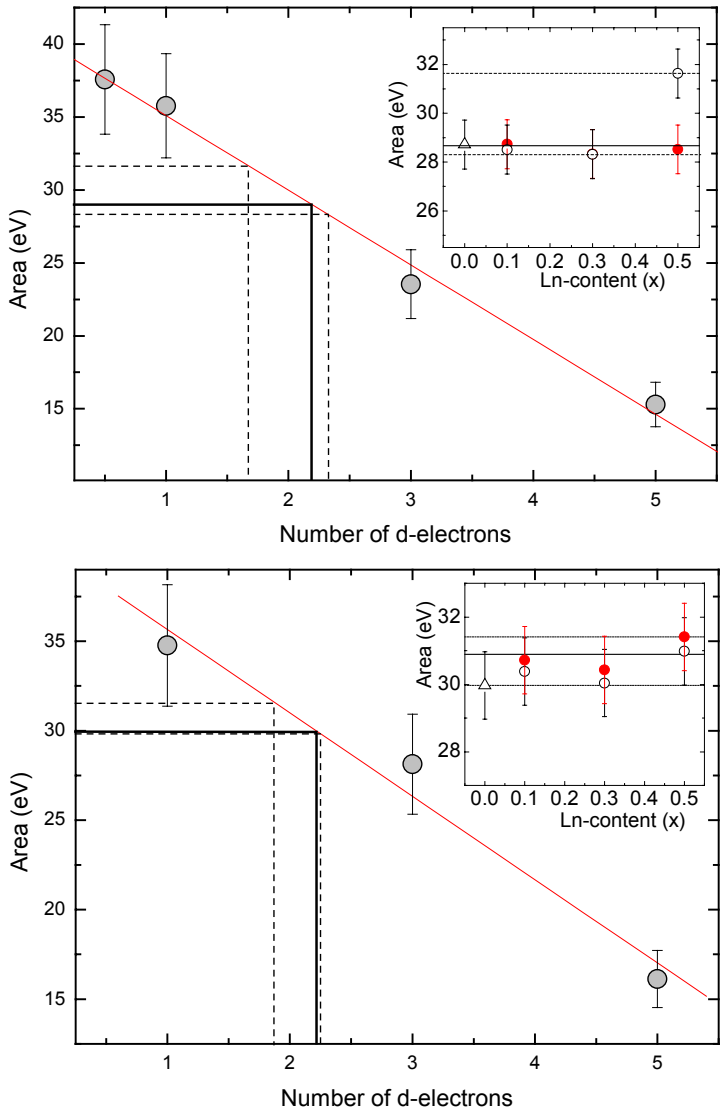

Figure 5.21. The total area below two Lorentz peaks fitted to the white line for the standards (circles) together with the linear fit. The solid line indicates the area for Sr_2CrReO_6 sample and relates it to the number of the 5d electrons. The dashed lines are the limit values of the lowest and highest area and thus the limit values of the 5d-band occupation. In the inset: peaks areas for the Sm and Nd doped samples (closed and opened circles respectively) and the undoped material (opened triangle). Solid and dashed lines have the same meaning as in the main figure. Top panel refers to the L_2-edge while the bottom one to the L_3-edge.

The total area (sum of two Lorentzian components) of the white line for the double perovskite samples varies from 28.3 to 31.6 eV for the L_2-edge (however only

the Nd x = 0.5 sample overcomes the 28.8 eV limit) as presented in the inset of the Figure 5.21.a. In the case of the L_3-edge the white line area for the doped samples series is found to be between 30 and 31.4 eV as presented in the inset of the Figure 5.21.b. Taking into account both edges we do not observe a systematic dependence of the area covered by two fitted symmetric Lorenz peaks on the doping level.

To sum up, the obtained results of the analysis of the L-edges of the Rhenium show that we deal with the formal electronic state of $5d^2$ for all the samples (exact range is 1.61 – 2.20, 1.68 – 2.29 and 1.88 – 2.26 for L_1, L_2 and L_3-edge respectively). Clearly we obtain consistent results at the L-edges so we can claim the oxidation state of Re to be 5+. Concerning the Cr K-edge we have obtained the oxidation state 3+. The same result was obtained for the parent Sr_2CrReO_6 and the samples doped with Nd and Sm. It suggests that the doping does not lead to the introduction of additional electrons to the system (at least into the Cr/Re bands).

The detailed analysis of the EXAFS part of the X-ray absorption spectra have been accomplished in the framework of collaborative investigation by dr. Javier Blasco [147].

The Cr K-edge EXAFS spectra were collected for the Sm doped Sr_2CrReO_6 samples up to $k \sim 13$ Å^{-1} for chosen temperatures between 25 and 290 K. These measurements were not possible for the Nd-based compounds due to the proximity of the Nd L_3- and Cr K-edges. The Fourier transform (FT) of the k-weighted EXAFS spectra was calculated between 3 and 12 Å^{-1} using a sine window and is plotted in the Figure 5.22.a. EXAFS spectra were also measured at the Re L_3-edge. In this case, measurements of the doped Sr_2CrReO_6 samples were possible for both the Sm- and Nd-doped compounds. Oscillations at this edge are still visible up to 15 Å^{-1} and the FT of the *k*-weighted spectra shown in Figure 5.22.b was calculated between 2.8 and 15 Å^{-1} using a sine window as in the previous case.

The FT of the Cr K-edge EXAFS shows a strong peak at ~ 1.55 Å corresponding to the Cr – O distance without a phase-shift correction. The 2nd and 3rd coordination

shells show two peaks between 2.5 and 3.8 Å. Contributions from single, Cr – Re and Cr – Sr(Sm) paths, together with multiple scattering paths, mainly Cr – O – O and Cr – O – Re, account for both peaks. The Re L_3-edge FT spectra reveal similar features with a strong peak around 1.5 Å (without a phase shift correction), which corresponds to the Re – O distance. Also two noticeable peaks are observed between 2.5 and 3.8 Å ascribed to Re – Cr, Re – Sr(Sm) single-scattering paths and multiple scattering contributions.

The structural analyse between 1 and 4 Å and between 1.2 and 3.9 Å were performed using the Artemis software [148] in the R-space fitting mode for the Cr and Re edges respectively. The fits are displayed in Figure 5.22. a and b and the main structural parameters for the 1st shell are summarized in the Table 5.10 for two selected temperatures. In the Cr K-edge fits, the coordination numbers were fixed to their crystallographic values and the amplitude reduction factor, s_0^2, was set at 0.7 in agreement with previous calculations [150]. In the case of the Re L_3-edge, the s_0^2 factor was fixed to 0.78 [150] and the crystallographic data were taken as coordination number. Only the E_0, bond-lengths and Debye-Waller factors were refined as in the previous case. The interatomic distances remain practically constant in the whole series and minor changes are noticed with decreasing temperature.

All samples exhibit an average Cr – O bond-length close to 1.955 Å similar to either the reported value [151] in $LaCrO_3$ or the theoretical value expected for a Cr^{3+} ion [57]. The Re – O bond-lengths also concur with the previous crystallographic study and their values are around 1.935 Å, very similar to those found in other double perovskites showing Re^{5+} [122]. Moreover, oxides with formal Re^{6+}, such as ReO_3, show Re – O distances [152] around 1.87 Å, significant smaller than the present case. Therefore, the EXAFS analysis concurs with the XANES study that Ln-addition does not induce significant changes in the Cr oxidation state and agrees with the presence of Re^{5+} for all samples.

The data from Table 5.10 also reveal that CrO_6 octahedron is a bit bigger than ReO_6 one. However, one observes no important difference between Re – O and Cr – O

distances that explains the tendency to form antisite defects in these compounds, the problem that was already raised in the previous subsections. Both atoms have very symmetric octahedral environments as deduced from the small value of the Debye-Waller factors found. These factors remain small even for samples with high Ln-content (where more Cr is located on the Re-site with slight different distances as suggested by the no-doping model assumptions). This suggests that our EXAFS analysis is not sensitive to this minor local change. In fact, the environment changes produced by anti-site defects in these materials are still lower than the spread of Cr – O distances (between 1.94 and 1.99 Å) in the reference compound $LaCrO_3$ [151].

Table 5.10. Structural parameters for the 1st coordination shell (bond-lengths and Debye-Waller factors). They are extracted from the fits of Figure 5.22 for Sr_2CrReO_6 (denoted as Sr_2) and Ln doped samples (denoted as Ln_x – Ln = Sm and Nd) samples. The reliability factors, defined in ref. [148] and [95] refer to the whole fit (not only the 1st shell). Coordination number is fixed to six for all cases.

Sample	*T* (K)	Cr K-edge			Re L_3-edge		
		Cr-O (Å)	σ^2(Å^2)×10^{-3}	R_F	Re-O (Å)	σ^2(Å^2)×10^{-3}	R_F
Sr_2	25	1.954(12)	1.5(7)	0.012	1.935(4)	1.3(5)	0.016
	290	1.957(12)	1.8(7)	0.015	1.937(5)	1.7(5)	0.014
$Sm_{0.1}$	25	1.947(12)	2.0(7)	0.015	1.933(4)	1.8(5)	0.013
	290	1.951(12)	2.2(7)	0.015	1.935(5)	2.1(4)	0.014
$Sm_{0.3}$	25	1.954(12)	1.5(7)	0.017	1.935(4)	1.6(5)	0.018
	290	1.960(12)	1.9(7)	0.018	1.936(5)	2.0(5)	0.017
$Sm_{0.5}$	25	1.961(12)	2.2(7)	0.014	1.935(5)	1.5(4)	0.019
	290	1.965(12)	2.4(7)	0.019	1.937(4)	2.1(5)	0.017
$Nd_{0.1}$	25	-	-	-	1.933(5)	1.6(5)	0.014
	290	-	-	-	1.934(5)	1.7(4)	0.016
$Nd_{0.3}$	25	-	-	-	1.939(4)	1.2(6)	0.018
	290	-	-	-	1.940(5)	1.6(5)	0.02
$Nd_{0.5}$	25	-	-	-	1.937(4)	1.3(5)	0.019
	290	-	-	-	1.939(4)	2.4(6)	0.017

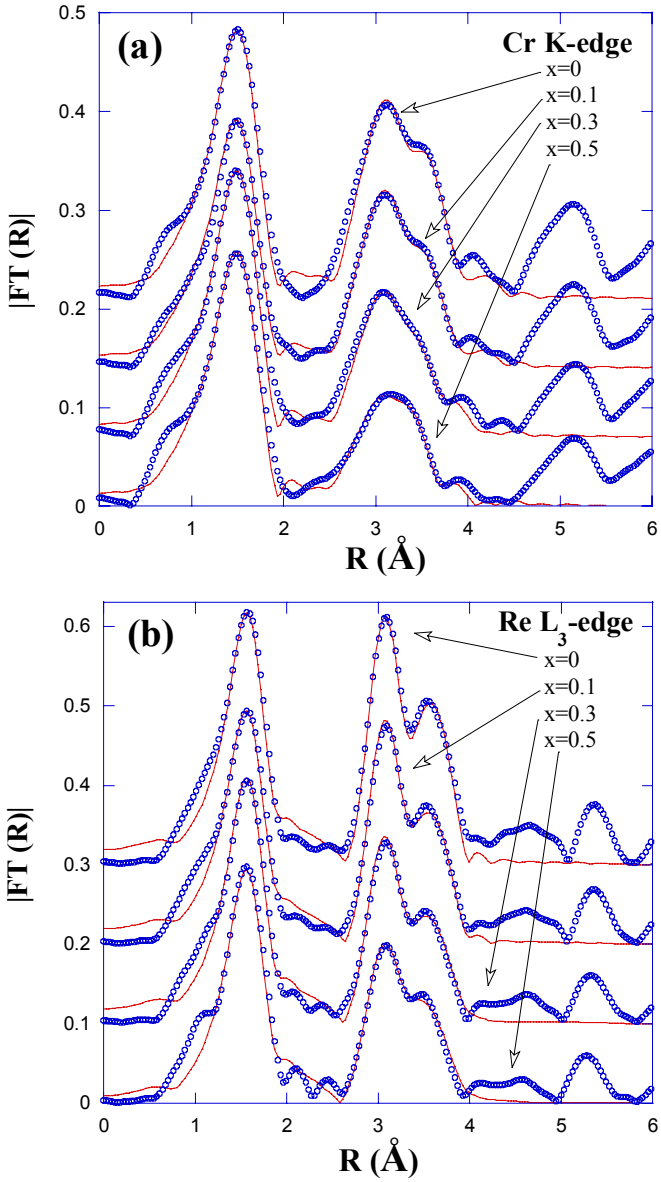

Figure 5.22. a) Fourier transforms of the EXAFS spectra, kχ(k), at the Cr K-edge (a) and Re L_3-edge (b) for Sm doped series at 25 K. Solid lines are the best-fit simulations only considering contributions between 1 and 4 Å for the Cr K-edge 1.2 and 3.9 Å for the Re L_3-edge (as described in the text). The x-values are given for each curve and the spectra are offset for the sake of clarity.

5.4. Electrical properties

We have examined the influence of the Lanthanide addition in terms of the electrical transport properties. The experiments have been performed using a four contact method. Samples were bar shaped with rectangular cross section. The contacts were prepared with silver paste in such way that the spacing between them was as small as possible assuring a lack of direct electrical contact. We have measured the resistance of the material under low and high temperatures for La doping with x = 0.1 as well as for Nd doping with substitution level 0.1 and 0.3. Measurements in function of magnetic field have been performed as well, allowing the investigation of the magnetoresistance effect in the Ln-doped double perovskites. The results of the La 0.1, Nd 0.1 and Nd 0.3 compounds are collected in the Table 5.11. As can be noticed, the low temperature resistance is several orders of magnitude higher compared to the room temperature values. Moreover, there is no significant difference between the resistances of the material doped with different ions. At 10 K the difference between Nd and La doped material with x = 0.1 is less than 2% and it reaches only 6% at 300 K. On the other hand, much more important differences are observed taking into account the different doping levels. This fact can be observed analyzing the data presented in Table 5.11 for Nd doped material (x = 0.1 and 0.3). At 300 K we observe 0.49 Ohm cm for x = 0.1 and 0.73 Ohm cm for x = 0.3. At 10 K the difference becomes even more pronounced. For lower doping (x = 0.1) the resistivity is about 70 times lower than at higher doping level (x = 0.3). If we take a look at the La doped samples the same behavior can be observed.

At Figure 5.23.a the temperature dependence of the resistance (normalized at 350 K) of two samples from this series with nominal doping level x = 0.1 and 0.2 is presented. As can be noticed, the measurement was possible only down to 50 K for higher doping due to the instrumental limitations in the maximum resistance measureable. At this temperature the difference in resistance is about 40 times. In

Table 5.11. Resistance and resistivity of the La and Nd doped samples with nominal doping level x = 0.1 and 0.3 (labeled as La 0.1, Nd 0.1 and Nd 0.3) under various temperatures. In the last column, the magnitude of the magnetoresistance effect is shown.

	T (K)	R_{max} (Ohm)	ρ_{max} (Ohm cm)	MR_h at 9 T (%)
La 0.1	10	5146.0	423	-15.64%
	100	114.0	9.5	-5.61%
	200	16.4	1.4	-2.78%
	300	5.1	0.46	-1.52%
Nd 0.1	10	5390.8	416	-17.39%
	300	6.4	0.49	-1.90%
Nd 0.3	10	$351*10^3$	$28*10^3$	-17.06%
	300	9.2	0.73	-1.15%

order to explain such large variations in electrical transport properties we shall keep in mind important differences in microstructure rather than local ordering and bonding. On the one hand, our Cr K-edge XANES analysis reveals that the orbital overlapping of the Cr and oxygen orbitals changes (diminishes) on doping possibly due to structural effects. However, the impact of the deviation of the bond angles in the Cr – Re – Cr paths on the transport properties is not sufficient to produce such large changes in the conductivity. On the other hand, transport properties of the granular polycrystalline material are mainly controlled by the grain-grain interface. The grain boundaries are proven to have several kinds of defects, producing an insulating behavior. These are structural defects, oxygen vacancies and magnetic imperfections. All of them are of great importance from the conductivity point of view, as they tend to enhance electron scattering. The most important feature, nevertheless, is the change of microstructure that was observed by Scanning Electron Microscopy. The presence of larger amount of small grains as the doping level increases results in the increase of grain boundaries per unit volume of the material. Moreover, as was said before,

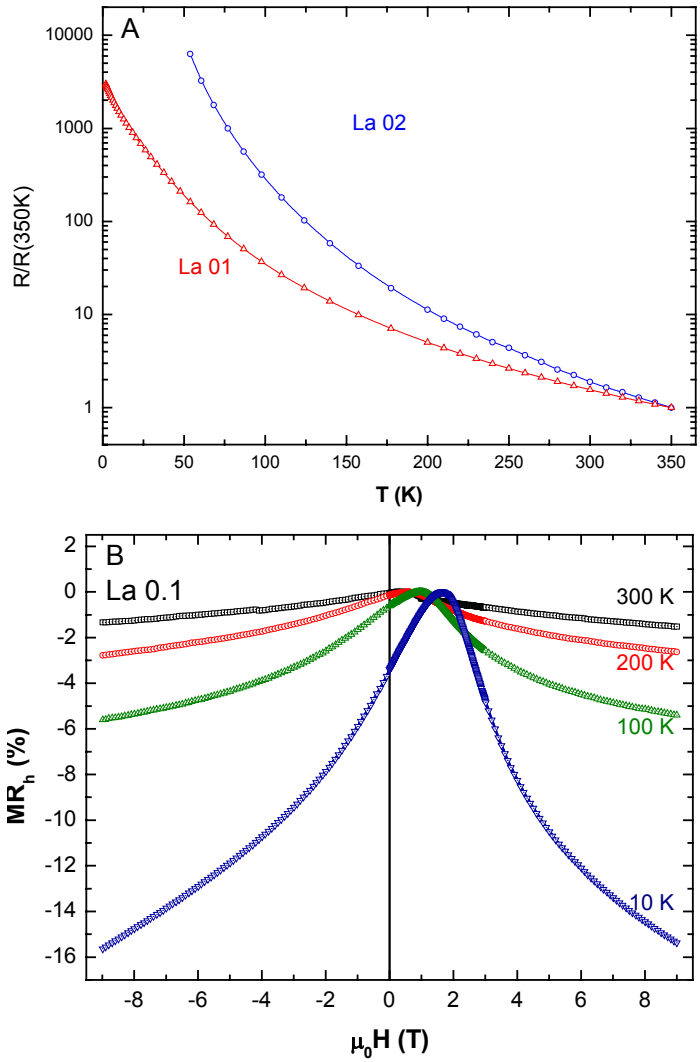

Figure 5.23.(a) Thermal evolution of the resistance (normalised at 350 K) for the two La doped samples. (b) Magnetoresistance curves for the $Sr_{1.9}La_{0.1}CrReO_6$ sample at different temperatures (as indicated in the figure). The magnetoresistive effect is more pronounced at lower temperatures.

heavily doped samples exhibit more porosity, so less conducting paths can be found through the bulk sample. Thus, we would rather assign the observed behavior to extrinsic effects rather than arising from intrinsic band effects caused by doping.

We shall focus for a while on the magnetic field influence on the conductivity. As in the case of the parent compound (Sr_2CrReO_6) an important contribution of the

insulating grain boundary to the resistance allows anticipating the Intergrain Tunneling Magnetoresistance (ITMR) effect to be present also in the Lanthanide doped material. The doped material, similarly to the undoped one, is magnetically hard (as presented in the following subsections), making difficult the study of its magnetotransport properties. As can be seen in the Figure 5.23.b an enormous magnetic field is needed in order to saturate the magnetoresistance effect for a Lanthanum doped sample with $x = 0.1$. The MR_h value reached at 9 T at low temperature is about 15% and a lack of saturation of the effect is clearly visible. At higher temperatures the magnetoresistance is diminished and at room temperature it is less than 2%. Even though the effect is poorly pronounced up to the applied fields of 9 T, a butterfly-like shape of the MR_h vs. applied field curves evidences a presence of the ITMR effect. This indicates that the bands lying at the Fermi level are spin polarized. The effects producing low values of the magnetoresistance effect can be: a large coercivity, a reduced level of spin polarization due to the spin orbit-coupling coupling in the Re ion (as described in previous chapters), a non-spin-polarized conduction channel due to antisite defects and other types of defects, especially those occurring at the grain boundaries, etc. Moreover, in contrast to the previous results presented by De Teresa et al [133] at low temperatures the magnetoresistance peak appears closely to the coercive field, however at room temperature the coercivity is almost twice the field at which the MR peak is located.

5.5. Magnetic studies of lanthanide doped family

The magnetic properties of the doped series were first investigated under low magnetic fields (up to 5 T) both in high and low temperatures range. Also high pulsed fields (up to 50 T) experiments have been performed. However, in this chapter we will focus mainly on the data obtained with SQUID magnetometer under fields up to 5 T at low temperatures (below room temperature) and with VSM magnetometer at high temperatures (from room temperature up to temperatures above magnetic ordering). As will be discussed later, the latter will give further support to the model of the doped series that considers a lack of electron doping and destruction of the double perovskite ordering in the doped material.

5.5.1. Low field (up to 5 T) experiments: consequences of doping on the magnetic properties

The low field (up to 5 T) magnetisation measurements allowed us the examination of the consequences of the doping on magnetic properties. However the lack of magnetic saturation under 5 T already disclosed in Sr_2CrReO_6 avoids detailed studies of the impact of the introduction of additional electrons on the saturation magnetization. The electron doping model assumes that the saturation magnetization should be lowered on increasing doping level as discussed in chapter 1.5. The measurements (see Figure 5.24) show a clear dependence of the maximum magnetization M_{max} (at 5 K and 5 T) on the doping level. Naively, one could conclude that electron doping is indeed present in the system. If the data on M_{max} presented in the Table 5.12 is plotted as a function of x, as presented in the Figure 5.25 we observe a linear decrease with the amount of Lanthanide introduced. The slope of the line is similar to that one theoretically proposed for the electron doping in double perovskites and the lower absolute values compared to the theoretical line could be attributed to the presence of antisite disorder. Nevertheless, the high field measurements, see the inset of the Figure 5.25, indicate that taking the 5 T magnetization and using it as an electron doping model testing is not a correct approach because magnetic saturation only occurs under ~20 T. At this point, we can conclude that the electron doping model cannot be confirmed on the basis of the low field magnetization measurements.

Let us focus for a while on the coercive field of the different compounds belonging to the Lanthanide doped series. As can be seen in the Table 5.12 the coercivity of the material differs for samples with diverse doping. However, it is impossible to find any systematic variation among the series. We have tried to find a correlation between the mean ionic radius at the A crystallographic site (see Table 5.1) and the coercive field. For all the samples the coercive field is higher compared to the parent Sr_2CrReO_6 compound [H_C = 1.2(9) T]. The two highest values are obtained for Nd x = 0.5 and Sm x = 0.3 samples (H_C = 1.9(4) and 2.1(8) T respectively). Between

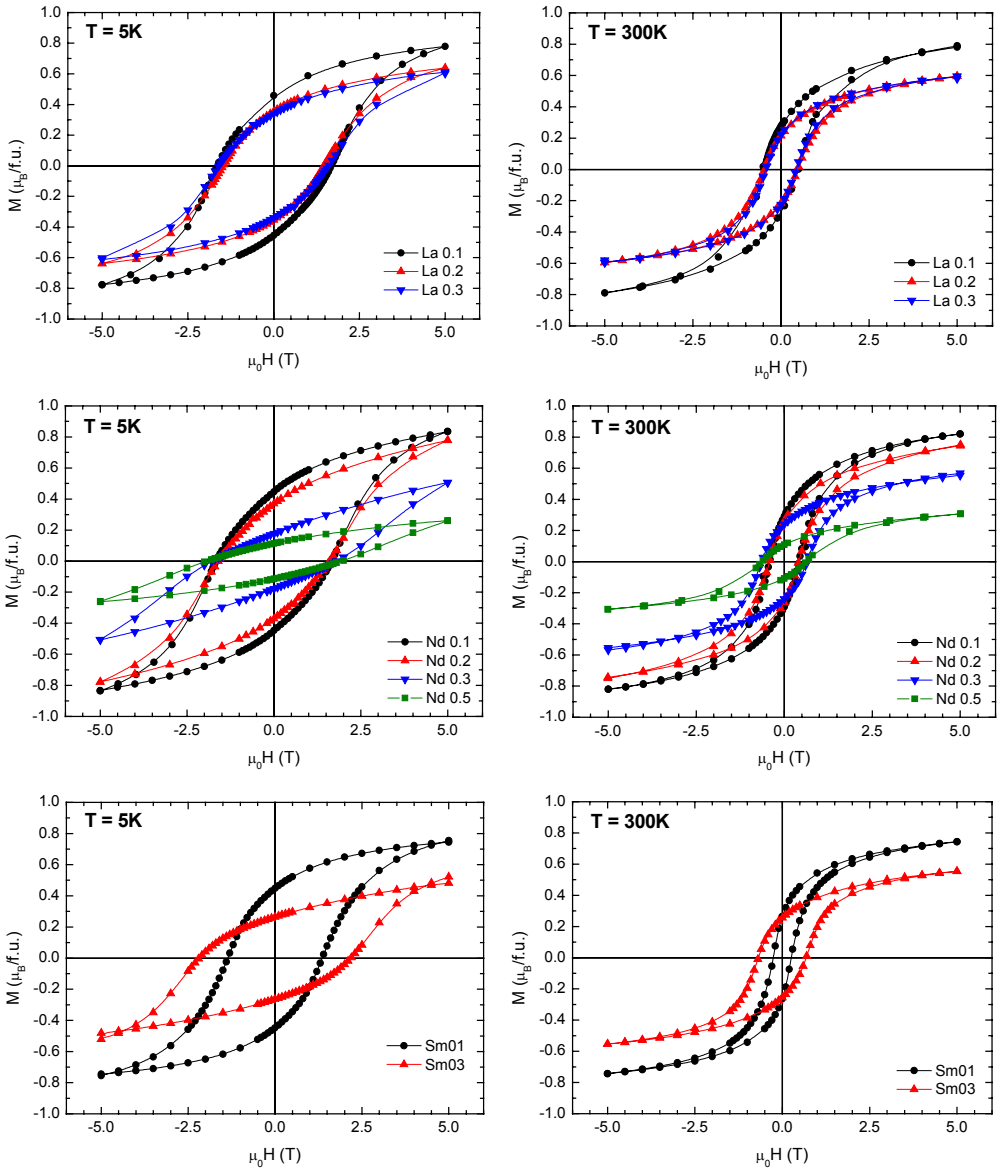

Figure 5.24. Magnetization curves at 5 K (left column) and 300 K (right column) for La, Nd and Sm doped samples (as indicated in the figures). The maximum value of the magnetisation measured at 5 T is varying with the doping level, but it does not change significantly between 5 and 300 K.

those values the variation becomes in the range of experimental error and the linear fitting of the data becomes untrustworthy. In conclusion, it is not possible to establish any correlation between the coercive field and the magneto-crystalline anisotropy

through the variation of the mean ionic radius at the *A* site. Together with this type of intrinsic dependence, an extrinsic dependence related to the microstructure or presence of defects cannot be discarded.

Table 5.12. Magnetic properties extracted from the 5 K magnetization loops (maximum magnetization and coercive field) for samples belonging to the Lanthanide doped series for various Ln contents.

Ln	doping level (x)	Magnetisation at 5 T (μ_B/f.u.)	Coercive field (T)	Bond angle around in plane / apical oxygen atoms
		5 K	5 K	
--	0	0.89(4)	1.2(9)	173.9(9) / 180.0(1)
La	0.1	0.77(6)	1.6(8)	171.4(3) / 180.0(3)
	0.2	0.63(8)	1.4(6)	
	0.3	0.61(2)	1.5(9)	167.9(6) / 180.0(4)
Nd	0.1	0.83(4)	1.6(6)	170.7(5) / 180.0(13)
	0.2	0.77(8)	1.6(1)	168.7(6) / 180(1)
	0.3	0.49(6)	1.7(2)	166.7(6) / 180(1)
	0.5	0.26(1)	1.9(4)	
Sm	0.1	0.74(5)	1.3(5)	
	0.3	0.52(1)	2.1(8)	

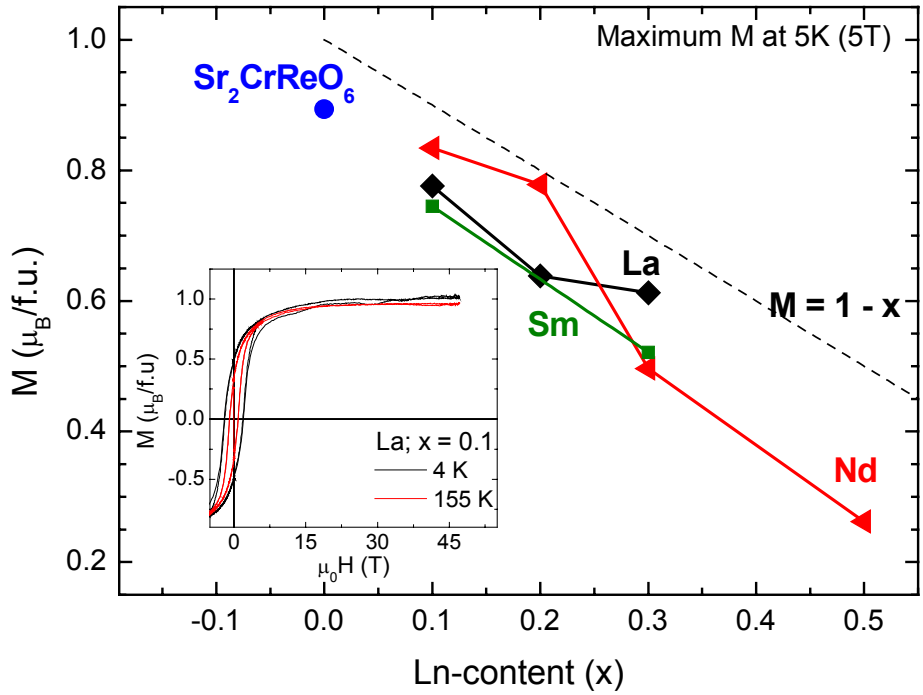

Figure 5.25. Magnetisation values under an applied field of 5 T at 5 K for different doping levels and different dopants. The dependence of the magnetisation under such condition on the doping level is clearly visible, and is not influenced by the doped ions type. The dashed line is the spin-only ionic model prediction of the saturation magnetisation variation on electron doping. In the inset: magnetization loops up to high fields for La x = 0.1 sample at 4 and 155 K showing a saturation only at a applied field of 20 T and the decrease of the coercive field on temperature rise.

If the electron doping is indeed present in the CrRe based double perovskite, the Curie temperature should rise on increasing the doping level. We have measured the magnetisation versus temperature for Neodymium doped samples for x = 0.1, 0.2, 0.3 and 0.5. In this way we were able to examine the influence of Lanthanide addition on the strength of magnetic interactions. In the top panel of the Figure 5.26 we present the magnetisation curves measured with the VSM magnetometer under an applied field of 1 T in the temperature range from 300 to 700 K. Taking into account that the application of a high magnetic field produces a broadening of the transition from magnetically ordered to magnetically disordered state, a correct estimation of T_C is more difficult. On the other hand, we have observed that at lower applied fields

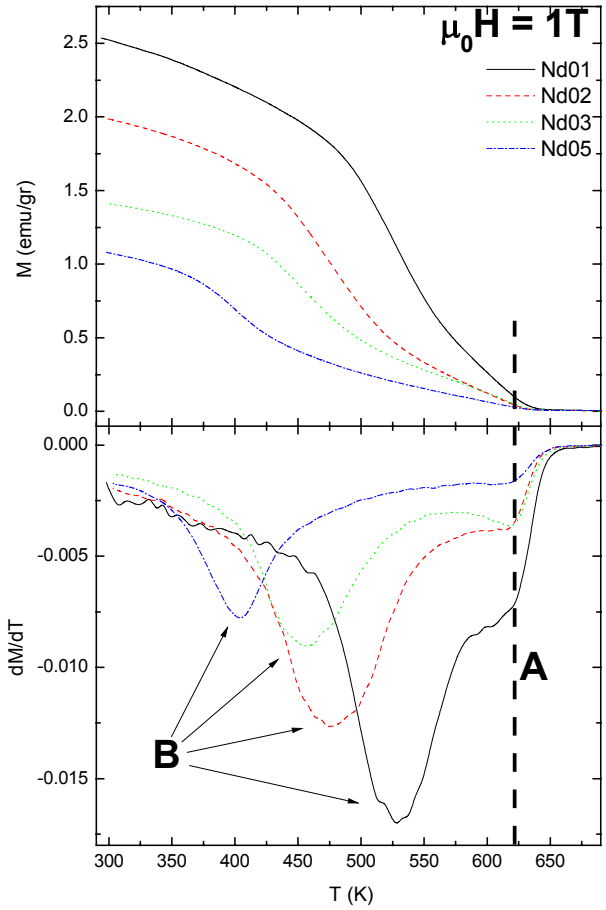

Figure 5.26. Magnetisation versus temperature curves measured between 300 and 700 K under an applied field of 1 T for four Nd doped samples (doping level x = 0.1, 0.2, 0.3 and 0.5 as shown in the figure) together with the derivative of the magnetisation with respect to the temperature showing two peaks (denoted as A and B).

(~100 Oe) the magnetisation tends to exhibit two slopes, which eventually results in a rising and a falling part. The double slope shape is visible even under the field of 1 T that together with lower field measurements indicate the presence of two magnetically ordered phases with different magnetic ordering temperatures.

The maximum slope extrapolation method is not sufficiently accurate in the present case so we have decided to search for the maximum of the first derivative of the magnetisation with respect to the temperature. This corresponds to the temperature at which the inflection of the magnetisation curve is present. In this way all changes of

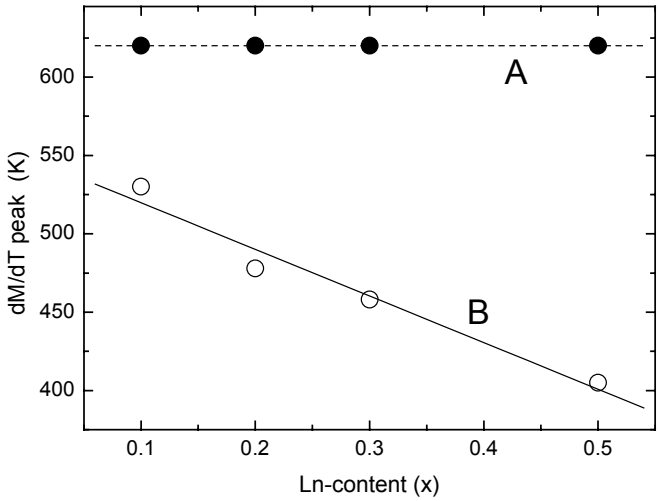

Figure 5.27. Dependence of the first derivative maximum position in the temperature scale on Ln-content (x). A and B correspond to the peaks shown in the Figure 5.26.

the slope of the magnetisation curve are easily traced. First derivatives of the magnetisation curves are presented in the bottom panel of the Figure 5.26. At first sight, a maximum is visible. However there is also an interesting feature at higher temperatures. A shoulder of the first derivative peak is present at 620 K (labelled A in the Figure 5.26) for all doping levels. On the contrary the first maximum (marked as B in same figure) is moved towards lower temperatures on increasing a doping level x (see also Figure 5.27). This clearly proves the presence of two phases in the material, both magnetically ordered. One of the phases is formed with dependence on the doping level, while the other seems to be independent on it. At this point we may attribute the A feature to a perfect Sr_2CrReO_6 double perovskite as the Curie temperature for this compound is reported to be about 620 K in perfect agreement with the result just shown.

Not only the direct magnetization versus temperature curves can give some information about the magnetic interactions in the material. From the inversed magnetization loops one can learn on the kind of magnetic ordering – whether the dominating mechanism is ferromagnetic or antiferromagnetic in its nature. In the Figure 5.28 the inversed magnetization versus temperature curves are presented. Up to temperature of about 600 K, the value of $1/M$ is close to zero. Beyond that temperature

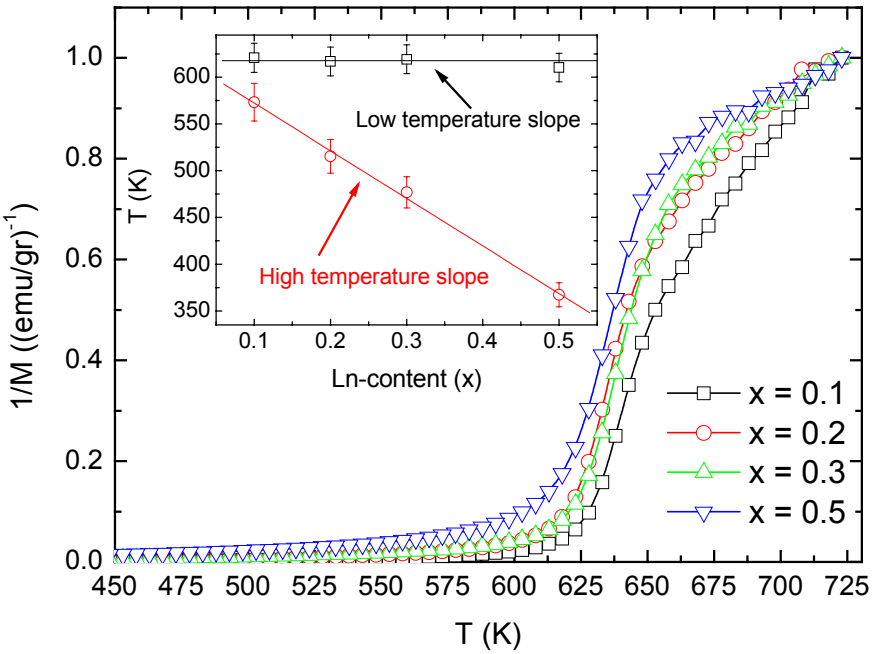

Figure 5.28. Inversed magnetisation curves as a function of temperature for Nd doped samples with different doping levels normalised at 725 K for clarity. The curves have been fitted with linear functions for higher and lower temperature ranges independently. In the inset: the point of the intersection of the temperature scale with a linear extrapolation of the two linear parts of the inversed magnetisation loops presented in the main figure.

the shape of the curve becomes more complex. For a single phase ferromagnetic material one would expect a linear part and the intersection of the extrapolation of such growing part would give the information on the magnetic ordering temperature. In our case, there are two linear parts for each sample.

As can be seen in the figure for the samples with different doping levels in the temperature range between 625 and 660 K the slope is nearly the same. Over the 660 K temperature the samples start to behave in different manner, depending on the doping level. One can see that the slope becomes lower on higher doping levels so it is the biggest (and similar to the lower temperatures one) in case of $x = 0.1$ and the lowest in the heavily doped sample ($x = 0.5$) (see Figure 5.29 and the inset in the Figure 5.28). On intermediate doping the slope is between the former two. Again

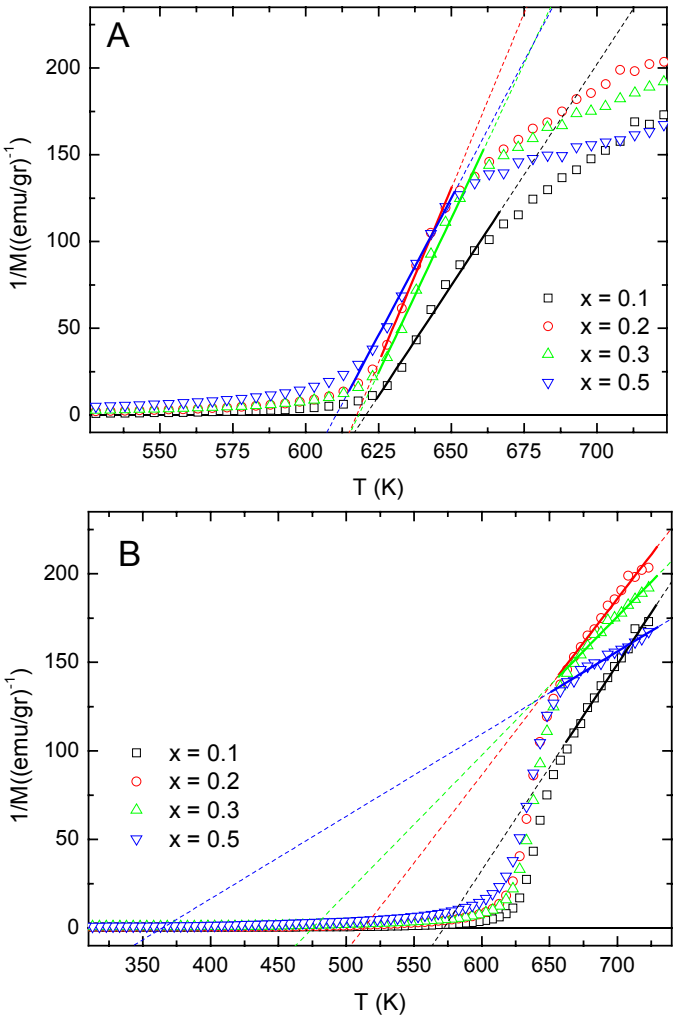

Figure 5.29.Linear fits of the low (a) and high (b) temperature inversed magnetization curves for Nd doped samples.

extrapolating a linear fit performed in the range 665 to 725 K one can obtain the characteristic temperatures values. As could have been expected, the intersection point is lower the higher the doping level is. Indeed, it closely follows the B peak in the first derivative of the M vs. T curves. This indicates that the nature of the magnetic interaction of the second phase is ferromagnetic (or ferrimagnetic) and that the strength of this interaction decreases with the doping.

5.6. Verification of the models

At the beginning of the chapter we have proposed two possible models to explain the behaviour of the Sr_2CrReO_6 double perovskite when the Sr ions are replaced with a Lanthanide.

The first one was the electron doping model which assumed in terms of crystallography no change in the ordered double perovskite structure apart of steric effects due to different ionic radius of dopant with respect to the Sr cation. Assuming this model to be true we have expected a change of magnetic interactions strength and consequently enhancement of the Curie temperature. The introduction of the electrons into the system should have also been reflected in changes in the electronic state of Cr and/or Re ions that could have been detected by XANES spectroscopy. On the other hand, within the simplest spin-only ionic picture we have predicted the lowering of the saturation magnetisation (that should hold true even for the system with important spin-orbit coupling). Obviously the stress induced lowering of the symmetry could have an impact on the magnetic properties such as coercivity.

During the work on doped samples characterisation the idea of the new model arose. We have called it the no-doping model. In this case the typical DPs stoichiometry is not maintained. Then the rest of the study was aimed to investigate which of the models holds true. Hereafter we will revise the results step by step.

The SEM imaging allowed the study of microstructure and, together with EDX the chemical composition. For the first time we have observed a stoichiometry different from the desired one. Later on the EDS results have been confirmed by the fluorescence measurements.

The complex structural and magnetic study by means of NPD showed the distinguishable differences between the models. First, the structural and stoichiometry information given as an input results in fits having different quality. Moreover, the goodness-of-the-fit depends on doping level. We would rather conclude that high temperature spectra analysis supports the no-doping model. The magnetic phase

refinements have revealed the quite surprising inversion of the magnetisation of the Re ions at certain temperature and more visible for higher x. Also, the e-doping model fails in refining the La x = 0.5 sample in the magnetic phase temperature range. The magnetic study does not give a clear answer about which of the models works better. However, together with the structural part at low temperatures, it still suggests the no-doping option.

The XAS measurements in the XANES range are certainly proving a lack of electron doping. We have observed that the electronic state of Cr and Re ions of the parent Sr_2CrReO_6 double perovskite is preserved over the whole doping range. Such conclusion is strongly supported by the Cr K-edge and $L_{1,2,3}$-edge spectra analysis. We do observe some systematic changes in the spectra on doping at the Cr K-edge that are due to the bond angles deviation from 180°. That is not only in agreement with the NPD structural results, but ensures the XANES spectroscopy has enough resolution to distinguish the doping levels varying of 10%.

The electric and magnetotransport properties are not giving support for any of the models, as they can be explained on the basis of microscopic properties of the material, without going deeper into the underlying physics.

The magnetic study reveals the importance of the crystallographic structure (bond angles and lengths). The saturation magnetisation is not obtained in conventional laboratory equipment so we lack data showing the impact of the electrons added into the system on the magnetic interactions. We observe an impurity phase (a clearly visible double transition to the magnetically disordered state on heating), which has been assigned to the parent compound Sr_2CrReO_6.

To put everything into a nutshell we would rather claim the electron doping fails in case of the Sr_2CrReO_6 double perovskite. The reason why it was possible to perform such doping in the FeRe and FeMo based compounds in sharp contrast to our case remains open. This may be due to the high stability of the electronic $Cr^{3+} - O - Re^{5+}$ state, rather than a crystallographic structure reason. On the other hand it was

proposed [153] that a rise of Curie temperature may be achieved not by the electron doping itself as proposed for FeRe and FeMo double perovskites, but by the magnetically ordered state stabilization caused by the increased structural defects amount while additional atoms are introduced.

Conclusions

Summarizing, we have performed a detailed characterization of the Re-based double perovskite samples by means of a wide range of experimental techniques. Our work has focused on the study of the A_2FeReO_6 series (with A = Ba, Sr and Ca), the Sr_2CrReO_6 compound, and the $Sr_{2-x}Ln_xCrReO_6$ (with Ln = La, Nd and Sm). The main obtained results are:

We have presented detailed structural studies of the Sr_2CrReO_6 sample by x-ray diffraction and Neutron Powder Diffraction. On the basis of the available data we have shown the procedure of estimating the amount of structural defects (the antisites). We have also discussed the thermal evolution of the lattice constants for CrRe-based material, as well as the local magnetic moments carried by the Cr and Re ions.

The low field magnetization experiments confirm the high Curie temperature of the Sr_2CrReO_6. We have also obtained the information on the magnetic purity of the double perovskite samples from the high-temperature low-field magnetization data.

We have studied the magnetization of Sr_2CrReO_6 samples (with different levels of antisite defects) as well as Ca_2FeReO_6, $BaSrFeReO_6$ and Sr_2FeReO_6 samples up to very high field demonstrating the saturation magnetization is reached only at very high magnetic fields. Moreover, even in the case of lack of full saturation, the obtained values overcome the limits given by the intuitive spin-only ionic model. This has been explained in terms of a significant Re orbital moment that is antiparallel to the Re spin moment but parallel to the Fe magnetic moment. The impact of this finding on the presumed half-metallicity of these compounds has been discussed. Implications of these results for the physics of Re-based compounds, in particular concerning magnetostructural effects and application of these compounds in the field of spin electronics, have also been raised.

On the basis of high field magnetization measurements we have performed a

detailed study of the magnetic properties of the Re-based double perovskite series. We have ascribed the lack of saturation under an applied magnetic field as high as 30 T to the influence of magnetically disordered grain boundaries. We have successfully applied the approach to saturation model widely used in spin-glasses with a weak random anisotropy field to the investigated materials. As the electrical transport is strongly dependent on the tunneling intergrain resistance, the understanding of the effects caused by the magnetic field on these grain boundaries in defect-free samples will be of great importance. We have also investigated the thermal evolution of the saturation magnetization, remanence and the coercive field.

Results of the high field magnetization measurements encouraged us to use a local probe method of investigating the magnetic moments carried by the particular ions in the material. We are reporting the pulsed-field X-ray Magnetic Circular Dichroism results obtained in the pioneer experiments, clearly showing that the orbital contribution of the Re magnetic moment is coupled to the Fe and Cr spin magnetic moments. Such coupling causes the Re orbital part of the magnetic moment to be aligned parallel to the Fe spin moment, and consequently, the Re-spin moment to be antiparallel to the former contributions.

The importance of the unquenched Re orbital moment in the magnetism of the Re-based double perovskite family was demonstrated by the relation between the coercivity of the material and the magnetocrystalline anisotropy.

The second part of the work is related to the electron doping of the Sr_2CrReO_6 double perovskite and makes it doubtful that such doping is really achieved. We have discussed the electron doping model previously used in other double perovskite systems. We have also proposed the no-doping model that explains a lack of electron doping in the system. Comparing the results for the two models obtained on the basis of the Rietveld refinement of the diffraction data we are able to support the no-doping model rather than the e-doping one. The structural part of the refinements of the diffraction data finds support in the EDX and fluorescence experiments. The XAS experiments give further support to the no-doping model. In the XANES range we do

not observe any systematic changes in the absorption spectra due to the *d*-band filling effects. Also the EXAFS study reveals no change in the oxidation state of neither Cr or Re on increasing doping. We have found the low field magnetization data rather insufficient to elucidate the correctness of one of the model as a lack of magnetic saturation makes the analysis doubtful. On the other hand, the magnetotransport properties can be related to microstructural effects observed by SEM rather than to intrinsic structural or electronic effects. In order to conclude this part of the work we have to say that we would rather incline towards the no-doping model than to the e-doping one. We are not able, however, to discard the possibility of the electron doping to be achieved via different synthesis routes.

References

[1] I. I. Mazin, *How to Define and Calculate the Degree of Spin Polarization in Ferromagnets*, Phys. Rev. Lett. **83**, 1427-30 (1999)

[2] J. M. D. Coey and S. Sanvito, *Magnetic semiconductors and half-metals,* J. Phys. D: Appl. Phys. **37**, 988-93 (2004)

[3] R. A. de Groot, F. M. Mueller, P. G. van Engen and K. H. J. Buschow, *New Class of Materials: Half-Metallic Ferromagnets*, Phys. Rev. Lett. **50**, 2024-2027 (1983)

[4] *Technology Roadmap for Nanoelectronics*, European Commission IST programme, Edited by: R. Compaño, L. Molenkamp, D.J. Paul, 001 ISBN 92-894-1070-2 (KK-29-00-755-EN-C)

[5] G. A. Prinz, *Magnetoelectronics applications*, J. Magn. Magn. Mat. **200**, 57-68 (1999)

[6] Ching Tsang, Tsann Lin, S. MacDonald, M. Pinarbasi, N. Robertson, H. Santini, M. Doerner, T. Reith, Vo Lang, T. Diola and P. Arnett, *5 Gb/in^2 recording demonstration with conventional AMR dual element heads and thin film disks*, IEEE Trans. Magn. **33**, 2866-2871 (1997);

P. Grunberg, *Magnetic Field Sensor With Ferromagnetic Thin Layers Having Magnetically Antiparallel Polarized Components*, U.S. Patent 4.949.039

[7] T. Matsuno, S. Sugahara and M. Tanaka, *Novel Reconfigurable Logic Gates Using Spin Metal–Oxide–Semiconductor Field-Effect Transistors*, Japan. J. Appl. Phys. **43**, 6032-6037 (2004)

[8] M. Tanaka, *Spintronics: recent progress and tomorrow's challenges*, J. Cryst. Growth **278**, 25-37, (2005)

[9] P. Sharma, *How to Create a Spin Current*, Science **307**, 531-533 (2005)

[10] I. Žutić, J. Fabian and S. Das Sarma, *Spintronics: Fundamentals and applications*, Rev. Mod. Phys. **76**, 323-410 (2004)

[11] F. Y. Yang, Kai Liu, Kimin Hong, D. H. Reich, L P. C. Searson and C. L. Chien, *Large Magnetoresistance of Electrodeposited Single-Crystal Bismuth Thin Films,* Science **284** 1335-7 (1999)

[12] W. Thomson, Proc. R. Soc. London Ser. A **8**, 546 (1857)

[13] M. Ziese and H. J. Blythe, *Magnetoresistance of magnetite*, J. Phys.: Condens. Matter **12**, 13-28 (2000)

[14] P. G. De Gennes and J. Friedel, *Anomalies de résistivité dans certains métaux magniques*, Journal of Physics and Chemistry of Solids **4**, 71-7 (1958)

[15] M. E. Fisher and J. S. Langer, *Resistive Anomalies at Magnetic Critical Points*, Phys. Rev. Lett. **20**, 665-8 (1968)

[16] R. von Helmolt, J. Wecker, B. Holzapfel, L. Schultz and K. Samwer, *Giant Negative Magnetoresistance in Perovskitelike $La_{2/3}Ba_{1/3}MnO_x$ Ferromagnetic Films*, Phys. Rev. Lett. **71**, 2331-3 (1993);

S.-H. Jin, T. H. Tiefel, M. McCormack, R. A. Fastnacht, R. Ramesh and L. H. Chen, *Thousendfold change in resistivity in magnetoresistive La-Ca-Mn-O films*, Science **264**, 413 (1994);

G. Jeffrey Snyder, Ron Hiskes, Steve DiCarolis, M. R. Beasley and T. H. Geballe, *Intrinsic electrical transport and magnetic properties of $La_{0.67}Ca_{0.33}MnO_3$ and $La_{0.67}Sr_{0.33}MnO_3$ MOCVD thin films and bulk material*, Phys. Rev. B **53**, 14434-44 (1996);

[17] A. P. Ramirez, *Colossal magnetoresistance*, J. Phys.: Cond. Matter **9**, 8171-99 (1997)

[18] D. Serrate, J. M. De Teresa, P. A. Algarabel, J. Galibert, C. Ritter, J. Blasco and M. R. Ibarra, *Colossal magnetoresistance in $Ca_xSr_{2-x}FeReO_6$ double perovskites due to field-induced phase transition*, Phys. Rev. B **75** 165109 (2007)

[19] J. M. de Teresa, M. R. Ibarra, J. Blasco, J. Garca, C. Marquina, P. A. Algarabel, Z. Arnold, K. Kamenev, C. Ritter and R. von Helmot, *Spontaneous behaviour and magnetic field and pressure effects on $La_{2/3}Ca_{1/3}MnO_3$ perovskite*, Phys. Rev. B **54**, 1187-93 (1996)

[20] A. Fert, *Nobel Lecture: Origin, development, and future of spintronics*, Rev. Mod. Phys. **80**, 1517-30 (2008)

[21] G. Binasch, P. Grünberg, F. Saurenbach and W. Zinn, *Enhanced magnetoresistance in layered magnetic structures with antiferromagnetic interlayer exchange*, Phys. Rev. B **39**, 4828-30 (1989)

[22] M. N. Baibich, J. M. Broto, A. Fert, F. N. V. Dau and F. Petroff, *Giant Magnetoresistance of (001)Fe/(001)Cr Magnetic Superlattices*, Phys. Rev. Lett **61**, 2472-5 (1988)

[23] P. Grünberg, R. Schreiber, Y. Pang, M. B. Brodsky and H. Sowers, *Layered Magnetic Structures: Evidence for Antiferromagnetic Coupling of Fe Layers across Cr Interlayers*, Phys. Rev. Lett. **57**, 2442-5 (1986);

C. Carbona and S. F. Alvarado, *Antiparallel coupling between Fe layers separated by a Cr interlayer: Dependence of the magnetization on the film thickness*, Phys. Rev. B **36**, 2433-5 (1987)

[24] C. Chappert, A. Fert and F. Nguyen Van Dau, *The emergence of spin electronics in data storage*, Nature Materials **6**, 813-23 (2007)

[25] A. Barthélémy, A. Fert and F. Petroff, *Giant magnetoresistance in magnetic multilayers*, Handbook of Magnetic Materials **12** (edited by K. H. J. Buschow) Elsevier Science 1999

[26] M. Julliére, Phys. Lett. **74**, 3273 (1975)

[27] J. S. Moodera and G. Mathon, *Spin polarized tunneling in ferromagnetic junctions*, J. Magn. Magn. Materi. **200**, 248-73 (1999)

[28] C. Tiusan, F. Greullet, M. Hehn, F. Montaigne, S. Andrieu and A. Schuhl, *Spin tunnelling phenomena in single-crystal magnetic tunnel junction systems*, J. Phys.: Condens. Matter **19,** 165201(2007)

[29] J. S. Moodera, T. S Santos and T.Nagahama, *The phenomena of spin-filter tunnelling*, J. Phys.: Condens. Matter **19**, 165202 (2007)

[30] H. Y. Hwang, S-W. Cheong, N. P. Ong and B. Batlogg, *Spin-Polarised Intergrain Tunneling in* $La_{2/3}Sr_{1/3}MnO_3$, Phys. Rev. Lett. **77**, 2041-4 (1996)

[31] J. Inoue and S. Maekawa, *Theory of tunnelling magnetoresistance in granular magnetic films*, Phys. Rev. B **53**, R11927 (1996)

[32] A. del Moral, P. A: Algarabel, J. I. Arnaudas, L. Benito, M. Ciria, C. de la Fuente, B. García-Landa, M. R. Ibarra, C. Marquina, L. Morellón and J. M. De Teresa, *Magnetostriction effects*, J. Magn. Magn. Mater. **242-245**, 788-96 (2002)

[33] F. Bloch, Z. Physik **61**, 206 (1930);

F. Bloch, Z. Physik **74**, 295 (1932)

[34] F. J. Dyson, *General Theory of Spin-Wave Interactions*, Phys. Rev. **102,** 1217-30 (1956);

[35] F. J. Dyson, *Thermodynamic Behaviour of an Ideal Ferromagnet*, Phys. Rev. **102**, 1230-44 (1956)

[36] T. Oguchi, *Theory of Spin-Wave Interactions in Ferro- and Antiferromagnetism*, Phys. Rev. **117**, 117-23 (1960)

[37] C. M. Srivastava and R. Aiyar, *Spin wave stiffness constants in some ferrimagnets*, J. Phys. C: Solid State Phys. **20**, 1119-28 (1987)

[38] C. Kittel, Introduction to solid state physics, PWN, Third edition, 1976

[39] A. Z. Solontsov, *Finite-temperature magnons in itinerant ferromagnetism*, Journal. Magn. Magn. Matter **140-144**, 215-6 (1995)

[40] D. Zając, M. Sikora, V. Prochazka, M. Borowiec, J. Stępień, Cz. Kapusta, P. C. Riedi, C. Marquina, J. M. De Teresa and R. Ibarra, *Local Magnetic and Electronic Properties of the* $A_2FeM'O_6$ *(A = Ba, Sr, Ca,, M' = Mo, Re) Double Perovskites*, Acta Phys. Pol. A **111**, 797-820 (2007)

[41] A. Yanase and K. Siratori, *Band structure in the high temperature phase of* Fe_3O_4, J. Phys. Soc. Jpn. **53**, 312-317 (1984)

[42] K. Schwartz, CrO_2 *predicted as a half-metallic ferromagnet*, J. Phys. F, Met. Phys. **16**, L211 (1986);

J. M. D. Coey and M. Venkatesan, *Half-metallic ferromagnetism: Example of CrO2 (invited)*, J. Appl. Phys. **91**, 8345-50 (2002)

[43] W. Pickett and D. Singh, *Electronic structure and half-metallic transport in the $La_{1-x}Ca_xMnO_3$ system*, Phys. Rev. B **53**, 1146-60 (1996)

[44] M. Bibes and A. Barthélémy, *Oxide Spintronics*, IEEE Trans. on Electron Devices **54**, 1003-23 (2007)

[45] D. J. Huang, C. F. Chang, J. chen, L. H. Tjeng, A. D. Rata, W. P. Wu, S. C. Chung, H. J. Lin, T. Hibma and C. T. Chen, *Spin-resolved photoemission studies of epitaxial Fe_3O_4(100) thin films*, J. Magn. Magn. Mater. **239**, 261-265 (2002);

Y. S. Dedkov, U. Rüdiger and G. Güntherodt, *Evidence for the half-metallic ferromagnetic state of Fe_3O_4 by spin-resolved photoelectron spectroscopy*, Phys. Rev. B **65**, 064417 (2002)

[46] K. S. Yoon, J. Y. Yang, K. W. Kim, J. H. Koo, C. O. Kimans and J. P. Hong, *Room temperature operation of magnetic tunnel transistors with half-metallic Fe_3O_4 emitter source*, J. Appl. Phys **95**, 6933-5 (2004)

[47] S. van Dijken, X. Fain, S. M. Watts, K. Nakajima and J. M. D. Coey, *Magnetoresistance of Fe_3O_4/Au/Fe spin-valve structures*, J. Magn. Magn. Mater. **280**, 322-6 (2004)

[48] R. J. Soulen, J.M. Byers, M. S. Osofsky, B. Nadgorny, T. Ambrose, S. F. Cheng, P. R. Broussard, C. T. Tanaka, J. Nowak, J. S. Moodera, A. Barny and J. M. D. Coey, *Measuring the spin polarization of a metal with a superconducting point contact*, Science **282**, 85-8 (1998)

[49] A. Gupta, X. W. Li and G. Xiao, *Inverse magnetoresistance in chromium-dioxide-based magnetic tunnel junctions*, Appl. Phys Lett. **78,** 1894-6 (2001)

[50] S. Parker, P. G. Ivanov, D. M. Lind, P. Xiong and Y. Xin, *Large inverse magnetoresistance of CrO_2/Co junctions with an artificial barrier*, Phys. Rev. B **69**, 220413(R) (2004)

[51] J. H. Park, E. Vescovo, H. J. Kim, C. Kwon, R. Ramesh and T. Venkatesan, *Direct evidence for a half-metallic ferromagnet*, Nature **392**, 794-6 (1998)

[52] M. Bowen, M. Bibes, A. Barthélémy, J.-P. Contour, A. Anane, Y. Lemaître, and A. Fert, *Nearly total spin polarization in $La_{2/3}Sr_{1/3}MnO_3$ from tunnelling experiments*, Appl. Phys. Lett. **82**, 233 (2003)

[53] J. Longo and R. Ward, J. Am. Chem. Soc. **83**, 2816-2818 (1961)

[54] K.-I.Kobayashi, T. Kimura, H. Sawada, K. Terakura and Y. Tokura, *Room-temperature magnetiresistance in an oxide material with an ordered double-perovskite structure*, Nature **395**, 677-680 (1998)

[55] K.-I. Kobayashi , T. Kimura, Y. Tomioka, H. Sawada, K. Terakura and Y. Tokura, *Intergrain tunneling magnetoresistance in polycrystals of the ordered double perovskite Sr_2FeReO_6*, Phys. Rev. B **59**, 11159-62, (1999)

[56] A. M. Glazer, *The Classification of Tilted Octahedra in Perovskites*, Acta Cryst. B **28**, 3384-96 (1972);

P. M. Woodward, *Octahedral Tilting in Perovskites. I. Geometrical Considerations*, Acta Cryst. B **53**, 32-43 (1997)

[57] R. D. Shannon, *Revised Effective Ionic Radii and Systematic Studies of Interatomic Distances in Halides and Chalcogenides*, Acta Cryst. **A** 32, 751-67 (1976)

[58] D. Serrate, J. M. De Teresa and M. R. Ibarra, *Double perovskites with ferromagnetism above room temperature*, J. Phys.: Cond. Matter **19**, 02321 (2007)

[59] L. F. Mattheiss, *Band Structure and Fermi Surface for Rhenium*, Phys. Rev. **151**, 450-64 (1966)

[60] J. B. Philipp, P. Majewski, L. Alff, A. Erb, R. Gross, T. Graf. M. S. Brandt, J. Simon, T. Walter, W. Mader, D. Topwal and D. D. Sarma, *Structural and doping effects in the half-metallic double perovskite A_2CrWO_6 (A=Sr, Ba, and Ca)*, Phys. Rev. B **68**, 144431 (2003)

[61] G. Vaitheeswaran, V. Kanachana and A. Delin, *Pseudo-half-metallicity in the double perovskite Sr_2CrReO_6 from density-functional calculations*, Applied Phys. Lett. **86**, 032513 (2005)

[62] W. Westerburg, O. Lang, C. Ritter, C. Felser, W. Tremel and G. Jakob, *Magnetic and structural properties of the double-perovskite Ca_2FeReO_6*, Solid State Commun. **122**, 201-6 (2002)

[63] E. Granado, Q. Huang, J. W. Lynn, J. Gopalakrishnan, R. L. Greene and K. Ramesha, *Spin-orbital ordering and mesoscopic phase separation in the double perovskite Ca_2FeReO_6*, Phys. Rev. B **66**, 064409 (2002)

[64] J. Navarro, C. Frontera, Ll. Balcells, B. Martínez and J. Foncuberta, *Raising the Curie temperature in Sr_2FeMoO_6 double perovskites by electron doping*, Phys. Rev. B **64**, 092411 (2001)

[65] D. Rubi, C. Frontera, J. Nogués and J. Fontcuberta, *Enhanced ferromagnetic interactions in electron doped $Nd_xSr_{2-x}FeMoO_6$ double perovskites*, J. Phys.: Condens. Matter **16**, 3173-82 (2004)

[66] D. Rubi, C. Frontera, J. Foncuberta, M. Wojcik, E. Jedryka and C. Ritter, *Ferromagnetic coupling in $Nd_xCa_{2-x}FeMoO_6$ double perovskites: Dominant band-filling effects*, Phys. Rev. B **70**, 094405 (2004)

[67] D. Serrate, J. M. De Teresa, J. Blasco, M. R. Ibarra and L. Morellon, *Large low-field magnetoresistance and T_C in polycrystalline $(Ba_{0.8}Sr_{0.2})_{2-x}La_xFeMoO_6$ double perovskite*, Appl. Phys. Lett. **80**, 4573-5 (2002)

[68] D. Serrate, J. M. De Teresa, J. Blasco, M. R. Ibarra, L. Morellon and C. Ritter, *Increase of Curie temperature in fixed ionic radius $Ba_{1+x}Sr_{1-3x}La_{2x}FeMoO_6$ double perovskites*, Eur. Phys. J. B **39**, 35-40 (2004)

[69] A. P. Douvalis, M. Venkatesan, J. M. D. Coey, T. Alamelu and U. V. Varadaraju, *^{57}Fe Mössbauer Studies of $Sr_{2-x}Ca_xFeReO_6$ Double Perovskite Compounds*, Hyperfine Interactions **144/145**, 267-72 (2002);

J. Lindén, H. Yamauchi and M. Karppinen, *^{57}Fe Mössbauerspectroscopy investigation of the $Fe^{II/III}$mixed-valance state and the B-site order in double perovskite A_2FeMoO_6*, Journal Magn. Magn. Mat. **272-276**, 843-4 (2004)

[70] P. A. Algarabel, L. Morellon, J. M. De Teresa, J. Blasco, J. García, M. R. Ibarra, T. Hernández, F. Plazaola and J. M. Barandiarán, *Mössbauer spectroscopy in Sr_2FeMoO_6 double perovskite*, Journal Magn. Magn. Mat. **226-230**, 1089-91 (2001)

[71] J. Navarro, Ll. Balcells, F. Sandiumenge, M. Bibes, A. Roig, B. Martínez and J. FFontcuberta, *Antisite defects and magnetoresistance in Sr_2FeMoO_6 double perovskite*, J. Phys.: Condens. Matter **13**, 8481-8 (2001)

[72] J-M. Greneche, M. Venkatesan, M. Grafouté, M. Douvalis, A. Surynarayan and J. M. D. Coey, *Mössbauer spectrometry of A_2FeMoO_6 .A = Ca, Sr, Ba: Search for antiphase domains*, Phys. Rev. B **63**, 174403 (2001)

[73] I. V. Solovyev, *Electronic structure and stability of the ferromagnetic ordering in double perovskites*, Phys. Rev. B **65** 144446 (2002)

[74] T. Saha-Dasgupta and D. D. Sarma, *Ab initio study of disorder effects on the electronic and magnetic structure of Sr_2FeMoO_6*, Phys. Rev. B **64** 064408 (2001)

[75] Ll. Balcells, J. Navarro, M. Bibes, A. Roig, B. Martínez and J. Foncuberta, *Cationic ordering control of magnetization in Sr_2FeMoO_6 double perovskite*, Appl. Phys. Lett. **78**, 781-3 (2001)

[76] J. M. Michalik, J. M. De Teresa, C. Ritter, J. Blasco, D. Serrate, M. R. Ibarra, C. Kapusta, J. Freudenberger and N. Kozlova, *High-field magnetization measurements in Sr_2CrReO_6 double perovskite: Evidence for orbital contribution to the magnetization*, Europhys. Lett. **78**,17006 (2007)

[77] H. Krug, M. Doerr, D. Eckert, H. Wschrig, F. Fisher, P. Fulde, R. Groessinger, A. Handstein, F. Herlach, D. Hinz, R. Kratz, M. Loewenhaupt, K.-H. Müller, F. Pobell, L. Schulz, H. Siegel, F. Steglich and P. Verges, *The Dresden high-magnetic field laboratory – overview and first results*, Physica B **294-295**, 605-11 (2001)

[78] D. Eckert, R. Grössinger, M. Doerr, F. Fisher, A. Handstein, D. Hinz, H. Siegel, P. Verges and K.-H. Müller, *High precision pick-up coils for pulsed field magnetization measurements*, Physica B **294-295**, 705-8 (2001)

[79] M. D. Bird, S. Bole, Y. M. Eyssa, B.-J. Gao and H.-J.Schneider-Muntau, *Design of a Poly-Bitter Magnet at the NHMFL*, IEEE Transactions on Magnetics **32**, 2542-5 (1996)

[80] J. A. A. J. Perenboom, J. C. Maan and S. A. J. Wiegers, *The New Nijmegen Installation for DC and Pulsed High Magnetic Fields*, IEEE Transactions on Applied Superconducticity **10**, 1549-51 (2000)

[81] G. Asti and S. Rinaldi, *Nonanaliticity of the Magnetization Curve: Application to the Measurement of Anisortopy in Polycrystaline Samples*, Phys. Rev. Lett. **28**, 1584-1586 (1972)

[82] G. Asti and S. Rinaldi, *Singular points in the magnetization curve of a*

polycrystalline ferromagnet, J. Appl. Phys. **45**, 3600-10 (1974)

[83] G. Asti, F. Bolzoni and R. Cabassi, *Singular point detection in multidomain samples*, J. Appl. Phys. **73**, 323-33 (1993)

[84] F. Bolzoni, *Role of sample resistivity in pulsed field anisotropy measurements*, Meas. Sci. Technol. **6**, 1186-92 (1995)

[85] F. Bolzoni, *The high-field installation at the MASPEC Institute*, Physica B **294-295**, 618-23 (2001)

[86] A. Uhlir Jr., *The Potentials of Infinite Systems of Sources and Numerical Solutions of Problems in Semiconductor Engineering,* Bell System Tech. Journal **34**, 105-28 (1955);

E. B. Hansen, Appl. Sci. Res. Sect. B **8**, 93-104 (1960)

[87] G. E. Bacon and K. Lonsdale, *Neutron Diffraction*, Oxford 1962

[88] H. M. Rietveld, Acta Cryst **22**, 151 (1967), H. M. Rietveld, *A Profile Refinement Method for Nuclear and Magnetic Structures*, J. Appl. Cryst. **2**, 65-71 (1969)

[89] L. W. Finger, D. E. Cox and A. P. Jephcoat, *A correction for powder diffraction peak asymmetry due to axial divergence*, J. Appl. Cryst. **27**, 892-900 (1994)

[90] L. B. McCusker, R. B. Von Dreele, D. E. Cox, D. Louér and P. Scardi, *Rietveld Refinement Guidelines*, J. Appl. Cryst. **32**, 36-50 (1999)

[91] J.L. Rodríguez-Carvajal, and M.A. Panetier, ILL report 87TR014T (1987); J. Ridriguez-Carvajal, *Reference Guide for the Computer Program FullProf*, Laboratoire Léon Brillouin CEA-CNRS, Saclay, France (1996)

[92] H. Shaked, *A note on the limitations of the magnetic axis direction determination by neutron powder diffraction*, Physica B **335**, 310-3 (2004)

[93] D. E. Sayesrs, E. A. Stern and F. W. Lytle, *New Technique for Investigating Noncrystalline Structures: Fourier Analysis of the Extended X-Ray—Absorption Fine Structure*, Phys. Rev. Lett. **27**, 1204-7 (1971)

[94] G. Meitzner G. Meitzner, G. H. Via, F. W. Lytle and J. H. Sinfelt, *Analysis of X-ray Absorption Edge Data on Metal Catalysts,* J. Phys. Chem. **96**, 4960-4 (1992)

[95] J. J. Rehr and R. C. Albers, *Theoretical approaches to x-ray absorption fine structure*, Rev. Mod. Phys. **72,** 621-55 (2000)

[96] M. Faraday, Philosophical Transactions of The Royal Society **136**, 1 (1846)

[97] J. Kerr, Philosophical Magazine **3,** 321 (1877)

[98] G. Schütz, W. Wagner, W. Wilhelm, P. Kienle, R. Zeller, R. Frahm and G. Materlink, *Absorption of Circularly Polarized X Rays in Iron*, Phys. Rev. Lett. **58**, 737-40 (1987)

[99] C.S. Hwang and P.H. Lin, *Comparison of two superconducting elliptical undulators for generating circularly polarized light*, Phys. Rev. Special Topics -

Accelerators and Beams **7**, 090701 (2004)

[100] P. Carra and M. Altarelli, *Dichroism in the X-Ray Absorption Spectra of Magnetically Ordered System*, Phys. Rev. Lett. **64**, 1286-8 (1990);

B. T. Thole, P. Carra, F. Sette and G. van der Laan, *X-Ray Circular Dichroism as a Probe of Orbital Magnetization*, Phys. Rev. Lett. **68**, 1943-6 (1992);

P. Carra, B. T. Thole, M. Altarelli and X. Wang, *X-Ray Circular Dichroism and Local Magnetic Fields*, Phys. Rev. Lett. **70**, 694-7 (1993)

[101] C. T. Chen, Y. U. Idzerda, H.-J. Lin, N. V. Smith, G. Meigs, E. Chaban, G. H. Ho, E. Pellegrin and F. Sette, *Experimental Confirmation of the X-Ray Magnetic Circular Dichroism Sum Rules for Iron and Cobalt*, Phys. Rev. Lett. **75**, 152-5 (1995)

[102] P. Majewski, S. Geprägs, O. Sanganas, M. Opel, R. Gross, F. Wilhelm, A. Rogalev and L. Alff, *X-ray magnetic circular dichroism study of Re 5d magnetism in Sr_2CrReO_6*, Appl. Phys. Lett. **87**, 202503 (2005)

[103] P. Majewski, S. Geprägs, A. Boger, M. Opel,A. Erb, R. Gross, G. Vaitheeswaran, V. Kanchana, A. Delin, F. Wilhelm, A. Rogalev and L. Alff, *Magnetic moments of W 5d in Ca_2CrWO_6 and Sr_2CrWO_6 double perovskites*, Phys. Rev. B **72**, 132402 (2005)

[104] M.Sikora, Cz. Kapusta, M. Borowiec, C. J. Oates, V. Prochazka, D. Rybicki, D. Zajac, J. M. De Teresa, C. Marquina and M. R. Ibarra, *Evidence of unquenched Re orbital magnetic moment in AA'$FeReO_6$ double perovskites*, Appl. Phys. Lett. **89**, 062509 (2006)

[105] C. Azimonte, E. Granado, J. C. Cezar, J. Gopalakrishnan and K. Ramesha, *Investigation of the local Fe magnetic moments at the grain boundaries of the Ca_2FeReO_6 double perovskite*, Journal of Appl. Phys. **101**, 09H115 (2007)

[106] M. Hagelstein, A. Fontaine and J. Goulon, *High Brilliance Beamline for Time Resolved X-ray Absorption Spectroscopy at ESRF*, Jpn. J. Appl. Phys. **32-2**, 240-2 (1993);

M. Hagelstein, A. San Miguel, A. Fontaine and J. Goulon, *The beamline ID24 at ESRF for energy dispersive x-ray absorption*, J. Phys. IV **C2**, 303-308 (1997);

S. Pascarelli, O. Mathon and G. Aquilanti, *New opportunities for high pressure X-ray absorption spectroscopy using dispersive optics*, J. Alloys Compd. **362**, 33-40 (2004)

[107] J. Stöhr, *Exploring the microscopic origin of magnetic anisotropies with X-ray magnetic circular dichroism (XMCD) spectroscopy*, Journal of Magn. and Magn. Meterials **200**, 470-97 (1999)

[108] P. J. E. M. van der Linden, O. Mathon, C. Strohm, and M. Sikora, *Miniature pulsed magnet system for synchrotron x-ray measurements*, Rev. Sci. Instrum. **79**, 075104 (2008)

[109] O. Mathon, P. van der Linden, T. Neisius, M. Sikora, J. M. Michalik, C. Ponchut, J. M. De Teresa and S. Pascarelli, *XAS and XMCD under high magnetic field and low temperature on the energy-dispersive beamline of the ESRF*, J. Synchrotron Rad. **14**, 409-15 (2007)

[110] O. Mathon, F. Baudelet, J.-P. Itié, S. Pasternak, A. Polian and S. Pascarelli, J. Synchrotron Rad. **11**, 423-7 (2004)

[111] H. Kato, T. Okuda, Y. Okimoto, Y. Tomioka, Y. Takenoya, A. Ohkubo, M. Kawasaki and Y. Tokura, *Metallic ordered double-perovskite Sr_2CrReO_6 with maximal Curie temperature of 635 K*, Appl. Phys. Lett. **81**, 328-30 (2002)

[112] H. Asano, N. Kozuka, A. Tsuzuki and M. Matsui, *Growth and properties of high-Curie-temperature Sr_2CrReO_6 thin films*, Appl. Phys. Lett. **85**, 263-265 (2004)

[113] B. Martínez, J. Navarro, Ll. Balcells, and J. Fontcuberta, *Electronic transfer in Sr_2FeMoO_6 perovskites*, J. Phys.: Condens. Matter **12**, 10515-21 (2000); D. Rubí, J. Nogués, J. S. Muñoz and J. Fontcuberta, *Spin polarized itinerant electrons in Ca_2FeMoO_6 double perovskites*, Mater. Sci. Eng. B **126**, 279-82 (2006)

[114] K. G. Bramnik, G. Miehe, H. Ehrenberg, H. Fuess, A. M. Abakumov, R. V. Shapanchenko, V. Yu. Pomjakushin and A. M. Balagurov, *Preparation, Structure and Magnetic Studies of a New $Sr_{11}Re_4O_{24}$ Double Oxide*, J. Solid State Chem., **149**, 49-55 (2000)

[115] J. M. De Teresa, D. Serrate, C. Ritter, J. Blasco, M.R. Ibarra, L. Morellon and W. Tokarz, *Investigation of high Curie temperature in Sr_2CrReO_6*, Phys. Rev. B **71,** 092408 (2005);

W. Prellier, V. Smolyaninova, A. Biswas, C. Galley, R.L. Greene, K. Ramesha and J. Gopalakrishnan, *Properties of the ferrimagnetic double perovskites A_2FeReO_6 (A = Ba and Ca),* J. Phys.: Condens. Matter **12**, 965 (2000)

[116] T. Alamelu, U.V. Varadaraju, M. Venkatesan, A.P. Douvalis and J.M.D. Coey, *Structural and magnetic properties of $(Sr_{2-x}Ca_x)FeReO_6$*, J. Appl. Phys. **91**, 8909 (2002)

[117] K. Oikawa, T. Kamiyama, H. Kato and Y. Tokura, *Structural Distortion on Metal–Insulator Transition in Ordered Double Perovskite Ca_2FeReO_6*, J. Phys. Soc. Jpn. **72**, 1411-7 (2003);

[118] J.M. De Teresa, D. Serrate, J. Blasco, M.R. Ibarra and L.Morellon, *Impact of cation size on magnetic properties of .$(AA')_2FeReO_6$ double perovskites*, Phys. Rev. B **69**, 144401 (2004)

[119] J. M. Michalik, J. M. De Teresa, J. Blasco, P. A. Algarabel, M. R. Ibarra, C. Kapusta and U. Zeitler, *Temperature dependence of magnetization under high fields in Re-based double perovskites*, J. Phys.: Cond. Matter **19**, 50206 (2007)

[120] H. Kato, T. Okuda, Y. Okimoto, Y. Tomioka, K. Oikawa, T. Kamiyama and Y. Tokura, *Metal-insulator transition of ferromagnetic ordered double perovskites: $(Sr_{1-y}Ca_y)_2FeReO_6$,* Phys. Rev. B **65**, 144404 (2002)

[121] D. Serrate, J. M. De Teresa, P. A. Algarabel, C. Marquina, L. Morellon, J. Blasco and M. R. Ibarra, *Giant magnetostriction in Ca_2FeReO_6 double perovskite*, J. Magn. Magn. Matter **290-291**, 843-5 (2005)

[122] J. Herrero-Martín, G. Subías, J. Blasco, J. García and M. C. Sánchez, *X-ray absorption spectroscopic study on A_2FeReO_6 double perovskites*, J. Phys.:Condens. Matter **17**, 4963-76 (2005)

[123] A Manceau, A. Gorshkov and V. A. Grits, *Structural chemistry of Mn, Fe, Co, and Ni in manganese hydrous oxides: Part I. Information from XANES spectroscopy*, Am. Mineralogist **77**, 1133-43 (1992);

F. Farges, G. E. Brown and J. J. Rehr, *Ti K-edge XANES studies of Ti coordination and disorder in oxide compounds: Comparison between theory and experiment*, Phys. Rev. B **56**, 1809-19 (1997);

T. E. Wessel, P. Kennepohl, J. G. DeWitt, B. Hedman, K. O. Hodgson and E. I. Solomon, *A Multiplet Analysis of Fe K-Edge 1s→3d Pre-Edge Features of Iron Complexes*, J. Am. Chem. Soc. **119**, 6297-314 (1997)

[124] Z. Y. Wu, D. C. Xian, T. D. Hu, Y. N. Xie, Y. Tao, C. R. Natoli, E. Paris and A. Marcelli, *Quadrupolar transitions and medium-range-order effects in metal K-edge x-ray absorption spectra of 3d transition-metal compounds*, Phys. Rev. B **70**, 033104 (2004)

[125] X. Yu, T. Asaka, Y. Tomioka, C. Tsuruta, T. Naai, K. Kimoto, Y. Kaneko, Y. Tokura and Y. Matsui, *TEM study of the influence of antisite defects on magnetic domain structures in double perovskite Ba_2FeMoO_6*, J. Electron. Microsc. **54**, 61-5 (2005)

[126] D. D. Sarma, P. Mahadevan, T. Saha-Dasgupta, S. Ray and A. Kumar, *Electronic Structure of Sr_2FeMoO_6*, Phys. Rev. Lett. **85,** 2549-552 (2000)

[127] Horng-Tay Jeng and G.Y. Guo, *First-principles investigations of orbital magnetic moments and electronic structures of the double perovskites Sr_2FeMoO_6, Sr_2FeReO_6, and Sr_2CrWO_6*, Phys. Rev. B **67**, 094438 (2003)

[128] G. Vaitheeswaran, V. Kanchana, and A. Delin, *Electronic structure of the ferromagneticdouble-perovskites Sr_2CrReO_6, Sr_2CrWO_6, and Ba_2FeReO_6*, J. Phys.: Conference Series **29**, 50-3 (2006)

[129] Y. Tomioka, T. Okuda, Y. Okimoto, R. Kumai, K. I. Kobayashi and Y. Tokura, *Magnetic and electronic properties of a single crystal of ordered double perovskite* Sr_2FeMoO_6, Phys. Rev. B **61**, 422-7 (2000)

[130] O. Chmaissem, R. Kruk, B. Dabrowski, D. E. Brown, X. Xiong, S. Kolesnik J. D. Jorgensen and C. W. Kimball, *Structural phase transition and the electronic and magnetic properties of Sr_2FeMoO_6*, Phys. Rev B **62**, 14197-205 (2000)

[131] E. M. Chudnovsky, W. M. Saslow and R. A. Serota, *Ordering in ferromagnets with random anisotropy*, Phys. Rev. B **33,** 251-61, (1986);

J. Tejada, B. Martinez, A. Labarta and E. M. Chudnovsky E, *Correlated spin glass*

generated by structural disorder in the amorphous $Dy_6Fe_{74}B_{20}$ alloy, Phys. Rev. B **44**, 7698-700 (1991)

[132] E. M. Chudnovsky and R. A. Serota, *Spin-glass and ferromagnetic states in amorphous solids*, Phys. Rev. B **26**, 2697-99 (1982); Chudnovsky E M, *Disorder and spin correlations in an amorphous ferromagnet*, Phys. Rev. B **33**, 2021-3 (1986)

[133] J. M. De Teresa, D. Serrate, J. Blasco, M. R. Ibarra and L. Morellon, *Large magnetoresistance in $(AA')_2FeReO_6$ double perovskites*, J. Magn. Magn. Mater. **290–291**, 1043-9 (2005)

[134] S. E. Lofland, T. Scabarozi, Y. Morimoto and Xu Sh, *Magnetism of the double perovskite Sr_2FeMoO_6*, J. Magn. Magn. Mater. **260** 181-3 (2003)

[135] A. Z. Solontsov*, Finite-temperature magnons in itinerant ferromagnetism*, J. Magn. Magn. Mater. **140-144** 215-6 (1995)

[136] R. Pauthenet, *Experimental verification of spin-wave theory in high fields*, J. Appl. Phys **53** 8187-92 (1982)

[137] M. Sikora, O. Mathon,P. van der Linden, J. M. Michalik, J.M. de Teresa, Cz. Kapusta, and S. Pascarelli, *Investigation of the field-induced magnetostructural transition in Ca_2FeReO_6 double perovskite by XMCD measurements up to 30 T*, Manuscript under preparation.

[138] D. Drouin, A. R. Couture, D. Joly, X. Tastet, V. Aimez and R. Gauvin, *CASINO V2.42 - A Fast and Easy-to-use Modeling Tool for Scanning Electron Microscopy and Microanalysis Users*, Scanning **29**, 92-101 (2007)

[139] J. S. Stephans and D. W. J. Cruickshank, *The Crystal Structure of $(Cr0_3)_\infty$*, Acta Crystall. B **26**, 222-6 (1970)

[140] C. Brouder, *Angular dependence of X-ray absorption spectra*, J. Phys.: Cond. Matter **2**, 701-38 (1990)

[141] Y. Joly, D. Cabaret, H. Renevier and C. R. Natoli, *Electron Population Analysis by Full-Potential X-Ray Absorption Simulations*, Phys. Rev. Lett. **82**, 2398-401 (1999)

[142] A. Magneli, *Orthorhombic rhenium dioxide: a representative of a hypothetic structure type predicted by Pauling & Sturdivant*, Acta Crystall. **9**, 1038-9 (1956)

[143] G. Popov, M. Greenblatt and M. Croft, *Large effects of A-site average cation size on the properties of the double perovskites $Ba_{2-x}Sr_xMnReO_6$: Ad^5-d^1 system*, Phys. Rev. B **67**, 024406 (2003)

[144] J-H. Choy, D-K Kim, S-H. Hwang, G. Demazeau and D-K. Jung, *XANES and EXAFS Studies on the Ir-O Bond Covalency in Ionic Iridium Perovskites*, J. Am. Chem. Soc. **117**, 8557-66 (1995)

[145] Z. Hu, H. Von lips, M. S. Golden, J. Fink, G. Kaindl, F. M. F. de Groot, S. Ebbinghauss and A. Reller, *Multiplet effects in the Ru $L_{2,3}$ x-ray-absorption spectra*

of Ru(IV) and Ru(V) compounds, Phys. Rev. B **61**, 5262-6 (2000)

[146] L. M. F. de Groot, Z. W. Hu, M. F. Lopez, G. Kaindl, F. Guillot and M. Tronc, *Differences between L_3 and L_2 x-ray absorption spectra of transition metal compounds*, J. Chem. Phys. **101**, 6570 (1994)

[147] J. Blasco, J. M. Michalik, J. García, G. Subías, and J. M. De Teresa, *Effects of the lanthanide addition to the Sr_2CrReO_6 double perovskite*, Phys. Rev. B **76**, 144402 (2007)

[148] B. Ravel and M. Newville, *ATHENA, ARTEMIS, HEPHAESTUS: data analysis for X-ray absorption spectroscopy using IFEFFIT*, J. Synchr. Rad. **12**, 537-41 (2005).

[149] Z. Hu, H. Von lips, M. S. Golden, J. Fink, G. Kaindl, F. M. F. de Groot, S. Ebbinghauss and A. Reller, *Multiplet effects in the Ru $L_{2,3}$ x-ray-absorption spectra of Ru(IV) and Ru(V) compounds*, Phys. Rev. B **61**, 5262-6 (2000).

[150] M. Roy, S. J. Gurman and G. van Dorssen, J. de Physique IV **7** (C2), 151-2 (1997).

[151] H. Taguchi, M. Nagao and Y. Takeda, *Relationship between the Electrical Properties and Crystal Structure of $(La_{1-x}Nd_x)CrO_3$ ($0 \leq x \leq 1.0$)*, J. Sol. State Chem. **114**, 236-41 (1995).

[152] A. Kuzmin, J. Purans, G. Dalba, P. Fornasini and F. Rocca, *A high-temperature x-ray absorption spectroscopy study of ReO_3*, J. Phys.: Condens. Matter **8**, 9083-102 (1996).

[153] Dr. J. Blasco – private communication

List of abbreviations

AMR	Anisotropic Magnetoresistance
AS	Antisite (defect)
CMR	Colossal Magnetoresistance
DOS	Density Of States
DP	Double Perovskite
EDX	Energy Dispersive X-ray Spectroscopy
EXAFS	Extended X-ray Absorption Fine Structure
FT	Fourier Transform
GMR	Giant Magnetoresistance
ITMR	Intergrain Tunnel Magnetoresistance
MR	Magnetoresistance
NPD	Neutron Powder Diffraction
PPMS	Physical Properties Measuring System
SDMR	Spin-Disorder Magnetoresistance
SEM	Scanning Electron Microscopy
SO	Spin-Orbit (coupling)
SQUID	Superconducting Quantum Interference Device
TMR	Tunnel Magnetoresistance
VSM	Vibrating Sample Magnetometer
XANES	X-ray Absorption Near Edge Structure
XAS	X-ray Absorption Spectroscopy
XMCD	X-ray Magnetic Circular Dichroism
XRD	X-ray Diffraction

ISBN 978-84-92774-06-7

Prensas Universitarias de Zaragoza